Andreas Fuchs

Localization in Dense-Multipath Channels for Massive IoT Deployments

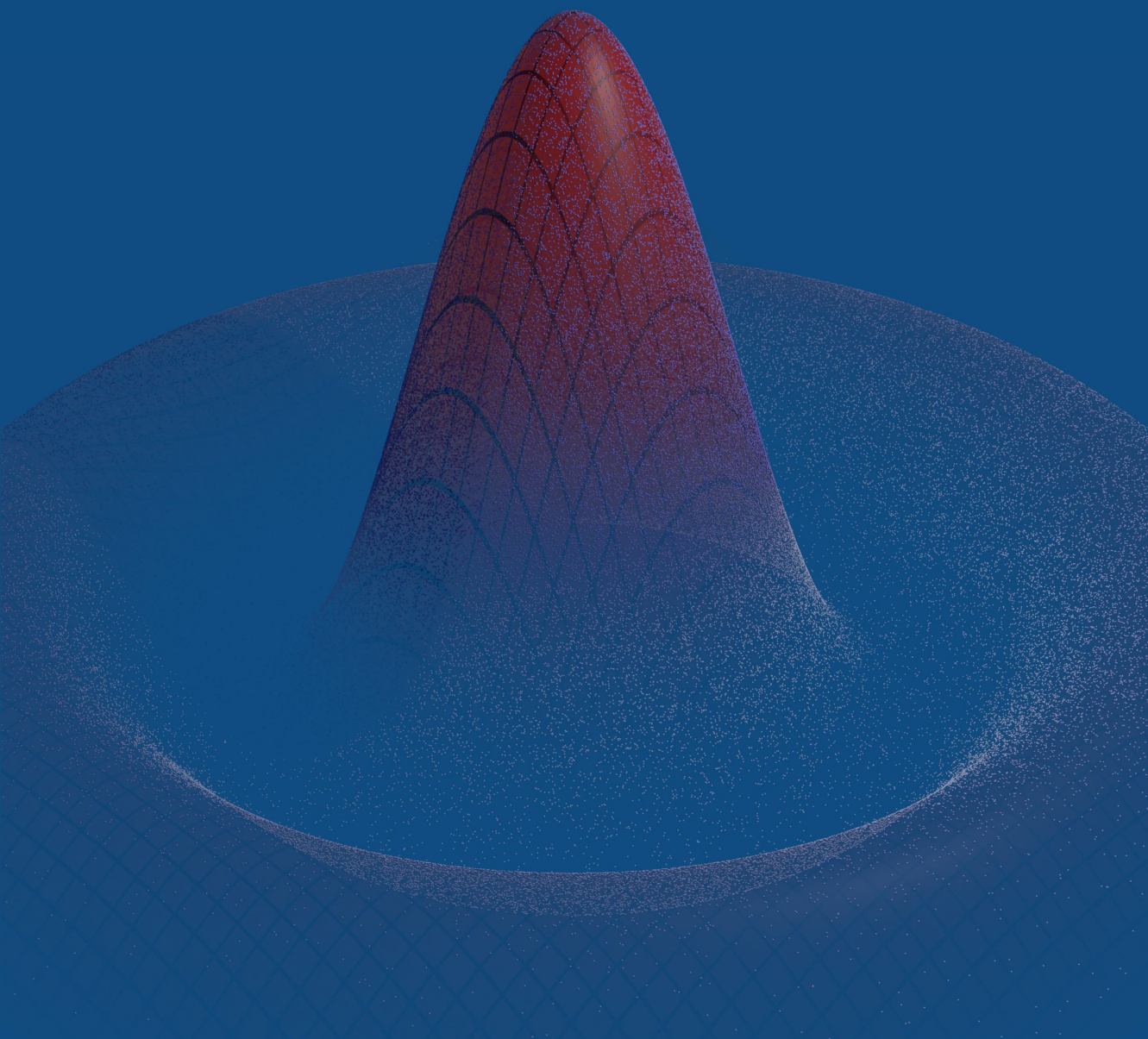

Dipl.-Ing. Andreas Fuchs, BSc

Localization in Dense-Multipath Channels for Massive IoT Deployments

DOCTORAL THESIS

to achieve the university degree of

Doktor der technischen Wissenschaften

submitted to

Graz University of Technology

Supervisors

Univ.-Prof. Dipl.-Ing. Dr. Klaus Witrisal

Institute of Communication Networks and Satellite Communications

Graz, March 2025

Acknowledgment

First and foremost, I would like to express my deepest gratitude to my supervisor, Klaus Witrisal, for his unwavering patience and invaluable guidance in all scientific aspects. It has been a privilege to learn and grow under your supervision.

Next, I extend my heartfelt thanks to Katrin for her everlasting understanding and support. Your willingness to listen to my scientific dilemmas and provide the emotional encouragement I needed throughout this journey has been truly invaluable.

A special thank you also goes to my parents, Bernhard and Irene, whose immense support throughout my studies paved the way for me to reach this point. I am deeply grateful for your encouragement and belief in me.

Another thank you goes to Prof. Christoph Mecklenbräuker, for taking time to examine this thesis.

I would also like to acknowledge a certain group of friends who, in all likelihood, prolonged the completion of this dissertation – but made the journey far more enjoyable. Additionally, they taught me to harbor a strong aversion to jam. Thank you, Leon, Lukas, Paul, and Tobias!

Furthermore, I am grateful to my colleagues from the two institutes I was fortunate to work with during this journey, namely the teams at IKS and SPSC. I have had many enriching discussions with you, especially with those working under Klaus' supervision. A special thanks to my office mates—Agnes, Alexander, Benjamin, Lukas, Maximilian, Thomas, and Vicky—for the camaraderie and engaging exchanges we shared.

I would also like to express my appreciation to those I had the pleasure of collaborating with on this project: Christoph, Daniel, and Holger from TU Wien, whose contributions made many of the measurements in this work possible, as well as Lukas and Stefan, whose insights helped me understand numerous concepts and algorithms incorporated into this thesis.

Finally, I want to thank you, the reader. Many theses end up archived and unread for years, so I truly appreciate you taking the time to engage with this work. I hope you find it insightful and of value.

Abstract

This thesis addresses the challenges of accurate and robust indoor localization in dense multipath (DM) environments, where bandwidth limitations hinder accurate time-of-flight-based position estimation. Focusing on the exploitation of the often-discarded information contained in the DM and of mutual information between nodes, the research develops novel, improved algorithms, that exploit the information contained in the DM. This is shown to be possible through different methods, including extraction of information by a generalized cross-correlation (GCC) and direct estimation of DM parameters. The primary motivation stems from the increasing demand for precise indoor positioning in various applications, coupled with the constraints imposed by low-power, low-cost wireless technologies operating in unlicensed bands like the industrial, scientific, and medical (ISM) band.

The thesis investigates three core hypotheses. The first hypothesis posits that the additional information embedded within the DM can be effectively exploited for ranging and localization, even with limited bandwidth. This is addressed by developing a novel model-based delay estimation method that explicitly incorporates a parametric model of the DM. By directly modeling the DM rather than treating it as interference, this approach achieves significant improvements in both accuracy and robustness, especially in non-line-of-sight (NLOS) scenarios where traditional methods often fail.

The second hypothesis explores the potential for enhancing time-difference-of-arrival (TDoA)-based wideband localization by leveraging mutual information between closely-spaced transmitters. This hypothesis is tackled by introducing a cooperative localization algorithm that utilizes a GCC framework. The GCC captures the similarity of wideband measurements between nodes in close proximity, effectively exploiting the shared information embedded in their multipath profiles. To address the computational complexity of GCC in large-scale scenarios, a computationally efficient approximation based on perceptual hashing is proposed. This method compresses wideband signals into compact hashes and introduces a distance metric based on the similarity of these hashes, providing a practical alternative for information coupling, which is a term describing correlations between transmitters. Furthermore, the algorithm incorporates a geometric prior within a message-passing framework to constrain the search space to plausible locations, enhancing the accuracy and efficiency of position estimation. The performance is compared to a cooperative localization method that utilizes additional received signal strength (RSS) measurements, demonstrating that comparable or even superior accuracy can be achieved without requiring these extra measurements.

The third hypothesis investigates the feasibility of implementing these computationally demanding algorithms efficiently, enabling their application to large datasets. This is addressed through algorithm optimization and the use of particle-

based estimators, demonstrating practical implementation strategies for both the model-based dense multipath component (DMC) estimation and the cooperative localization algorithm. A clustering approach based on RSS measurements is also introduced as a means of further reducing the computational burden in large-scale deployments. By grouping nodes based on RSS, this approach enables efficient joint processing of wideband measurements within clusters, significantly reducing the computational complexity while maintaining acceptable accuracy.

To validate the proposed methods and quantify their performance limits, the thesis derives theoretical performance bounds, including the Cramér-Rao lower bound (CRLB) for various scenarios. The impact of clustering on the CRLB is analyzed, introducing a correction factor to account for the information loss associated with approximating node positions by a cluster center. A biased lower bound is also analyzed to account for the discrepancy between the estimated cluster position and the true node position.

Extensive simulations and real-world experiments using wideband measurements validate the theoretical analysis and demonstrate significant performance gains compared to conventional methods for all methods described in this thesis.

Affidavit

I declare that I have authored this thesis independently, that I have not used other than the declared sources/resources, and that I have explicitly indicated all material which has been quoted either literally or by content from the sources used. The text document uploaded to TUGRAZonline is identical to the present doctoral thesis.

(date) (signature)

Contents

I Introduction and Main Results **1**

1 Introduction to Research Topics **3**
1.1 Introduction . . . 3
1.2 Research Hypotheses . . . 8
1.3 Contribution and Outline . . . 9

2 System and Signal Models **11**
2.1 Wideband Signal Model . . . 11
2.1.1 Signal Model for Pulse Signal . . . 12
2.1.2 Signal Model for Chirp Signal . . . 14
2.2 RSS Signal Model . . . 15

3 Likelihood Models and Estimators **17**
3.1 MAP-based Estimation and its Application in Localization . . . 17
3.2 Time-of-Arrival Estimation in DMC under Bandwidth Limitation . . 18
3.3 Coherent Chirp Synthesis of Multiband Signals . . . 19
3.4 Cooperative Localization and Clustering . . . 20
3.4.1 Posterior PDF for Cooperative Localization . . . 20
3.4.2 Single-Node Likelihood for WB . . . 22
3.4.3 Likelihoods for Inter-Node Coupling . . . 23
3.4.4 Likelihood for Clustering . . . 25

4 Selected Results **27**
4.1 Time-of-Arrival Estimation in Bandwidth-Limited DMC . . . 27
4.2 Coherent Chirp Synthesis of Multiband Signals . . . 31
4.3 TDoA Localization . . . 34
4.3.1 Scenario for TDoA Localization . . . 35
4.3.2 CRLB for Clustering . . . 35
4.3.3 Results for TDoA Localization . . . 38

5 Conclusion **41**

II Included Papers **51**

A Time-of-Arrival Estimation for Positioning in Bandwidth-Limited Dense Multipath Channels **53**
A.1 Introduction . . . 54

A.2 Signal Model 55
A.3 Ranging Error Bound 57
A.4 Numeric evaluation 58
A.5 Conclusion 61
A.6 Appendix 62

B Wideband TDoA Positioning Exploiting RSS-Based Clustering 65
B.1 Introduction 65
B.2 Notation 69
B.3 Signal Model 70
B.4 Clustering Approach 71
B.5 Cramér-Rao Lower Bound 72
B.6 Numeric Evaluation 75
B.7 Conclusion 88
B.8 Appendix: Derivation of equivalent Fisher information matrix (EFIM) 88
B.9 Appendix: Derivation of the ranging error bound (REB) and correction Factor Λ 89
B.10 Appendix: Derivation the AEB 91

C Wideband Cooperative Localization through Generalized Cross-Correlation 97
C.1 Introduction 98
C.2 Signal Models 101
C.3 System model 103
C.4 Inter-node localization 111
C.5 Experimental Evaluation 112
C.6 Conclusion 120

D Performance Bounds for Coherent Chirp Synthesis in Multiband Signals 131
D.1 Introduction 131
D.2 Signal Model 133
D.3 Cramér-Rao lower bound 136
D.4 Evaluation 139
D.5 Conclusion 140

Notation

x	Scalar values are denoted by non-bold characters.
$\mathbf{x}$	Vectors are denoted by boldface lower-case characters.
$\mathbf{X}$	Matrices are denoted by boldface upper-case characters.
$\mathcal{L}$	Sets are denoted by calligraphic notation.
$\mathbf{x}^T$	The transpose of a vector is denoted by superscript T.
$\mathbf{x}^H$	The hermitian transpose of a vector is denoted by superscript H.
x^*	The complex conjugate of a value is denoted by a superscript $*$. This also applies to vectors, but element-wise.
$\angle x$	The argument of a scalar is denoted by the symbol $\angle$. This also applies to vectors, but element-wise.
$[\mathbf{X}]_{N\times N}$	This denotes the upper left $N \times N$ sub-block of a matrix.
$[\mathbf{X}]_{n,m}$	This denotes the n, m-th element of a matrix.
$[\mathbf{x}]_n$	This denotes the n-th element of a vector.
$\lvert\mathbf{x}\rvert$	The vector of absolute values is denoted by the symbols $\lvert$ encasing the vector.
$\lVert\mathbf{x}\rVert$	The Euclidean norm of a vector is denoted by the symbols $\lVert$ encasing the vector.
$\mathbb{E}[\mathbf{x}]$	The expectation operator is denoted by $\mathbb{E}$.
$\mathrm{tr}\{\mathbf{X}\}$	The trace of a matrix is denoted by the operator tr.
$\det(\mathbf{X})$	The determinant of a matrix is denoted by the operator det.
$F(\mathbf{x})$	The Fourier-transform of a vector is denoted by the operator F.
$F^{-1}(\mathbf{x})$	The inverse Fourier-transform of a vector is denoted by the operator F^{-1}.
$\mathbf{W}$	A Fourier-transformation matrix of corresponding size.
$f(\mathbf{x} \mid \mathbf{y})$	The probability density function of a vector $\mathbf{x}$ depending on a parameter set $\mathbf{y}$ is denoted by the operator f.
$O(x)$	The operator O denotes big-O notation for computational complexity.

Part I

Introduction and Main Results

1 Introduction to Research Topics

1.1 Introduction

Indoor localization has emerged as a critical enabling technology for a plethora of applications across various sectors. From enhancing navigation and logistics within complex environments like hospitals, hotels, and shopping malls to enabling precise asset tracking in industrial settings, and facilitating location-aware services in smart homes utilizing internet of things (IoT) devices [1–9], the demand for accurate and reliable indoor positioning systems continues to grow. However, the very nature of indoor environments poses significant challenges to achieving the desired levels of accuracy and reliability. These challenges primarily stem from the complex propagation characteristics of radio signals, which are the most commonly used medium for indoor localization [7, 10–16].

Unlike outdoor environments where line-of-sight (LoS) propagation often dominates, indoor scenarios are characterized by the presence of numerous obstacles, such as walls, furniture, and people, that cause reflection, diffraction, and scattering of radio waves. This leads to multipath propagation, where multiple copies of the transmitted signal arrive at the receiver with varying delays, amplitudes, and phases [1, 13, 17–21]. The resulting channel impulse response (CIR) exhibits a complex structure, especially in dense multipath (DM) environments, where the number of multi-path components (MPCs) is high and their propagation delays are closely spaced. This complexity makes it difficult to accurately extract the LoS component, which is the primary source of information for many localization techniques, especially time-based methods. The detrimental effects of multipath become even more pronounced when the signal bandwidth is limited, as is often the case with low-power wireless technologies operating in unlicensed frequency bands, such as the industrial, scientific, and medical (ISM) band [3, 5, 22–24].

Several techniques have been proposed to address the challenges of indoor localization. They can broadly be categorized based on the type of measurements they employ:

- Time-based techniques: These techniques utilize the time-of-flight (ToF) or time-difference-of-arrival (TDoA) of radio signals to estimate distances between nodes. Time-based techniques are heavily affected by DM. Accurate

extraction of the LoS signal is of vital importance to achieve precise distance measurements. Ultra-wideband (UWB) signals are beneficial due to their resolvability of multipath because of their large bandwidth [14,15,25,26]. However, the wide bandwidth comes with an increase of cost and complexity of the transceiver chips, making them economically unviable for many applications. Therefore, there is still an urge to develop new and efficient time-based techniques for other signals with smaller bandwidths, where an accurate resolution of discrete multipath components is often not possible [27, 28].

- Received signal strength (RSS)-based techniques: These techniques leverage the attenuation of radio signals with distance to estimate the proximity between nodes [10, 29, 30]. While often relatively simple to implement, RSS-based methods are very susceptible to multipath fading and shadowing, which affects signal attenuation and degrades localization accuracy, due to small bandwidths. These methods mostly suffer from smaller information content, requiring more measurements for the same localization performance.

- Angle-based techniques: These techniques estimate the angle of arrival (AoA) of radio signals at the receiver, often employing antenna arrays [9, 31]. AoA estimation can be used in conjunction with other techniques, like TDoA, to improve localization accuracy, sometimes called direct positioning algorithms [28]. However, accurate AoA estimation can be challenging in DM environments, where the presence of multiple signal paths can lead to ambiguities in the estimated angle. In practice, these techniques also require delicate calibration of array antennas, making these techniques expensive to implement.

- Hybrid techniques: These techniques combine different types of measurements, such as time-of-arrival (ToA), RSS, and AoA, to leverage their complementary strengths and improve localization performance [5, 32–35]. Hybrid methods often exhibit higher computational complexity than single-measurement methods, as they require fusion of information from multiple sources, but can benefit from the strengths, while mitigating their respective errors.

- Cooperative localization techniques: These techniques are able to exploit (relative) information between multiple nodes to be positioned. They may incorporate a large number of so-called "cooperative measurements", but solutions can often be time-intensive to compute. A special field of algorithms is utilized, namely cooperative localization algorithms [36–45], which are able to estimate a joint solution to a sufficient degree, in a time-efficient manner.

- Fingerprinting and machine learning-based techniques: These techniques create a database of RSS or CIR measurements at known locations, which is then used to match online measurements and estimate the location of a device [30, 46–48]. Fingerprinting-based methods can achieve high accuracy in static environments but often require extensive training efforts and are sensitive to changes in the environment and scenario.

This dissertation focuses mainly on two measurement methods, namely wideband and RSS. The wideband measurements are acquired from radio nodes at

unknown positions, briefly notated as “nodes”, which are able to transmit wide-band radio signals to so-called “access points (APs)” at known positions. The APs typically consist of multiple receiving antennas, connected to general-purpose software-defined radios (SDRs). Additionally, the nodes can transmit and receive signals from which one can extract cooperative RSS measurements, although with smaller bandwidths. Using these two measurements methods, we can acquire wide-band measurements with relatively high information content from nodes to infrastructure, with bandwidths covering the whole industrial, scientific, and medical (ISM) band, extending over 80 MHz at 2.4 GHz, and so-called cooperative RSS measurements between every node, with smaller information content.

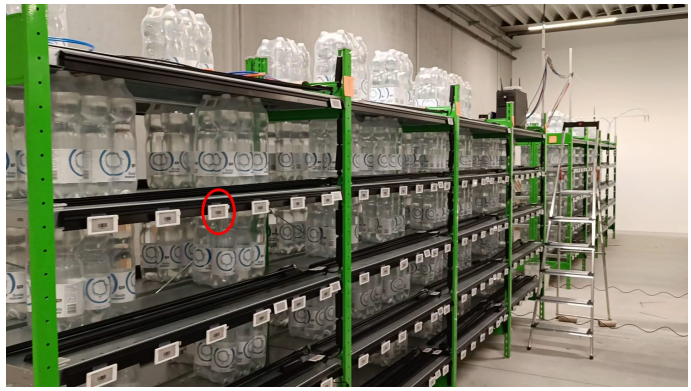

Figure 1.1: Red ellipse marking one node.

Figure 1.2: A typical node shown in detail, containing a display, a radio transceiver and several other electronic components.

RSS-measurements are acquired by every node within the measurement scenario. Every node is able to communicate and store RSS-measurements from every other node within range. This quickly leads to a very large number of measurements, but as their bandwidth is low and as these measurements can be strongly affected by fading, the information content of each individual measurement is very small [44]. A few of the nodes that were used for this work are shown in Figure 1.1 within a typical measurement scenario, and one node can be seen in detail in Figure 1.2.

Figures 1.3 and 1.4 illustrate the same typical scenario, showing APs (in blue) and 1073 node positions (in black) from an isometric and top-down perspective, respectively.

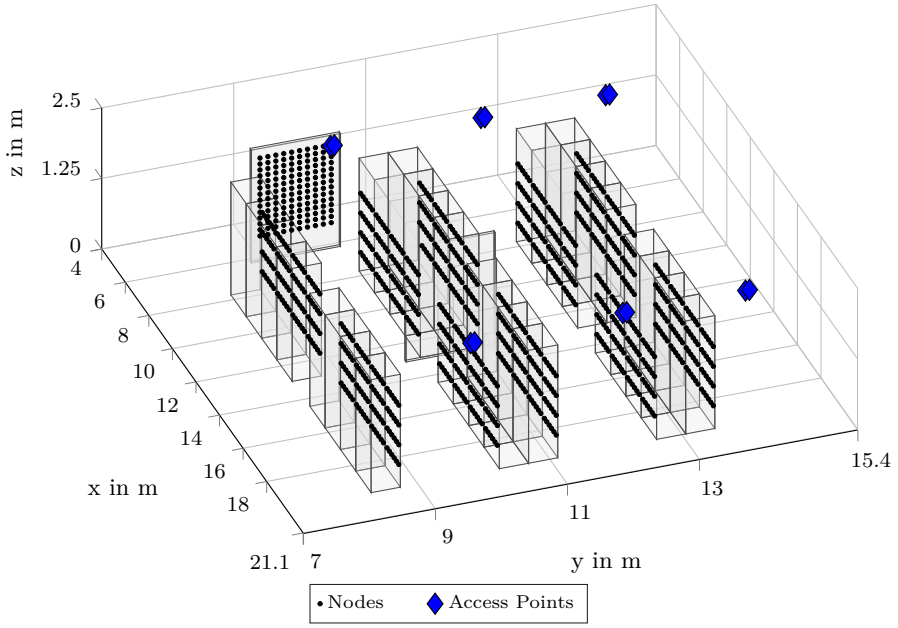

Figure 1.3: Isometric view of scenario.

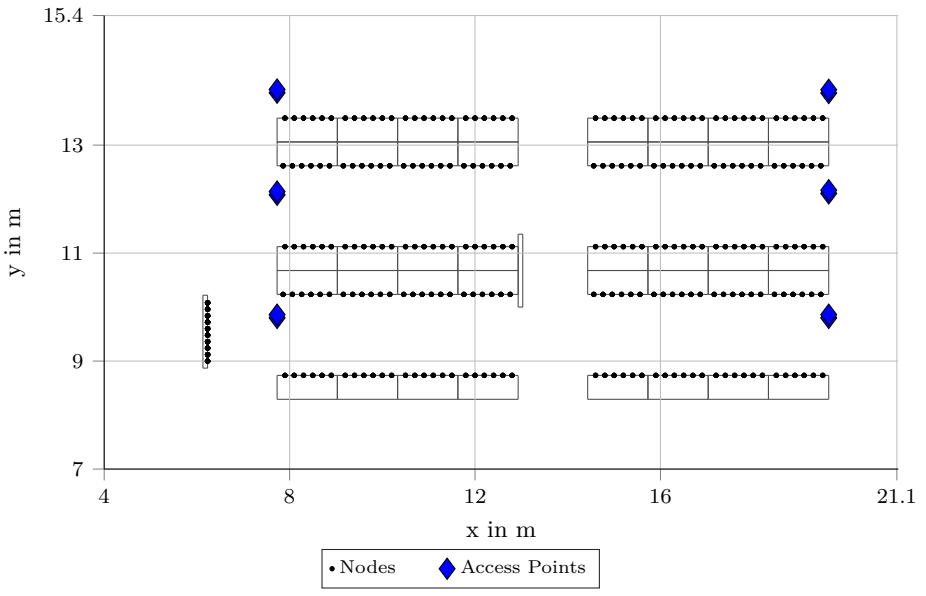

Figure 1.4: Top view of scenario.

Figure 1.5: Red ellipse marking one AP, consisting of one linear 2-antenna array.

Figure 1.6: The measurement PC is marked in red, which is connected to the SDRs, orchestrating all wideband measurements.

Wideband measurements are in our case acquired from wideband chirps. Here, we have to mitigate a limitation of our measurement system, being a small maximum coherent transmit bandwidth. Thus, the nodes transmit multiple so-called subchirps, which span only a fraction of the whole measurement bandwidth. These subchirps are shifted in starting frequency in such manner that the subchirps overlap in their respective sub-bands. From these subchirps, a full chirp spanning the whole measurement bandwidth can be reconstructed [3, 49]. The reconstructed chirp is then compressed into a pulse, containing most of the ToF and AoA information from the chirps. These preprocessing steps are executed for each receive antenna of each access point. Typically the APs are equipped with two to four antennas each. All measurements are sample-coherent between APs and phase-coherent within the antennas of every AP [5, 50]. This leads to wideband measurements, which contain information for each single node. A picture of this wideband measurement system can be seen in Figure 1.5, where a single AP consisting of two antennas is marked in red. The measurement PC, orchestrating all measurements in conjunction with the SDRs, can be seen in Figure 1.6, where it is marked in red. These pictures additionally show a typical measurement scenario, for which

Figure 1.7: The outcome from replacing the batteries of about 1000 nodes, signifying the need for low battery consumption.

the algorithms in this work are validated.

The wideband measurement method has some limitations, which are to be mitigated by algorithms. First of all, the absolute transmit time of a node is not known at the receiving APs, which has to be considered as an additional degree of freedom for localization. This can be mitigated by a large enough number of receiving APs, using either a TDoA or a direct positioning approach for localization. Furthermore, these measurements, while being much larger in bandwidth than RSS measurements, still suffer from fading, shadowing and DM. This leads to some combinations of measurement nodes and receiving antennas being relatively uninformative, i.e. the LoS is not dominating the measurement, but other (dense) multipath components are larger in measured amplitude and energy.

To improve the positioning performance of nodes affected by these impairments, new algorithms are developed in this work, where not only the information of the DM is exploited, but also mutual information in-between nodes. The latter is obtained either by additional measurements, or by exploiting the similarity of statistics between close-by transmitting nodes. This has been shown in theoretical work to be possible for very small numbers of nodes. For example, theoretical work regarding only three cooperating agents [51] exists, which derives the achievable accuracy from the Fisher information (FI). Slightly larger scenarios, up to 40 nodes, are exploited in simulations for mutual information [52, 53] and hybrid localization using ToA and AoA [54]. But these works only show theoretical and some simulation results, and do not incorporate prior information for single nodes.

1.2 Research Hypotheses

This dissertation answers three main hypotheses, all of which are solved by new algorithmic concepts presented in the appended papers (in the following notated as Papers [A]-[D]) .

Current approaches for delay and position estimation in radio channels often disregard additional information from DM, trying to mitigate the interference from it [17]. This leaves information unused, weakening performance of the estimator. Some existing work incorporates the additional information for higher bandwidths,

e.g. in UWB based positioning systems [55], but existing estimators for wideband applications neglect this. This work anticipates that the additional information from the DM can be used in various different ways, leading to our first hypothesis.

Hypothesis 1

It is possible to exploit **additional information from DM** for ranging and localization, in spite of a small (sub-UWB) measurement bandwidth.

Existing work shows that it is possible to improve the localization performance of single nodes by incorporating additional (prior) information on their relative position to other nodes [38–41], but this was not yet tried for localization utilizing wideband measurements. This work argues that we can improve the localization performance for single nodes either by incorporating additional measurements between nodes (i.e. RSS measurements), or by extracting relative position information between nodes from the measured wideband signals themselves. This leads us to our second hypothesis.

Hypothesis 2

The performance of TDOA-based wideband localization can be improved by utilizing **(mutual) relative position information from closely-spaced transmitters**

It has been shown in literature that maximum likelihood (ML) and maximum a-posteriori (MAP) estimation can be computationally demanding, especially when models are becoming increasingly complex. These estimation algorithms tend to be impractical for use-cases where results are needed within relatively short time frames. Thus, this work shows that many of these algorithms can either be made computationally viable by simplification, approximation, or by exploitation of mathematical properties of the estimator. The takeaway from this is the following hypothesis:

Hypothesis 3

Algorithms for (cooperative) localization and ranging can be **implemented or approximated in an efficient manner**, allowing to work on large-scale scenarios.

1.3 Contribution and Outline

The thesis is split into two parts:

Part I, gives an introduction and overview to the topics of appended Papers [A]-[D] and shows main results.

Chapter 2 describes the underlying signal models that are used in this work.

Chapter 3 then describes the system model and likelihoods, being the foundation of all algorithms of this thesis. Additionally, it gives an overview of MAP-based estimation. Afterwards, in Chapter 4, selected results of the appended Papers [A]-[D] are shown, aiming to give an impression on how well the algorithms perform compared to their theoretical bounds. Lastly, Chapter 5 gives a conclusion for the first part of this thesis.

In Part II, the Papers [A]-[D] in are given in their full form, where [A] investigates an algorithm for delay and parameter estimation in dense multipath channels, [B] shows an algorithm for the fusion of multiple wideband measurements by a clustering algorithm, [C] extends this concept to a joint posterior estimation of many nodes, exploiting mutual information of nodes within a vicinity, and [D] describes and validates the theoretical performance bounds for chirp synthesis, which is a necessary pre-processing step for our physical measurements to be used in the previous publications.

List of Included Publications

[A] A. Fuchs and K. Witrisal, "Time-of-Arrival Estimation for Positioning in Bandwidth-Limited Dense Multipath Channels," in *2022 IEEE 23rd International Workshop on Signal Processing Advances in Wireless Communication (SPAWC)*, 2022, doi: 10.1109/SPAWC51304.2022.9833995.

[B] A. Fuchs, L. Wielandner, D. Neunteufel, H. Arthaber and K. Witrisal, "Wideband TDoA Positioning Exploiting RSS-Based Clustering," in *Sensors 2023, 23, 5772*, 2023, doi:10.3390/s23125772

[C] A. Fuchs, L. Wielandner and K. Witrisal, "Wideband Cooperative Localization through Generalized Cross-Correlation," in *IEEE Access*, 2024, doi:10.1109/ACCESS.2024.3518073

[D] A. Fuchs, A. Feiersinger and K. Witrisal, "Performance Bounds for Coherent Chirp Synthesis in Multiband Signals," in *2025 19th European Conference on Antennas and Propagation (EuCAP) (EuCAP 2025)*, 2025, submitted and accepted.

2
System and Signal Models

For a better understanding of the included Papers [A]-[D], this Chapter gives generalized signal models. Formulated are two main signal models for ToF and RSS. For the wideband signal model, two signal atoms are formulated, as to represent all signal models used within the papers.

Figure 2.1 illustrates an overview of the signal models used in this work. Here, the transmitted ToF signals between agents l and anchors m are shown as $\mathbf{r}_{l,m}$, $m = 1, 2$. Between agents l and i, a cooperative signal is shown as $\mathbf{z}_{l,i}$. The cooperative signal will be interchanged in this work with either RSS signals (which are measured by the agents themselves), or a (correlation) metric between ToF signals of the corresponding agents.

2.1 Wideband Signal Model

For ToF, a wideband signal model is used for all incorporated papers, however Paper [D] uses a different signal atom, namely a chirp signal instead of a pulse signal.

The wideband signal model is similar to [18, 22, 56]. The system model comprises L transmitting nodes at coordinates $\mathbf{p}_l = [p_{l,\mathrm{x}}, p_{l,\mathrm{y}}, p_{l,\mathrm{z}}]^T \in \mathbb{R}^3$ for $l \in \{1, \ldots, L\}$, and receiving antennas at positions $\mathbf{q}_{m,k} \in \mathbb{R}^3$ for $m \in \{1, \ldots, M\}$ and $k \in \{1, \ldots, K\}$. The indices k and m denote the antennas within each anchor and the anchors, respectively.

The radio channel between the transmitting node l and the receiving antenna k of anchor m is given by

$$h_{l,m,k}(t; \mathbf{p}_l) = \alpha_{l,m} \delta\left(t - \tau(\mathbf{p}_l, \mathbf{q}_{m,k})\right) + \nu_{l,m,k}(t), \tag{2.1}$$

with propagation delay $\tau(\mathbf{p}_l, \mathbf{q}_{m,k}) = \frac{1}{c} \|\mathbf{p}_l - \mathbf{q}_{m,k}\|$, the speed of light c, and the complex amplitude $\alpha_{l,m}$ of the received LoS signal from node l to anchor m, assuming one complex amplitude per anchor, consisting of multiple antennas. Position-dependent phase shifts between antennas are described later. The dense multipath component (DMC) $\nu_{l,m,k}(t)$ is described by a zero-mean complex Gaussian random process. Assuming uncorrelated scattering, this is modeled by the auto-correlation

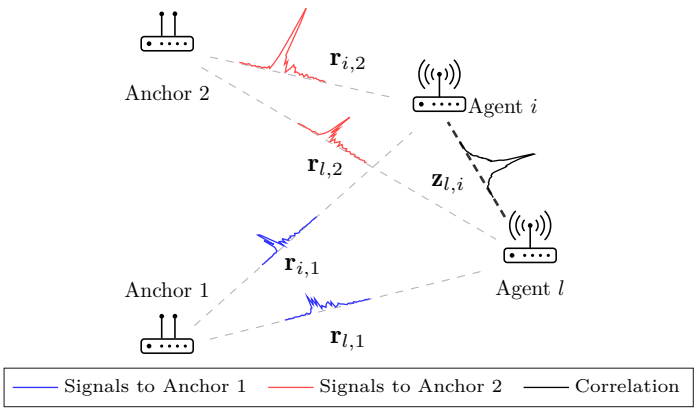

Figure 2.1: Conceptual overview of cooperation between two agent nodes and two anchors as well as directly transmitted signals.

function

$$\begin{aligned}\mathbb{E}\left[\nu_{l,m,k}(t)\nu^{*}_{l',m',k'}\left(t'\right)\right] = S_{\nu}\left(t-\tau(\mathbf{p}_l,\mathbf{q}_m),\tilde{\boldsymbol{\eta}}_{l,m}\right)\delta\left(t-t'\right)\\ \delta\left[l-l'\right]\delta\left[m-m'\right]\delta\left[k-k'\right],\end{aligned} \tag{2.2}$$

where $\tau(\mathbf{p}_l,\mathbf{q}_m) = \frac{1}{c}\left(\|\mathbf{p}_l-\mathbf{q}_m\|\right)$ is a mean delay per anchor m, with $\mathbf{q}_m$ being the mean antenna position per anchor m. We introduce the delay power spectrum (DPS) $S_{\nu}(t;\tilde{\boldsymbol{\eta}})$ similar to [17, 25] as

$$S_{\nu}(t;\tilde{\boldsymbol{\eta}}) = \Omega_1 \frac{\gamma_f+\gamma_r}{{\gamma_f}^2}\mathrm{e}^{-t/\gamma_f}(1-\mathrm{e}^{-t/\gamma_r})u(t), \tag{2.3}$$

where $\tilde{\boldsymbol{\eta}} = [\Omega_1,\gamma_f,\gamma_r]^T$ corresponds to the normalized power of the DMC Ω_1, the fall time γ_f, and the rise time γ_r. The step function $u(t)$ is defined as 1 for $t \geq 0$, and 0 otherwise.

2.1.1 Signal Model for Pulse Signal

This subsection describes the signal model for a pulse signal atom. A conceptual visualization of this can be seen in Figure 2.2, where a pulse with a bandwidth of 80 MHz is illustrated. Assuming each node l transmits a baseband signal $s(t)$ at frequency f_c, the received signal at anchor m and antenna k is

$$\begin{aligned}r_{l,m,k}(t) =& \tilde{\alpha}_{l,m,k}s(t-\tau(\mathbf{p}_l,\mathbf{q}_{m,k})-\epsilon_l)\\ &+\int s(t-\lambda)\nu_{l,m,k}(\lambda+\epsilon_l)d\lambda + w_{l,m,k}(t),\end{aligned} \tag{2.4}$$

with a complex amplitude $\tilde{\alpha}_{l,m,k} = \alpha_{l,m}\mathrm{e}^{-j2\pi f_c(\tau(\mathbf{p}_l,\mathbf{q}_{m,k})+\epsilon_l)}$ that accounts for the phase shift at antenna k with respect to the joint amplitude $\alpha_{l,m}$ at array antenna m, ϵ_l is the transmit time of node l, and $w_{l,m,k}(t)$ is additive white Gaussian noise (AWGN) with double-sided power spectral density (PSD) $N_0/2$. The sampled and stacked received signals are described as

$$\mathbf{r}_{l,m} = \mathbf{s}(\mathbf{p}_l,\mathbf{q}_m,\epsilon_l)\alpha_{l,m} + \mathbf{w}_{l,m} \in \mathbb{C}^{N_s K\times 1}, \tag{2.5}$$

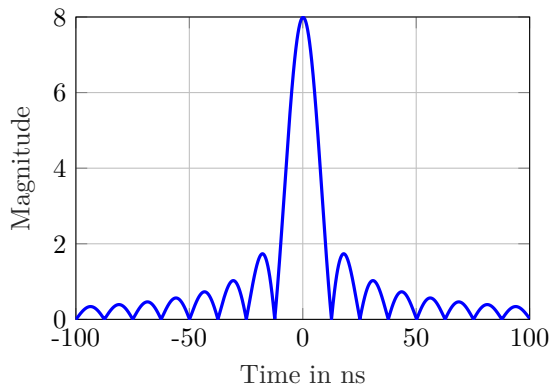

Figure 2.2: Conceptual illustration of a pulse signal atom with a bandwidth of 80 MHz.

where $\mathbf{r}_{l,m} = \left[\mathbf{r}_{l,m,1}^T, \ldots, \mathbf{r}_{l,m,K}^T\right]^T$ stacks the received signals of K antennas at anchor m. The noise vector $\mathbf{w}_{l,m}$ describes the DMC and AWGN. The baseband signal vector in (2.5) accounts for the phase shifts at the array antennas,

$$\begin{aligned}\mathbf{s}(\mathbf{p}_l, \mathbf{q}_m, \epsilon_l) = [&\mathrm{e}^{-j2\pi f_c(\tau(\mathbf{p}_l,\mathbf{q}_{m,1})+\epsilon_l)}\tilde{\mathbf{s}}(\tau(\mathbf{p}_l,\mathbf{q}_m)+\epsilon_l)^T, \ldots, \\ &\mathrm{e}^{-j2\pi f_c(\tau(\mathbf{p}_l,\mathbf{q}_{m,K})+\epsilon_l)}\tilde{\mathbf{s}}(\tau(\mathbf{p}_l,\mathbf{q}_m)+\epsilon_l)^T]^T\end{aligned} \tag{2.6}$$

where

$$\begin{aligned}\tilde{\mathbf{s}}(t) \in \mathbb{C}^{N_s\times 1} = [&s(-t), s(-t+T_s), \ldots, \\ &s(-t+(N_s-1)T_s)]^T\end{aligned} \tag{2.7}$$

is a sampled version of $s(t)$ with T_s being the sampling time interval. This represents a wideband phased-array signal model with identical envelopes, and phase shifts which allow us to exploit AoA information.

The covariance matrix $\mathbf{C}_{l,m}$ characterizes the noise vector $\mathbf{w}_{l,m}$, representing AWGN and DMC. We define $\mathbf{C}_{l,m}$ as a block-diagonal matrix composed of the matrices $[\mathbf{C}_{l,m}]_k$ for each antenna k of anchor m. This k-th matrix is defined as $[\mathbf{C}_{l,m}]_k = [\mathbf{C}_{l,m}^{(\nu)}]_k + [\mathbf{C}_{l,m}^{(w)}]_k \in \mathbb{C}^{N_s\times N_s}$, with the AWGN component $[\mathbf{C}_{l,m}^{(w)}]_k = \sigma_{l,m}^2\mathbf{I}$, where $\mathbf{I}$ is the identity matrix of according dimensions, and noise variance $\sigma_{l,m}^2 = N_0/T_s$. The covariance for the DMC is

$$\left[\mathbf{C}_{l,m}^{(\nu)}\right]_k = \int S_\nu\left(\lambda - \tau(\mathbf{p}_l,\mathbf{q}_m) - \epsilon_l; \tilde{\boldsymbol{\eta}}_{l,m}\right)\tilde{\mathbf{s}}(\lambda)\tilde{\mathbf{s}}(\lambda)^{\mathrm{H}}d\lambda. \tag{2.8}$$

This signal model applies directly to Papers [B] and [C], where there are multiple transmitting nodes and receive antennas. In the case described in Paper [A], this signal model simplifies, as there is only one transmitting node and receiving antenna taken into consideration. For this case, we must assume that the positions of antennas are known, and only an unknown relative delay remains within the signal model. Therefore, we obtain the following simplified received signal for Paper [A]

given as

$$r(t) = \tilde{\alpha} s(t-\tau) + \int s(t-\lambda)\nu(\lambda)d\lambda + w(t), \tag{2.9}$$

where the delay τ is an unknown delay. Please note that for simplicity, the indices l, m, k are neglected, as this signal model is only used for single transmitted signals. Further derivation steps remain the same.

2.1.2 Signal Model for Chirp Signal

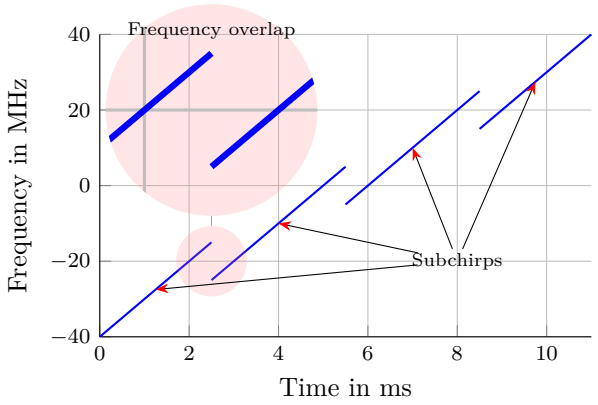

Figure 2.3: Concept for overlapping multiband subchirps which illustrate the signal atoms.

The signal model given in Section 2.1.1 assumes pulse signals. Paper [D] of this work focuses on an efficient method to combine incoherent (phase-shifted) chirps over different frequency bands into one coherent chirp signal. These coherent chirp signals can be compressed into pulse signals, but for further considerations regarding Paper [D], we introduce a chirp signal model. A conceptual visualization of multiple so-called subchirps can be seen in Figure 2.3, with an overall bandwidth of 80 MHz over a duration of 11 ms. Additionally, a frequency overlap between the subchirps is illustrated. Please note again, that the indices l, m, k are neglected, as this signal model is only used for single transmitted signals.

The instantaneous frequency of the p-th subchirp with the starting frequency f_p and the chirp rate c_r is expressed as

$$f_p(t) = c_r t + f_p \tag{2.10}$$

with index $p = [1, \ldots, N_p]$ and N_p representing the number of subchirps. A time variable t is bounded by $0 \leq t \leq T_c$. The instantaneous phase of the p-th subchirp is derived by integrating the instantaneous frequency with an initial phase ϕ_p:

$$\phi_p(t) = \phi_p + 2\pi \left(\frac{c_r t^2}{2} + f_p t \right). \tag{2.11}$$

Substituting with a sampling frequency normalized chirp rate $m_r = c_r T_s$, with T_s being the sampling periods, leads to

$$s_p[n] = x_p[n]\Phi_p, \tag{2.12}$$

where

$$x_p[n] = \exp\left(j2\pi T_s\left(\frac{m_r n^2}{2} + f_p n\right)\right), \tag{2.13}$$

is the p-th subchirp signal without initial phase shift and $\Phi_p = \exp(j\phi_p)$ is the p-th initial phase shift term. The sample index is $n = [0, \ldots, N_c]$, with N_c being the length of each subchirp. The concatenation of all subchirps $x_p[n]$ can be written as $\boldsymbol{x} = \sum_{p=1}^{N_p} \boldsymbol{x}_p$, with subchirps in sequential order. For a definition of $\boldsymbol{x}_p$, refer to (D.7).

A vector form which contains all phase-shifted subchirps is given by $\boldsymbol{s} = \boldsymbol{X}\boldsymbol{\Phi}$, where $\boldsymbol{X} = \left[\boldsymbol{x}_1, \ldots, \boldsymbol{x}_{N_p}\right]$ is a stacked representation of all N_p subchirp signals. and $\boldsymbol{\Phi} = \left[\Phi_1, \ldots, \Phi_{N_p}\right]^T$ is a vector which contains all starting phase terms in the form of multiplicative complex-valued factors. Furthermore, the matrix representation of the chirp train vector $\boldsymbol{s}$ where the p-th column contains the phase shifted subchirp $\boldsymbol{x}_p\Phi_p$ is defined as $\boldsymbol{S} = \boldsymbol{X}\,\mathrm{diag}(\boldsymbol{\Phi})$ where the diagonal matrix $\mathrm{diag}(\boldsymbol{\Phi})$ has the entries $[\mathrm{diag}(\boldsymbol{\Phi})]_{p,p} = \Phi_p$.

With this, we can derive a vector notation for the received signal as

$$\boldsymbol{r}_{\mathrm{pre}} = \alpha \boldsymbol{W}^H \boldsymbol{P}(\tau)\boldsymbol{W}\boldsymbol{s} + \boldsymbol{w} \in \mathbb{C}^M, \tag{2.14}$$

where $\boldsymbol{w}$ is the sum of the DM and AWGN processes, and $\boldsymbol{P}(\tau)$ is a time-shifting operation, as described in Section D.2.

In the case that the starting phase vector is unknown, the LoS channel coefficient α simplifies to $|\alpha|$, leading to

$$\boldsymbol{r} = |\alpha|\boldsymbol{W}^H \boldsymbol{P}(\tau)\boldsymbol{W}\boldsymbol{s} + \boldsymbol{w}, \tag{2.15}$$

which describes the signal model for the chirp train signal.

2.2 RSS Signal Model

This section describes the RSS signal model, used for Papers [B] and [C].

The distance between two nodes l and i is denoted as $d_{l,i} = \|\mathbf{p}_l - \mathbf{p}_i\|$. Assuming the measurements adhere to a log-distance dependent pathloss model [11] [57, Sec. 9.2], the path loss $L(\mathbf{p}_l, \mathbf{p}_i, P, \rho)$ between nodes l and i is expressed as

$$L(\mathbf{p}_l, \mathbf{p}_i, P, \rho) = P - \rho\ 10\log\left(||\mathbf{p}_l - \mathbf{p}_i||/d_0\right), \tag{2.16}$$

where P is the reference pathloss at a distance d_0, and ρ is the path-loss exponent [37]. The received RSS value $z_{l,i}^{\mathrm{RSS}}$ between nodes l and i is then given by

$$z_{l,i}^{\mathrm{RSS}} = L(\mathbf{p}_l, \mathbf{p}_i, P, \rho) + w_{l,i}, \tag{2.17}$$

with $w_{l,i}$ being the noise term, assumed to follow a Gaussian distribution $\mathcal{N} \sim (0, \sigma^2)$.

3

Likelihood Models and Estimators

This chapter focuses on the explanation of the likelihoods incorporated in Papers [A]-[D]. It should be noted that the full derivations of these likelihoods can be seen in the appended Papers [A]-[D] at their respective referenced positions. But, beforehand, a short discourse on maximum a-posteriori (MAP)-based estimation will be given, to motivate the importance of the likelihood functions for localization.

3.1 MAP-based Estimation and its Application in Localization

MAP-based estimation provides a powerful framework for parameter estimation by allowing to incorporate prior knowledge about the parameters of interest in addition to the information contained in the observed data. This Bayesian approach contrasts with maximum likelihood (ML) estimation without prior information, which relies solely on the likelihood function. In scenarios with limited or noisy data, the inclusion of prior information can significantly improve the accuracy and robustness of the estimates [58–60].

Given a parameter vector $\boldsymbol{\theta}$ and a vector of observations $\mathbf{r}$, Bayes' theorem expresses the posterior probability density function (PDF) as

$$f(\boldsymbol{\theta}|\mathbf{r}) = \frac{f(\mathbf{r}|\boldsymbol{\theta})f(\boldsymbol{\theta})}{f(\mathbf{r})}, \tag{3.1}$$

where $f(\mathbf{r}|\boldsymbol{\theta})$ is the likelihood function, $f(\boldsymbol{\theta})$ is the prior PDF, and $f(\mathbf{r})$ is the marginal likelihood. Given some observation $\mathbf{r}$, the MAP estimate $\hat{\boldsymbol{\theta}}_{\mathrm{MAP}}$ maximizes the posterior PDF

$$\hat{\boldsymbol{\theta}}_{\mathrm{MAP}} = \underset{\boldsymbol{\theta}}{\operatorname{argmax}} f(\boldsymbol{\theta}|\mathbf{r}) = \underset{\boldsymbol{\theta}}{\operatorname{argmax}} f(\mathbf{r}|\boldsymbol{\theta})f(\boldsymbol{\theta}). \tag{3.2}$$

As $f(\mathbf{r})$ does not depend on $\boldsymbol{\theta}$, it is omitted from the maximization. Hence, MAP estimation aims to find the $\boldsymbol{\theta}$ that maximizes the product of the likelihood and the prior. A uniform (uninformative) prior reduces MAP estimation to ML estimation.

In radio-based localization, MAP-based estimation is a tool that is used very commonly, as it is often easy to implement, fast to compute, and it leads to very reliable results.

The choice of prior plays a crucial role in MAP estimation. Informative priors, reflecting strong prior beliefs, can significantly influence the estimates, pulling them towards the prior distribution. Weak priors, on the other hand, have a less pronounced impact, allowing the data to dominate the estimation. Selecting an appropriate prior requires careful consideration of the specific application and the available prior knowledge. The appended Papers [A]-[D] implicitly or explicitly make assumptions on these priors which can impact accuracy for various real-world scenarios and thus have to be carefully considered.

From a computational perspective, MAP estimation can be more challenging than ML estimation, especially when the posterior PDF doesn't have a closed-form solution. Numerical optimization methods or sampling techniques, such as particle filters or Monte-Carlo simulation (MCS) methods, are often required to find the MAP estimate. The appended Papers [B]-[D] utilize particle filters and message-passing algorithms, offering computationally tractable solutions for approximating the posterior and performing MAP estimation in complex, high-dimensional parameter spaces. These methods offer a viable approach to performing localization in real-world scenarios without having excessive computational demand, but need to be carefully evaluated for each application.

3.2 Time-of-Arrival Estimation in DMC under Bandwidth Limitation

The work in Paper [A] focuses on the estimation of time-of-arrival in DMC, but aims to exploit the additional signal energy within the DM to improve the estimation of the transmit delay. We neglect indices for the receive array m and antenna k and node l for this section, as we assume only one receive antenna. As this only focuses on delay estimation, dependencies on the positions of nodes and anchors are also neglected. The parameter vector for estimation within this algorithm is defined as $\boldsymbol{\theta} = [\tau, \boldsymbol{\eta}, \alpha]^T$, as described in Subsection 2.1.1.

This leads to the likelihood function

$$f(\boldsymbol{r} \mid \tau, \boldsymbol{\eta}, \alpha) = \frac{\mathrm{e}^{-(\boldsymbol{r}-\boldsymbol{s}(\tau)\alpha)^{\mathrm{H}}\boldsymbol{C}^{-1}(\boldsymbol{r}-\boldsymbol{s}(\tau)\alpha)}}{\pi^N \det \boldsymbol{C}}, \tag{3.3}$$

where it should be noted that $\boldsymbol{C}$ is dependent on the parameters $\boldsymbol{\eta}$ for the power delay profile (PDP) and the transmit delay.

This likelihood can be simplified for easier calculation, which leads to a log-likelihood denoted as

$$\begin{aligned} \ln\left(f(\boldsymbol{r} \mid \tau, \boldsymbol{\eta}, \alpha)\right) &= -N_s \ln(\pi) - \sum_n \ln(A\lambda_n + \sigma^2) \\ &- \sum_n (A\lambda_n + \sigma^2)^{-1} \left|\boldsymbol{u}_n \left[\boldsymbol{P}^{\mathrm{H}}(\tau)\tilde{\boldsymbol{r}} - \tilde{\boldsymbol{s}}(0)\alpha\right]\right|^2 \end{aligned}, \tag{3.4}$$

where N_s is the number of samples, $A = \Omega_1(\gamma_f + \gamma_r)$ is an energy scaling factor for the DM, λ_n corresponds to the n-th eigenvalue of the covariance matrix $\boldsymbol{C}$,

$\boldsymbol{u}_n$ corresponds to the n-th orthogonal eigenvector of $\boldsymbol{C}$, $\boldsymbol{P}^{\mathrm{H}}(\tau)$ is a delay shift operator, and $\tilde{\boldsymbol{r}}$ and $\tilde{\boldsymbol{s}}(0)$ are Fourier transformed versions of $\boldsymbol{r}$ and $\boldsymbol{s}(0)$ respectively. The exact derivation for this is shown in Section A.2.

The simplified notation has two key advantages: First, the Fourier-transformed signal atom $\tilde{\boldsymbol{s}}(0)$ stays constant for estimation. Furthermore, it is possible to precompute the eigenvector decomposition for different parameters $\boldsymbol{\eta}$. This allows for a fast and efficient computation of the likelihood, paving the way for fast parameter estimation.

Paper [A] employs MAP estimation implicitly. While Equation (3.4) represents the log-likelihood function, the subsequent maximization to obtain point estimates assumes a uniform prior over a large region of the parameters, which does not influence the result. A more informative prior on the delay τ, reflecting knowledge about the possible node locations (e.g., constrained to a room), could be introduced. This would transform the estimation into a more explicit form of MAP estimation and could further improve robustness.

3.3 Coherent Chirp Synthesis of Multiband Signals

This section focuses on the likelihood described in Paper [D], which aims to improve the estimation of the transmit delay of multiple subchirps with overlapping frequency bands. This is done in a two-step approach. In a first step, the phase offsets are estimated using a cross-correlation approach of the overlapping frequency bands, which can be seen as a likelihood [61, 62]. This leads to a prior distribution for the phases, which is then incorporated into a joint MAP estimator for delay and phases. The parameter vector for this algorithm is defined as $\boldsymbol{\theta} = [\tau, |\alpha|, \phi_1, \ldots, \phi_{N_p}]^T = [\tau, |\alpha|, \boldsymbol{\Phi}]^T$, as described in Subsection 2.1.2.

We use the signal model described in Equation (2.15), from which we can formulate a traditional estimator neglecting the overlap as

$$\begin{aligned}\hat{\tau}, |\hat{\alpha}|, \hat{\boldsymbol{\Phi}} &= \underset{\tau, |\alpha|, \boldsymbol{\Phi}}{\arg\max} \left(f_1(\boldsymbol{r} \mid \tau, |\alpha|, \boldsymbol{\Phi}) \right) \\ &= \underset{\tau, |\alpha|, \boldsymbol{\Phi}}{\arg\max} (-\|\boldsymbol{r} - |\alpha| \boldsymbol{W}^H \boldsymbol{P}(\tau) \boldsymbol{W} \boldsymbol{X} \boldsymbol{\Phi}\|),\end{aligned} \tag{3.5}$$

which neglects the additional information in the overlapping frequency bands. To incorporate the additional information from the DM in the overlapping bands, a likelihood, based on a generalized cross-correlation, for the phases is derived as

$$\begin{aligned}f(\boldsymbol{r} \mid \phi_p, \phi_{p+1}) = &|(\boldsymbol{r}[t_p^{(l)}, \ldots, t_p^{(u)}] \exp(-j\phi_p)) \times \\ &(\boldsymbol{r}[t_{p+1}^{(l)}, \ldots, t_{p+1}^{(u)}] \exp(-j\phi_{p+1}))^H|,\end{aligned} \tag{3.6}$$

where $t_p^{(l)}$ and $t_p^{(u)}$ and $t_{p+1}^{(l)}$ and $t_{p+1}^{(u)}$ describe the lower and upper frequency overlap samples between two subsequent subchirps p and $p+1$. This assumes no dependency between phases of subchirps and delay in this estimation step. This condition applies when both subchirps are shifted by the same transmit delay.

Assuming there is no prior information for the first phase ϕ_1, we can denote a joint likelihood as

$$f(\boldsymbol{r} \mid \tau, |\alpha|, \boldsymbol{\Phi}) \propto f_1(\boldsymbol{r} \mid \tau, |\alpha|, \boldsymbol{\Phi}) \prod_{p=1}^{N_p-1} f(\boldsymbol{r} \mid \phi_p, \phi_{p+1}), \tag{3.7}$$

which similarly can now be maximized to find the delay. This can be seen as a two-step estimation approach, where $f(\boldsymbol{r} \mid \phi_p, \phi_{p+1})$ is estimated beforehand, and $f_1(\boldsymbol{r} \mid \tau, |\alpha|, \boldsymbol{\Phi})$ is estimated in a second step. This is possible because there is no dependency of $f(\boldsymbol{r} \mid \phi_p, \phi_{p+1})$ on transmit delay τ and amplitude $|\alpha|$. In effect, this can also be seen as a Bayesian likelihood, where f_1 acts as a prior likelihood for phase differences. This joint likelihood benefits from the additional energy incorporated into the cross-correlation when estimating the phases between two subchirps. For parameter estimation, the phases ϕ_p are estimated in a first step by

$$\hat{\phi}_p = \arg\max_{\phi_p} f(\boldsymbol{r} \mid \phi_p, \phi_{p+1}) f(\phi_p), \tag{3.8}$$

using $f(\phi_p) = \delta(\phi_p - \hat{\phi}_p)$. This leads to

$$\hat{\boldsymbol{\Phi}} = \arg\max_{\boldsymbol{\Phi}} \prod_{p=1}^{N_p-1} f(\boldsymbol{r} \mid \phi_p, \phi_{p+1}) \delta(\phi_p). \tag{3.9}$$

In a second step, the joint-likelihood can then be maximized to find estimates for unknown parameters by

$$\hat{\tau}, |\hat{\alpha}| = \arg\max_{\tau, |\alpha|} f(\boldsymbol{r} \mid \tau, |\alpha|, \hat{\boldsymbol{\Phi}}). \tag{3.10}$$

This uses MAP estimation for the estimation of phases, as shown in Equation (3.7). It combines the likelihood function with a prior term (3.6) and performs MAP estimation by maximizing the joint-likelihood function for obtaining the most probable solution based on prior knowledge and observations. A similar concept could be applied for the delay estimation as well, leveraging available prior information.

3.4 Cooperative Localization and Clustering

This section focuses on the cooperative localization and clustering likelihoods described in Papers [B] and [C]. The clustering approach described in Paper [B] can be seen as a special case of the posterior PDF for cooperative localization described in Paper [C]. Thus this section first describes the posterior PDF, and then shows the two different solutions in detail.

3.4.1 Posterior PDF for Cooperative Localization

We factorize the joint posterior PDF of all nodes l as:

$$f(\boldsymbol{\theta} \mid \mathbf{r}, \mathbf{z}) \propto \; f(\mathbf{q}) \prod_{l \in \mathcal{L}} f(\mathbf{p}_l) f(\mathbf{r}_l \mid \mathbf{p}_l, \mathbf{q}) \prod_{i \in \mathcal{C}_l} f(\mathbf{z}_{l,i} \mid \mathbf{p}_l, \mathbf{p}_i). \tag{3.11}$$

Here, the stacked measurement vector is given by $\mathbf{r} = [\mathbf{r}_1^T, \ldots, \mathbf{r}_L^T]^T$, with $\mathbf{r}_l = \left[\mathbf{r}_{l,1}^T, \ldots, \mathbf{r}_{l,M}^T\right]^T$. The stacked vector $\mathbf{z}$ represents all cooperative measurements $\mathbf{z}_{l,i} \forall l, i$. Finally, $\boldsymbol{\theta} = [\mathbf{p}_1^T, \ldots, \mathbf{p}_L^T]^T$ is a stacked vector of all position parameters of according length, and $\mathbf{q} = [\mathbf{q}_1^T, \ldots \mathbf{q}_M^T]^T$ represents a stacked vector of all anchor positions. We define a set of all nodes as $\mathcal{L} = \{1, \ldots, L\}$ and subsets $\mathcal{C}_l \subseteq \mathcal{L}$, which define the nodes for which cooperative measurements are incorporated with regard to node l.

The term cooperative measurements refers to the interchangeable data $\mathbf{z}_{l,i}$, which may also encompass measures such as generalized cross-correlation (GCC) and perceptual hashing. These are not directly measured but are computed from the measurements $\mathbf{r}_l$ and $\mathbf{r}_i$, as described below.

The geometric prior $f(\mathbf{p}_l)$ restricts the evaluation of nodes to plausible positions within a room, $f(\mathbf{q})$ defines the anchor positions. The third term in the Equation (3.11) corresponds to the single-node likelihood described in Section 3.4.2. The fourth term represents a cooperative likelihood. It is interchangeable, and three different variants will be presented in Section 3.4.3.

It is important to note that we assume independence between the single-node likelihood and the cooperative likelihoods. This assumption is not entirely accurate since the same sets of measurements are used for both the single-node likelihood and the cooperative measures in some of the proposed methods (e.g., GCC and perceptual hashing). For practical reasons, we neglect these dependencies.

It should be noted that the posterior PDF is computed by two different means in this work: One is a message-passing (MP) algorithm, based on the sum-product-algorithm (SPA), similar to [36–44]. In general this is a method to reliably approximate the posterior PDF described in (3.11), which for example is similar to [36, Eq. 7]. For details, refer to the previous work mentioned. This explicitly uses a geometric prior $f(\mathbf{p}_l)$ in the joint posterior PDF to restrict the node positions to plausible locations within a room. This prior incorporates knowledge about the environment and prevents the algorithm from exploring impossible or unlikely positions. The message-passing algorithm employed to approximate the posterior does not carry out MAP estimation, instead iteratively refining the node location estimates by combining the likelihood derived from wideband measurements and the information coupling with the geometric prior. But, this process can lead to the MAP estimate, by using the maxima of the single-node distributions as point estimates for the positions [63].

Alternatively, a clustering algorithm assumes a simplification described in Subsection 3.4.4. This assumes that the fourth term in the inter-node likelihood are multiplicative δ distributions depending on the positions of nodes. A set of incorporated wideband measurements is then defined by RSS measurements, and reciprocity is neglected. This leads to a simplified likelihood which can then be directly estimated by a particle-based estimator. This algorithm establishes an implicit prior on the node positions. The clustered nodes are assumed to be in proximity to each other, which constrains their possible locations. This performs MAP estimation, finding the most probable cluster position given the measurements and the implicit prior derived from clustering. Node positions can be restricted to areas where they are possible, resulting in an additional geometric prior.

3.4.2 Single-Node Likelihood for WB

Assuming the wideband signal model presented in Section 2.1.1, the likelihood function for a single node measuring to M anchors can be expressed as

$$f(\mathbf{r}_l \mid \mathbf{p}_l, \mathbf{q}, \epsilon_l, \boldsymbol{\eta}_l, \boldsymbol{\alpha}_l) = \prod_{m=1}^{M} f(\mathbf{r}_{l,m} \mid \mathbf{p}_l, \mathbf{q}_m, \epsilon_l, \boldsymbol{\eta}_{l,m}, \alpha_{l,m}), \tag{3.12}$$

where ϵ_l is the unknown transmit time per node l and independence of the DMC and AWGN between anchors is assumed. The single-node, multi-antenna likelihood function is given by

$$f(\mathbf{r}_{l,m} \mid \mathbf{p}_l, \mathbf{q}_m, \epsilon_l, \boldsymbol{\eta}_{l,m}, \alpha_{l,m}) = \frac{\mathrm{e}^{-(\mathbf{r}_{l,m}-\mathbf{s}(\mathbf{p}_l,\mathbf{q}_m,\epsilon_l)\alpha_{l,m})^{\mathrm{H}}(\mathbf{C}_{l,m})^{-1}(\mathbf{r}_{l,m}-\mathbf{s}(\mathbf{p}_l,\mathbf{q}_m,\epsilon_l)\alpha_{l,m})}}{\pi^{N_s K}\det(\mathbf{C}_{l,m})}, \tag{3.13}$$

with noise parameter vector $\boldsymbol{\eta}_{l,m} = \left[\sigma^2_{l,m},\ \tilde{\boldsymbol{\eta}}^T_{l,m}\right]^T$.

Assuming that the transmit time ϵ_l is independent, the joint likelihood can be factorized as

$$f(\mathbf{r}_l, \epsilon_l \mid \mathbf{p}_l, \mathbf{q}, \boldsymbol{\eta}_l, \boldsymbol{\alpha}_l) = f(\epsilon_l) f(\mathbf{r}_l \mid \mathbf{p}_l, \mathbf{q}, \epsilon_l, \boldsymbol{\eta}_l, \boldsymbol{\alpha}_l), \tag{3.14}$$

where $f(\epsilon_l)$ denotes the prior for the parameter ϵ_l. To marginalize out the nuisance parameter ϵ_l, we define

$$f(\mathbf{r}_l \mid \mathbf{p}_l, \mathbf{q}, \boldsymbol{\eta}_l, \boldsymbol{\alpha}_l) = \int f(\mathbf{r}_l, \epsilon_l \mid \mathbf{p}_l, \mathbf{q}, \boldsymbol{\eta}_l, \boldsymbol{\alpha}_l)\ d\epsilon_l, \tag{3.15}$$

yielding the single-node likelihood function that leverages TDoA information between anchors. For two anchors in a 2D setting, this describes the classic hyperbola of possible node locations derived from TDoA. Here, $\boldsymbol{\alpha}_l = [\alpha_{l,1}, \ldots, \alpha_{l,M}]^T$, and $\boldsymbol{\eta}_l = \left[\boldsymbol{\eta}^T_{l,1}, \ldots, \boldsymbol{\eta}^T_{l,M}\right]^T$ represent the LoS amplitudes and noise parameters, respectively.

For computational efficiency, we neglect the effect of DMC within the parameter estimation (while retaining it for simulations and channel modeling), assuming that the covariance matrix $\mathbf{C}_{l,m}$ is diagonal. This approximation corresponds to estimating only the strongest signal component, leading to a simplified likelihood:

$$f(\mathbf{r}_l \mid \mathbf{p}_l, \mathbf{q}, \boldsymbol{\sigma}^2_l, \boldsymbol{\alpha}_l) = \int f(\mathbf{r}_l, \epsilon_l \mid \mathbf{p}_l, \mathbf{q}, \boldsymbol{\sigma}^2_l, \boldsymbol{\alpha}_l)\ d\epsilon_l, \tag{3.16}$$

where $\boldsymbol{\sigma}^2_l = \left[\sigma^2_{l,1}, \ldots, \sigma^2_{l,M}\right]^T$ contains the stacked noise variances.

Further simplification can be achieved by using least-squares estimates for $\boldsymbol{\sigma}^2_l$ and $\boldsymbol{\alpha}_l$, as detailed in [28], resulting in the likelihood for the measurement vector $\mathbf{r}_l$ conditioned on the node position $\mathbf{p}_l$ and anchor positions $\mathbf{q}$ being

$$f(\mathbf{r}_l \mid \mathbf{p}_l, \mathbf{q}) = \int f(\mathbf{r}_l, \epsilon_l \mid \mathbf{p}_l, \mathbf{q})\ d\epsilon_l. \tag{3.17}$$

3.4.3 Likelihoods for Inter-Node Coupling

This subsection focuses on the cooperative likelihood

$$\prod_{i \in \mathcal{C}_l} f(\mathbf{z}_{l,i} \mid \mathbf{p}_l, \mathbf{p}_i), \tag{3.18}$$

being the last term of the posterior PDF given in (3.11).

This term describes a generalized distribution for a subset of nodes $\mathcal{C}_l$, meaning that for any given node l there is a subset of nodes with measurements that allow us to construct a likelihood, constraining the positions $\mathbf{p}_l$ for $l \in \mathcal{C}_l$. Generally, it would be assumed that these distributions are constructed from measurement data between two nodes in the set $\mathcal{C}_l$. This is the case for RSS data in this work, where a log-distance dependent model is used for the construction of a likelihood depending on cooperative RSS measurements.

But these measurements can also be substituted by other metrics, for example by extracting so-called mutual information from the wideband measurements directly. This assumes that there is some degree of correlation or similarity between wideband measurements of nodes in a geometric vicinity. The term mutual information refers to the information within these measurements that is shared(or similar) between nodes.

As this cooperative term of the posterior PDF is interchangeable, three different possible likelihoods are given in the following, two of which are dependent on wideband measurements only, and the third is a benchmark method using additional cooperative RSS measurements. Other likelihoods can be incorporated into this, either by another measurement method, or by other means of extracting mutual information. Also, it should be noted that multiple likelihoods could be utilized jointly, for example RSS measurements in combination with perceptual hashing. This could lead to better localization performance and robustness, but is neglected in this work, as it does not lead to any new insights.

GCC-Phat

The first inter-node likelihood is determined using GCC between two signals $\mathbf{r}_l$ and $\mathbf{r}_i$ with the phase transform (PHAT) assumption [61]. This likelihood does not rely on separate measurements but instead leverages information coupling or mutual information. We introduce a Fourier-transformed version of $\mathbf{r}_{l,m,k}$ as $\breve{\mathbf{r}}_{l,m,k} = F(\mathbf{r}_{l,m,k})$ which is the frequency response of the signal. Based on this, we define a time-shifted version as

$$[\tilde{\mathbf{r}}_{l,m,k}]_n = e^{-j\omega_n \tau_l} [\breve{\mathbf{r}}_{l,m,k}]_n \tag{3.19}$$

where the baseband frequencies are given by $\omega_n = (2\pi \frac{n}{N} - \pi)B$, with B denoting the baseband bandwidth of the signal, a delay $\tau_l = \tau(\mathbf{p}_l, \mathbf{q}_m) + \epsilon_l$ and $n = [0, \dots, N_s - 1]^T$ being a sample index. Using this time-shifted representation, we define a cross power spectral density for the PHAT between nodes l and i as

$$[\mathbf{\Psi}_{l,i,m,k}]_n = \frac{[\tilde{\mathbf{r}}_{i,m,k}]_n [\tilde{\mathbf{r}}_{l,m,k}]_n^*}{|[\tilde{\mathbf{r}}_{l,m,k}]_n [\tilde{\mathbf{r}}_{i,m,k}]_n^*|}, \tag{3.20}$$

which relates to the differences of the arguments of the frequency responses $[\tilde{\mathbf{r}}_{l,m,k}]_n$ and $[\tilde{\mathbf{r}}_{i,m,k}]_n$. The log-likelihood for GCC with the PHAT assumption can be

expressed as

$$\log f(\mathbf{z}_{l,i}^{\mathrm{GCC}} \mid \mathbf{p}_l, \mathbf{p}_i, \epsilon_l, \epsilon_i) \propto -\frac{1}{N_s} \sum_{k=1}^{K} \sum_{m=1}^{M} \sum_{n=0}^{N_s-1} [\mathbf{\Psi}_{l,i,m,k}]_n, \tag{3.21}$$

based on the assumption that the noise is uncorrelated across antennas. This has been shown to be a log-likelihood function in [61, 62]. The measurement vector for the GCC is defined as $\mathbf{z}_{l,i}^{\mathrm{GCC}} = [\mathbf{r}_l^T, \mathbf{r}_i^T]^T$. We assume that the transmit times ϵ_l and ϵ_i are independent. We marginalize over the parameters ϵ_l and ϵ_i, and define the marginal for GCC as

$$f(\mathbf{z}_{l,i}^{\mathrm{GCC}} \mid \mathbf{p}_l, \mathbf{p}_i) = \int\int f(\epsilon_l) f(\epsilon_i) f(\mathbf{z}_{l,i}^{\mathrm{GCC}} \mid \mathbf{p}_l, \mathbf{p}_i, \epsilon_l, \epsilon_i) d\epsilon_i d\epsilon_l, \tag{3.22}$$

where $f(\epsilon_l)$ and $f(\epsilon_i)$ are the priors for the parameters ϵ_l and ϵ_i respectively. The PHAT assumption, while not strictly necessary, improves the estimation for practical cases. This is similar to acoustic applications, as seen in [61, 64, 65] and can be explained by the similarity of reverb in acoustics to DMC in radio-based channels. Both are dependent on the room geometry, but the channel statistics are similar for close-by nodes. I.e. we can assume that $\mathbf{C}_{l,m}^{(\nu)} \approx \mathbf{C}_{i,m}^{(\nu)}$.

Further information on this approach can be examined in Paper [C], where several illustrations (Figures C.3a.i to C.4) show how this behaves in a typical scenario.

Perceptual Hashing Likelihood

Perceptual hashing yields an efficient approximation of GCC. We define a measurement matrix for each node l as $\mathbf{X}_l = [\mathbf{r}_{l,1}, \dots \mathbf{r}_{l,M}]^T$. We then compute $\mathbf{X}_{\mathrm{DCT}} = \mathrm{DCT}_{\mathrm{II}}(\mathbf{X}_l)$, where $\mathrm{DCT}_{\mathrm{II}}$ denotes the Type-II discrete cosine transform. To focus on lower frequencies of the DCT, filtering high-frequency features consisting mostly of noise, we define a reduced version $\mathbf{X}_{\mathrm{DCT}}^{\mathrm{red}} = [\mathbf{X}_{\mathrm{DCT}}]_{N_{\mathrm{D}} \times N_{\mathrm{D}}}$, where N_{D} defines a cutoff for the used frequency bins of the DCT. We also define the average value of the reduced DCT as κ_{DCT} being the mean of all elements of $\mathbf{X}_{\mathrm{DCT}}^{\mathrm{red}}$. We apply an element-wise threshold function as follows:

$$[\mathbf{X}^{\mathrm{thr}}]_{n,m} = \begin{cases} 0 & [\mathbf{X}_{\mathrm{DCT}}^{\mathrm{red}}]_{n,m} \leq \kappa_{\mathrm{DCT}} \\ 1 & [\mathbf{X}_{\mathrm{DCT}}^{\mathrm{red}}]_{n,m} > \kappa_{\mathrm{DCT}} \end{cases}. \tag{3.23}$$

The vectorized binary representation of the matrix $\mathbf{X}^{\mathrm{thr}}$ is denoted by $z^{\mathrm{PH}}(\mathbf{r}_l)$. We then define a similarity measure between nodes l and i as

$$z_{l,i}^{\mathrm{PH}} = N_D^2 - H(z^{\mathrm{PH}}(\mathbf{r}_l), z^{\mathrm{PH}}(\mathbf{r}_i))/N_D^2, \tag{3.24}$$

where $H(z^{\mathrm{PH}}(\mathbf{r}_l), z^{\mathrm{PH}}(\mathbf{r}_i))$ is the Hamming distance between two hashes. This measure is bounded by $z_{l,i}^{\mathrm{PH}} \in [0, 1]$, with larger values indicating greater similarity between signals. It equates to a normalized Hamming distance between two perceptual hashes and behaves according to a distance-dependent model in a Euclidean sense. The normalization is not strictly necessary, but allows the similarity measure

to behave like a statistical distance (i.e. Hellinger distance, Jensen-Shannon divergence). Assuming this follows a saturated log-distance-dependent linear model, we express the likelihood for perceptual hashing as

$$f(z_{l,i}^{\mathrm{PH}} \mid \mathbf{p}_l, \mathbf{p}_i) = \frac{1}{\sqrt{2\pi\sigma^2}} \exp \frac{-(z_{l,i}^{\mathrm{PH}} - \tilde{z}_{l,i}^{\mathrm{PH}})^2}{2\sigma^2}, \tag{3.25}$$

with

$$\tilde{z}_{l,i}^{\mathrm{PH}} = P - \rho 10 \log\left((d_{l,i}/d_0) + \chi\right), \tag{3.26}$$

where P and ρ are used similarly to (2.16), and χ is a parameter describing a saturation effect for small values. This is due to a characteristic of perceptual hashing: similar measurement matrices can lead to similarity measures being 1. For further dissimilarity, the behavior is similar to a log-normal pathloss model, as the differences in the measurement matrices are also log-distance-dependent on the mean signal energy. This model is a modification of a log-normal pathloss model, very similar to [57, Ch. 3], where for small distances a minimum pathloss is assumed. This gives the aforementioned saturation effect by an additional parameter χ. This stems from the filtering of high-frequency components by the cutoff N_D, resulting in a compression of signal components into a smaller number of features. For very similar signals (i.e. signals from nodes with similar statistics and amplitudes), this results in an exactly same perceptual hash, giving perfect similarity. For larger distances, this model behaves similar to a log-normal pathloss model, as statistics and amplitudes of signals tend to become increasingly different for larger distances between nodes.

RSS-dependent Likelihood

The inter-node likelihood for RSS relies on separate RSS measurements and serves as a benchmark for comparing the other methods. This is a cooperative likelihood, requiring direct cooperation between nodes. For the RSS case, the cooperative likelihood is given by

$$f(z_{l,i}^{\mathrm{RSS}} \mid \mathbf{p}_l, \mathbf{p}_i) = \frac{1}{\sqrt{2\pi\sigma^2}} \exp \frac{-(z_{l,i}^{\mathrm{RSS}} - \tilde{z}_{l,i}^{\mathrm{RSS}})^2}{2\sigma^2}, \tag{3.27}$$

where $\tilde{z}_{l,i}^{\mathrm{RSS}}$ is defined as:

$$\tilde{z}_{l,i}^{\mathrm{RSS}} = L(\mathbf{p}_l, \mathbf{p}_i, P, \rho). \tag{3.28}$$

Here, $\tilde{z}_{l,i}^{\mathrm{RSS}}$ represents the log-distance-dependent model discussed in Section 2.2.

3.4.4 Likelihood for Clustering

Paper [B] describes a clustering approach, where measurements of multiple nodes are combined by another metric, for example RSS measurements. This can be seen as a computational simplification of the posterior PDF in (3.11). For this simplification, we assume that wideband measurements of nodes have no co-dependency. Furthermore, we assume that the underlying wideband likelihood of nodes within

a vicinity of a node l reasonably approximate the cooperative likelihood term in the posterior. This simplifies the last term of the posterior to

$$\prod_{i \in \mathcal{C}_l} f(\mathbf{z}_{l,i} \mid \mathbf{p}_l, \mathbf{p}_i) \approx \prod_{i \in \mathcal{C}_l} f(\mathbf{r}_i \mid \mathbf{p}_i, \mathbf{q}) \delta(\mathbf{p}_l - \mathbf{p}_i) \tag{3.29}$$

where $\mathcal{C}_l$ is defined by a sorting metric, like RSS measurements. For example, one could define this as a fixed number of nodes with the largest measured RSS values to the node l. The node l itself is excluded from this set. It should be noted that this assumes the cooperative measurements $\mathbf{z}_{l,i}$ to be replaced by the single wideband measurements $\mathbf{r}_i$. This is due to the cooperative information being implicitly contained within $\mathcal{C}_l$. Assuming no co-dependencies between nodes in the estimation, we can neglect the term $\delta(\mathbf{p}_l - \mathbf{p}_i)$. This is equivalent to assuming no distance between node positions $\mathbf{p}_i$ of the set $\mathcal{C}_l$ and the position $\mathbf{p}_l$ of node l, meaning $\delta(\mathbf{p}_l - \mathbf{p}_i) \overset{!}{=} 1$ and $\mathbf{p}_i = \mathbf{p}_l$. We can evaluate this for every node l separately, leading to

$$f_l(\mathbf{p}_l, \mathbf{q} \mid \mathbf{r}) \propto \; f(\mathbf{q}) f(\mathbf{p}_l) f(\mathbf{r}_l \mid \mathbf{p}_l, \mathbf{q}) \prod_{i \in \mathcal{C}_l} f(\mathbf{r}_i \mid \mathbf{p}_l, \mathbf{q}), \tag{3.30}$$

where $f_l(\boldsymbol{\theta} \mid \mathbf{r})$ is the likelihood of a single node depending on measurements of the node l and nodes within a vicinity $\mathcal{C}_l$.

This can be further simplified by just including the measurement of our node l in a set $\mathcal{D}_l = \mathcal{C}_l \cup \{l\}$, leading us to

$$f(\mathbf{p}_l \mathbf{q} \mid \mathbf{r}) \propto \; f(\mathbf{q}) f(\mathbf{p}_l) \prod_{l \in \mathcal{D}_l} f(\mathbf{r}_l \mid \mathbf{p}_l, \mathbf{q}). \tag{3.31}$$

It should be noted that this is just an alternative way to arrive at a very similar solution as in (B.12) described in Paper [B], with the only difference being the marginalization of transmit delay ϵ_l. This likelihood has a great advantage computationally, as no cooperations between nodes remain, thus allowing us to estimate the position $\mathbf{p}_l$ completely separately. In practice, this is done by a relatively simple particle based estimator. The disadvantage of this method is that this leads to a biased estimate. Essentially, this estimates the geometric mean of node positions within the set $\mathcal{D}_l$, and assumes this to be a reasonable estimate of the node position $\mathbf{p}_l$.

4
Selected Results

This section shows selected results from the appended Papers [A]-[D] and gives an overview of the derived Cramér-Rao lower bounds (CRLBs) in three of the appended Papers [A], [B] and [D]. The CRLB is a theoretical limit that quantifies the lowest possible variance of an unbiased estimator, given the information contained in the data as measured by the Fisher information (FI). The FI is a measure of the amount of information a random variable carries about an unknown parameter, defined as the expected value of the second derivative of the log-likelihood function with respect to that parameter. This implies that the derived bounds in this chapter depend on the properties of signal models and measured parameters. The derivations mostly focus on the equivalent Fisher information (EFI) for either delays or positions. For more information and detailed results, it is advised to take a look into the respective papers themselves.

4.1 Time-of-Arrival Estimation in Bandwidth-Limited DMC

The derivations presented this Section rely on the wideband pulse signal model described in Subsection 2.1.1. The EFI for the parameter τ, as described in Subsection 2.1.1, can be approximated as

$$\mathcal{I}_\tau \approx 8\pi^2\beta^2\gamma_\tau \mathrm{SINR}\sin^2(\xi) + \mathcal{I}_\tau^{\mathrm{DMC}}. \tag{4.1}$$

The first part of the equation ($\approx 8\pi^2\beta^2\gamma_\tau \mathrm{SINR}\sin^2(\xi)$) corresponds to the information from direct estimation of the LoS component, neglecting additional information from the DMC. The second part $\mathcal{I}_\tau^{\mathrm{DMC}}$ introduces the additional information for exploiting the estimation of DMC parameters. Here, $\beta^2 = \|\dot{\mathbf{s}}\|^2 / \left(4\pi^2 \|\mathbf{s}\|^2\right)$ represents the mean-squared bandwidth [66] of the transmitted signal, defined with a normalized pulse $\|\mathbf{s}\|^2 T_s = 1$, and $\dot{\mathbf{s}}$ is the sampled derivative of $\mathbf{s}$ w.r.t τ. The whitening gain $\gamma_\tau = \frac{\beta_w^2}{\beta^2}$ is described in [34] as the increased ranging information due to the equalization of the DMC by means of the inverse covariance matrix. The extended bandwidth after whitening $\beta_w^2 = \|\dot{\mathbf{s}}\|_{\mathcal{H}}^2 / \left(4\pi^2 \|\mathbf{s}\|_{\mathcal{H}}^2\right)$ is a corresponding

bandwidth after the equalization, where $\|\mathbf{s}\|^2_{\mathcal{H}}$ is the weighted norm of $\mathbf{s}$ in a corresponding Hilbert space $\mathcal{H}$, see Appendix A.6.2 of Paper [A]. Furthermore, $\sin^2(\xi)$ is a factor stemming from the loss from estimation of the parameter $\tilde{\alpha}$, shown in (2.9). This is also further described in Appendix A.6.2 of Paper [A]. The signal-to-interference-plus-noise-ratio (SINR) is a factor describing the influence of the DMC on the estimation of the LoS signal. It is calculated as $\text{SINR} = |\tilde{\alpha}|^2\|\boldsymbol{s}\|^2_{\mathcal{H}}T_s/N_0$. The term $\mathcal{I}_\tau^{\text{DMC}}$ can be evaluated numerically by computing the partial derivatives $\dot{\mathbf{C}}(\boldsymbol{\eta})$ of $\mathbf{C}(\boldsymbol{\eta})$ and evaluating the trace. With the EFI $\mathcal{I}_\tau$ the ranging error bound (REB) can be written as $\mathcal{R}(\tau) = \sqrt{\mathcal{I}_\tau^{-1}}$.

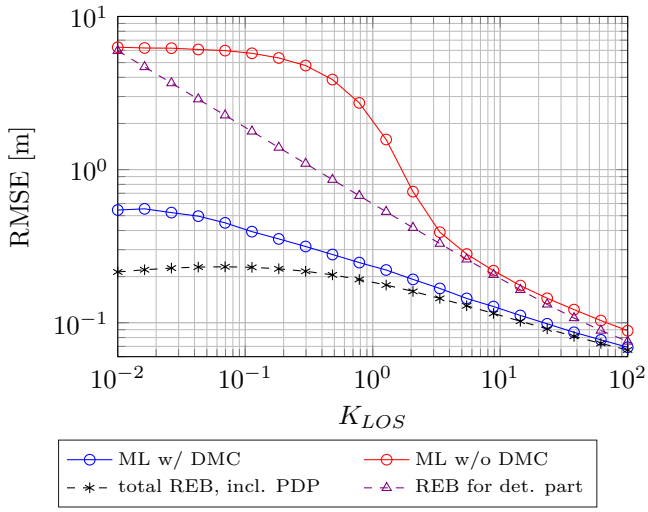

Figure 4.1: Comparison of REBs and ML estimator with and without exploitation of DMC.

The main result of Paper [A] is shown in Figure 4.1. Here a comparison of the REB, and root-mean-square error (RMSE) of the ML estimators, with and without incorporation of the DMC, is shown, as described in Section 3.2. This evaluation was done in a simulation environment, over the parameter K_{LOS}. For this evaluation, we chose a bandwidth of 80 MHz, a fall time of $\gamma_f = 20$ ns and a rise time of $\gamma_r = 5$ ns.

The performance for both estimators improves for larger values of K_{LOS}. A large performance gap exists at low values of K_{LOS}, where a conventional ToA estimator, which does not exploit the DMC, fails. For the estimator with DMC exploitation, the performance is consistently improved over the full range of K_{LOS}. This is also represented by the bounds for both estimators. The ML estimator without DMC exploitation diverges from the bound below a threshold of about $K_{\text{LOS}} \leq 2$, which can be attributed to the estimation of (dominant) multipath components instead of the LoS. For larger values of K_{LOS}, this estimator attains the REB. The estimator exploiting DMC mitigates the drop-off in performance below $K_{\text{LOS}} \leq 2$, and also attains the corresponding bound for large values of K_{LOS}. For smaller values of K_{LOS}, the estimator is not able to attain the bound, but still improves performance significantly. The remaining divergence between this estimator and the REB can be attributed to the additional estimation of nuisance parameters, which in turn

reduce the achievable accuracy.

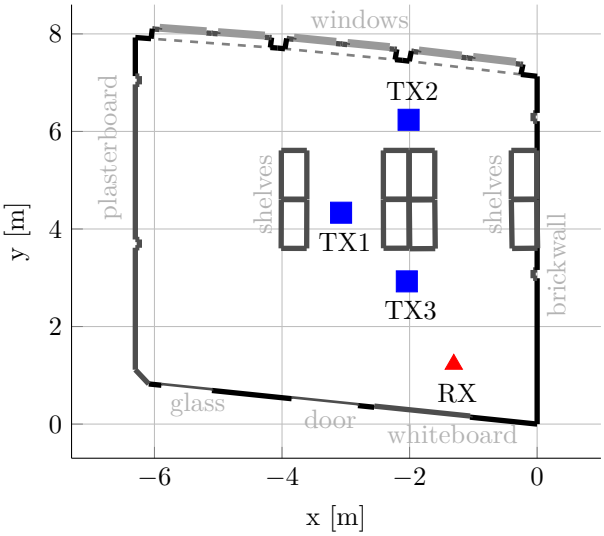

Figure 4.2: Floorplan of the measurement scenario.

To further validate the algorithms described in Paper [A], UWB measurement data was acquired in a small laboratory room at our institute, using a bandwidth of 1 GHz. This dataset was subsequently downsampled to 80 MHz to align with the simulated data. The dataset includes 3654 measured CIRs, of which 2310 were recorded under LoS conditions and 1254 under non-LoS conditions.

Measurements were performed at multiple positions on a 2 cm grid over an area of 64 cm × 70 cm, with the receiver antenna fixed, as illustrated in Figure 4.2. For an evaluation of the estimation performance of the algorithm, real values of the parameters are necessary. As the parameters depend heavily on individual measurement realisations and have to be extracted from measurement data, the high-resolution measurements at the full bandwidth of 1 GHz are used for comparison. Specifically, the parameter $\hat{K}_{\mathrm{LOS}}$, which describes the ratio of energy within the LoS and the DMC, was derived using an ML estimator to estimate the amplitude and delay of the LoS component $\hat{\tau}$, without explicitly modeling the DMC, in proximity to the actual distance [27]. The estimator is defined as

$$\hat{K}_{\mathrm{LOS}} = \frac{\left|\langle \mathbf{r}, \mathbf{s}(\hat{\tau})\rangle\right|^2}{\|\mathbf{r} - \langle \mathbf{r}, \mathbf{s}(\hat{\tau})\rangle \mathbf{s}(\hat{\tau})\|^2 - N\hat{\sigma}^2}, \tag{4.2}$$

where the numerator is the LoS energy, computed from the projection of the received signal $\mathbf{r}$ onto the signal template $\mathbf{s}(\hat{\tau})$ at the estimated delay $\hat{\tau}$, and the denominator is the energy of the residual signal minus the estimated energy of the noise component. The noise variance $\hat{\sigma}^2$ was estimated by using samples where the DM is assumed to be well-attenuated, e.g. at very late delays [19].

The datasets were analyzed using a grid search for the ML algorithm without DMC modeling and an interior-point optimization algorithm incorporating DMC modeling, as described in Equation (3.4). The parameter γ_r was fixed at 5 ns,

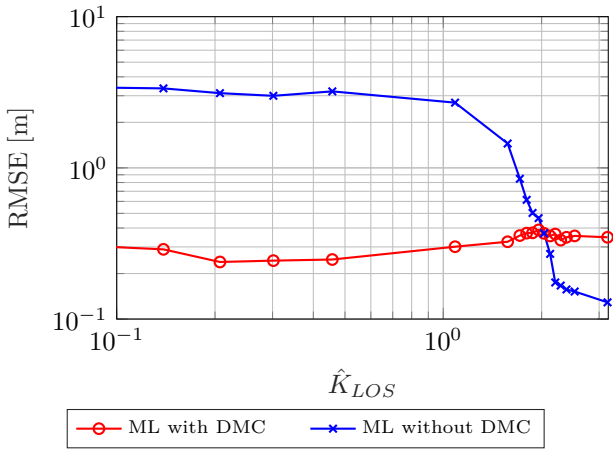

Figure 4.3: Comparison of ML with and without model for DMC, with $\gamma_r = 5\,\text{ns}, T_p = 12.5\,\text{ns}$.

as joint estimation of γ_r and $\hat{\tau}$ was found to be challenging. This assumption is supported by the rise time's dependence on room geometry [25]. Other parameters were initialized corresponding to $K_{\text{LOS}} = 1$, c.f. Paper [A].

Figure 4.3 shows the results grouped by $\hat{K}_{\text{LOS}}$, with each point representing an equal subset of measurements. For small $\hat{K}_{\text{LOS}}$ values, our algorithm significantly outperforms the conventional ML algorithm, aligning with simulated data performance. However, for large $\hat{K}_{\text{LOS}}$ values, the conventional algorithm performs better. This discrepancy arises from the estimation of nuisance parameters γ_f and A, which negatively affect the accuracy of $\hat{\tau}$ estimation.

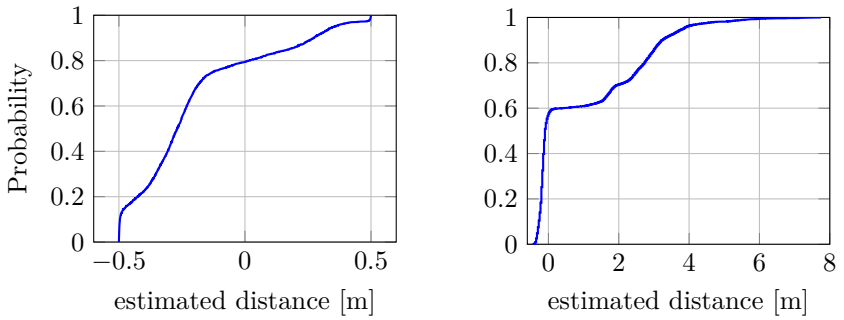

(a) cumulative distribution function (CDF) with DMC model

(b) CDF without DMC model

Figure 4.4: CDFs of the RMSE of the whole dataset.

Evaluation of the data reveals a bias in our algorithm at the highest $\hat{K}_{\text{LOS}}$ value, corresponding to an error of approximately 33 cm (or 1 ns). Figure 4.4 illustrates this bias, likely due to an overestimation of the rise time parameter γ_r, which limits performance. While the conventional ML algorithm is unbiased, it exhibits significant outliers for non-line-of-sight (NLOS) data with delayed estimates. Overall, for

the full dataset, the conventional algorithm achieved an RMSE of 1.89 m, compared to 33.4 cm for our algorithm incorporating DMC modeling. This suggests that the proposed algorithm can improve performance in most indoor scenarios, but can still be improved. Especially for larger values of $\hat{K}_{LOS}$, it is advisable to use the ML estimator without DMC exploitation. This can be achieved by incorporating a metric for the model match, and choosing the applicable estimator, for example by using the Bayesian information criterion, as described in [67].

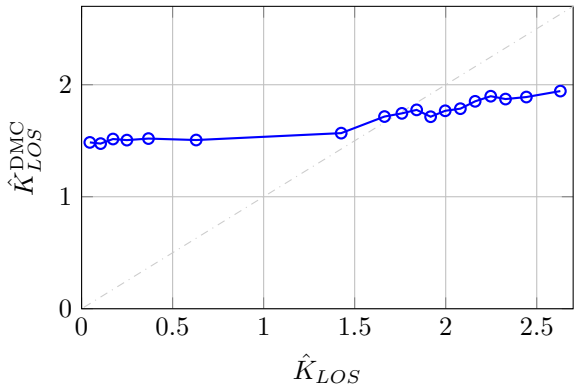

Figure 4.5: Median ratio between estimated $\hat{K}_{LOS}$.

Figure 4.5 illustrates the ratio of $\hat{K}_{\mathrm{LOS}}^{\mathrm{DMC}} = |\hat{\alpha}|^2/\hat{\Omega}_1$, derived from nuisance parameters in the DMC-based algorithm, to $\hat{K}_{\mathrm{LOS}}$ computed from UWB-data using Eq. 4.2. For high $\hat{K}_{\mathrm{LOS}}$ values, the estimation is relatively accurate. However, at low $\hat{K}_{\mathrm{LOS}}$, the estimation becomes unreliable, as more DMC energy is incorrectly attributed to the LoS component due to the reduced bandwidth. For high values of $\hat{K}_{\mathrm{LOS}}$, the wideband estimation of $\hat{K}_{\mathrm{LOS}}^{\mathrm{DMC}}$ is too small, which can be attributed to the smaller signal bandwidth. This leads to an overestimation of energy in the DM, as the LoS is less distinguishable from DMC. On the other hand, for small values of $\hat{K}_{\mathrm{LOS}}$, the energy in the DM is underestimated. Similarly, this can be attributed to a worse separability of DM and the LoS component. Overall, this shows a tendency of the algorithm to converge to a $\hat{K}_{\mathrm{LOS}}^{\mathrm{DMC}}$ of about 2, meaning energy within DM and LoS is estimated to be in the same magnitude order.

4.2 Coherent Chirp Synthesis of Multiband Signals

The derivations presented in this section rely on the wideband chirp signal model described in Subsection 2.1.2. The derivation of the CRLB is split into two parts, one where the overlapping frequency bands of the chirps are neglected, and another where the additional information from overlap is derived. This section aims to give an overview of the results, focusing on only the Fisher information matrix (FIM) terms for delay τ and unknown phases ϕ_p, but a full derivation can be found in Paper [D], Section D.3. The parameter vector for this is defined as $\boldsymbol{\theta} = [\tau, |\alpha|, \phi_1, \ldots, \phi_{N_p}]^T = [\tau, |\alpha|, \boldsymbol{\Phi}]^T$, as described in Subsection 2.1.2.

The inverse of the first entry of the FIM, corresponding to the delay estimation bound, can be expressed as

$$[\boldsymbol{\mathcal{I}}^{-1}(\boldsymbol{\theta})]_{1,1} = \left(2\frac{|\alpha|^2}{\sigma_w^2}\left(\|\dot{\boldsymbol{s}}\|_{\mathcal{H}}^2 - \boldsymbol{G}\boldsymbol{H}^{-1}\boldsymbol{G}^T\right) + \mathrm{tr}[\bullet]\right)^{-1}. \tag{4.3}$$

The matrices $\boldsymbol{G}$ and $\boldsymbol{H}$ (as described in Section D.3) correspond to the diminished information from estimating the nuisance parameters for amplitude $|\alpha|$ and phases ϕ_p, and are calculated using the Schur complement. The trace term $\mathrm{tr}[\bullet]$ describes additional information from the DMC, which can be assumed to be negligibly small for practical use-cases, if the signal-to-noise ratio (SNR) is sufficiently large. Additionally, estimation of additional information in the trace term $\mathrm{tr}[\bullet]$ is computationally complex, and thus is not deemed useful in this evaluation.

The FI for the p-th phase, neglecting overlap, can be expressed as

$$[\boldsymbol{\mathcal{I}}(\boldsymbol{\theta})]_{(p+2),(p+2)} = \frac{2|\alpha|^2}{\sigma_w^2}\mathrm{Re}\ \langle \boldsymbol{S}, \boldsymbol{S}\rangle_{\mathcal{H}}, \tag{4.4}$$

where $\boldsymbol{S}$ is the matrix representation of phase-shifted subchirps, as described in Subsection 2.1.2.

We can exploit the assumption that a realisation of the dense multipath does not change within a single-shot measurement. Therefore, we can exploit overlapping parts of chirps in the frequency domain. Using the estimator in (3.7), we can define a prior information term for $\boldsymbol{\phi}_p$ as

$$[\boldsymbol{\mathcal{B}}(\boldsymbol{\theta})]_{(p+2),(p+2)} = \widetilde{\mathrm{SNR}}\ 2\tilde{N} \tag{4.5}$$

for all $p \geq 2$, meaning additional information is available for all $\phi_p \forall p \neq 1$. The number of overlapping samples in the frequency domain for two chirps is expressed as $\tilde{N}$. This is similar to [58, p. 33, Ex 3.4], which describes the estimation of a phase term in AWGN. The additional SNR is defined as

$$\widetilde{\mathrm{SNR}} = \frac{\sigma_\nu^2}{\sigma_w^2} = \frac{\Omega_1 T_s}{N_0}, \tag{4.6}$$

which is the ratio between the variance of the dense multipath and the variance of the AWGN. Note that this neglects the energy in the signal $\boldsymbol{s}$, as no additional information can be gained from the signal energy when it is already used in the estimator. Combining the prior information term $[\boldsymbol{\mathcal{B}}(\boldsymbol{\theta})]_{(p+2),(p+2)}$ with the phase information from the signal energy as described in (3.5), we derive a modified phase information term

$$[\widetilde{\boldsymbol{\mathcal{I}}}(\boldsymbol{\theta})]_{(p+2),(p+2)} = [\boldsymbol{\mathcal{B}}(\boldsymbol{\theta})]_{(p+2),(p+2)} + [\boldsymbol{\mathcal{I}}(\boldsymbol{\theta})]_{(p+2),(p+2)} \tag{4.7}$$

From this, a solution for the FIM entry for the delay can be found similarly as for (4.3).

The FI $[\boldsymbol{\mathcal{I}}(\boldsymbol{\theta})]_{(p+2),(p+2)}$ expressed here neglects the additional assumption of an unchanged realisation of the DM within the time-frame of all transmitted subchirps. This additional information is accounted for within $[\boldsymbol{\mathcal{B}}(\boldsymbol{\theta})]_{(p+2),(p+2)}$. An intuitive explanation for this can be found easily: One can assume that the geometry of the room and other conditions influencing multipath propagation in general

(both DM and resolvable multipath reflections) stay constant over the transmission time-frame of one node, when this time-frame is reasonably short, i.e. in the order of magnitude of a few ms. Within this time-frame, two signals that are identical with the exception of a phase shift, generate identical multipath with the same phase difference between each other. This is exploited in the phase estimation within the same frequencies of consecutive subchirps, as these parts of subchirps are mathematically the same, with the exception of a phase shift. For the additional FI, the already used information for the phase estimation within the LoS in the two-step estimation has to be accounted for. This is done by neglecting the energy within the LoS for the term $[\boldsymbol{\mathcal{B}}(\boldsymbol{\theta})]_{(p+2),(p+2)}$, which is already accounted for in $[\boldsymbol{\mathcal{I}}(\boldsymbol{\theta})]_{(p+2),(p+2)}$.

For the numerical evaluation of chirp synthesis in multiband signals, a simulation environment was used. The simulation was done according to the signal model described in Subsection 2.1.2, with random transmit delays and phase offsets.

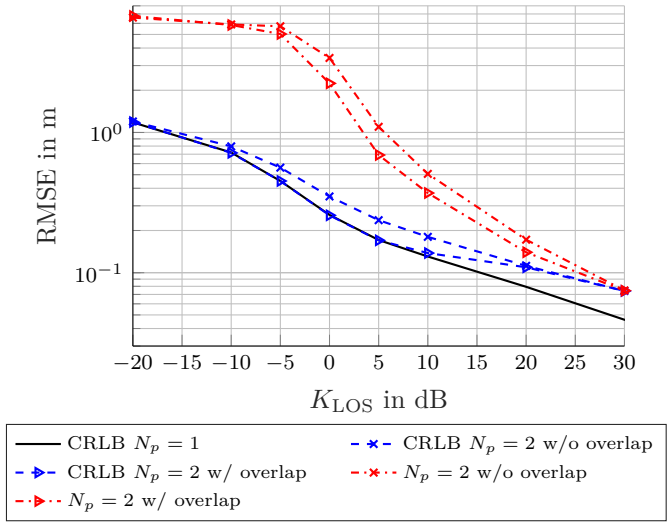

Figure 4.6: CRLB and RMSE for 2 subchirps. Comparison with CRLB of one subchirp. 200 realizations for evaluation, SNR = 40dB, $\gamma_r = 5$ns, $\gamma_f = 20$ns.

We simulated 200 realizations of the DMC under varying transmission times while maintaining a constant overall SNR across different values of K_{LOS}. The SNR is defined as $\mathrm{SNR} = \frac{|\alpha|^2+\Omega_1}{N_0}$, representing the ratio of signal energy, including the DM, to noise.

A particle-based estimator with 5000 particles was used to jointly estimate delays and phases. For scenarios with $N_p = 2$ or $N_p = 4$ subchirps, the subchirps were evenly distributed across the frequency band with a 20% overlap, ensuring consistent total signal energy. As a comparison, a continuous chirp ($N_p = 1$) over the full bandwidth 80MHz is illustrated, with $N = 300$ samples per chirp.

Figure 4.6 illustrates the results for $N_p = 2$ subchirps. Overall, a clear trend can be seen for all estimators, where for larger values of K_{LOS} the RMSE improves. For large K_{LOS} values, all evaluations for $N_p = 2$ converge to the same performance level, indicating that when DM energy is negligible, phase estimation within over-

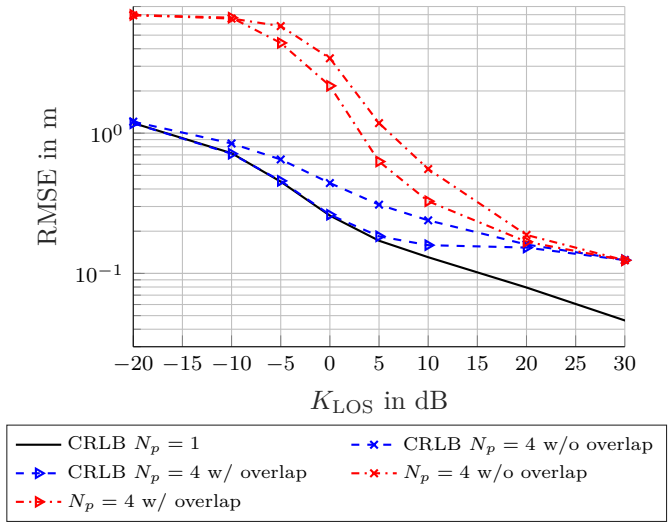

Figure 4.7: CRLB and RMSE for 4 subchirps. Comparison with CRLB of one subchirp. 200 realizations for evaluation, SNR = 40dB, $\gamma_r = 5$ns, $\gamma_f = 20$ns.

lapping frequency bands does not improve delay estimation. For small K_{LOS}, the estimators deviate from the CRLB, limited primarily by the delay estimation prior. In the intermediate range, the CRLB without overlap exploitation exhibits a noticeable offset compared to the CRLB for a continuous chirp ($N_p = 1$). This is attributed to the partial coherence between the two subchirps, where phase estimation reduces the available information. However, exploiting overlap significantly improves performance, bringing the CRLB closer to that of a continuous chirp for smaller K_{LOS} values. Although the evaluations do not achieve the CRLB in this range, the improvement from overlap exploitation is evident and comparable to the gains predicted by the CRLB.

Figure 4.7 presents similar results for $N_p = 4$ subchirps. The behavior for extreme K_{LOS} values remains consistent with or without overlap exploitation. In the threshold region, overlap exploitation yields slightly greater performance gains than for $N_p = 2$. This can be attributed to the increased loss from phase estimation, which is partially mitigated by additional energy contributions from overlapping signal segments. Nevertheless, performance for multiple phase-offset chirps decreases under LoS conditions as the number of subchirps increases due to additional nuisance parameters introduced by the phase offsets.

4.3 TDoA Localization

This section examines the works presented in [B] and [C], which share a common large-scale scenario for TDoA-based localization. As detailed in Subsection 3.4.4, the algorithm described in [B] serves as a computational simplification of the posterior likelihood estimation approach introduced in [C].

It is important to note that this section does not provide a comprehensive overview of all evaluations and simulations conducted in these studies. Only the

most relevant results are presented. For principal evaluations of how these algorithms work (especially in smaller scenarios and well-controlled simulations) the reader is referred to the original papers.

4.3.1 Scenario for TDoA Localization

The scenario considered in these evaluations is identical to the one described in Section 1.1, which corresponds to a specialized hall for testing and measurements located in Graz. Figures 1.3 and 1.4 illustrate this scenario, showing APs (in blue) and 1073 node positions (in black) from an isometric and top-down perspective, respectively. Additional views of the same scenario can be found in Figures 1.1–1.6, also in Chapter 1.

The test setup consisted of six APs, each equipped with two antennas spaced 6 cm apart, corresponding approximately to half the wavelength of the transmitted signals. The signals were recorded using SDRs from National Instruments. The hardware limitations of these SDRs were deemed negligible for the purpose of these evaluations.

The nodes in this setup were electronic shelf labels, as shown in Figure 1.2. These devices operate within the ISM band at 2.4 GHz, transmitting chirps that span sub-bands within the ISM band but do not cover the entire band. For the TDoA evaluations, an idealized pre-processing step is assumed, yielding measurements across the entire ISM band that resemble ideal pulses, as described in [49].

Additionally, these nodes supported cooperative measurements, allowing each node to obtain data from every other node. However, these cooperative measurements were limited to narrower bandwidths giving RSS values, thereby providing lower information content per measurement. These data were utilized in the clustering algorithm to define the nearest neighboring nodes, represented by the set $\mathcal{D}_l$ for node $l \in \mathcal{L}$. These measurements were also incorporated into one variant of the cooperative localization algorithm.

It should be emphasized that this section is focused exclusively on measurement-based evaluations. Additional simulation results for the same scenario can be found in Subsections B.6.3 and B.6.4 of the appended papers.

4.3.2 CRLB for Clustering

This section will focus only on the main results of the CRLB for the clustering algorithm. For a full derivation and more insights, please refer to Paper [B], section B.5. Note that this subsection does not focus on results for the cooperative localization algorithm, as the CRLB for this algorithm is out of scope for this thesis. This subsection uses the wideband pulse signal model, described in Subsection 2.1.1.

We define a so-called ranging direction matrix (RDM) [68] as

$$\boldsymbol{R}_r(\phi_m, \vartheta_m) = \boldsymbol{e}(\phi_m, \vartheta_m)\boldsymbol{e}^T(\phi_m, \vartheta_m) \tag{4.8}$$

where $\boldsymbol{e}(\phi_m, \vartheta_m)$ is a unit vector pointing from array m in the direction of the node l. The main result from Paper [B] is the equivalent Fisher information matrix

(EFIM) for the position $\boldsymbol{p}_l$ which is decomposed into three components corresponding to the delay and angle terms as

$$\boldsymbol{\mathcal{I}}_l \approx \sum_{m=1}^{M} \Bigg[\frac{8\pi^2}{d_m^2} D_\lambda^2(\phi_m)\ KD_l\ \mathrm{SINR}_m \boldsymbol{R}_r(\phi_m + \frac{\pi}{2}, \vartheta_m) \tag{4.9}$$

$$+ \frac{8\pi^2}{d_m^2} D_\lambda^2(\vartheta_m)\ KD_l\ \mathrm{SINR}_m \boldsymbol{R}_r(\phi_m, \vartheta_m + \frac{\pi}{2}) \tag{4.10}$$

$$+ \Lambda \frac{8\pi^2}{c^2} \beta^2\ KD_l\ [\widetilde{\mathrm{SINR}}_\tau]_m \boldsymbol{R}_r(\phi_m, \vartheta_m) \Bigg], \tag{4.11}$$

using the results from Appendices B.9 and B.10. The sum $\sum_{m=1}^{M}$ represents a sum over the information of all anchors m, $D_\lambda^2(\phi_m)$ and $D_\lambda^2(\vartheta_m)$ are the array apertures in azimuth and elevation, stemming from the array geometry. SINR_m and $[\widetilde{\mathrm{SINR}}_\tau]_m$ account for the interference by the DM, β^2 is the mean-squared signal bandwidth, and d_m, ϕ_m, and ϑ_m are the distances between the array centers and the cluster center and the corresponding angle parameters. Additionally, this equation scales with K and D_l, where K is the number of anchors per AP and D_l is the size of the cluster, meaning the number of nodes in the set $\mathcal{D}_l$. This shows that for an increasing number of nodes in the cluster, the FI increases linearly.

As this would only be true in an ideal scenario, where all nodes within a cluster are at the same position. An additional correction factor Λ is introduced, which accounts for diminished information from non-ideal clusters, i.e. cluster nodes spaced over a room. This can also be interpreted as an effective reduction of bandwidth. The derivation of the correction factor Λ can be found in Section B.9. This FI is also strongly dependent on anchor placement and geometry of the nodes.

With this, we can define the position error bound (PEB) for multiple anchors m and multiple nodes $l \in \mathcal{D}_l$ as

$$\mathrm{var}(\hat{\boldsymbol{p}}_l^{(c)}) \geq \mathcal{P}_c = \sqrt{\mathrm{tr}\{\boldsymbol{\mathcal{I}}_l^{-1}\}}, \tag{4.12}$$

where the operator var denotes the sum over the variances of the three cartesian coordinates respectively. It should be noted that this bound only holds true for an estimated cluster position $\hat{\boldsymbol{p}}_l^{(c)}$.

For real-world applications, the cluster position would be mostly of no importance, but it can be assumed that the cluster position is within a vicinity of the position of the node l which has been used to define the cluster. Equality holds true for scenarios where all nodes $\mathcal{D}_l$ are distributed in such way that the cluster position $\boldsymbol{p}_l^{(c)} = \boldsymbol{p}_l$. In real-world scenarios this assumption often does not hold, thus we propose a biased lower bound for the node l

$$\mathrm{var}(\hat{\boldsymbol{p}}_l) \geq \mathcal{P}_l = \sqrt{\mathcal{P}_c^2 + \|\boldsymbol{p}_l^{(c)} - \boldsymbol{p}_l\|^2}. \tag{4.13}$$

This biased lower bound has the advantage of easier representation of relevant errors, and comparability with the RMSE of the node position $\boldsymbol{p}_l$. It should be noted that this biased bound can only be evaluated if the ground-truth of positions is known. This is the case for comparisons with the CRLB in controlled environments, but may not be true for real-world applications. Thus, this bound has only informative character for scientific evaluations.

For the evaluation of the clustering algorithm, the likelihood (3.31) was estimated using a particle-based approach. This enabled efficient computation of the position $\hat{\boldsymbol{p}}_l$ for each node l by identifying the likelihood's maximum, serving as the estimate for $\boldsymbol{p}_l$. The set $\mathcal{D}_l$ was defined based on strongest RSS measurements, with the cluster size (number of nearest nodes) varied. Detailed explanations of this algorithm are provided in Section B.6.

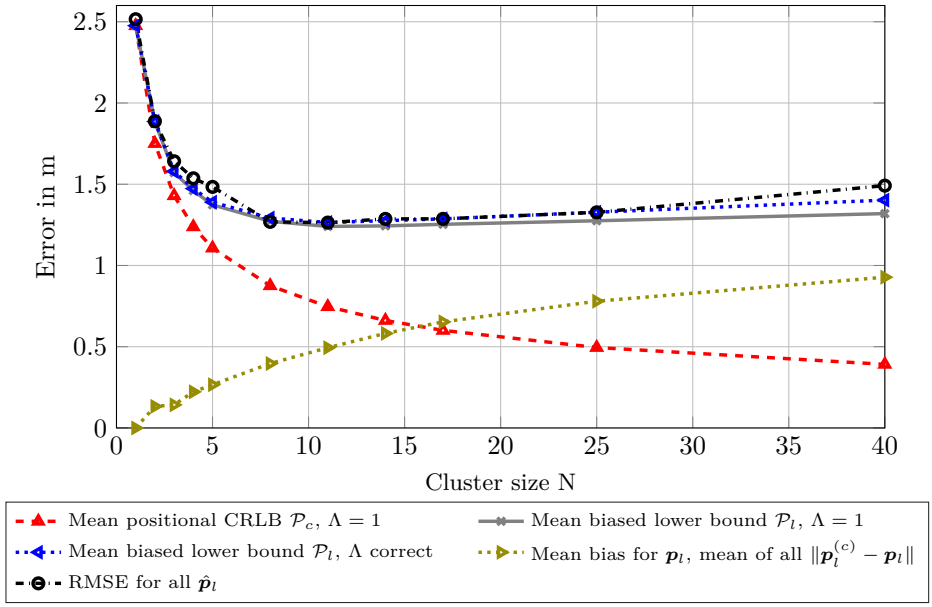

Figure 4.8: Results for large-scale synthetic scenario with RSS-based clusters

Figure 4.8 shows results for a synthetic scenario using RSS-based clusters compared to the CRLB for clustering. The simulated scenario is equal to the scenario described in 4.3.1, but a simulation environment for wideband signals was used, as described in B.6. This figure shows that for small cluster sizes (up to D_l of 11), the RMSE improves almost with the square-root of D_l. This is in accordance with the mean positional CRLB for this scenario, which is also improving approximately with the square-root of D_l, which can be attributed to the information for a cluster increasing linearly with D_l. For larger cluster sizes ($D_l \geq 11$), the RMSE is increasing. This effect can be attributed to the bias term ($\|\boldsymbol{p}_l^{(c)} - \boldsymbol{p}_l\|^2$), which shows that there can be a significant offset between the estimated cluster position and the position of the node of interest. This bias term is almost negligible for smaller cluster sizes, but dominates for larger cluster sizes. This can be seen well when directly comparing the mean positional CRLB with the bias term, where for cluster sizes of $D_l = 17$, these two effects are approximately equal. Additionally, this figure shows the biased lower bound, with and without the correction factor Λ. This biased lower bound incorporates the effects of the CRLB and the bias term, and corresponds very well to the achieved RMSE. The corrections factor Λ has negligible effects on the bound for small cluster sizes, but for very large clusters ($D_l = 40$), a significant offset can be seen. The RMSE also shows the same increase for very large clusters, showing that the biased lower bound with correction factor

Λ being a good approximation of actual performance.

4.3.3 Results for TDoA Localization

The results in this subsection were obtained using two approaches. First, for the clustering algorithm, the likelihood (3.31) was estimated using a particle-based approach, as describe in the previous subsection.

The other method incorporates a particle-based belief-propagation (BP) algorithm, estimating the posterior distribution of the cooperative localization method described in (3.11). This algorithm gave us estimates for $\boldsymbol{p}_l \forall l \in \mathcal{L}$, by using the mean of the marginal distributions for the node positions. Evaluations for this algorithm were done for two different inter-node likelihoods or measurement methods: Perceptual hashing and RSS. While GCC likely outperforms these in accuracy, it was computationally prohibitive for the large scenario considered here. For smaller scenarios, evaluations are shown with all three methods in Paper [C], see Section C.5.

For the following results, a uniform prior over the all possible node positions was used. This means that no restrictions regarding for example nodes being solely in aisles were used. For evaluations on how these restrictions can improve results, refer to Section B.6.

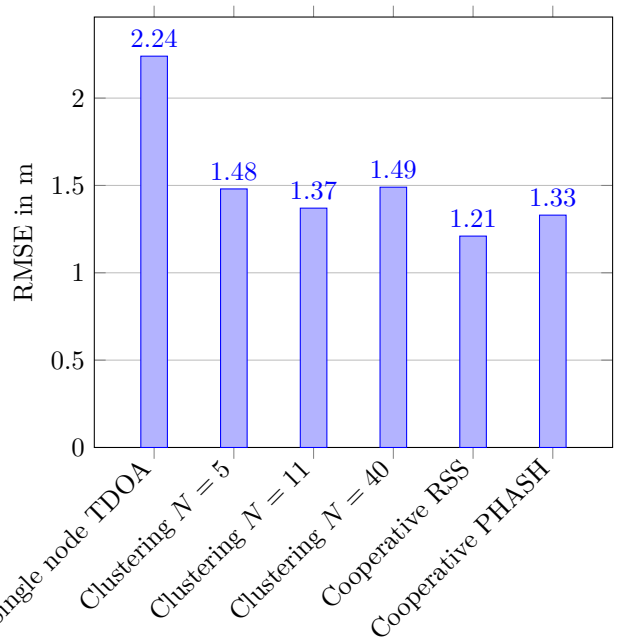

Figure 4.9: RMSE of the results for the two TDoA based algorithms shown in Papers [B] and [C]. The number N refers to the cluster size, defining the number of nearest nodes incorporated into the estimation.

Figure 4.9 shows selected results for the RMSE for the aforementioned algorithms. Overall, one can see that both the cooperative localization exploiting

mutual information and the clustering approach improved the performance over single-node TDoA based localization. The single node-estimation maximizes the likelihood given in (3.15) $\forall l \in \mathcal{L}$.

As one can see, this reference method performs worst, with an RMSE greater than 2m. The performance improves quickly just by using a cluster size of $N = 5$ defined by the strongest RSS measurements, and improves further by using a cluster size of $N = 11$. This alone almost doubles the overall precision of the estimation. More nodes within the set may lead to diminishing returns, as one can see in the RMSE for a cluster size of $N = 40$. This can be explained by the estimation of the cluster position $\boldsymbol{p}_c$ not being a reasonable estimate for the node position $\boldsymbol{p}_l$ anymore, as the cluster position can get biased over the node position in realistic scenarios.

The cooperative localization algorithm improves performance further. The RSS-based method achieves the best results overall, while perceptual hashing performs slightly worse but offers the advantage of using mutual information from wideband measurements without additional RSS data.

Further evaluations and descriptions for both GCC and perceptual hashing can be found in Section C.3.3, where it is also shown in detail how these methods can exploit mutual information between wideband measurements.

Evaluations for clustering and cooperative algorithms are done using 500 particles. Evaluations with more particles do lead to better results, suggesting that the underlying distributions are approximated sufficiently well.

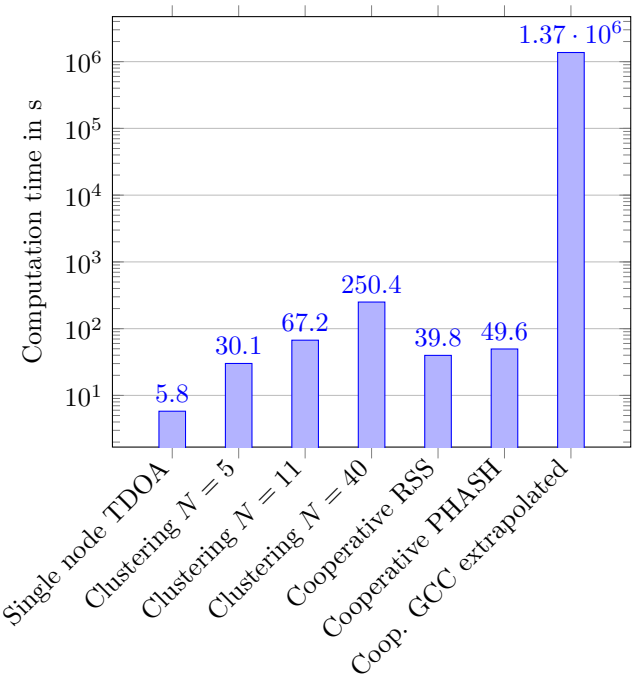

Figure 4.10: Approximate single-shot computation times for the two TDoA based algorithms shown in Papers [B] and [C], for all nodes within the set $\mathcal{L}$.

Figure 4.10 shows the computation times for the different algorithms and variations in seconds for all 1078 nodes. All of these were approximated by a single-shot estimation using the algorithms on a typical workstation (AMD Ryzen 9 3900X, 64 GB RAM, other components not relevant for the evaluation). The computation time of these algorithms relies mostly on CPU performance.

It can be seen that Clustering increases the computational complexity approximately linearly with the number of nodes in a cluster. As the sweet spot for this algorithm is mostly within smaller number of nodes in a cluster (i.e. $N = 11$), results can be expected within about a minute of time. Additionally, this algorithm is able to evaluate results only for single nodes of interest, which is not possible for the algorithm incorporating cooperative localization.

For the cooperative localization algorithm, RSS and perceptual hashing perform similarly well, as the computational complexity of both algorithms is comparable when the hashes for perceptual hashing are already computed. The time discrepancy between these two algorithms stems solely from the additional calculation of hashes, which takes about 10s for this scenario. Additionally, an estimation of computation time is given for GCC, which is several orders of magnitude larger. This stems from the large computational load from even a single cross correlation between wideband measurements.

It should also be noted that the clustering algorithm scales linearly in computation time for the overall number of nodes. The cooperative localization algorithm on the other hand scales quadratically in computation time, and additionally will run into memory limitations for larger scenarios, as marginal likelihoods have to be stored.

Considering this, it would be advisable for very large scenarios (i.e. 10000 nodes and more) to weigh between the benefits and disadvantages of these two algorithms.

5 Conclusion

This thesis addresses the three hypotheses stated in the introduction. Let's take a final look at the hypotheses, and see if they hold true:

Hypothesis 1

It is possible to exploit **additional information from DM** for ranging and localization, in spite of a small (sub-UWB) measurement bandwidth.

The research within this thesis shows that DM is not merely an obstacle, but a resource packed with valuable information when approached correctly. Taking a look at this hypothesis, one can see that DM is exploited in multiple ways: The additional information from the DM improves the ranging performance in Papers [A] and [D], and gives a possibility to improve the overall positioning performance in a large scenario by exploiting statistical similarities within the DM for multiple nodes, as seen in Paper [C].

Paper [A] demonstrates that the structure of the DM itself can be explicitly incorporated into a ranging estimator rather than treated solely as interference. This is achieved by parameterizing the DM through a statistical model and using a model-based ML approach. By explicitly modeling the DMC, rather than discarding it as interference, the estimator can more accurately estimate the LoS delay even in situations where the LoS component is not the strongest component of the received signal. This method improves performance especially under NLOS conditions where traditional methods fail, thus extending the performance boundaries of ranging in DM conditions. Paper [D] similarly shows how the coherent synthesis of multi-band chirps allows to exploit the DM inbetween chirps, increasing performance and increasing effective bandwidth for delay estimation.

This improvement is particularly relevant in practice, because many low-power, low-cost wireless systems operate in bandwidth-limited environments, where DM is often a significant problem and conventional methods tend to be less robust. The ability to exploit the DM, rather than just trying to suppress it, makes accurate ranging and localization feasible even in challenging, bandwidth-constrained scenarios, especially when robust positioning of many transmitting nodes is relevant.

This in turn, leads directly to our second Hypothesis.

Hypothesis 2

The performance of TDOA-based wideband localization can be improved by utilizing **(mutual) relative position information from closely-spaced transmitters**

The results from Papers [B] and [C] provide substantial evidence for the validity of this hypothesis. The thesis successfully shows that by leveraging the similar statistical characteristics observed for closely-spaced nodes, cooperative localization performance can be substantially improved without any additional required measurements. Paper [B] presents a clustering algorithm, exploiting additional relative position information using RSS measurements. This improves localization performance significantly, but necessitates additional energy-consumption for RSS measurements.

Paper [C] elaborates this concept further, exploring how mutual information can be extracted from wideband measurements using perceptual hashing and GCC. This mutual information encodes relative position information between nodes, leading to more accurate location estimates. The implementation of a message-passing framework allows this relative information to be incorporated within a joint estimation approach, further enhancing performance. These methods demonstrate that by leveraging mutual information, accurate localization can be achieved even with limited information from individual nodes.

A small disadvantage of the cooperative localization algorithm is the additional computational load, as such algorithms tend to increase computation times quickly with increasingly large scenarios. This leads to our third Hypothesis.

Hypothesis 3

Algorithms for (cooperative) localization and ranging can be **implemented or approximated in an efficient manner**, allowing to work on large-scale scenarios.

The third Hypothesis also holds true, as seen in Papers [A]-[C]. Paper [A] shows that an efficient estimator for ranging and DM parameter estimation can be derived, Paper [B] shows an efficient implementation of a cluster-based joint positioning algorithm, which can be seen as a simplification of the cooperative algorithm in Paper [C], and Paper [C] shows perceptual hashing to be a computationally viable option to exploit mutual information between wideband measurements of a large number of nodes.

Overall, this thesis shows that the mutual information inbetween measurements and information from the DM can be exploited to improve the localization performance significantly. But, it should be noted that there is still room for improvement, especially for the cooperative localization algorithm described in [C].

As these algorithms are all “classic” model-based algorithms, not based on

machine learning, an interesting approach is to extract the mutual information by some form of neural network or similar. This is a logical step, as perceptual hashing, used for extracting mutual information, has its roots in image processing, where it has been superseded by specialized neural networks.

Furthermore, the algorithms for estimating DM parameters described in [A] are still computationally slow, even when using the efficient implementation presented in this work. This could be further improved, for example, by finding a reasonable prior distribution for the parameters of the DM with an even more efficient algorithm. Also, the issue of biased estimation of DM parameters could be mitigated by intelligent selection between the proposed algorithm and an LoS estimator.

The algorithms described in Paper [D] allow for more classical algorithmic research, as this paper focuses solely on chirp signals. A generalization to other signal atoms should be straightforward, but further research could investigate if the information gain from overlapping bands could also be exploited from communication signals, where the so-called aggregate bandwidth [69] is large, but often only smaller bands can be used at a single moment in time.

In conclusion, this thesis has successfully addressed all three core hypotheses, demonstrating that dense multipath channels can be exploited for improved localization performance in resource-constrained large-scale scenarios. The thesis not only advances the state-of-the-art in DM exploitation for ranging and localization, but also provides practical tools and algorithms that can be readily implemented, thus opening up avenues for deployment in real-world applications.

Bibliography

[1] K. Witrisal, P. Meissner, E. Leitinger, Y. Shen, C. Gustafson, F. Tufvesson, K. Haneda, D. Dardari, A. F. Molisch, A. Conti, and M. Z. Win, "High-Accuracy Localization for Assisted Living: 5G systems will turn multipath channels from foe to friend," *IEEE Signal Processing Magazine*, 2016, doi: 10.1109/MSP.2015.2504328.

[2] A. Yassin, Y. Nasser, M. Awad, A. Al-Dubai, R. Liu, C. Yuen, R. Raulefs, and E. Aboutanios, "Recent Advances in Indoor Localization: A Survey on Theoretical Approaches and Applications," *IEEE Communications Surveys and Tutorials*, 2017, doi: 10.1109/COMST.2016.2632427.

[3] D. Neunteufel, A. Fuchs, and H. Arthaber, "ToF-based Indoor Positioning for Low-power IoT Nodes," in *2020 54th Asilomar Conference on Signals, Systems, and Computers*, Nov 2020, doi: 10.1109/IEEECONF51394.2020.9443431.

[4] J. A. del Peral-Rosado, R. Raulefs, J. A. López-Salcedo, and G. Seco-Granados, "Survey of Cellular Mobile Radio Localization Methods: From 1G to 5G," *IEEE Communications Surveys Tutorials*, Secondquarter 2018, doi: 10.1109/COMST.2017.2785181.

[5] D. Neunteufel, S. Grebien, and H. Arthaber, "Indoor Positioning of Low-Cost Narrowband IoT Nodes: Evaluation of a TDoA Approach in a Retail Environment," *Sensors*, 2022, doi: 10.3390/s22072663.

[6] P. Zand, J. Romme, J. Govers, F. Pasveer, and G. Dolmans, "A high-accuracy phase-based ranging solution with Bluetooth Low Energy (BLE)," in *2019 IEEE Wireless Communications and Networking Conference (WCNC)*, 2019, doi: 10.1109/WCNC.2019.8885791.

[7] A. Comuniello, A. Angelis, A. Moschitta, and P. Carbone, "Using Bluetooth Low Energy Technology to Perform ToF-Based Positioning," *Electronics*, 12 2021, doi: 10.3390/electronics11010111.

[8] S. Sadowski and P. Spachos, "RSSI-Based Indoor Localization With the Internet of Things," *IEEE Access*, 2018, doi: 10.1109/ACCESS.2018.2843325.

[9] M. Kotaru, K. Joshi, D. Bharadia, and S. Katti, "SpotFi: Decimeter Level Localization Using WiFi," in *Proceedings of the 2015 ACM Conference on Special Interest Group on Data Communication*, 2015, doi: 10.1145/2785956.2787487.

[10] S. Kumar, "Performance Analysis of RSS-Based Localization in Wireless Sensor Networks," *Wireless Personal Communications*, Sep 2019, doi: 10.1007/s11277-019-06428-5.

[11] T. Gigl, G. J. Janssen, V. Dizdarevic, K. Witrisal, and Z. Irahhauten, "Analysis of a UWB Indoor Positioning System Based on Received Signal Strength," in *2007 4th Workshop on Positioning, Navigation and Communication*, 2007, doi: 10.1109/WPNC.2007.353618.

[12] J. Tiemann, F. Schweikowski, and C. Wietfeld, "Design of an UWB indoor-positioning system for UAV navigation in GNSS-denied environments," in *2015 International Conference on Indoor Positioning and Indoor Navigation (IPIN)*, Oct 2015, doi: 10.1109/IPIN.2015.7346960.

[13] I. Oppermann, M. Hämäläinen, and J. Iinatti, *UWB: Theory and Applications*. NJ,USA: John Wiley and Sons: Hoboken, 2005.

[14] J. Kulmer, S. Hinteregger, B. Großwindhager, M. Rath, M. S. Bakr, E. Leitinger, and K. Witrisal, "Using DecaWave UWB transceivers for high-accuracy multipath-assisted indoor positioning," in *2017 IEEE International Conference on Communications Workshops (ICC Workshops)*, May 2017, doi: 10.1109/ICCW.2017.7962828.

[15] D. Dardari, A. Conti, U. Ferner, A. Giorgetti, and M. Z. Win, "Ranging with Ultrawide Bandwidth Signals in Multipath Environments," *Proceedings of the IEEE*, Feb 2009, doi: 10.1109/JPROC.2008.2008846.

[16] G. Kia, L. Ruotsalainen, and J. Talvitie, "Toward Accurate Indoor Positioning: An RSS-Based Fusion of UWB and Machine-Learning-Enhanced WiFi," *Sensors*, 2022, doi: 10.3390/s22093204.

[17] K. Witrisal, E. Leitinger, S. Hinteregger, and P. Meissner, "Bandwidth Scaling and Diversity Gain for Ranging and Positioning in Dense Multipath Channels," *IEEE Wireless Communications Letters*, vol. 5, no. 4, pp. 396–399, 2016.

[18] S. Grebien, E. Leitinger, K. Witrisal, and B. H. Fleury, "Super-Resolution Estimation of UWB Channels including the Dense Component — An SBL-Inspired Approach," *IEEE Transactions on Wireless Communications*, 2024, doi: 10.1109/TWC.2024.3371352.

[19] J. Kulmer, S. Grebien, E. Leitinger, and K. Witrisal, "Delay Estimation in Presence of Dense Multipath," *IEEE Wireless Communications Letters*, Oct 2019, doi: 10.1109/LWC.2019.2923409.

[20] S. Jiang, W. Wang, Y. Miao, W. Fan, and A. F. Molisch, "A Survey of Dense Multipath and Its Impact on Wireless Systems," *IEEE Open Journal of Antennas and Propagation*, 2022, doi: 10.1109/OJAP.2022.3168400.

[21] J. Li, B. Ai, R. He, M. Yang, and Z. Zhong, "On Modeling of Dense Multipath Component for Indoor Massive MIMO Channels," *IEEE Antennas and Wireless Propagation Letters*, 2019, doi: 10.1109/LAWP.2019.2896088.

[22] E. Leitinger, M. Fröhle, P. Meissner, and K. Witrisal, "Multipath-assisted maximum-likelihood indoor positioning using UWB signals," in *2014 IEEE International Conference on Communications Workshops (ICC)*, 2014, doi: 10.1109/ICCW.2014.6881191.

[23] E. Leitinger, "Cognitive Indoor Positioning and Tracking using Multipath Channel Information," dissertation, Graz University of Technology, Austria, 2015.

[24] H. MacLeod, C. Loadman, and Z. Chen, "Experimental studies of the 2.4-GHz ISM wireless indoor channel," in *3rd Annual Communication Networks and Services Research Conference (CNSR'05)*, May 2005, doi: 10.1109/CNSR.2005.33.

[25] J. Karedal, S. Wyne, P. Almers, F. Tufvesson, and A. F. Molisch, "A Measurement-Based Statistical Model for Industrial Ultra-Wideband Channels," *IEEE Transactions on Wireless Communications*, vol. 6, no. 8, pp. 3028–3037, 2007.

[26] D. B. Jourdan, D. Dardari, and M. Z. Win, "Position error bound for UWB localization in dense cluttered environments," *IEEE Transactions on Aerospace and Electronic Systems*, 2008, doi: 10.1109/TAES.2008.4560210.

[27] S. Hinteregger, J. Kulmer, M. Goller, F. Galler, H. Arthaber, and K. Witrisal, "UHF-RFID backscatter channel analysis for accurate wideband ranging," in *2017 IEEE International Conference on RFID (RFID)*, May 2017, doi: 10.1109/RFID.2017.7945596.

[28] S. Grebien, F. Galler, D. Neunteufel, U. Mühlmann, S. J. Maier, H. Arthaber, and K. Witrisal, "Experimental Evaluation of a UHF-MIMO RFID System for Positioning in Multipath Channels," in *2019 IEEE International Conference on RFID Technology and Applications (RFID-TA)*, Sep. 2019, doi: 10.1109/RFID-TA.2019.8892179.

[29] F. Lampel, "RSS-Based Localization of Smart Labels," Master's thesis, Graz University of Technology, Austria, 2018.

[30] S. R. Jondhale, V. Mohan, B. B. Sharma, J. Lloret, and S. V. Athawale, "Support Vector Regression for Mobile Target Localization in Indoor Environments," *Sensors*, 2022, doi: 10.3390/s22010358.

[31] P. V. Nikitin, R. Martinez, S. Ramamurthy, H. Leland, G. Spiess, and K. V. S. Rao, "Phase based spatial identification of UHF RFID tags," in *2010 IEEE International Conference on RFID (IEEE RFID 2010)*, April 2010, doi: 10.1109/RFID.2010.5467253.

[32] S. Tomic, M. Beko, R. Dinis, and L. Bernardo, "On Target Localization Using Combined RSS and AoA Measurements," *Sensors*, 2018, doi: 10.3390/s18041266.

[33] T. Wilding, S. Grebien, U. Miihlmann, and K. Witrisal, "AoA and ToA Accuracy for Antenna Arrays in Dense Multipath Channels," in *2018 8th International Conference on Localization and GNSS (ICL-GNSS)*, June 2018, doi: 10.1109/ICL-GNSS.2018.8440909.

[34] T. Wilding, S. Grebien, U. Mühlmann, and K. Witrisal, "Accuracy Bounds for Array-Based Positioning in Dense Multipath Channels," *Sensors*, 2018, doi: 10.3390/s18124249.

[35] M. A. Landolsi and R. Shubair, "TOAI/AOA/RSS Maximum Likelihood Data Fusion for Efficient Localization in Wireless Networks," in *2018 15th International Multi-Conference on Systems, Signals and Devices (SSD)*, 2018, doi: 10.1109/SSD.2018.8570432.

[36] L. Wielandner, E. Leitinger, and K. Witrisal, "RSS-Based Cooperative Localization and Orientation Estimation Exploiting Antenna Directivity," *IEEE Access*, 2021, doi: 10.1109/ACCESS.2021.3070441.

[37] N. Patwari, J. Ash, S. Kyperountas, A. Hero, R. Moses, and N. Correal, "Locating the nodes: cooperative localization in wireless sensor networks," *IEEE Signal Processing Magazine*, 2005, doi: 10.1109/MSP.2005.1458287.

[38] B. Cakmak, D. Urup, F. Meyer, T. Pedersen, B. Fleury, and F. Hlawatsch, "Cooperative Localization for Mobile Networks: A Distributed Belief Propagation - Mean Field Message Passing Algorithm," *IEEE Signal Processing Letters*, 12 2015, doi: 10.1109/LSP.2016.2550534.

[39] P. Corke, T. Wark, R. Jurdak, W. Hu, P. Valencia, and D. Moore, "Environmental Wireless Sensor Networks," *Proceedings of the IEEE*, 12 2010, doi: 10.1109/JPROC.2010.2068530.

[40] H. Wymeersch, J. Lien, and M. Win, "Cooperative Localization in Wireless Networks," *Proceedings of the IEEE*, 03 2009, doi: 10.1109/JPROC.2008.2008853.

[41] M. Win, F. Meyer, Z. Liu, W. Dai, S. Bartoletti, and A. Conti, "Efficient Multisensor Localization for the Internet of Things: Exploring a New Class of Scalable Localization Algorithms," *IEEE Signal Processing Magazine*, 09 2018, doi: 10.1109/MSP.2018.2845907.

[42] L. Wielandner, E. Leitinger, F. Meyer, and K. Witrisal, "Message Passing-Based 9-D Cooperative Localization and Navigation With Embedded Particle Flow," *IEEE Transactions on Signal and Information Processing over Networks*, 2023, doi: 10.1109/TSIPN.2023.3239697.

[43] L. Wielandner, E. Leitinger, F. Meyer, B. Teague, and K. Witrisal, "Message Passing-Based Cooperative Localization with Embedded Particle Flow," in *ICASSP 2022 - 2022 IEEE International Conference on Acoustics, Speech and Signal Processing (ICASSP)*, 2022, doi: 10.1109/ICASSP43922.2022.9747585.

[44] L. Wielandner, "Bayesian methods for cooperative localization and navigation," dissertation, Graz University of Technology, Austria, 2022.

[45] E. D. Nerurkar, S. I. Roumeliotis, and A. Martinelli, "Distributed maximum a posteriori estimation for multi-robot cooperative localization," in *2009 IEEE International Conference on Robotics and Automation*, 2009, doi: 10.1109/ROBOT.2009.5152398.

[46] H. T. Gidey, X. Guo, K. Zhong, L. Li, and Y. Zhang, "Data Fusion Methods for Indoor Positioning Systems Based on Channel State Information Fingerprinting," *Sensors*, 2022, doi: 10.3390/s22228720.

[47] A. S. Yaro, F. Maly, and P. Prazak, "A Survey of the Performance-Limiting Factors of a 2-Dimensional RSS Fingerprinting-Based Indoor Wireless Localization System," *Sensors*, 2023, doi: 10.3390/s23052545.

[48] J. Bi, M. Zhao, G. Yao, H. Cao, Y. Feng, H. Jiang, and D. Chai, "PSOSVRPos: WiFi indoor positioning using SVR optimized by PSO," *Expert Systems with Applications*, 2023, doi: https://doi.org/10.1016/j.eswa.2023.119778.

[49] D. Neunteufel, S. Grebien, S. Hechenberger, K. Witrisal, and H. Arthaber, "Coherent Chirp Generation by Narrowband Transceiver Chips for ToF Indoor Localization," in *GLOBECOM 2020 - 2020 IEEE Global Communications Conference*, 2020, doi: 10.1109/GLOBECOM42002.2020.9348025.

[50] D. Neunteufel, S. Grebien, and H. Arthaber, "Bayesian CRLB for Blind Indoor Localization with Imperfect Receiver Synchronization," in *2021 55th Asilomar Conference on Signals, Systems, and Computers*, Oct 2021, doi: 10.1109/IEEECONF53345.2021.9723254.

[51] S. Mazuelas, Y. Shen, and M. Z. Win, "Information Coupling in Cooperative Localization," *IEEE Communications Letters*, 2011, doi: 10.1109/LCOMM.2011.060111.110402.

[52] X. Shen, Y. Liu, and Y. Shen, "On the Spatial Information Coupling in Relative Localization Networks," in *ICC 2021 - IEEE International Conference on Communications*, 2021, doi: 10.1109/ICC42927.2021.9500501.

[53] Y. Li, W. Yu, and X. Guan, "Hybrid TOA-AOA Cooperative Localization for Multiple AUVs in the Absence of Anchors," *IEEE Transactions on Industrial Informatics*, 2024, doi: 10.1109/TII.2023.3266362.

[54] S. Mazuelas, Y. Shen, and M. Z. Win, "Spatiotemporal Information Coupling in Network Navigation," *IEEE Transactions on Information Theory*, 2018, doi: 10.1109/TIT.2018.2859330.

[55] A. Venus, E. Leitinger, S. Tertinek, and K. Witrisal, "A Graph-Based Algorithm for Robust Sequential Localization Exploiting Multipath for Obstructed-LOS-Bias Mitigation," *IEEE Transactions on Wireless Communications*, 2024, doi: 10.1109/TWC.2023.3285530.

[56] A. Fuchs, L. Wielandner, D. Neunteufel, H. Arthaber, and K. Witrisal, "Wideband TDoA Positioning Exploiting RSS-Based Clustering," *Sensors*, 2023, doi: 10.3390/s23125772.

[57] T. Rappaport, *Wireless communications: Principles and practice.* Prentice Hall, 1996.

[58] S. M. Kay, *Fundamentals of Statistical Signal Processing: Estimation Theory.* USA: Prentice-Hall, Inc., 1993.

[59] D. Cousineau and S. Helie, "Improving maximum likelihood estimation using prior probabilities: A tutorial on maximum a posteriori estimation and an examination of the weibull distribution," *Tutorials in Quantitative Methods for Psychology*, vol. 9, no. 2, pp. 61–71, 2013.

[60] M. Osman, A. Hussein, and A. Al-Kaff, "Intelligent Vehicles Localization Approaches between Estimation and Information: A Review," in *2019 IEEE International Conference on Vehicular Electronics and Safety (ICVES)*, 2019, doi: 10.1109/ICVES.2019.8906426.

[61] C. Knapp and G. Carter, "The generalized correlation method for estimation of time delay," *IEEE Transactions on Acoustics, Speech, and Signal Processing*, 1976, doi: 10.1109/TASSP.1976.1162830.

[62] V. H. MacDonald and P. M. Schultheiss, "Optimum Passive Bearing Estimation in a Spatially Incoherent Noise Environment," *The Journal of the Acoustical Society of America*, 07 1969, doi: 10.1121/1.1911659.

[63] R. Bassett and J. Deride, "Maximum a posteriori estimators as a limit of Bayes estimators," *Mathematical Programming*, Mar 2019, doi: 10.1007/s10107-018-1241-0.

[64] B. Lee, A. Said, T. Kalker, and R. W. Schafer, "Maximum Likelihood Time Delay Estimation with Phase Domain Analysis in the Generalized Cross Correlation Framework," in *2008 Hands-Free Speech Communication and Microphone Arrays*, 2008, doi: 10.1109/HSCMA.2008.4538695.

[65] C. Zhang, Z. Zhang, and D. Florencio, "Maximum Likelihood Sound Source Localization for Multiple Directional Microphones," in *2007 IEEE International Conference on Acoustics, Speech and Signal Processing - ICASSP '07*, 2007, doi: 10.1109/ICASSP.2007.366632.

[66] R. A. Scholtz, "How do you define Bandwidth?" *International Telemetering Conference Proceedings*, 1972. [Online]. Available: http://hdl.handle.net/10150/605545

[67] A. A. Neath and J. E. Cavanaugh, "The Bayesian information criterion: background, derivation, and applications," *WIREs Computational Statistics*, 2012, doi: https://doi.org/10.1002/wics.199.

[68] Y. Shen and M. Z. Win, "Fundamental Limits of Wideband Localization—Part I: A General Framework," *IEEE Transactions on Information Theory*, 2010, doi: 10.1109/TIT.2010.2060110.

[69] H. Wymeersch, A. Pärssinen, T. E. Abrudan, A. Wolfgang, K. Haneda, M. Sarajlic, M. E. Leinonen, M. F. Keskin, H. Chen, S. Lindberg, P. Kyösti, T. Svensson, and X. Yang, "6G Radio Requirements to Support Integrated Communication, Localization, and Sensing," in *2022 Joint European Conference on Networks and Communications & 6G Summit (EuCNC/6G Summit)*, 2022, doi: 10.1109/EuCNC/6GSummit54941.2022.9815783.

Part II

Included Papers

A

Time-of-Arrival Estimation for Positioning in Bandwidth-Limited Dense Multipath Channels

Andreas Fuchs and Klaus Witrisal

2022 IEEE 23rd International Workshop on Signal Processing Advances in Wireless Communication (SPAWC), Oulu, Finland, 2022, pp. 1-5

doi: 10.1109/SPAWC51304.2022.9833995

Abstract— For time-of-flight-based wireless positioning systems operating in (dense) multipath propagation channels, the accuracy is severely influenced by the signal bandwidth, because the dense multipath component (DMC) interferes with the desired, information-bearing line-of-sight (LoS) signal. Several such systems make use of bandwidth-limited frequency resources, e.g. the industrial, scientific, and medical (ISM) bands, therefore the achievable position estimation accuracy is limited. In this paper, we propose a model-based delay-estimation method which takes into account a parametric model of the DMC and thus exploits the signal energy carried in the DMC. The resulting algorithm exhibits an enhanced delay estimation accuracy and remarkable robustness in non-LoS situations. The algorithm is benchmarked against a maximum likelihood (ML) estimator not incorporating a model for the DMC and against the estimated Cramér-Rao lower bound (CRLB) in presence of DMC. Results show a significant performance gain for scenarios where the conventional ML estimator performs poorly. An evaluation of measurement data validates the simulation, showing a root-mean-square error (RMSE) of 33.4 cm compared to 1.89 m for the conventional ML estimator, at a signal bandwidth of 80 MHz.

The financial support by the Christian Doppler Research Association and the Austrian Federal Ministry for Digital and Economic Affairs is gratefully acknowledged.

A.1 Introduction

Reliable and accurate indoor positioning is hindered by multipath propagation and other environmental influences [1]. Existing mitigation methods use machine learning for bias-removal in non-line-of-sight (LoS) measurements [2] or exploit a known room geometry [3]. Both methods exploit ultra-wideband (UWB) measurement signals. The latter involve modeling of specular components, which assumes that the components are separable in the time-domain and therefore a geometric environment model can be used. As existing consumer hardware is often not capable of operating with the needed bandwidth, some reduction of accuracy [4] and measurement bias is often unavoidable. This problem holds for many low-power internet of things (IoT) nodes [5,6], for 5G radios using the sub-6 GHz frequency band [7], and for Bluetooth [8,9] or WiFi devices [10].

The most useful measurement parameter for robust positioning is the time-of-flight (ToF) of the LoS signal component. However, in environments with strong dense multipath (DM) and limited bandwidth, separation of multipath components is not viable, as there is significant overlap in time, c.f. Fig. A.1. In [4, 11], a statistical model of the dense multipath component (DMC) has been used to quantify the performance of time-of-arrival (ToA) estimators in DMC. As expected, the performance deteriorates severely at small bandwidth, but, interestingly, a simple matched-filter estimator outperforms in such situations the more advanced maximum likelihood (ML) estimator which makes use of model knowledge.

To address this observation, we re-visit the problem of estimating the ToF in dense multipath channels. In contrast to [4,11], we also estimate parameters of the DMC model, in particular its ToA, and thereby we exploit the signal energy in this component. We also introduce an efficient implementation of the ML estimator and we analyze the ranging error bound (REB) for this model. An evaluation is done with a simulation model, to verify the performance of the algorithm under ideal conditions, and with indoor measurement data, to validate if this algorithm can be applied to real-world situations.

The paper is organized as follows. A.2 focuses on the derivation of the signal model and likelihood, and further shows an analytical solution for the covariance-matrix describing the DMC. A.3 derives the REB for our signal model. In A.4, an evaluation of the REB (A.4.1), simulation results (A.4.2) and an experimental validation using measurement data (A.4.3) are shown.

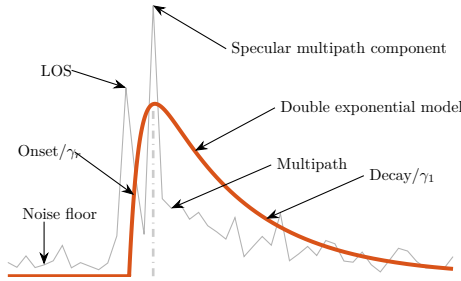

Figure A.1: Illustration of signal model and parameters

A.2 Signal Model

We define a channel model for an LoS component and a DMC

$$h(t) = \alpha\delta\left(t-\tau\right) + \nu(t) \tag{A.1}$$

with complex amplitude $\alpha \in \mathbb{C}$ and relative delay $\tau \in \mathbb{R}$. The DMC is modeled as a zero-mean complex Gaussian random process. With the assumption of uncorrelated scattering, the autocorrelation is defined as

$$\mathbb{E}\left[\nu\left(t'\right)\nu^*(t)\right] = S_\nu(t-\tau;\boldsymbol{\theta})\delta\left(t'-t\right), \tag{A.2}$$

with the power delay spectrum $S_\nu(t;\boldsymbol{\theta})$, defined by a parameter vector $\boldsymbol{\theta}$. For our purposes, we have to assume that neither τ, nor the parameters $\boldsymbol{\theta}$ of the DMC are known. The sampled received signal vector $\boldsymbol{r}$ with length N is described as

$$\boldsymbol{r} = \alpha\boldsymbol{s}\left(\tau\right) + \boldsymbol{n}, \tag{A.3}$$

where $\boldsymbol{s}\left(\tau\right)$ is the sampled transmitted signal $s(t-\tau)$ with delay τ, i.e. $\left[\boldsymbol{s}\left(\tau\right)\right]_i = s(iT_s-\tau)$, $i = 0, 1, \ldots, N-1$, and sampling period T_s. The noise vector $\boldsymbol{n}$ is defined by covariance matrix $\boldsymbol{C}(\tau;\boldsymbol{\eta})$ with parameter vector $\boldsymbol{\eta}$. The covariance matrix is further defined as

$$\boldsymbol{C}(\tau;\boldsymbol{\eta}) = \boldsymbol{C}_\nu(\tau;\boldsymbol{\theta}) + \sigma^2\boldsymbol{I}, \tag{A.4}$$

with the covariance of the DMC $\boldsymbol{C}_\nu(\tau;\boldsymbol{\theta})$, the variance σ^2 of an additive white Gaussian noise component and the identity matrix of according size $\boldsymbol{I}$.

From this signal model, the Gaussian likelihood-function can be formulated as

$$f(\boldsymbol{r} \mid \tau, \boldsymbol{\eta}, \alpha) = \frac{\mathrm{e}^{-(\boldsymbol{r}-\boldsymbol{s}(\tau)\alpha)^{\mathrm{H}}\boldsymbol{C}(\tau;\boldsymbol{\eta})^{-1}(\boldsymbol{r}-\boldsymbol{s}(\tau)\alpha)}}{\pi^N \det \boldsymbol{C}(\tau;\boldsymbol{\eta})}, \tag{A.5}$$

which will be the basis for evaluating the Cramér-Rao lower bound (CRLB) and parameter estimation algorithms, which yield point estimates by implementing the function $\operatorname{argmin}_{\tau,\boldsymbol{\eta},\alpha} f(\boldsymbol{r} \mid \tau, \boldsymbol{\eta}, \alpha)$. Two variants for this were implemented, one for a full estimation of the covariance matrix and one for a additive white Gaussian noise (AWGN)-only estimation neglecting DMC.

To achieve an efficient implementation of such algorithms, we will make use of a time-shifting operator that is defined in frequency domain as $\boldsymbol{\Phi}(\tau) = \mathrm{diag}(\boldsymbol{w}(\tau))$, where element i of vector $\boldsymbol{w}(\tau)$ is $[\boldsymbol{w}(\tau)]_i = \mathrm{e}^{j\pi\tau f_i}$, corresponding to frequency sample f_i. A time-domain shift operator is then written as a convolution matrix $\boldsymbol{\Delta}(\tau) = \mathbf{F}^{-1}\boldsymbol{\Phi}(\tau)\mathbf{F}$ using the DFT matrix $\boldsymbol{F}$. With this, the received signal can be re-written as

$$\boldsymbol{r} = \boldsymbol{\Delta}(\tau)\boldsymbol{s}\,(0) + \boldsymbol{n} \tag{A.6}$$

and

$$\begin{aligned}\boldsymbol{C}_\nu(\tau;\boldsymbol{\theta}) &= \int S_\nu(\lambda-\tau;\boldsymbol{\theta})\boldsymbol{s}(\lambda)\boldsymbol{s}^{\mathsf{H}}(\lambda)\;d\lambda \\ &= \int S_\nu(\lambda;\boldsymbol{\theta})\boldsymbol{s}(\lambda+\tau)\boldsymbol{s}^{\mathsf{H}}(\lambda+\tau)\;d\lambda \\ &= \boldsymbol{\Delta}(\tau)\int S_\nu(\lambda;\boldsymbol{\theta})\boldsymbol{s}(\lambda)\boldsymbol{s}^{\mathsf{H}}(\lambda)\;d\lambda\;\boldsymbol{\Delta}^{\mathsf{H}}(\tau) \\ &= \boldsymbol{\Delta}(\tau)\boldsymbol{C}_\nu(\boldsymbol{\theta})\boldsymbol{\Delta}^{\mathsf{H}}(\tau)\end{aligned}, \tag{A.7}$$

where $^{\mathsf{H}}$ denotes the Hermitian transpose. The latter has the advantage that the delay parameter has been separated from the covariance matrix. For the computation of the inverse and determinant of $\boldsymbol{C}_\nu(\boldsymbol{\theta})$, we introduce a frequency-domain representation of the covariance matrix $\boldsymbol{C}_\nu(\boldsymbol{\theta}) = \mathbf{F}^{\mathsf{H}}\tilde{\boldsymbol{C}}_\nu(\boldsymbol{\theta})\mathbf{F}$ and the singular value decomposition (SVD) of this matrix $\tilde{\boldsymbol{C}}_\nu(\boldsymbol{\theta}) = A\boldsymbol{U}\boldsymbol{\Lambda}\boldsymbol{U}^{\mathsf{H}}$, where A represents the power of the DMC. This yields the noise covariance matrix

$$\begin{aligned}\boldsymbol{C}(\boldsymbol{\eta}) &= \mathbf{F}^{\mathsf{H}}(\tilde{\boldsymbol{C}}_\nu(\boldsymbol{\theta}) + \sigma^2\boldsymbol{I})\mathbf{F} \\ &= \mathbf{F}^{\mathsf{H}}\boldsymbol{U}(A\boldsymbol{\Lambda} + \sigma^2\boldsymbol{I})\boldsymbol{U}^{\mathsf{H}}\mathbf{F},\end{aligned} \tag{A.8}$$

with inverse

$$\boldsymbol{C}(\boldsymbol{\eta})^{-1} = \mathbf{F}^{\mathsf{H}}\boldsymbol{U}(A\boldsymbol{\Lambda} + \sigma^2\boldsymbol{I})^{-1}\boldsymbol{U}^{\mathsf{H}}\mathbf{F} \tag{A.9}$$

and determinant

$$\det(\boldsymbol{C}(\boldsymbol{\eta})) = \prod_i (A\lambda_i + \sigma^2), \tag{A.10}$$

where λ_i is the i-th diagonal element of $\boldsymbol{\Lambda}$.

We can now re-write the likelihood function as

$$\begin{aligned}f(\boldsymbol{r} \mid \tau,\boldsymbol{\eta},\alpha) &= \frac{\mathrm{e}^{-(\boldsymbol{\Delta}(-\tau)\boldsymbol{r}-\boldsymbol{s}(0)\alpha)^{\mathrm{H}}\boldsymbol{C}(\boldsymbol{\eta})^{-1}(\boldsymbol{\Delta}(-\tau)\boldsymbol{r}-\boldsymbol{s}(0)\alpha)}}{\pi^N \det\boldsymbol{C}(\boldsymbol{\eta})} \\ &= \frac{\mathrm{e}^{-(\boldsymbol{\Phi}^{\mathrm{H}}(\tau)\tilde{\boldsymbol{r}}-\tilde{\boldsymbol{s}}(0)\alpha)^{\mathrm{H}}\boldsymbol{U}(A\boldsymbol{\Lambda}+\sigma^2\boldsymbol{I})^{-1}\boldsymbol{U}^{\mathrm{H}}(\boldsymbol{\Phi}^{\mathrm{H}}(\tau)\tilde{\boldsymbol{r}}-\tilde{\boldsymbol{s}}(0)\alpha)}}{\pi^N\prod_i(A\lambda_i+\sigma^2)},\end{aligned} \tag{A.11}$$

with frequency-domain versions $\tilde{\boldsymbol{r}} = \mathbf{F}\boldsymbol{r}$ and $\tilde{\boldsymbol{s}}(0) = \mathbf{F}\boldsymbol{s}(0)$ of received signal and transmitted signal, respectively. This equates to a log-likelihood of

$$\begin{aligned}\ln(f(\boldsymbol{r} \mid \tau,\boldsymbol{\eta},\alpha)) &= -N\ln(\pi) - \sum_i \ln(A\lambda_i+\sigma^2) \\ &- \sum_i (A\lambda_i+\sigma^2)^{-1}\left|\boldsymbol{u}_i\left[\boldsymbol{\Phi}^{\mathrm{H}}(\tau)\tilde{\boldsymbol{r}} - \tilde{\boldsymbol{s}}(0)\alpha\right]\right|^2\end{aligned}. \tag{A.12}$$

This form has the advantage that parameters τ, α, and A are separated and the expensive matrix operations are avoided, reducing computations for an ML-based parameter estimator. The actual shape of the PDP is expressed by the eigenvectors $\boldsymbol{u}_i$ and eigenvalues λ_i of $\tilde{\boldsymbol{C}}_\nu(\boldsymbol{\theta})$, which can be pre-calculated for different parameters $\boldsymbol{\theta}$.

In fact, an analytical solution can be found for $\tilde{\boldsymbol{C}}_\nu(\boldsymbol{\theta})$ for the double-exponential power delay profile (PDP)

$$S_\nu(t;\boldsymbol{\theta}) = A(1-\mathrm{e}^{\frac{-t}{\gamma_r}})\mathrm{e}^{\frac{-t}{\gamma_1}} \tag{A.13}$$

illustrated in A.1 with $\boldsymbol{\theta} = [A, \gamma_1, \gamma_r]$. This model corresponds to a normalized power of the DMC of Ω_1, where $A = \Omega_1(\gamma_1 + \gamma_r)$. Appendix A.6.1 shows the derivation of $\tilde{\boldsymbol{C}}_\nu(\boldsymbol{\theta})$ for this PDP.

A.3 Ranging Error Bound

As the parameters for the Covariance matrix are not known, additional estimation is necessary. From previous work [4, 11, 12] we can see that a derivation of the equivalent Fisher information (EFI) is necessary. A generalized form of the Fisher information (FI) matrix for a complex Gaussian data model is shown as [13, Sec. 15.7]

$$\begin{aligned}[\boldsymbol{\mathcal{I}}(\boldsymbol{\eta})]_{ij} =& 2\mathrm{Re}\left\{\left(\frac{\partial \mathbf{r}}{\partial \boldsymbol{\eta}_i}\right)^{\mathrm{H}} \mathbf{C}(\boldsymbol{\eta})^{-1}\left(\frac{\partial \mathbf{r}}{\partial \boldsymbol{\eta}_j}\right)\right\} \\ &+ \mathrm{tr}\left[\mathbf{C}(\boldsymbol{\eta})^{-1}\frac{\partial \mathbf{C}(\boldsymbol{\eta})}{\partial \boldsymbol{\eta}_i}\mathbf{C}(\boldsymbol{\eta})^{-1}\frac{\partial \mathbf{C}(\boldsymbol{\eta})}{\partial \boldsymbol{\eta}_j}\right]\end{aligned}, \tag{A.14}$$

where i and j are the i-th and j-th corresponding element of $\boldsymbol{\eta}$. The first term of this equation has already been derived [11] and described in detail. The second term of the equation describes the information gain from estimating the parameters of the covariance matrix and thus the gain introduced by the PDP model. The EFI for the parameter τ can be approximated as

$$\mathcal{I}_\tau \approx 8\pi^2\beta^2\gamma_\tau \mathrm{SINR}\sin^2(\xi) + \mathcal{I}_\tau^{\mathrm{DMC}} \tag{A.15}$$

where $\beta^2 = \|\dot{\mathbf{s}}\|^2 / \left(4\pi^2 \|\mathbf{s}\|^2\right)$ is the mean-squared bandwidth [14] of the transmitted signal, defined with a normalized pulse $\|\mathbf{s}\|^2 T_s = 1$, and $\dot{\mathbf{s}}$ is the sampled derivative of $\mathbf{s}$ w.r.t τ. The whitening gain $\gamma_\tau = \frac{\beta_w^2}{\beta}$ is described in literature [11] as the increased ranging information due to the equalization of the DMC by means of the inverse covariance matrix, c.f. (A.11). The extended bandwidth after whitening $\beta_w^2 = \|\dot{\mathbf{s}}\|_{\mathcal{H}}^2 / \left(4\pi^2 \|\mathbf{s}\|_{\mathcal{H}}^2\right)$ is a corresponding bandwidth after the equalization, where $\|\mathbf{s}\|_{\mathcal{H}}^2$ is the weighted norm of $\mathbf{s}$ in a corresponding Hilbert space $\mathcal{H}$, see Appendix A.6.2. Furthermore, $\sin^2(\xi)$ is a factor stemming from the loss from estimation of the parameter α, which is also further described in Appendix A.6.2. The signal-to-interference-plus-noise-ratio (SINR) is a factor describing the influence of the DMC on the estimation of the LoS signal, it is calculated as $\mathrm{SINR} = |\alpha|^2\|\boldsymbol{s}\|_{\mathcal{H}}^2 T_s/N_0$. The term $\mathcal{I}_\tau^{\mathrm{DMC}}$ can be evaluated numerically

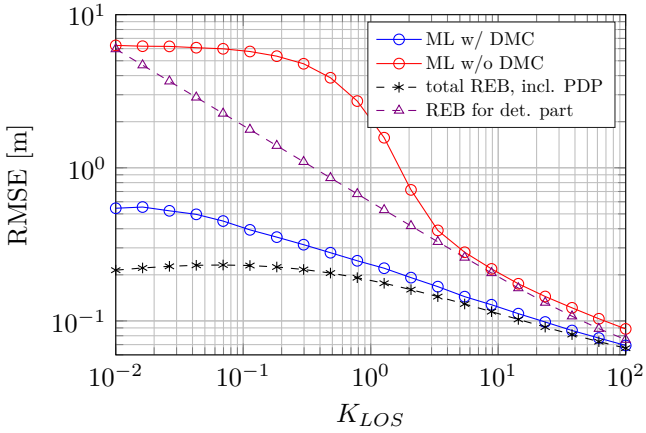

Figure A.2: Comparison of REB with ML with and without model for DMC, with $\gamma_1 = 20\,\text{ns}, \gamma_r = 5\,\text{ns}, \frac{E_{LOS}}{N_0} = 30\,\text{dB}, T_p = 12.5\,\text{ns}$

by computing the partial derivatives $\dot{\mathbf{C}}(\boldsymbol{\eta})$ of $\mathbf{C}(\boldsymbol{\eta})$ and evaluating the trace. With the EFI $\mathcal{I}_\tau$ the REB can be written as $\mathcal{R}(\tau) = \sqrt{\mathcal{I}_\tau^{-1}}$.

A.4 Numeric evaluation

A.4.1 Ranging Error Bound

In order to verify the potential performance gain from exploiting the DMC, we evaluated the REB as a function of the energy ratio $K_{\text{LOS}} = \frac{E_{LOS}}{E_{DMC}}$ between the LoS-component and the DMC. The bandwidth was set to 80 MHz, represented by the pulse duration $T_p = 12.5\,\text{ns}$, which corresponds to a typical bandwidth of a non-UWB radiopositioning system. The channel parameters γ_1, γ_r and the signal-to-noise ratio (SNR) $\frac{E_{LOS}}{N_0}$ were chosen to represent a typical indoor measurement scenario. The energy ratio K_{LOS} was varied, as this parameter expresses how well the information-bearing LoS is visible at some position and geometry within a room. High values for K_{LOS} represent a scenario where the LoS dominates over the DM, meaning an undisturbed path in a large room without reflections. Low values represent the opposite case, where the DM dominates over the LoS. Note that a fixed SNR is defined for the E_{LOS}, which implies that E_{DMC} increases for decreasing K_{LOS}.

In A.2 we evaluate the REB for the LoS component only (- ▵ -, first term of (A.14) only), where the DMC represents limiting interference, and for the total REB, which also accounts for delay information contained in the DMC (- ∗ -, both terms of (A.14)). The REBs diverge significantly for small K_{LOS}, meaning that, in a case where there is a significant amount of energy in the DMC, a much better estimation performance can be achieved. This can be attributed to the additional information expressed by the second term in (A.14). The conventional estimator exploits only the energy in the LoS, and thus the additional information in the multipath is lost. For large K_{LOS}, the estimation accuracy gain of the model with

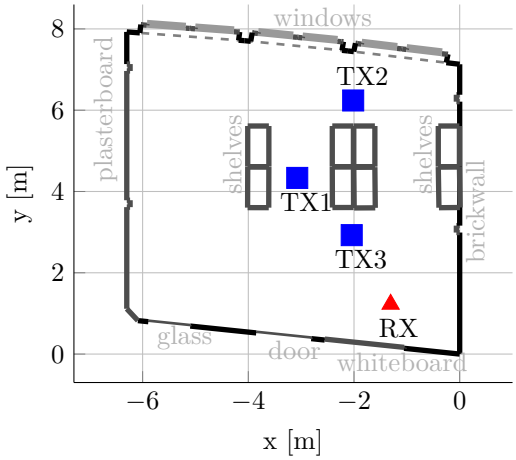

Figure A.3: Floorplan of the measurement scenario

DMC is negligible over the model without DMC, which can be simply attributed to the fact that E_{DMC} for this region is very small. This means that the information gain from the DMC in this region is also negligible.

A.4.2 Simulation Results

A Monte-Carlo simulation (MCS) with independent realisations of the DMC was done in order to compare the ML estimator using the DMC model to one that assumes an LoS in AWGN only. We chose to draw 10000 samples per evaluation point using the same PDP model as for the estimator. Estimation of the parameters was done via Nelder-Mead method with random starting points in the vicinity of the real values. As can be seen in A.2, the ML estimator without incorporating a model for the DMC performs near the REB neglecting the DMC for high K_{LOS}, but for low values the estimator diverges. This can be attributed to the strong DMC causing estimation outliers, i.e. finding a random peak of the DMC. The estimator incorporating the model for the DMC shows a significant performance gain, especially for low values of K_{LOS}. Still, an offset between the total REB and the ML with DMC can be seen. This can be attributed to the estimation of nuisance parameters [15].

A.4.3 Experimental validation

For the validation of the algorithms, UWB-measurement data, acquired at a bandwidth of 1 GHz in a small lab room at our institute, was downsampled to 80 MHz, corresponding to the simulated data. The data set consists of 3654 measured channel impulse responses (CIRs), of which 2310 were in LoS and 1254 were measured under non-LoS conditions. The data sets were acquired by measuring multiple positions on a 2 cm grid of 64 cm by 70 cm placed at positions TX1 to TX3; the RX antenna was kept at a fixed position, as illustrated in A.3. The parameter $\hat{K}_{\mathrm{LOS}}$ was computed from the high-resolution data at 1 GHz, estimating amplitude and delay of the LoS component $\hat{\tau}$ with an ML estimator (without modeling for DMC)

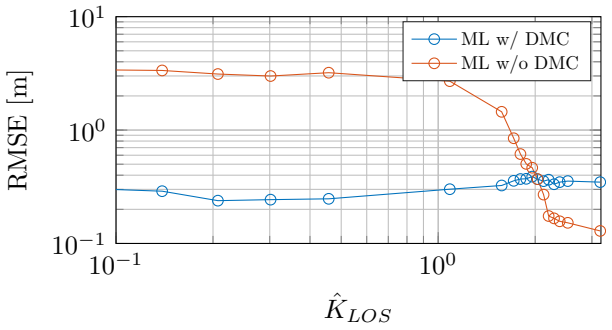

Figure A.4: Comparison of ML with and without model for DMC, with $\gamma_r = 5\,\text{ns}, T_p = 12.5\,\text{ns}$

in the vicinity of the real distance [16]. We get

$$\hat{K}_{\text{LOS}} = \frac{|\langle \mathbf{r}, \mathbf{s}(\hat{\tau})\rangle|^2}{\|\mathbf{r} - \langle \mathbf{r}, \mathbf{s}(\hat{\tau})\rangle \mathbf{s}(\hat{\tau})\|^2 - N\hat{\sigma}^2}, \tag{A.16}$$

where $\hat{\sigma}^2$ was estimated by using samples where the DM is assumed to be well-attenuated, i.e. at very late delays [17].

These datasets were evaluated via grid search for the ML without DMC modeling and respectively with an interior-point algorithm with DMC modeling. Parameter γ_r was assumed to be known and fixed at 5 ns, as joint estimation of γ_r and $\hat{\tau}$ proved difficult and the rise time can be assumed to be constant. This can be attributed to the rise time being mostly dependent on overall room geometry [18]. Other parameters were initialized as $\left[\tau = 0, A = 10^{7.7}, \sigma^2 = 0.1, \gamma_1 = 20\,\text{ns}\right]$. These values correspond to $K_{\text{LOS}} = 1$. In A.4, evaluated data was grouped by $\hat{K}_{\text{LOS}}$, each point representing an equally sized subset of measurements. At low values of $\hat{K}_{\text{LOS}}$, our algorithm outperforms the ML without DMC by a significant margin, corresponding to the performance for simulated data. For high $\hat{K}_{\text{LOS}}$ the performance of the conventional algorithm seems to be better than the performance of our algorithm. This can be attributed to the nuisance parameters γ_1, and A, which have to be estimated, lowering estimation performance for $\hat{\tau}$. Evaluations of our data showed that with our algorithm, there was a bias for the estimation at the highest value of $\hat{K}_{\text{LOS}}$ of 33 cm, or about 1 ns.

The CDF for our algorithm is shown in A.5 and compared to the conventional algorithm. It illustrates this bias towards earlier delays, which could mean that our assumed γ_r was chosen slightly too large, thus limiting the performance. Evaluation with the conventional ML was unbiased, but as expected, for data sets with non-line-of-sight (NLOS) data, it shows many outliers with late delays. Overall, for the whole data set, the AWGN-based ML achieves an root-mean-square error (RMSE) of 1.89 m, compared to 33.4 cm achieved by our algorithm incorporating the model for the DMC.

Note that the estimate $\hat{K}_{\text{LOS}}^{\text{DMC}}$ from the UWB data differs from K_{LOS} estimated from the interior point algorithm. A.6 illustrates the ratio between $\hat{K}_{\text{LOS}}^{\text{DMC}} = |\alpha|^2/\Omega_1$ computed from the nuisance parameters estimated within our DMC-based algorithm and $\hat{K}_{\text{LOS}}$ as described by A.16. The graph shows that the parameter

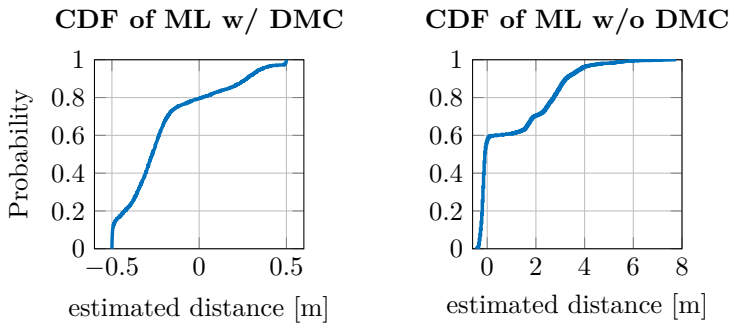

Figure A.5: cumulative distribution functions (CDFs) for whole dataset of ML with DMC model (left) and without (right)

estimation performs relatively accurate for high $\hat{K}_{\mathrm{LOS}}$, but for small values of $\hat{K}_{\mathrm{LOS}}$ the estimation becomes unreliable. This behaviour is expected, as with a smaller bandwidth there is increasingly more energy from the DMC being attributed to the LoS component.

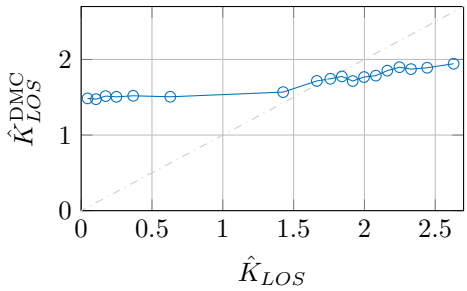

Figure A.6: Median ratio between estimated $\hat{K}_{LOS}$

A.5 Conclusion

An ML-based estimator is formulated for the ToA of radio signals in dense multipath channels, which exploits the energy of the dense multipath component rather than mitigating it. The observed performance is significantly improved over a conventional ML estimator in particular in situation with an obstructed-LoS. Our algorithm showed an RMSE of 33.4 cm compared to 1.89 m for the conventional ML estimator for the evaluated bandwidth. The performance is not significantly inhibited by estimation of additional nuisance parameters, as illustrated by analysis of the CRLB for this case. Computationally one estimation step of the classic ML algorithm can be computed in $\mathcal{O}(n^3)$, and efficient implementations of the SVD can be also computed in $\mathcal{O}(n^3)$ as the most demanding operation for both is a matrix multiplication and inversion, leading to only a linear increase in computation time.

A.6 Appendix

A.6.1 Covariance Matrix for the Double-Exponential PDP

Expressing the time-shifted signal vectors $\boldsymbol{s}(\lambda)$ in (A.7) by a frequency-domain representation $\tilde{\boldsymbol{s}}(\lambda) = \mathbf{F}\boldsymbol{s}(\lambda)$, we get

$$\begin{aligned}\boldsymbol{C}_\nu(\boldsymbol{\theta}) &= \int S_\nu(\lambda;\boldsymbol{\theta})\boldsymbol{s}(\lambda)\boldsymbol{s}^{\mathsf{H}}(\lambda)\ d\lambda \\ &= \mathbf{F}^{\mathsf{H}} \int S_\nu(\lambda;\boldsymbol{\theta})\tilde{\boldsymbol{s}}(\lambda)\tilde{\boldsymbol{s}}^{\mathsf{H}}(\lambda)\ d\lambda\ \mathbf{F} \\ &= \mathbf{F}^{\mathsf{H}}\tilde{\boldsymbol{C}}_\nu(\boldsymbol{\theta})\mathbf{F}\end{aligned} \tag{A.17}$$

with $\mathbf{F}^{\mathsf{H}} = \mathbf{F}^{-1}$. Next we evoke our time-shift operator to get $\tilde{\boldsymbol{s}}(\lambda) = \boldsymbol{\Phi}(\lambda)\tilde{\boldsymbol{s}}(0)$ and $\tilde{\boldsymbol{s}}(\lambda) = \tilde{\boldsymbol{S}}\boldsymbol{w}(\lambda)$, where $\tilde{\boldsymbol{S}} = \mathrm{diag}(\tilde{\boldsymbol{s}}(0))$ (and, remember, $\boldsymbol{\Phi}(\lambda) = \mathrm{diag}(\tilde{\boldsymbol{w}}(\lambda))$). With this, we can deduct

$$\tilde{\boldsymbol{C}}_\nu(\boldsymbol{\theta}) = \tilde{\boldsymbol{S}} \int S_\nu(\lambda;\boldsymbol{\theta})\boldsymbol{w}(\lambda)\boldsymbol{w}^{\mathsf{H}}(\lambda)\ d\lambda\ \tilde{\boldsymbol{S}}^{\mathsf{H}}, \tag{A.18}$$

which can be solved analytically for the double-exponential PDP in (A.13). We obtain

$$\tilde{\boldsymbol{C}}_\nu(\boldsymbol{\theta}) = A\tilde{\boldsymbol{S}}\boldsymbol{C}_{\mathsf{FD}}(\boldsymbol{\theta})\tilde{\boldsymbol{S}}^{\mathsf{H}}, \tag{A.19}$$

where $\boldsymbol{C}_{\mathsf{FD}}(\boldsymbol{\theta})$ is a symmetric Toeplitz matrix with elements

$$c_i = \frac{1}{1/\gamma_1 - j2\pi\Delta_f i} - \frac{1}{1/\gamma_0 - j2\pi\Delta_f i} \tag{A.20}$$

on the i-th diagonal, $\gamma_0 = \frac{\gamma_1\gamma_r}{\gamma_1+\gamma_r}$, and Δ_f is the frequency spacing between the elements of $\tilde{\boldsymbol{s}}(\lambda)$.

A.6.2 Fourier-Weighted Inner Product

The weighted inner product in the Hilbert Space $\mathcal{H}$ is defined as

$$\begin{aligned}\langle \boldsymbol{x}, \boldsymbol{y}\rangle_{\mathcal{H}} &= \sigma^2 \boldsymbol{y}^{\mathrm{H}}\boldsymbol{C}(\boldsymbol{\eta})^{-1}\boldsymbol{x} \\ &= \sum_{i=1}^{N} \frac{\boldsymbol{y}^{\mathrm{H}}\boldsymbol{u}_i\boldsymbol{u}_i^{\mathrm{H}}\boldsymbol{x}}{\lambda_i/\sigma^2 + 1}\end{aligned} \tag{A.21}$$

where $\boldsymbol{u}_i$ is the i-th eigenvector of $\boldsymbol{U}$. Furthermore, the induced norm in $\mathcal{H}$ is defined as $\|\mathbf{x}\|_{\mathcal{H}}^2 = \langle \boldsymbol{x}, \boldsymbol{x}\rangle_{\mathcal{H}}$ for a covariance matrix $\boldsymbol{C}(\boldsymbol{\eta})$. There is a loss factor associated with estimating α, which equates to [11]

$$\sin^2(\xi) = 1 - \frac{\left|\langle \boldsymbol{s}, \dot{\boldsymbol{s}}\rangle_{\mathcal{H}}\right|^2}{\|\boldsymbol{s}\|_{\mathcal{H}}^2 \|\dot{\boldsymbol{s}}\|_{\mathcal{H}}^2} \tag{A.22}$$

Bibliography

[1] D. Dardari, A. Conti, U. Ferner, A. Giorgetti, and M. Z. Win, "Ranging with ultrawide bandwidth signals in multipath environments," *Proceedings of the IEEE*, Feb 2009, doi: 10.1109/JPROC.2008.2008846.

[2] H. Wymeersch, S. Marano, W. Gifford, and M. Win, "A machine learning approach to ranging error mitigation for uwb localization," *Communications, IEEE Transactions on*, 2012, doi: 10.1109/TCOMM.2012.042712.110035.

[3] J. Kulmer, S. Hinteregger, B. Großwindhager, M. Rath, M. S. Bakr, E. Leitinger, and K. Witrisal, "Using DecaWave UWB transceivers for high-accuracy multipath-assisted indoor positioning," in *2017 IEEE International Conference on Communications Workshops (ICC Workshops)*, May 2017, doi: 10.1109/ICCW.2017.7962828.

[4] K. Witrisal, E. Leitinger, S. Hinteregger, and P. Meissner, "Bandwidth scaling and diversity gain for ranging and positioning in dense multipath channels," *IEEE Wireless Communications Letters*, vol. 5, no. 4, pp. 396–399, 2016.

[5] D. Neunteufel, A. Fuchs, and H. Arthaber, "ToF-based indoor positioning for low-power IoT nodes," in *2020 54th Asilomar Conference on Signals, Systems, and Computers*, Nov 2020, doi: 10.1109/IEEECONF51394.2020.9443431.

[6] D. Neunteufel, S. Grebien, and H. Arthaber, "Indoor positioning of low-cost narrowband IoT nodes: Evaluation of a TDoA approach in a retail environment," submitted to MDPI Sensors.

[7] J. A. del Peral-Rosado, R. Raulefs, J. A. López-Salcedo, and G. Seco-Granados, "Survey of cellular mobile radio localization methods: From 1G to 5G," *IEEE Communications Surveys Tutorials*, Secondquarter 2018, doi: 10.1109/COMST.2017.2785181.

[8] P. Zand, J. Romme, J. Govers, F. Pasveer, and G. Dolmans, "A high-accuracy phase-based ranging solution with bluetooth low energy (ble)," in *2019 IEEE Wireless Communications and Networking Conference (WCNC)*, 2019, doi: 10.1109/WCNC.2019.8885791.

[9] A. Comuniello, A. Angelis, A. Moschitta, and P. Carbone, "Using bluetooth low energy technology to perform ToF-based positioning," *Electronics*, 12 2021, doi: 10.3390/electronics11010111.

[10] M. Kotaru, K. Joshi, D. Bharadia, and S. Katti, "Spotfi: Decimeter level localization using wifi," *SIGCOMM Comput. Commun. Rev.*, aug 2015, doi: 10.1145/2829988.2787487.

[11] T. Wilding, S. Grebien, U. Mühlmann, and K. Witrisal, "Accuracy bounds for array-based positioning in dense multipath channels," *Sensors*, 2018, doi: 10.3390/s18124249.

[12] E. Leitinger, P. Meissner, C. Rüdisser, G. Dumphart, and K. Witrisal, "Evaluation of position-related information in multipath components for indoor

positioning," *IEEE Journal on Selected Areas in Communications*, Nov 2015, doi: 10.1109/JSAC.2015.2430520.

[13] S. M. Kay, *Fundamentals of Statistical Signal Processing: Estimation Theory*. USA: Prentice-Hall, Inc., 1993.

[14] R. A. Scholtz, "How do you define bandwidth?" 1972. [Online]. Available: http://hdl.handle.net/10150/605545

[15] A. Abdi, C. Tepedelenlioglu, M. Kaveh, and G. Giannakis, "On the estimation of the K parameter for the Rice fading distribution," *IEEE Communications Letters*, March 2001, doi: 10.1109/4234.913150.

[16] S. Hinteregger, J. Kulmer, M. Goller, F. Galler, H. Arthaber, and K. Witrisal, "UHF-RFID backscatter channel analysis for accurate wideband ranging," in *2017 IEEE International Conference on RFID (RFID)*, May 2017, doi: 10.1109/RFID.2017.7945596.

[17] J. Kulmer, S. Grebien, E. Leitinger, and K. Witrisal, "Delay estimation in presence of dense multipath," *IEEE Wireless Communications Letters*, Oct 2019, doi: 10.1109/LWC.2019.2923409.

[18] J. Karedal, S. Wyne, P. Almers, F. Tufvesson, and A. F. Molisch, "A measurement-based statistical model for industrial ultra-wideband channels," *IEEE Transactions on Wireless Communications*, vol. 6, no. 8, pp. 3028–3037, 2007.

B

Wideband TDoA Positioning Exploiting RSS-Based Clustering

Andreas Fuchs, Lukas Wielandner, Daniel Neunteufel, Holger Arthaber, Klaus Witrisal

Sensors 2023, 23, 5772 doi: 10.3390/s23125772

Abstract—The accuracy of radio-based positioning is heavily influenced by a dense multipath (DM) channel, leading to a poor position accuracy. The DM affects both, time-of-flight (ToF)-measurements extracted from wideband (WB) signals—specifically, if the bandwidth is below 100 MHz—as well as received signal strength (RSS) measurements, due to the interference of multipath signal components onto the information-bearing line-of-sight (LoS) component. This work proposes an approach for combining these two different measurement technologies, leading to a robust position estimation in presence of DM. We assume that a large ensemble of densely-spaced devices is to be positioned. We use RSS measurements to determine "clusters" of devices in the vicinity of each other. Joint processing of the WB-measurements from all devices in a cluster efficiently suppresses the influence of the DM. We formulate an algorithmic approach for the information fusion of those two technologies and derive the corresponding Cramér-Rao lower bound (CRLB) to gain insight in the performance trade-offs at hand. We evaluate our results by simulations and validate the approach with real-world measurement data. The results show that the clustering approach can halve the root-mean-square error (RMSE) from about 2 m to below 1 m, using WB signal transmissions in the 2.4 GHz ISM band at a bandwidth of about 80 MHz.

B.1 Introduction

B.1.1 State of the Art

Radio based indoor localization is an increasingly important research topic, as many modern electronic devices are dependent on robust and accurate position information to provide location-dependent services and applications. Exemplary applications include positioning in retail scenarios guiding costumers to products they are looking for, tracking medical devices in healthcare environments, providing

guests of museums with accurate position dependent interactive tours, tracking articles in warehouses and logistic centers and many more [1–8].

Current state-of-the-art algorithms focus mostly on one measurement method, which can, for example, include received signal strength (RSS) measurements from multiple devices to each other, wideband (WB) measurements to infrastructure like wireless modems and other equipment or measurements with higher bandwidths like ultra-wideband (UWB).

These multiple measurement methods have their own advantages and disadvantages, as the used technology imposes direct limitations. Measurements of RSS values are, for example, relatively easy to acquire, but the information content of a single measurement is low, and thus a single measurement provides only marginal positional information. Therefore, a need arises for a large number of (independent) measurements to increase the positional information to an acceptable level, and additionally a significant number of fixed "anchor nodes" are necessary for reference [9]. Other technologies, for example time-difference-of-arrival (TDoA) based localization utilizing WB measurements in the industrial, scientific, and medical (ISM) bands (i.e. 80 MHz at 2.4 GHz), provide much more information with a single measurement, but additional WB anchor infrastructure is necessary, so called access points (APs), similar to [10, Ch. 6]. In this case, the devices and APs need more complicated radio chips to send and receive higher bandwidth signals. Chips providing even higher bandwidths are increasingly cost-intensive and power-hungry, and thus not economical for many applications.

All of the previously mentioned radio-based localization technologies have in common that multipath-propagation influences the measurements [11], which can affect the results negatively. For bandwidths smaller than 100 MHz, at which in typical indoor scenarios multipath components can not be discerned anymore, the interfering dense multipath component (DMC) leads to diminished performance [12].

Algorithms which were developed in recent years focus on many different approaches, including machine learning [13] or classical signal processing [14, 15], but focus mostly on single measurement methods. For many of these approaches, essential performance bounds like the Cramér-Rao lower bound (CRLB) are also derived [16–20].

Combining multiple measurement methods allows to use complimentary gains from each method, but will increase the complexity of the system architecture and of the algorithms [21], thus this has to be regarded when developing new approaches. Some research was done to fuse multiple localization and measurement methods [1, 22]. These algorithms combine position estimates, but do not fuse measurement data directly. Other existing methods incorporate maximum likelihood estimates for time-of-arrival (ToA), angle of arrival (AoA) and RSS, but those methods rely on fusing multiple measurements from a single node [23, 24], they do not fuse the information of multiple nodes. Also, there is no research yet done which focuses on the derivation of a CRLB for such fused algorithms. Other methods for data fusion of multiple measurements incorporate machine learning, for example methods based on channel state information [25, 26], or support vector regression [27, 28]. Machine learning algorithms need training data to work, which is not necessary for our proposed algorithm.

B.1.2 Concept

This work proposes a method which combines WB time-of-flight (ToF) and AoA measurements of multiple nodes in an indoor scenario. To overcome the limitations of single WB measurements, RSS measurements are collected inbetween the nodes, to determine those which are in the vicinity of each other. By selecting the WB measurements of those nodes, we get access to multiple realisations of the interfering dense multipath component (DMC) and thus an additional information gain for every measurement.

This is achieved by an approach we further call clustering, where RSS-measurements are used to find the nearest nodes, for which WB measurements are then processed jointly. In the following, we will describe likelihoods for node and

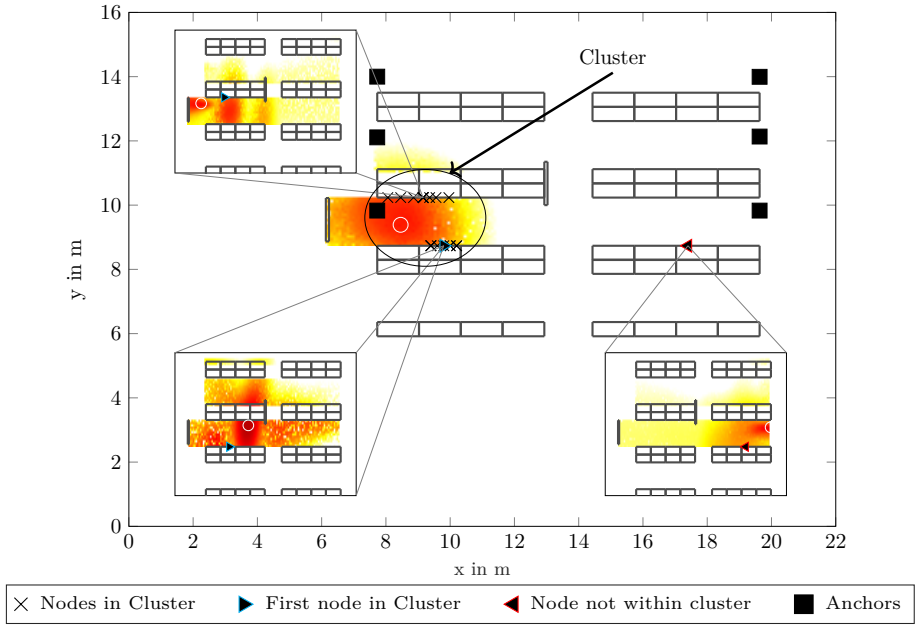

Figure B.1: Visualization of the RSS-based Clustering, excerpts show single likelihoods over a floorplan, overall graphic shows a combined likelihood from a set of 15 nodes

cluster positions, which describe regions with likelihoods of a node being at one position. In Figure B.1, this concept is visualized in a typical warehouse scenario, incorporating multiple shelves defining aisles, nodes placed on these shelves, and multiple anchors over the room.

Here, the likelihood over a room with measurements to six antenna-arrays, each incorporating two antennas, can be seen, where red regions show a large likelihood for a node to be in a position.

The antenna arrays allow for coherent processing, yielding information on the AoA. Different anchor positions allow for a TDoA positioning approach. In the upper-left subplot, a single likelihood for WB measurements is shown. One can see that the resulting likelihood is multi-modal, and the position with the largest likelihood (shown as a white circle) is at one of the false modes. This multi-modality

stems from the estimation of false peaks in the time-domain, which are caused by multipath components dominating over the line-of-sight (LoS). The real position is shown as a blue triangle. The same can be seen in the lower-left subplot, for a node in the vicinity, showing similar effects. In addition, this measurement suffered from a poor signal-to-noise ratio (SNR), which broadens the likelihood in all spatial directions. The lower-right subplot shows a single node far away from the other two examples, for which the estimation is working rather bad. These cases can be mitigated by the clustering approach.

To improve the positioning accuracy and reliability of a single node, multiple nodes can be clustered, and thus a joint likelihood can be computed, which mitigates the uncertainties. But the strategy for clustering is not clear, as there is no previous information from WB measurements alone. Here, RSS measurements can be used, giving us a list of nodes which are likely near a node in a cluster (which is seen as a defining "first" node for the cluster), seen again as a blue triangle. All other nodes within this cluster are shown as black crosses. Now, the joint likelihood seen in Figure B.1 for the whole room is for a combination of all WB measurements within this cluster, applying our proposed algorithm. This shows a single defined mode, where the maximum is the estimated position for the defining node. Note that these nodes can be positioned at different heights, which the algorithm takes into account by a three-dimensional formulation. This approach would also be applicable to multiple measurements of a single node at different positions near each other, but this work focuses on static scenarios.

In order to assess the achievable performance, the CRLB for the cluster center incorporating the DMC was evaluated. The algorithm treats measurements from multiple nodes as different realisations of a single node, thus a correction factor is introduced. This factor regards the information loss from cluster nodes being in different positions. Therefore, we have to introduce a bias term on top of the CRLB since the algorithm leads to the estimation of the cluster center which differs from the true position of the node. This is verified by simulations of increasing complexity and by a real-world measurement campaign.

B.1.3 Contribution

The contributions of this work are the following:

- A concept for the information fusion of WB TDoA and AoA measurements exploiting RSS-based clustering of multiple agent nodes to jointly process their position information.
- A maximum likelihood estimation based algorithm for the mentioned concept.
- An efficient implementation of the proposed algorithm using a particle based estimator.
- A derivation of estimation performance bounds for this concept incorporating:
  - Results for a correction factor describing the loss of information from large clusters.
  - Derivation of the CRLB incorporating this correction factor and information gain from multiple measurements.

  - Introduction of a biased lower bound attributing for performance losses when estimating a single node within a cluster.

- Numeric evaluations of these bounds, showing the influence of parameters like number of nodes in the cluster, size of the cluster, and positions of nodes within a cluster. Specifically, we analyze the performance bounds for:
  - Single node positions, validating the information gain.
  - Increasing node distances for two nodes, validating the biased lower bound.
  - A fully synthetic measurement scenario with nodes over a simulated room with shelves, validating the data fusion concept.
  - The same scenario, incorporating real RSS measurements for clustering of adjacent nodes, but keeping synthetic WB measurements for positioning, validating the impact of realistic clustering with RSS data.
- A verification of the theoretical results with real-world measurement data for both WB and RSS, showing that the algorithm is applicable to real scenarios.

B.1.4 Paper Outline

The paper is structured as follows: Section B.2 defines the overall notation. The signal model for the WB-measurements and the resulting likelihood for single measurements to one agent node are presented in Section B.3. In Section B.4, we describe the clustering approach in detail and the conditions that have to be met to allow this approach. In Section B.5 we derive the CRLB for our system model, additionally focusing on the information loss dependent on the cluster geometry. Section B.6 focuses on evaluations of both synthetic scenarios and real-world measurements, verifying performance. Lastly, a conclusion can be found in Section B.7. Additional insights and detailed derivations are shown in Appendices B.8-B.10.

B.2 Notation

Column vectors are denoted by boldface lower-case letters, and matrices are denoted by boldface upper-case letters. The probability density function (PDF) of a random variable is denoted as $f(\boldsymbol{x})$. For any vector $\boldsymbol{x}$, we denote the transpose as $\boldsymbol{x}^T$, the Hermitian transpose as $\boldsymbol{x}^H$, the Euclidian norm as $\|\boldsymbol{x}\|$, the mean over all elements in the vector as $\overline{\boldsymbol{x}}$, the expectation operator as $\mathbb{E}_i[\boldsymbol{x}]$ in dimension i (where dimension i denotes the dimension along the expectation operator is calculated), and the complex conjugate as $\boldsymbol{x}^*$. The calligraphic notation $\mathcal{L}$ denotes a set, other usages of calligraphic fonts are described at their first occurrence. $\overline{\{\boldsymbol{x}_l\}_{\mathcal{L}}}$ denotes the mean operator over all vectors $\boldsymbol{x}_l$ for l in the set $\mathcal{L}$. Furthermore, we introduce a trace operator as $\mathrm{tr}\{\boldsymbol{X}\}$ for a matrix $\boldsymbol{X}$ and $\det(\boldsymbol{X})$ as it's determinant. Submatrices of a matrix $\boldsymbol{X}$ are written with their corresponding superscripts without parentheses, i.e., $\boldsymbol{X}^{i,i}$. A superscript with brackets $\boldsymbol{X}^{(i)}$ is used to denote a matrix designated by index i (notably used for matrices corresponding to a single anchor m) and $[\boldsymbol{X}]_{3\times3}$ is the upper-left 3×3 sub-block of a matrix. Real and imaginary parts of x are denoted as $\mathcal{R}x$ and $\mathcal{I}x$ respectively.

B.3 Signal Model

The system setup consists of L transmitting nodes that are located at positions $\boldsymbol{p}_l = [x_l, y_l, z_l]^T \in \mathbb{R}^3, \forall l \in \{1, \ldots, L\}$ and receiving antennas at positions $\boldsymbol{p}_{m,k} \in \mathbb{R}^3, \forall m \in \{1, \ldots, M\}, \forall k \in \{1, \ldots, K\}$, where index k describes the antennas within each anchor, and index m describes the anchor. The number of anchors and antennas per anchor are described by M and K respectively. The radio channel from the l-th transmitting node to the k-th receiving antenna of anchor m is given as

$$h_{l,m,k}(\tau; \boldsymbol{p}_l) = \alpha_{l,m}\delta\left(\tau - \tau_{m,k}(\boldsymbol{p}_l)\right) + \nu_{l,m,k}(\tau) \tag{B.1}$$

with propagation delay $\tau_{m,k}(\boldsymbol{p}_l) = \frac{1}{c}\left\|\boldsymbol{p}_l - \boldsymbol{p}_{m,k}\right\|$ and the complex amplitude $\alpha_{l,m}$ of the received LoS signal from node l to anchor m. The DMC is described by a zero-mean complex Gaussian random process. With the assumption of uncorrelated scattering, the auto-correlation of the random process $\nu_{l,m,k}(\tau)$ is defined as

$$\begin{aligned}&\mathbb{E}\left[\nu_{l,m,k}(\tau)\nu^*_{l',m',k'}\left(\tau'\right)\right] = \\ &\quad S_\nu\left(\tau - \tau_m(\boldsymbol{p}_l), \tilde{\nu}_{l,m}\right)\delta\left(\tau - \tau'\right)\delta\left[l - l'\right]\delta\left[m - m'\right]\delta\left[k - k'\right],\end{aligned} \tag{B.2}$$

where $\tau_m(\boldsymbol{p}_l) = \frac{1}{c}\left(\left\|\boldsymbol{p}_l - \boldsymbol{p}_m\right\|\right)$ is a mean delay per array m, with $\boldsymbol{p}_m = \overline{\{\boldsymbol{p}_{m,1}, \ldots, \boldsymbol{p}_{m,K}\}}$ being the mean antenna position. The delay power spectrum (DPS) $S_\nu\left(\tau - \tau_m(\boldsymbol{p}_l), \tilde{\nu}_{l,m}\right)$ is defined later in this section. With the assumption that every node l is transmitting a baseband signal $s(t)$ at frequency f_c, the received signal at anchor m is described by

$$r_{l,m,k}(t) = \tilde{\alpha}_{l,m,k}s(t - \tau_{m,k}(\boldsymbol{p}_l) - \epsilon_l) + \int s(t-\tau)\nu_{l,m,k}(\tau + \epsilon_l)d\tau + w_{l,m,k}(t), \tag{B.3}$$

with a complex amplitude $\tilde{\alpha}_{l,m,k} = \alpha_{l,m}\mathrm{e}^{-j2\pi f_c(\tau_{m,k}(\boldsymbol{p}_l)+\epsilon_l)}$ that accounts for the phase shift at antenna k, ϵ_l is the transmit time of node l and $w_{l,m,k}(t)$ is noise modeled as additive white Gaussian noise (AWGN) with double-sided power spectral density (PSD) $N_0/2$. With this, we can describe the sampled and stacked received signals as

$$\boldsymbol{r}_{l,m} = \boldsymbol{s}_{l,m}(\boldsymbol{p}_l, \epsilon_l)\alpha_{l,m} + \boldsymbol{w}^{l,m} \in \mathbb{C}^{N_s K \times 1}, \tag{B.4}$$

where $\boldsymbol{r}_{l,m} = \left[\boldsymbol{r}^T_{l,m,1}, \ldots, \boldsymbol{r}^T_{l,m,K}\right]^T$. Additive noise resulting from the DMC and AWGN is described within the noise vector $\boldsymbol{w}^{l,m}$. The baseband-signal vector is described as

$$\begin{aligned}\boldsymbol{s}_{l,m}(\boldsymbol{p}_l, \epsilon_l) = [&\mathrm{e}^{-j2\pi f_c(\tau_{m,1}(\boldsymbol{p}_l)+\epsilon_l)}\boldsymbol{s}(\tau_m(\boldsymbol{p}_l) + \epsilon_l)^T, \ldots, \\ &\mathrm{e}^{-j2\pi f_c(\tau_{m,K}(\boldsymbol{p}_l)+\epsilon_l)}\boldsymbol{s}(\tau_m(\boldsymbol{p}_l) + \epsilon_l)^T]^T\end{aligned} \tag{B.5}$$

where $\boldsymbol{s}(\tau) \in \mathbb{C}^{N_s \times 1} = [s(-\tau), s(\tau + T_s), \ldots, s(-\tau + (N_s - 1)T_s)]^T$ is a sampled version of $s(t-\tau)$. Note that T_s is the sampling time interval. This is a conventional "wideband" phased-array signal model with identical envelopes and phase shifts for the AoA.

The covariance matrix $[\boldsymbol{C}^{l,m}]_k$ describes the noise vector $\boldsymbol{w}^{l,m}$, and is the sampled noise covariance of the AWGN and DMC. We introduce a covariance-matrix for every array element k as $[\boldsymbol{C}^{l,m}]_k = [\boldsymbol{C}^{l,m}_\nu]_k + [\boldsymbol{C}^{l,m}_w]_k \in \mathbb{C}^{N_s \times N_s}$, where

$[\boldsymbol{C}_w^{l,m}]_k = \sigma_{l,m}^2 \boldsymbol{I}$, with $\boldsymbol{I}$ being the identity matrix of according dimensions and noise variance $\sigma_{l,m}^2 = N_0/T_s$. The covariance for the DMC is described as

$$\left[\boldsymbol{C}_\nu^{l,m}\right]_k = \int S_\nu\left(\tau - \tau_m(\boldsymbol{p}_l) - \epsilon_l; \tilde{\boldsymbol{\eta}}_{l,m}\right) \boldsymbol{s}(\tau)\boldsymbol{s}(\tau)^{\mathrm{H}} d\tau, \tag{B.6}$$

where $\tilde{\boldsymbol{\eta}}_{l,m}$ are parameters describing the shape of the DPS. Now, assuming that the DMC is a Gaussian process [16, 29], the likelihood-function of the model for a single node and antenna array equates to

$$f_{l,m}(\boldsymbol{r}_{l,m} \mid \boldsymbol{p}_l, \epsilon_l, \boldsymbol{\eta}_{l,m}, \alpha_{l,m}) = \frac{\mathrm{e}^{-(\boldsymbol{r}_{l,m} - \boldsymbol{s}_{l,m}(\boldsymbol{p}_l,\epsilon_l)\alpha_{l,m})^{\mathrm{H}} (\boldsymbol{C}^{l,m})^{-1} (\boldsymbol{r}_{l,m} - \boldsymbol{s}_{l,m}(\boldsymbol{p}_l,\epsilon_l)\alpha_{l,m})}}{\pi^{N_s K} \det(\boldsymbol{C}^{l,m})}, \tag{B.7}$$

with parameter vector $\boldsymbol{\eta}_{l,m} = \left[\sigma_{l,m}^2,\ \tilde{\boldsymbol{\eta}}_{l,m}^T\right]^T$ and $\boldsymbol{C}^{l,m}$ being a block diagonal matrix described by the k-th matrices $[\boldsymbol{C}^{l,m}]_k$ for every array element. To get a joint likelihood for a single node, the factorization of these likelihoods equates to

$$f_l(\boldsymbol{r}_l \mid \boldsymbol{p}_l, \epsilon_l, \boldsymbol{\eta}_l, \boldsymbol{\alpha}_l) = \prod_{m=1}^{M} f_{l,m}(\boldsymbol{r}_{l,m} \mid \boldsymbol{p}_l, \epsilon_l, \boldsymbol{\eta}_{l,m}, \alpha_{l,m}), \tag{B.8}$$

which assumes independence of the DMC and AWGN inbetween anchors. Here, $\boldsymbol{r}_l = \left[\boldsymbol{r}_{l,1}^T, \ldots, \boldsymbol{r}_{l,M}^T\right]^T$ is a stacked receive vector, $\boldsymbol{\alpha}_l = [\alpha_{l,1}, \ldots, \alpha_{l,M}]^T$ are the stacked LoS amplitudes and $\boldsymbol{\eta}_l = \left[\boldsymbol{\eta}_{l,1}{}^T, \ldots, \boldsymbol{\eta}_{l,M}{}^T\right]^T$ is a stacked parameter vector. Lastly, we introduce the DPS $S_\nu(\tau; \tilde{\boldsymbol{\eta}})$ similar to [12, 29] as

$$S_\nu(\tau; \tilde{\boldsymbol{\eta}}) = \Omega_1 \frac{\gamma_f + \gamma_r}{{\gamma_f}^2} \mathrm{e}^{-\tau/\gamma_f} (1 - \mathrm{e}^{-\tau/\gamma_r}) \Sigma(\tau), \tag{B.9}$$

with $\tilde{\boldsymbol{\eta}} = [\Omega_1, \gamma_f, \gamma_r]^T$ which corresponds to a normalized power of the DMC of Ω_1, a fall time for the process γ_f, and a rise time γ_r. Furthermore, a step-function $\Sigma(\tau)$ is defined as 1 for all $t \geq \tau$, and 0 else.

B.4 Clustering Approach

Incorporating a second measurement method, namely RSS measurements, multiple adjacent nodes can be processed jointly to improve the positioning accuracy and mitigate outliers due to the DMC. We focus on a node of interest l' at position $\boldsymbol{p}_{l'}$. We define a set of nodes $\mathcal{L}$ of size N, which incorporates all nodes l which we want to include in our evaluation. This set $\mathcal{L}$ can be defined in various ways, but notably we use RSS measurements and genie-aided methods to define the nodes within the set. The genie-aided method incorporates the $N-1$ nearest nodes (in geometrical sense) to l' and the node l' itself, where we use the ground-truth of all node positions $\boldsymbol{p}_l$. The RSS-based method uses RSS measurements from the node l' to all other nodes l, and incorporates the $N-1$ nodes l with the largest RSSs and the node l' itself. For our purposes, it is assumed that the node positions $\boldsymbol{p}_l$ are distributed around a mean cluster position $\boldsymbol{p}_c \approx \overline{\{\boldsymbol{p}_l\}}_{\mathcal{L}}$. The index l' is omitted from here on to improve readability.

Assuming that measurements between different positions $\boldsymbol{p}_l$ are independent, the joint likelihood for the set $\mathcal{L}$ equates to

$$f(\boldsymbol{r} \mid \boldsymbol{p}_c, \boldsymbol{\epsilon}, \boldsymbol{\eta}, \boldsymbol{\alpha}) = \prod_{l \in \mathcal{L}} \int_{\boldsymbol{p}_l \in \mathcal{L}} f_l(\boldsymbol{r}_l \mid \boldsymbol{p}_l, \epsilon_l, \boldsymbol{\eta}_l, \boldsymbol{\alpha}_l) f(\boldsymbol{p}_l \mid \boldsymbol{p}_c) d\boldsymbol{p}_l, \tag{B.10}$$

where $\boldsymbol{\alpha} = [\boldsymbol{\alpha}_l^T]^T$, $\boldsymbol{\epsilon} = [\boldsymbol{\epsilon}_l^T]^T$, and $\boldsymbol{\eta} = [\boldsymbol{\eta}_l^T]^T \ \forall l \in \mathcal{L}$ are stacked versions of their respective counterparts and $\boldsymbol{r}$ is a stacked vector of $[\boldsymbol{r}^T]^T$ with $l \in \mathcal{L}$. The term

$$f(\boldsymbol{p}_l \mid \boldsymbol{p}_c) = \delta(\boldsymbol{p}_l - \boldsymbol{p}_c - \boldsymbol{\Delta}_l) \approx \delta(\boldsymbol{p}_l - \boldsymbol{p}_c), \tag{B.11}$$

models the displacement between $\boldsymbol{p}_l$ and $\boldsymbol{p}_c$ by $\boldsymbol{\Delta}_l$. The approximation assumes that the term $f(\boldsymbol{p}_l \mid \boldsymbol{p}_c)$ is negligible because all likelihoods $f_l(\boldsymbol{r}_l \mid \boldsymbol{p}_l, \epsilon_l, \boldsymbol{\eta}_l, \boldsymbol{\alpha}_l)$ have wide main lobes in comparison to the offset distance $\boldsymbol{\Delta}_l$ from the cluster position $\boldsymbol{p}_c$. Thus a simplified log-likelihood for estimation and analysis is proposed as

$$\ln f(\boldsymbol{r} \mid \boldsymbol{p}_c, \boldsymbol{\epsilon}, \boldsymbol{\eta}, \boldsymbol{\alpha}) = \sum_{l \in \mathcal{L}} \ln f_l(\boldsymbol{r}_l \mid \boldsymbol{p}_c, \epsilon_l, \boldsymbol{\eta}_l, \boldsymbol{\alpha}_l). \tag{B.12}$$

For this factorized likelihood function $f(\boldsymbol{r} \mid \boldsymbol{p}_c, \boldsymbol{\epsilon}, \boldsymbol{\eta}, \boldsymbol{\alpha})$ it can be shown that there exists an unbiased estimator for the mean cluster position, if the regularity condition

$$\mathbb{E}\left[\frac{\partial \ln f(\boldsymbol{r} \mid \boldsymbol{p}_c, \boldsymbol{\epsilon}, \boldsymbol{\eta}, \boldsymbol{\alpha})}{\partial \boldsymbol{p}_c}\right] = \boldsymbol{0} \tag{B.13}$$

holds true [30], because the distribution of $\boldsymbol{p}_l \forall l \in \mathcal{L}$ around $\boldsymbol{p}_c$ is assumed to be zero-mean. Note that (B.13) defines implicitly the exact cluster position $\boldsymbol{p}_c$. This is similar to [31], where this assumption is used for spatial antenna-arrays. For all other parameters, this has already been shown in literature [12, 16].

B.5 Cramér-Rao Lower Bound

In order to evaluate the accuracy of results, the CRLB is derived, which is a general bound for the achievable accuracy. The CRLB is the inverse of the Fisher information (FI), for which derivations are shown in the following Subsections.

B.5.1 Introduction

The general form of the Fisher information matrix (FIM) for a PDF of the form $f(\boldsymbol{r} \mid \boldsymbol{\psi})$ is [30, 32]

$$\boldsymbol{J}_{\boldsymbol{\psi}} = \mathbb{E}_{\boldsymbol{r}|\boldsymbol{\psi}}\left[\left(\frac{\partial}{\partial \boldsymbol{\psi}} \ln f(\boldsymbol{r} \mid \boldsymbol{\psi})\right)\left(\frac{\partial}{\partial \boldsymbol{\psi}} \ln f(\boldsymbol{r} \mid \boldsymbol{\psi})\right)^T\right], \tag{B.14}$$

for which the CRLB of an unbiased estimator $\hat{\boldsymbol{\psi}}$ of the parameter vector $\boldsymbol{\psi}$ is defined as

$$\mathbb{E}_{\psi}\left[(\hat{\boldsymbol{\psi}} - \boldsymbol{\psi})(\hat{\boldsymbol{\psi}} - \boldsymbol{\psi})^H\right] \succeq \boldsymbol{J}_{\boldsymbol{\psi}}^{-1}, \tag{B.15}$$

where it should be noted that $\boldsymbol{A} \succeq \boldsymbol{B}$ indicates that $\boldsymbol{A} - \boldsymbol{B}$ is a positive semi-definite matrix.

B.5.2 Derivation of the Position Error Bound

To derive lower bounds on the error variance of position estimates, we first define a parameter vector $\boldsymbol{\psi}_{l,m} = [\phi_{l,m}, \vartheta_{l,m}, \tau_{l,m}, \mathcal{R}\alpha_{l,m}, \mathcal{I}\alpha_{l,m}]^T$ with an azimuth angle from anchor m to node l of $\phi_{l,m} = \text{atan2}(y_l - y_m, x_l - x_m)$, elevation angle $\vartheta_{l,m} = \text{atan2}(z_l - z_m, \sqrt{(x_l - x_m)^2 + (y_l - y_m)^2})$, and delay $\tau_{l,m} = \tau_m(\boldsymbol{p}_l) + \epsilon_l$.

The equivalent Fisher information matrix (EFIM) [33] on the delay $\tau_{l,m}$ and angle measurements $\phi_{l,m}$ and $\vartheta_{l,m}$ acquired by anchor m on each node l is then given as

$$\boldsymbol{J}_{\boldsymbol{\psi}_{l,m}} = \begin{bmatrix} J_{\phi_{l,m}} & 0 & 0 \\ 0 & J_{\vartheta_{l,m}} & 0 \\ 0 & 0 & J_{\tau_{l,m}} \end{bmatrix}, \tag{B.16}$$

where the diagonal elements $J_{\phi_{l,m}}$, $J_{\vartheta_{l,m}}$, and $J_{\tau_{l,m}}$ account for the information w.r.t. the different parameters. A derivation of this EFIM is given in Appendix B.8. Furthermore, we introduce the Jacobian matrix $\boldsymbol{P}_m(\boldsymbol{p}_l)$ for transforming spherical to Cartesian coordinates, which is defined as

$$\begin{aligned} \boldsymbol{P}_m(\boldsymbol{p}_l) &= \begin{bmatrix} \frac{\partial x_l}{\partial \phi_{l,m}} & \frac{\partial x_l}{\partial \vartheta_{l,m}} & \frac{\partial x_l}{\partial \tau_{l,m}} \\ \frac{\partial y_l}{\partial \phi_{l,m}} & \frac{\partial y_l}{\partial \vartheta_{l,m}} & \frac{\partial y_l}{\partial \tau_{l,m}} \\ \frac{\partial z_l}{\partial \phi_{l,m}} & \frac{\partial z_l}{\partial \vartheta_{l,m}} & \frac{\partial z_l}{\partial \tau_{l,m}} \end{bmatrix} \\ &= \begin{bmatrix} -\frac{\sin\phi_{l,m}\sin\vartheta_{l,m}}{\tau_{l,m}c} & \frac{\cos\phi_{l,m}\cos\vartheta_{l,m}}{\tau_{l,m}c} & \frac{\sin\phi_{l,m}\cos\vartheta_{l,m}}{c} \\ \frac{\sin\phi_{l,m}\cos\vartheta_{l,m}}{\tau_{l,m}c} & \frac{\cos\phi_{l,m}\sin\vartheta_{l,m}}{\tau_{l,m}c} & \frac{\sin\phi_{l,m}\sin\vartheta_{l,m}}{c} \\ 0 & -\frac{\sin\phi_{l,m}}{\tau_{l,m}c} & \frac{\cos\phi_{l,m}}{c} \end{bmatrix} \in \mathbb{R}^{3\times 3}, \end{aligned} \tag{B.17}$$

for node $l \in \mathcal{L}$ at position $\boldsymbol{p}_l = [x_l, y_l, z_l]^T$. Note that c is the speed of light.

Assuming independent noise for all nodes $l \in \mathcal{L}$ and knowledge of the displacement $\boldsymbol{\Delta}_l = \boldsymbol{p}_l - \boldsymbol{p}_c$ between the node positions $\boldsymbol{p}_l$ and the cluster position $\boldsymbol{p}_c$, the Cartesian EFIM for the cluster is expressed by the sum of the node EFIMs,

$$\boldsymbol{J}_{\boldsymbol{p}_c}^{(m)} = \sum_{l\in\mathcal{L}} \boldsymbol{P}_m(\boldsymbol{p}_l)\boldsymbol{J}_{\boldsymbol{\psi}_{l,m}}\boldsymbol{P}_m(\boldsymbol{p}_l)^T = \boldsymbol{P}_m(\boldsymbol{p}_c)\boldsymbol{J}_{\boldsymbol{\psi}_m^{(c)}}\boldsymbol{P}_m(\boldsymbol{p}_c)^T. \tag{B.18}$$

The right-hand side of this expression transforms the sum-information in Cartesian coordinates back to range and angle measurements. This yields a (non-diagonal) EFIM $\boldsymbol{J}_{\boldsymbol{\psi}_m^{(c)}}$ for the cluster center as

$$\boldsymbol{J}_{\boldsymbol{\psi}_m^{(c)}} = \sum_{l\in\mathcal{L}} \boldsymbol{P}_m(\boldsymbol{p}_c)^{-1}\boldsymbol{P}_m(\boldsymbol{p}_l)\boldsymbol{J}_{\boldsymbol{\psi}_{l,m}}(\boldsymbol{P}_m(\boldsymbol{p}_c)^{-1}\boldsymbol{P}_m(\boldsymbol{p}_l))^T, \tag{B.19}$$

where the off-diagonal elements describe some transformation of angle information to delay-information and vice versa. We thus argue that a diagonal EFIM, written as a sum of all delay and angle terms, serves as an upper bound on the delay and angle information for the cluster at $\boldsymbol{p}_c$, if the position offsets $\boldsymbol{\Delta}_l$ are unknown. I.e. we have

$$\widetilde{\boldsymbol{J}}_{\boldsymbol{\psi}_m^{(c)}} = \sum_{l\in\mathcal{L}} \boldsymbol{J}_{\boldsymbol{\psi}_{l,m}} \tag{B.20}$$

as an upper bound on the sum-information from all the delay and angle measurements for all nodes of the cluster and the corresponding bound on the position

information,

$$\widetilde{\boldsymbol{J}}_{\boldsymbol{p}_c}^{(m)} = \boldsymbol{P}_m(\boldsymbol{p}_c)\widetilde{\boldsymbol{J}}_{\boldsymbol{\psi}_m^{(c)}}\boldsymbol{P}_m(\boldsymbol{p}_c)^T. \tag{B.21}$$

From this, we define a multi-anchor EFIM for the cluster position $\boldsymbol{p}_c$ which is decomposed into three components corresponding to the delay and angle terms as

$$\boldsymbol{J}_{\boldsymbol{p}_c} = \sum_{m=1}^{M} \widetilde{\boldsymbol{J}}_{\boldsymbol{p}_c}^{(m)} \tag{B.22}$$

$$\approx \sum_{m=1}^{M} \Bigg[\frac{8\pi^2}{d_m^2} D_\lambda^2(\phi_m)\ KL\ \mathrm{SINR}_m \boldsymbol{R}_r(\phi_m + \frac{\pi}{2}, \vartheta_m) \tag{B.23}$$

$$+ \frac{8\pi^2}{d_m^2} D_\lambda^2(\vartheta_m)\ KL\ \mathrm{SINR}_m \boldsymbol{R}_r(\phi_m, \vartheta_m + \frac{\pi}{2}) \tag{B.24}$$

$$+ \Lambda \frac{8\pi^2}{c^2} \beta^2\ KL\ [\widetilde{\mathrm{SINR}}_\tau]_m \boldsymbol{R}_r(\phi_m, \vartheta_m) \Bigg], \tag{B.25}$$

using the results from Appendices B.9 and B.10. Here, d_m, ϕ_m, and ϑ_m are the distances between the array centers and the cluster center and the corresponding angle parameters, $D_\lambda^2(\phi_m)$ and $D_\lambda^2(\vartheta_m)$ are the array apertures in azimuth and elevation, β^2 is the mean-squared signal bandwidth, and SINR_m and $[\widetilde{\mathrm{SINR}}_\tau]_m$ accounts for the interference by the dense multipath (DM). The factor KL quantifies the number of antennas per anchor as well as the number of nodes in the cluster, which are interpreted as a boost in SINR, i.e. a suppression of the influence of the DM. Finally, the matrices $\boldsymbol{R}_r(\phi_m, \vartheta_m)$ are so-called ranging direction matrixs (RDMs) [33] defined as

$$\boldsymbol{R}_r(\phi_m, \vartheta_m) = \boldsymbol{e}(\phi_m, \vartheta_m)\boldsymbol{e}^T(\phi_m, \vartheta_m) \tag{B.26}$$

where $\boldsymbol{e}(\phi_m, \vartheta_m)$ is a unit vector pointing from array m in the direction of the node l.

This position error bound (PEB) (see B.22) also takes the correction factor Λ in account for the clustering, dissimilar to other related work only showing results for single nodes. It accounts for the spread of delays $\tau_m(\boldsymbol{p}_l)$ for $l \in \mathcal{L}$ around $\tau_m(\boldsymbol{p}_c)$ which leads to an apparent loss of bandwidth as derived in Appendix B.9.

With this, we can define the PEB for multiple anchors m and multiple nodes $l \in \mathcal{L}$ as

$$\mathcal{P}_c = \sqrt{\mathrm{tr}\{\boldsymbol{J}_{\boldsymbol{p}_c}^{-1}\}}. \tag{B.27}$$

B.5.3 Biased Lower Bound

In the previous subsection, we derived the PEB for the cluster position $\boldsymbol{p}_c$. For real-world applications, the cluster position would be mostly of no importance, but it can be assumed that the cluster position is within a vicinity of the position of the node l' which has been used to define the cluster. Equality holds true for scenarios where all nodes $l \in \mathcal{L} \setminus \{l'\}$ are distributed in such way that the cluster position $\boldsymbol{p}_c = \boldsymbol{p}_{l'}$. In real world scenarios this assumption often does not hold, thus we propose a biased lower bound for the node l'

$$\mathcal{P}_{l'} = \mathcal{P}_c + \|\boldsymbol{p}_c - \boldsymbol{p}_{l'}\|. \tag{B.28}$$

This biased lower bound has the advantage of easier representation of relevant errors, and comparability with the root-mean-square error (RMSE) of the first node position $\hat{\boldsymbol{p}}_{l'}$.

B.6 Numeric Evaluation

Note that in this section, if there is a discussion about the cluster position $\boldsymbol{p}_c$ or the position of the first node in a cluster $\boldsymbol{p}_{l'}$, it is always assumed to be for every possible set $\mathcal{L}$ for every node $l \in L$, meaning that this evaluation is done for every possible cluster in a scenario. To validate the CRLB and biased bound for $\boldsymbol{p}_{l'}$, we evaluated four simulation scenarios, two of which represent a realistic indoor scenario. Lastly an evaluation on measurement data was done, where the scenario corresponded to our simulations. For the evaluation, only the AWGN case was considered and all estimations were done in practice via a particle evaluation of the joint-likelihood $f(\boldsymbol{r} \mid \boldsymbol{p}_c, \boldsymbol{\eta}, \boldsymbol{\alpha})$ [34], described in (B.12), by

$$\hat{\boldsymbol{p}}_c = \underset{\boldsymbol{p}_c, \epsilon_l \forall l \in \mathcal{L}}{\arg\max}\, f(\boldsymbol{r} \mid \boldsymbol{p}_c, \boldsymbol{\epsilon}, \boldsymbol{\eta}, \boldsymbol{\alpha}). \tag{B.29}$$

For the parameter $\boldsymbol{\alpha}$, a least-squares solution can be found as

$$\hat{\alpha}_{l,m}(\boldsymbol{p}_c) = [\boldsymbol{s}_{l,m}(\boldsymbol{p}_c, \epsilon_l)^H \boldsymbol{s}_{l,m}(\boldsymbol{p}_c, \epsilon_l)]^{-1} \boldsymbol{s}_{l,m}(\boldsymbol{p}_c, \epsilon_l)^H \boldsymbol{r}_{l,m}, \tag{B.30}$$

calculated for every element $\alpha_{l,m}$. The parameters $\boldsymbol{\epsilon}$ had to be estimated also by the particle-filter. This particle-filter allowed us to estimate the position of a cluster with size $N = 40$ on a typical workstation in under 30 s of time, and for small cluster sizes the computation time decreases linearly.

As the estimations of DMC parameters are omitted, the state of this joint-likelihood can be represented by a parameter vector $\boldsymbol{\nu} = [x_c, y_c, z_c, \epsilon_1, \ldots, \epsilon_{N_l}]^T$, where ϵ_l represents the transmit time of each node in the set $\mathcal{L}$, and N_l represents the number of elements in the set $\mathcal{L}$. For the initialisation of the parameters $[x_c, y_c]^T$, a support over the simulated room was chosen, for the height z_c the support was chosen to be in the range between $[-6\,\mathrm{m}, 6\,\mathrm{m}]$ for scenarios with no shelf simulation, and $[0\,\mathrm{m}, 2\,\mathrm{m}]$ for scenarios with shelf simulation. For the measurement scenario, the particles were initialized within the aisles only. Transmit times ϵ_l were initialized on an interval of $[\frac{0\,\mathrm{m}}{c}, \frac{150\,\mathrm{m}}{c}]$, which represent all transmit times in simulated and measurement scenarios within a reasonable margin. Note that c again represents the speed of light.

Each particle $\boldsymbol{\nu}_p$ is initialized as one realisation of the parameter vector $\boldsymbol{\nu}$, meaning that each particle represents a cluster position and unknown transmit times of all nodes within the cluster. The likelihood is then evaluated for each and every particle.

All evaluations are done with 1000 particles, each of which represents one state $\boldsymbol{\nu}_p$. This was a reasonable trade-off between estimation time and accuracy. A three-step approach was chosen: After an initalization step, particles were resampled twice from the computed likelihoods. The first resampling step was done by resampling from the computed normalized log-likelihood and adding additional i.i.d. Gaussian noise to every resampled parameter. This noise was chosen as an i.i.d. Gaussian process described by a mean of 0 m and a standard deviation of

0.5 m for parameters $[x_c, y_c, z_c]^T$ and 0.5 m$\frac{1}{c}$ for parameters ϵ_l. The additional noise helps mitigating particle deprivation, where all particles are resampled from a single previous particle with an exceptionally large likelihood compared to all other particles. This first resampling step was chosen to better ensure resampling from modes which were underrepresented in the initialisation step, but avoiding to use a much larger number of particles beforehand. This strategy leads to a very coarse maximum for the particles, and thus a second resampling step is necessary. There we used a classical strategy where the resampling was done directly from the estimated normalized likelihood, once again adding the same i.i.d. noise. This resampling focused more on the dominant mode of the resulting distribution, and thus can be seen as a refinement in the vicinity of the dominant mode. This two-step resampling strategy allows us to use significantly fewer particles for our estimation problem. Only using the second resampling step, we needed a factor of at least 20 times the number of particles for comparable accuracy, which leads to a proportional increase of calculation time by the same factor. It should be noted that this implementation is capable to calculate positions in real-time, as the number of operations to be processed is fixed by the number of particles.

Note that the simulations and measurements used 6 antenna arrays with 2 antennas each. This is not a limitation of the algorithm. Arbitrary antenna configurations can be used, but the configuration in the simulations was chosen for easier comparison to the measurement scenario.

B.6.1 Cluster in Single Position

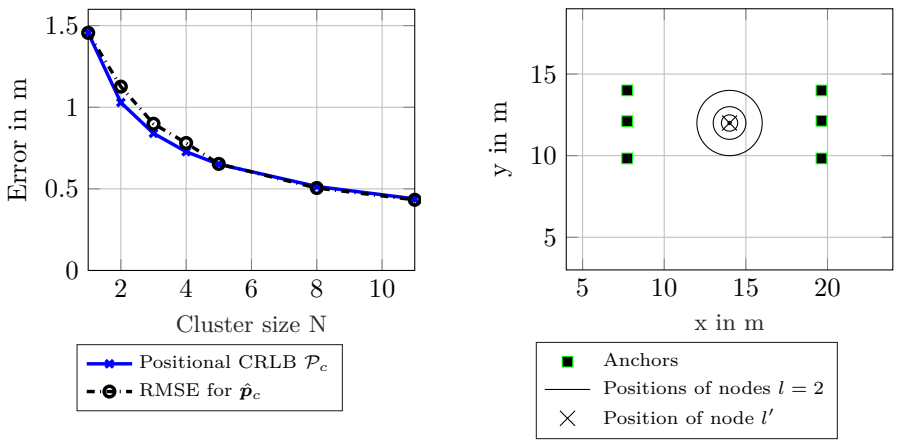

Figure B.2: Scenario 6.1 and 6.2: Results for synthetic scenario in single position with random clusters and schematic plot for clusters of size 1 and size 2 with variable distance.

For a first evaluation, we show that the PEB for the cluster position $\boldsymbol{p}_c$ holds true. To achieve this, we simulated a scenario with following parameters:

For placement of the antenna-arrays see Figure B.2. All antenna-arrays are

Table B.1: Settings for simulation

f_c	β	M	K	Antenna spacing
2.44 GHz	75.3 MHz	6	2	6 cm

shown as squares, and the positions of all nodes l are shown as a black cross. The arrays are all oriented such that they are spaced in the direction of the y-axis, therefore the positioning performance improves with the aperture of the arrays. The nodes are placed at $\boldsymbol{p}_c = [14\,\mathrm{m}, 12\,\mathrm{m}, 1\,\mathrm{m}]^T$. For this scenario 1100 realisations of a channel incorporating DMC was chosen, with an SNR at 1 m of $\frac{\alpha^2_{1\,\mathrm{m}}}{\sigma^2_{l,m,k}} = 25\,\mathrm{dB}$, where $\alpha_{1\,\mathrm{m}}$ is the equivalent amplitude of the normalized signal at 1 m. The cluster-size N was varied, where the first node was always one unique node from all 1110 simulated nodes, and every other node in the set was chosen randomly from all other remaining nodes.

The signal amplitude was then scaled according to Friis equation, leading to

$$\alpha_{l,m} = \alpha_{1\,\mathrm{m}} \left(\frac{\lambda_c}{4\pi d_{l,m}} \right), \tag{B.31}$$

where $\lambda_c = \frac{1}{f_c}$ and $d_{l,m}$ is the distance between node l and anchor m. The parameter Ω_1 of the DMC at 1 m was drawn from an i.i.d. Gaussian random process, and scaled according to the Friis equation [35] resulting in

$$[\Omega_1]_{l,m} \sim \mathcal{N}\left(\mu = 0\,\mathrm{dB}, \sigma^2 = 2.16\,\mathrm{dB} \times \left(\frac{\lambda_c}{4\pi d_{l,m}} \right)^2 \right), \tag{B.32}$$

where $\mathcal{N}(\mu, \sigma^2)$ is a random i.i.d Gaussian process. This describes one realisation of random variable for the parameter Ω_1. The parameters for the fall and rise time of the DMC were chosen as fixed values being $\gamma_r = 5\,\mathrm{ns}$ and $\gamma_f = 20\,\mathrm{ns}$, which are typical values for an indoor scenario [29, 36].

Figure B.2 shows that the CRLB can be attained for this scenario as the curve showing the RMSE for $\hat{\boldsymbol{p}}_c$ is almost identical to the theoretical bound. A small offset can be seen for small cluster-sizes (i.e., N in the range of 2 to 4), which can be attributed to the particle-based estimation not being perfect. This could be mitigated by using more particles. Note that the bias $\|\boldsymbol{p}_c - \boldsymbol{p}_{l'}\|$ and the correction factor Λ were both zero for all different cluster sizes in this scenario, and therefore the equivalent Fisher information (EFI) could be directly summed up, meaning the CRLB is scaling with $\frac{1}{\sqrt{N}}$, which can be interpreted as using different realisations from the same node.

B.6.2 Double-Node Clusters with Variable Distance

For this scenario, the same settings as in the previous section were used regarding antenna placement and signal parameters, see Table B.1. All other parameters of the signal are also defined the same as in Subsection B.6.1. In this scenario,

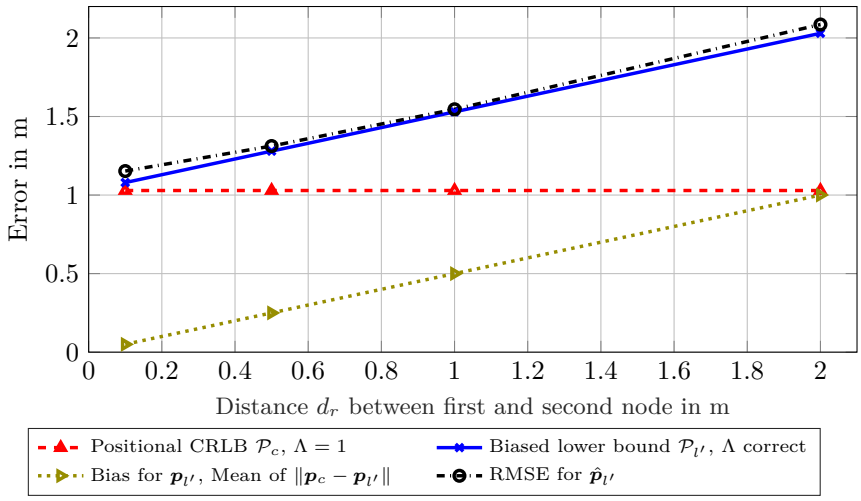

Figure B.3: Scenario 6.2: Results for synthetic scenario for clusters of size N=2 with fixed distance in a circle around node l'

1110 pairs of nodes were simulated, where for every node l' a new realisation of the channel was drawn at the position $\boldsymbol{p}_{l'}$ being the same as in the previous scenario, and for the corresponding node $l = 2$ another realisation of the channel was drawn at a position $\boldsymbol{p}_2 = \boldsymbol{p}_{l'} + [d_r \cos\phi_r, d_r \sin\phi_r, 0]^T$, where the distance d_r was evaluated at 4 distances from 0.1 m to 2 m, and the angle ϕ_r was drawn from a uniform random distribution with $\phi_r \sim [0, 2\pi)$. This is visualized as concentric circles in Figure B.2.

As can be seen in Figure B.3, the PEB $\mathcal{P}_c$ omitting the correction factor Λ is constant over distance, which is not representative for the RMSE for the estimated position $\hat{\boldsymbol{p}}_{l'}$ of the first node l'. Correcting for the mean distance $\|\boldsymbol{p}_c - \boldsymbol{p}_{l'}\|$, one can see that the performance of the estimator is attaining the biased lower bound $\mathcal{P}_{l'}$. Note that this biased lower bound is not only a linear offset due to geometric distance, but also incorporates a small information loss by the introduction of the evaluated correction factor Λ. This simulation shows that the introduction of a lower bound incorporating a bias between cluster center $\boldsymbol{p}_c$ and the position of the first node $\boldsymbol{p}_{l'}$ can be replicated in an evaluation of the according RMSE.

B.6.3 Simulated Scenario with Genie Aided Clusters

To further test our algorithm in a more realistic scenario, we simulated a room, where 1110 nodes are placed on shelves at different heights and positions in a room, for reference see Figure B.1. The signal parameters were again chosen according to Table B.1, and parameters Ω_1 and $\alpha_{l,m}$ were again scaled according to Equations (B.31),(B.32), but additionally for each intersection with a shelf of a ray casted from antenna array position $\boldsymbol{p}_m$ to a node position $\boldsymbol{p}_l$ distributions of parameters Ω_1 and $\alpha_{l,m}$ are changed according to Table B.2. These values were chosen to

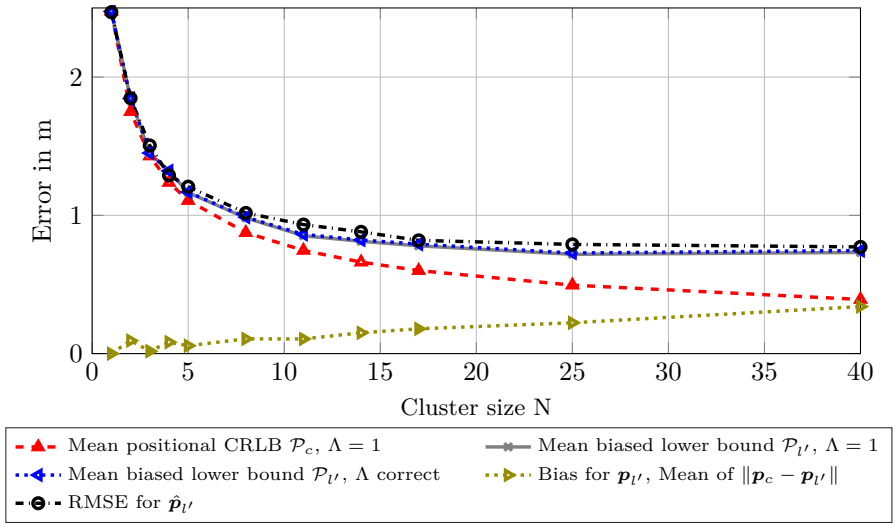

Figure B.4: Scenario 6.3: Results for synthetic scenario with genie-aided clusters (minimum distance to node 1)

Table B.2: Change of parameters

Intersections:	0	1	2	3
μ of Ω_1	−20 dB	−10 dB	0 dB	10 dB
σ^2 of Ω_1	2.16 dB	5.30 dB	7.15 dB	6.40 dB
$\frac{\alpha_{l,m}^2}{\sigma_{l,m,k}^2}$ at 1 m	25 dB	21.42 dB	19.46 dB	19.56 dB

represent empirical measurements for this type of shelf done in previous work [37]. Sets $\mathcal{L}$ for clusters were chosen in a way to minimize geometric cluster sizes, where nearest nodes from l' were selected, assuming side information provided by a genie. This was done to show a perfect scenario, minimizing other possible unknown effects to the estimation, and incorporates no model for the RSS, only geometric distances. As can be seen in Figure B.4, the RMSE almost attains the biased lower bound in this scenario. This shows that for a perfect selection of nearest nodes, the estimation of the position $\boldsymbol{p}_c$ can be also seen as a good estimate for the position $\boldsymbol{p}_{l'}$ of the first node in a cluster, improving accuracy significantly with bigger cluster sizes. As sizes of the clusters are relatively small, the correction factor Λ is almost negligible for all cluster sizes in this scenario. This can be seen in the lines for the biased lower bound with $\Lambda = 1$ and the biased lower bound with Λ correct being almost identical.

In Figures B.5a-B.5c the floorplans of the scenario can be seen, where red triangles show the estimated position and cyan crosses show the true position for every

10-th simulated node, omitting many measurements for better visibility. The true and estimated positions are connected by a dotted gray line. Similarly to Figure B.1, anchors are again shown as black squares. In Figure B.5a, many estimated node positions are outliers. This is due to the multi-modality of the likelihood for single nodes leading to false positions in the likelihood being dominant. This can be mitigated mostly by larger cluster sizes N, which can be seen in Figures B.5b-B.5c, where the position errors improve with larger cluster size N.

B.6.4 Simulated Scenario with RSS-based Clusters

To further show that the clustering approach works for realistic scenarios, the same simulation as in Subsection B.6.3 was done, but clusters were defined according to real RSS measurements done in a corresponding measurement scenario. All RSS measurements between every pair of nodes were known. Clusters were then defined by sorting the RSS values from the l'-th node to every other node in descending order, achieving the now measured sets $\mathcal{L}$ for every node l'. As these measurements are noisy and incorporate channel parameters, geometric cluster sizes are bigger and often biased for example in the direction of an aisle, compared to the genie-aided clusters in the previous subsection.

Figure B.6 shows the same results as in Figure B.4, but with clusters based on RSS measurements. The mean bias for $\boldsymbol{p}_{l'}$ is now significantly larger, leading to a diminished performance for bigger cluster sizes N. Still, the RMSE mostly attains the biased lower bound. It should be noted that the correction factor Λ is now showing a significant offset for larger clusters with the RMSE following the resulting offset. It can be seen that the effects of the bias for $\boldsymbol{p}_{l'}$ and the correction factor Λ dominate over the classical CRLB for large cluster sizes N, meaning that there is an optimum for the cluster size depending on the scenario.

Figure B.7 again shows a map of the environment as previously seen in Figure B.5a. Note that the results for single nodes differ, as these evaluations were done with different realisations for the channel. Now, for larger cluster sizes as seen in Figures B.7b-B.7c it can be seen that the estimated positions $\hat{\boldsymbol{p}}_{l'}$ are increasingly shifted into the aisles. This effect is attributed to the RSS measurements showing smaller values when the propagation path is through a shelf, which is an expected behaviour of the channel, biasing our clusters towards the centers of the aisles. As seen in Figure B.6, the RMSE is lower for clusters of size $N = 11$ than for clusters of size $N = 25$. This can be seen as smaller absolute errors in Figure B.7b than in Figure B.7c, but for some scenarios it may be preferable to achieve a slightly larger absolute positioning error in exchange for a more accurate classification of positions to the right aisle and/or shelf.

B.6.5 Experimental Validation

Figure B.8 shows parts of the measurement setup and room. Here, one can see the placement of nodes (in this case electronic shelf labels) mounted on industrial shelves, similar to those found in retail stores. The antennas seen in the picture correspond to the two upper-left positions for anchors seen in Figure B.1. The nodes allowed for cooperative RSS measurements inbetween each pair of nodes by using a proprietary protocol and transmission in the ISM-band at 2.4 GHz. The WB measurements were done according to a protocol described in detail in [4, 38].

To further validate results, we used WB measurement data from a scenario corresponding to our simulations. The geometry and number of anchors were the same as in the simulation scenarios in the previous two subsections, parameters from Table B.1 still apply. Corresponding RSS measurement data were also retrieved. These measurements were done for all 1100 nodes in a timeframe of approximately 24 hours, where most time was used for transmission of the RSS measurement data to infrastructure. In comparison, a single WB measurement took less than a minute with additional post-processing. Both genie-aided and RSS data based clustering approaches were evaluated. As we wanted these evaluations to show the optimal performance we could achieve in such a scenario, we further incorporated prior knowledge of the agent positions, restricting all particles to areas within aisles (see Figure B.1 for reference). This allows us to improve performance by incorporating knowledge about the room.

In Figure B.9 the results can be seen for the measurement scenario. Note that the CRLB and biased lower bound are not shown here, as an accurate estimation of these bounds requires appropriate channel parameters, which cannot be extracted from our measurements well enough. Therefore, one can see that the performance the clustering approaches corresponds to the two simulation scenarios seen in Subsections B.6.3 and B.6.4. It can also be seen that for the genie-aided clustering, the performance is getting better for all cluster sizes in this evaluation, though we expect the performance to worsen for even larger cluster sizes, as the bias term will dominate for large clusters. The evaluation using RSS measurement data again shows an ideal cluster size for the RMSE of $N = 11$, meaning that for real-world scenarios using the RSS-based clustering approach there is no need for more computationally intensive, larger cluster sizes. For reference, the RMSE is also plotted for an evaluation using RSS measurements, which does not incorporate a prior in the aisles. This evaluation was done with the same number of particles, as these proved to be still sufficient. Here we see that the estimation performance is worse over all cluster sizes, justifying the initialisation within aisles. As a side note, an evaluation with non-fixed cluster sizes, where clusters were determined by RSS-thresholds was also done. Over a wide range of thresholds, this did not improve results.

As seen in Figure B.10a, comparable to the synthetic scenarios, the estimation errors for non-clustered processing are rather large. Some effects of the geometry are more pronounced, which can be seen for example in the left-most nodes at $x \approx 6\,\mathrm{m}, y \approx 9\,\mathrm{m}$, being estimated very accurately in comparison to most other nodes. As these nodes are in the direct vicinity of an antenna-array, there is a pronounced LoS-component and a good SNR for WB-measurements. Also, the effects of the initialisation within possible aisles already leads to better results for the non-clustered case.

Looking at Figure B.10b, we again can see a significant performance improvement for the clustering algorithm using RSS-based clusters. It is worth noting that, again, the estimated positions $\hat{\boldsymbol{p}}_{l'}$ are increasingly shifted to within centers of aisles, which again can be contributed to RSS-measurements giving stronger indications for links with LoS conditions, which often happen to be on the opposite side of aisles for our scenario.

Figure B.11 shows a plot for the cumulative frequency (CF) of the error $\|\hat{\boldsymbol{p}}_c - \boldsymbol{p}_{l'}\|$ for both genie-aided and RSS-based clustering approaches. It can be seen that

especially outliers can be minimized by the clustering approaches compared to the non-clustered ($N = 1$) case. It should be noted that the genie-aided approach clearly outperforms the RSS-based method, but for the minimization of outliers ($> 2\,\mathrm{m}$) both methods are almost equal when using cluster sizes $N \geq 11$. Furthermore, one can see that the performance of the RSS-based clusters is worse for very small errors ($< 0.2\,\mathrm{m}$) than for a non-clustered approach. This can be attributed to the bias-term being dominant, as RSS-measurements to nodes on the other side of an aisle were often dominating, even in small cluster sizes.

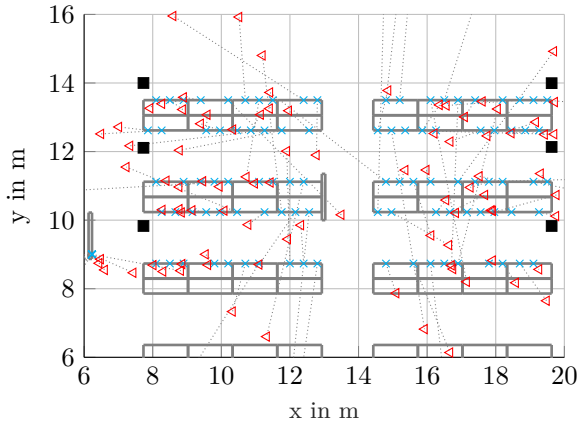

(a) N=1

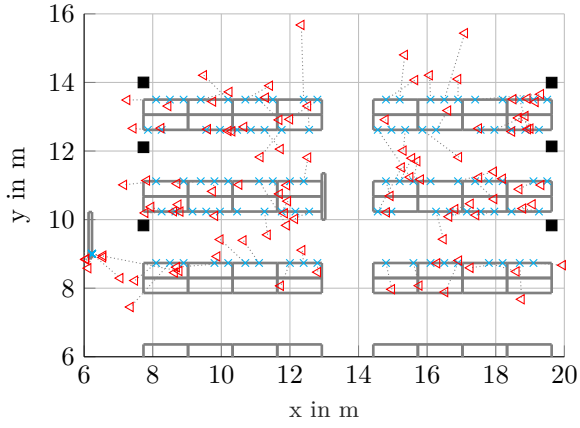

(b) N=11

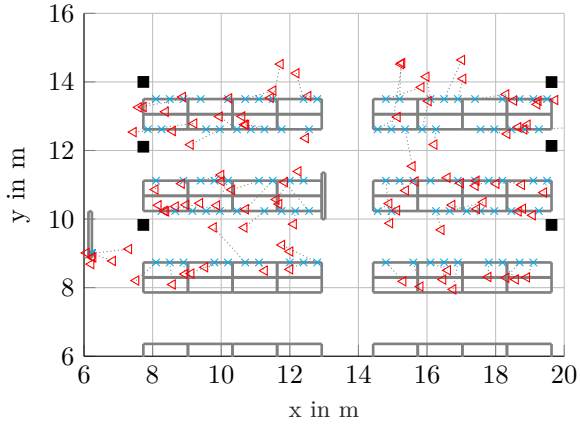

(c) N=25

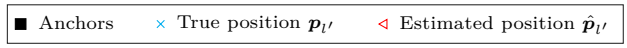

Figure B.5: Scenario 6.3: Floorplans with results for synthetic scenario with genie-aided clusters (showing only every 10-th processed node for better visibility)

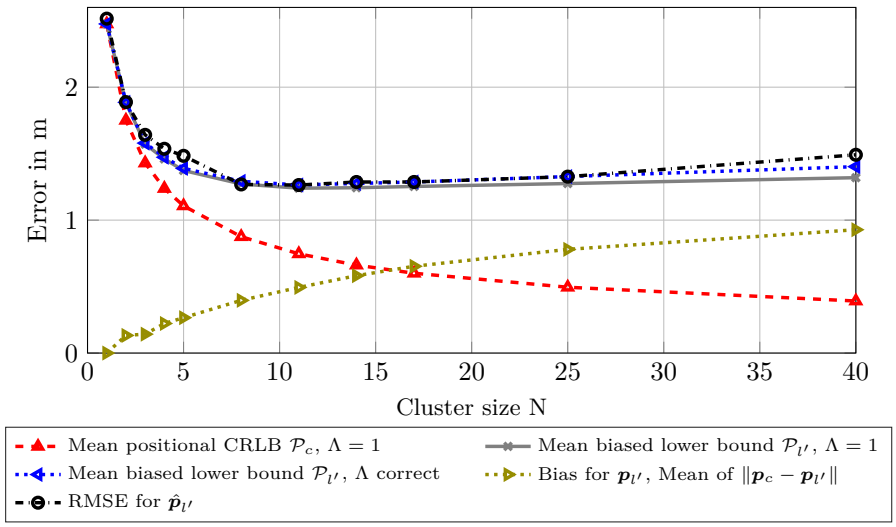

Figure B.6: Scenario 6.4: Results for synthetic scenario with RSS-based clusters

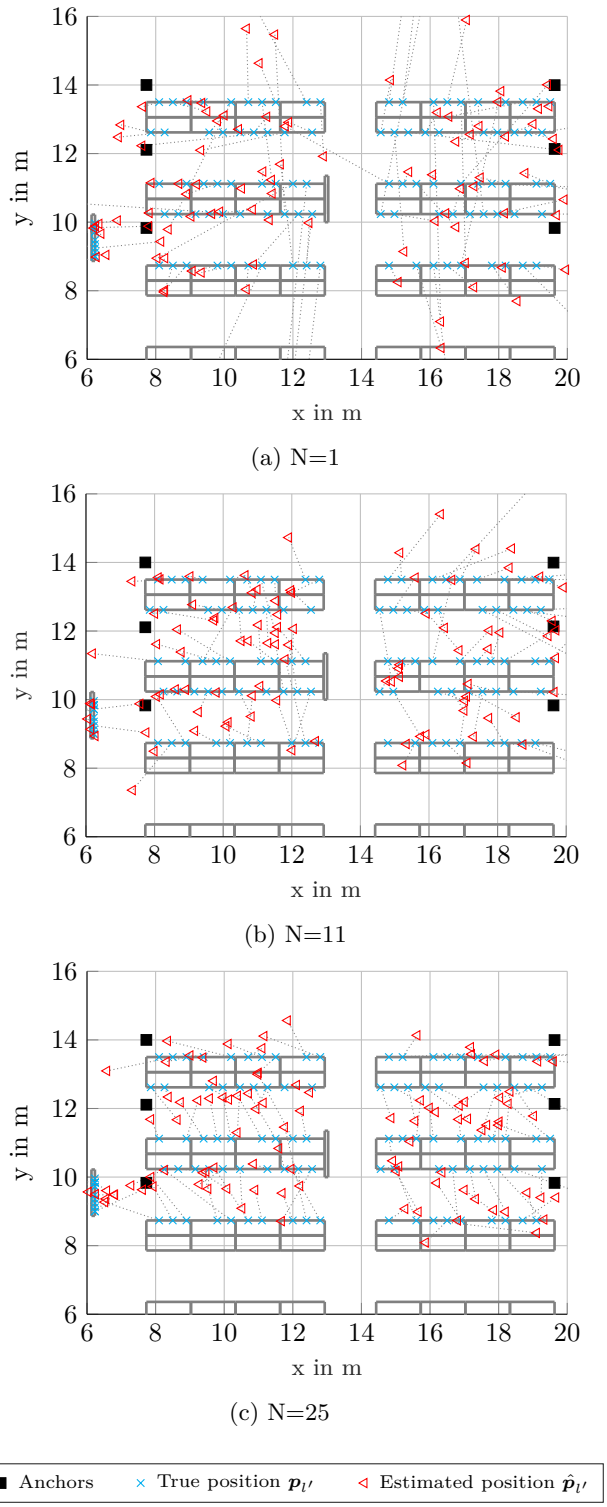

(a) N=1

(b) N=11

(c) N=25

Figure B.7: Scenario 6.4: Floorplans with results for synthetic scenario with RSS-based clusters (showing only every 10-th processed node for better visibility)

(a) Red ellipse marking one agent node

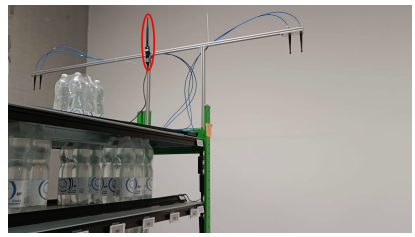

(b) Red ellipse marking the access point antenna for controlling the agent nodes

(c) Red ellipse marking one linear 2-antenna array

(d) Red ellipse marking the PC for measurement processing

Figure B.8: Scenario 6.4 and 6.5: Pictures of the measurement setup and room

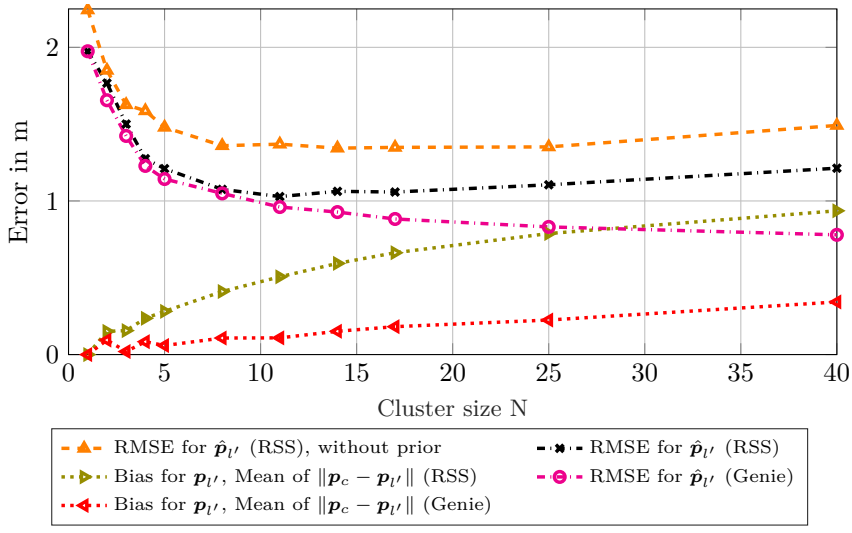

Figure B.9: Scenario 6.5: Results for measurement scenario

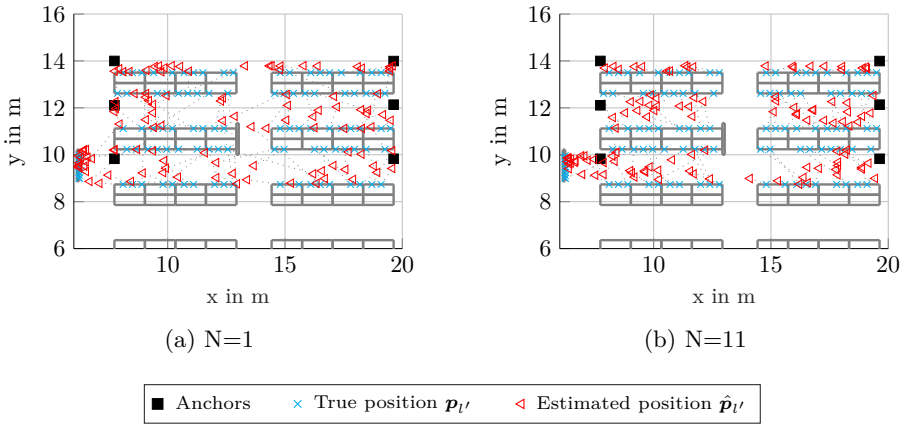

Figure B.10: Scenario 6.5: Floorplans with results from measurements with RSS-based clusters (showing only every 10-th processed node for better visibility)

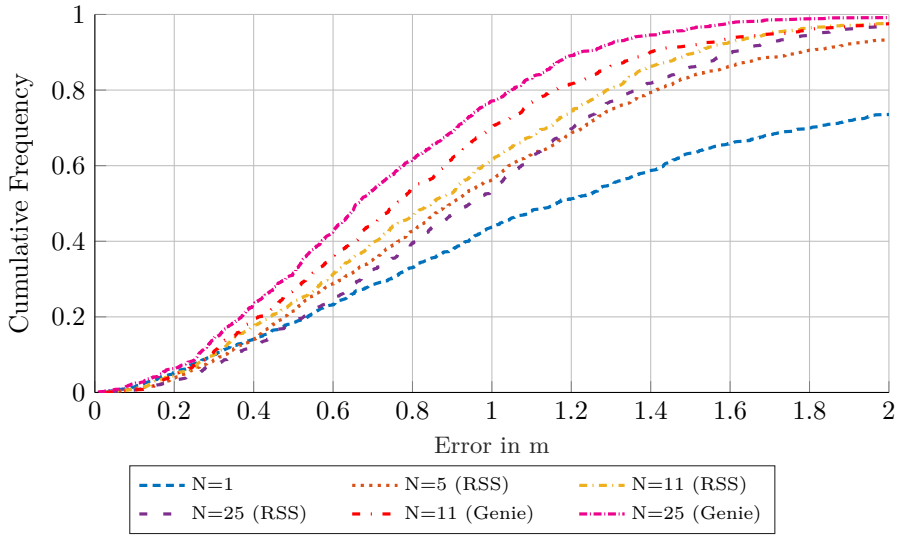

Figure B.11: Scenario 6.5: CF plot and excerpt for different cluster sizes and different cluster selection strategies, measurement data

B.7 Conclusion

This paper investigates an indoor position system that is capable of fusing WB ToF measurements and cooperative RSS measurements from a cluster of nodes located in close proximity of one another. We derive a lower bound on the position error for this setup to understand the scaling behavior and performance limits. We also formulate an approximated maximum likelihood algorithm for the setup and analyze the performance with synthetic data and real-world measurement data.

Our proposed approach demonstrates a performance gain of one node for a non-clustered approach being around 2 m to the performance of an RSS-clustered approach being around 1 m in our measurement scenario. Synthetic scenarios show that our RMSE can approach the derived biased lower bound, incorporating a correction factor that accounts for the precise scaling of delay information in case of clustering.

Also, an efficient implementation has been developed for our algorithm, based on an iterative implementation of a maximum likelihood estimator. Overall, we were able to show that the introduced approach mitigates mutual problems of both measurement methods, improving localization performance by incorporating information which can be processed jointly.

Results for the fusion of multiple measurement methods like the ones evaluated show that this is a promising field for future research, and further work should be done to incorporate other measurement methods and additional information to improve upon the principle findings of this paper. Future work for the presented method will focus on a fully Bayesian implementation supporting joint cooperative positioning based on both measurement types, directly incorporating the information content of RSS measurements into a joint algorithm.

B.8 Appendix: Derivation of EFIM

For ease of notation, indices l and m are omitted here without loss of generality, but these derivations apply for a single anchor m and node l. To derive position error bounds, we first derive a FIM for a spherical parameter vector $\boldsymbol{\psi} = [\phi, \vartheta, \tau, \mathcal{R}\alpha, \mathcal{I}\alpha]^T$ with nuissance parameter $\alpha \in \mathbb{C}$, as

$$\boldsymbol{J}_{\boldsymbol{\psi}} = \begin{bmatrix} \boldsymbol{A} & \boldsymbol{B} \\ \boldsymbol{B}^T & \boldsymbol{D} \end{bmatrix} \in \mathbb{R}^{5\times 5}. \tag{B.33}$$

The block matrices are defined similar to [16] as

$$\begin{aligned} \boldsymbol{A} &= \begin{bmatrix} J_{\phi\phi} & 0 & 0 \\ 0 & J_{\vartheta\vartheta} & 0 \\ 0 & 0 & J_{\tau\tau} \end{bmatrix} \\ \boldsymbol{B} &= \begin{bmatrix} 0 & 0 \\ 0 & 0 \\ J_{\tau\mathcal{R}\alpha} & J_{\tau\mathcal{I}\alpha} \end{bmatrix} \\ \boldsymbol{D} &= \begin{bmatrix} J_{\mathcal{R}\alpha\mathcal{R}\alpha} & 0 \\ 0 & J_{\mathcal{I}\alpha\mathcal{I}\alpha} \end{bmatrix}. \end{aligned} \tag{B.34}$$

The FIs between the parameters in the according subscript are denoted as $J_{\phi\phi}$, $J_{\vartheta\vartheta}$,$J_{\tau\tau}$, $J_{\tau\mathcal{R}\alpha}$, $J_{\tau\mathcal{I}\alpha}$, $J_{\mathcal{R}\alpha\mathcal{R}\alpha}$, $J_{\mathcal{I}\alpha\mathcal{I}\alpha}$. Note that the transmit time ϵ_l is also omitted, as for TDoA-positioning an unknown transmit time has negligible influence [39], given an appropriate geometry of anchor nodes. To gain further insight, we use the EFIM $[\boldsymbol{J}_{\boldsymbol{\psi}'}]_{3x3}^{-1}$ for the parameter vector $\boldsymbol{\psi}' = [\phi, \vartheta, \tau]^T$ by using the Schur complement on (B.33)

$$[\boldsymbol{J}_{\boldsymbol{\psi}'}{}^{-1}]_{3\times3} = (\boldsymbol{A} - \boldsymbol{B}\boldsymbol{D}^{-1}\boldsymbol{B}^T)^{-1} = \begin{bmatrix} J_\phi & 0 & 0 \\ 0 & J_\vartheta & 0 \\ 0 & 0 & J_\tau \end{bmatrix}^{-1}, \tag{B.35}$$

where J_ϕ, J_ϑ, and J_τ are the respective FI terms for the parameters. Due to the structure of the block matrices $\boldsymbol{A}$, $\boldsymbol{B}$ and $\boldsymbol{D}$, the EFIM $[\boldsymbol{J}_{\boldsymbol{\psi}'}^{-1}]_{3\times3}$ is a diagonal matrix, illustrating that range and angle information components are independent. To derive a CRLB for positioning, a transformation of the EFIM from the spherical parameter vector to a cartesian parameter vector $\boldsymbol{p} = [x, y, z]^T$ is necessary. For this, the corresponding FIM for the parameter vector $\boldsymbol{p}$ can be computed by

$$\boldsymbol{J}_{\boldsymbol{p}} = \boldsymbol{T}\boldsymbol{J}_{\boldsymbol{\psi}'}\boldsymbol{T}^T, \tag{B.36}$$

with $\boldsymbol{T}$ being the Jacobian matrix for transformation of spherical to cartesian coordinates incorporating partial derivatives of $\boldsymbol{p}$ with respect to $\boldsymbol{\psi}'$

$$\boldsymbol{T} = \frac{\partial \boldsymbol{p}^T}{\partial \boldsymbol{\psi}'} = \begin{bmatrix} \frac{\partial x}{\partial \phi} & \frac{\partial x}{\partial \vartheta} & \frac{\partial x}{\partial \tau} \\ \frac{\partial y}{\partial \phi} & \frac{\partial y}{\partial \vartheta} & \frac{\partial y}{\partial \tau} \\ \frac{\partial z}{\partial \phi} & \frac{\partial z}{\partial \vartheta} & \frac{\partial z}{\partial \tau} \end{bmatrix} = \begin{bmatrix} -\frac{\sin\phi\sin\vartheta}{\tau c} & \frac{\cos\phi\cos\vartheta}{\tau c} & \frac{\sin\phi\cos\vartheta_{l,m}}{c} \\ \frac{\sin\phi\cos\vartheta}{\tau c} & \frac{\cos\phi\sin\vartheta}{\tau c} & \frac{\sin\phi\sin\vartheta}{c} \\ 0 & -\frac{\sin\phi}{\tau c} & \frac{\cos\phi}{c} \end{bmatrix} \in \mathbb{R}^{3\times3}, \tag{B.37}$$

where c denotes the speed of light.

B.9 Appendix: Derivation of the ranging error bound (REB) and correction Factor Λ

B.9.1 Ranging Error Bound

The REB is derived from the likelihood function (B.7). To account for the DMC, an signal-to-interference-plus-noise-ratio (SINR) is introduced, which quantifies the reduction of the SNR due to the interfering DM [16, 39]. With this, we can define the EFI (which is the equivalent information neglecting nuisance parameters) for the delay $\tau_{l,m}$ for a single node as [16, 39]

$$J_{\tau_{l,m}} = 8\pi^2\beta^2\widetilde{\mathrm{SINR}}_{\tau_m}K, \tag{B.38}$$

where β^2 is the mean-squared bandwidth [40], which is defined as $\beta^2 = \|\dot{\mathbf{s}}\|^2/\left(4\pi^2\|\mathbf{s}\|^2\right) = \int_f f^2|S(f)|^2df$ for the normalized pulse $\|\mathbf{s}\|^2T_s = 1$, $\dot{\mathbf{s}}$ being the derivative of the sampled pulse with respect to the delay τ, and f is the frequency in the Fourier-domain, $[\widetilde{\mathrm{SINR}}_\tau]_m$ is the SINR for anchor m, and K is the number of antennas at anchor m. Additional parameters and further definitions are described in previous work (see Appendix A in [16] or [12]). With this, the

contribution of delay measurements to the FIM for measurements in-between multiple anchors and all nodes of a cluster can be written as

$$\boldsymbol{J}_{\boldsymbol{p}_c}^{(\tau)} = \sum_{m=1}^{M} \sum_{l \in \mathcal{L}} \Lambda \frac{8\pi^2}{c^2} \beta^2 [\widetilde{\mathrm{SINR}}_\tau]_m \; K \; \boldsymbol{R}_r(\phi_{l,m}, \vartheta_{l,m}), \tag{B.39}$$

where $\boldsymbol{R}_r(\phi_{l,m}, \vartheta_{l,m})$ is the previously mentioned RDM and Λ is the correction factor discussed in the following subsection. As argued in Section B.5, an upper bound on this component is used in (B.25).

B.9.2 Correction factor Λ

As the delays $\tau_m(\boldsymbol{p}_l)$ of each node in the cluster are in the vicinity of the delay $\tau_m(\boldsymbol{p}_c)$, we can assume that $\tau_m(\boldsymbol{p}_l) \approx \tau_m(\boldsymbol{p}_c)$ $\forall l \in \mathcal{L}$. Still, small offsets remain. To address this, we introduce an equivalent log-likelihood of Equation (B.12) as

$$\ln f(\boldsymbol{r} \mid \tau_m(\boldsymbol{p}_c), \boldsymbol{\epsilon}, \boldsymbol{\eta}, \boldsymbol{\alpha}) = \ln f(\boldsymbol{r}_c \mid \tau_m(\boldsymbol{p}_c), \boldsymbol{\alpha}), \tag{B.40}$$

with the assumption of parameters $\boldsymbol{\epsilon}$ being estimated correctly and omitting parameters $\boldsymbol{\eta}$ of the DMC. The vector $\boldsymbol{r}_c$ is a summed and weighted receive signal defined as

$$\boldsymbol{r}_c = \sum_{l \in \mathcal{L}} c_l^* \boldsymbol{r}_l, \tag{B.41}$$

with c_l^* being complex conjugate weights that are introduced to maximize the SNR for $\boldsymbol{r}_c$. The vector $\boldsymbol{r}_l$ is the received signal from Equation (B.3), omitting indices m and k for the sake of easier notation. We now define a summed and weighted received signal without noise as

$$\boldsymbol{r}_c^{(s)} = \sum_{l \in \mathcal{L}} c_l^* \boldsymbol{s}(\tau(\boldsymbol{p}_l)) \alpha_{l,m} \approx \boldsymbol{s}(\tau(\boldsymbol{p}_l)) \boldsymbol{c}^H \boldsymbol{\alpha}, \tag{B.42}$$

with $\boldsymbol{c} = [c_l]^T$ $\forall l \in \mathcal{L}$ being a stacked version of all weights within a cluster, where we assume the delays to be approximately equal for all $l \in \mathcal{L}$. Furthermore, we introduce a weighted noise vector $\boldsymbol{r}_c^{(n)} = \sum_{l \in \mathcal{L}} c_l^* \boldsymbol{w}_w$, again omitting indices m, k for easier notation. From this, we can define an SNR of this mean weighted signal as

$$\mathrm{SNR}_c = \frac{\|\boldsymbol{r}_c^{(s)}\|^2}{\mathbb{E}\{\|\boldsymbol{r}_c^{(n)}\|^2\}} \approx \frac{\|\boldsymbol{s}(\tau_{l,m})\|^2 \; |\boldsymbol{c}^H \boldsymbol{\alpha}|^2}{N_s \; \sigma_n^2 \; \|\boldsymbol{c}\|^2}. \tag{B.43}$$

Maximizing this SNR, we get

$$\mathrm{SNR}_c^{\max} \approx \frac{\|\boldsymbol{s}(\tau(\boldsymbol{p}_c)\|^2 \; \|\boldsymbol{\alpha}\|^2}{N_s \; \sigma_{l,m,k}^2}, \tag{B.44}$$

which maximizes the inner product $\boldsymbol{c}^H \boldsymbol{\alpha}$ by setting the weights $\boldsymbol{c} = \boldsymbol{\alpha}$. With this, we can see that the previous log-likelihood in (B.40) is proportional to

$$\ln f(\boldsymbol{r}_c \mid \tau_l(\boldsymbol{p}_c), \boldsymbol{\alpha}) \propto \|\boldsymbol{r}_c - \sum_{l \in \mathcal{L}} \|\boldsymbol{\alpha}_l\|^2 \boldsymbol{s}(\tau_{l,m})\|^2. \tag{B.45}$$

We can then express $\sum_{l\in\mathcal{L}} \|\boldsymbol{\alpha}_l\|^2 \boldsymbol{s}(\tau_{l,m}) = \mathbf{s}_c$, which is a weighted summed baseband signal with delays $\tau_m(\boldsymbol{p}_c)$. We introduce the Fourier transform of the delayed signal vector $\boldsymbol{s}(\tau_l)$ as $S(\tau_l, f) = S(f)e^{-j2\pi f\tau_l}$. With this, we can write the squared sum of time derivative of $\boldsymbol{s}_c$ as

$$\begin{aligned}\|\dot{\mathbf{s}}_c\|^2 &= \int_f \left|\sum_{l\in\mathcal{L}} \|\alpha_l\|^2 S(f)e^{-j2\pi f\tau_l}\right|^2 f^2 df \\ &= \int_f |S(f)|^2 \left|\sum_{l\in\mathcal{L}} \|\alpha_l\|^2 e^{-j2\pi f\tau_l}\right|^2 f^2 df \\ &= \int_f |S(f)|^2 |\Lambda(f)|^2 f^2 df\end{aligned} \tag{B.46}$$

where $\Lambda(f)$ has a low-pass characteristic, reducing the effective bandwidth of $S(f)$. We denote the effective reduction of bandwidth by the factor Λ as

$$\|\dot{\mathbf{s}}_c\|^2 = \Lambda\|\dot{\mathbf{s}}\|^2 = \Lambda\beta^2. \tag{B.47}$$

This correction factor Λ for the CRLB describing the relative bandwidth loss in a cluster with $\Lambda \in [0, 1]$, which corresponds to the factor Λ in Equation (B.25). This factor can also be interpreted as a mean information loss in a cluster due to mutual information within the clusters. Here β^2 is the mean squared bandwidth of the signal, defined in Appendix B.10.

B.10 Appendix: Derivation the AEB

The angulation error bound (AEB) for a general angle ϕ representing either azimuth or elevation, the EFI for the case incorporating DM is approximated by [16]

$$J_{AEB}(\phi) \approx 8\pi^2 \text{SINR}\ M\ D_\lambda^2(\phi), \tag{B.48}$$

where $D_\lambda^2(\phi)$ is the normalized squared array aperture, which is defined as

$$D_\lambda^2(\phi) = \frac{1}{M}\sum_{m=1}^{M} \frac{d_m^2}{\lambda^2}\sin^2(\phi - \phi_m), \tag{B.49}$$

with ϕ_m being the angle of array elements relative to the coordinate system per anchor, and d_m is the distance of array elements to the anchor position. With this, we can define the AEB for azimuth $\phi_{l,m}$ and elevation $\vartheta_{l,m}$ as $A_{\phi_{l,m}} = \sqrt{J^{-1}_{\phi_{l,m}}}$ and $A_{\vartheta_{l,m}} = \sqrt{J^{-1}_{\vartheta_{l,m}}}$. For the case of clustering, these bounds can then be found to be

$$A_{\phi_m} = \sqrt{[J_{\phi_m}]^{-1}} = \sqrt{[\sum_{l\in\mathcal{L}} J_{\phi_{l,m}}]^{-1}} \tag{B.50}$$

$$A_{\vartheta_m} = \sqrt{[J_{\vartheta_m}]^{-1}} = \sqrt{[\sum_{l\in\mathcal{L}} J_{\vartheta_{l,m}}]^{-1}}, \tag{B.51}$$

where J_{ϕ_m} and J_{ϑ_m} are the clustered EFIMs for azimuth and elevation respectively. Note that here no correction factor is required, as the equivalent aperture reduction is negligible in the case of the AEB due to $f_c^2 \gg (\Lambda\beta^2)$ [16]. Also, over a whole scenario, it can be assumed that $\mathbb{E}_l[\phi_{l,m}] \approx 0$ and $\mathbb{E}_l[\vartheta_{l,m}] \approx 0$, thus the dependency on different positions can be assumed to be negligible for the AEB. From this, we can define an EFI for a multi-anchor clustered case for azimuth and elevation as

$$\boldsymbol{J}_{\boldsymbol{p}_c}^{(\phi)} \approx \sum_{m=1}^{M} \sum_{l \in \mathcal{L}} \frac{8\pi^2}{d_{l,m}^2} D_\lambda^2(\phi_{l,m}) \mathrm{SINR}_m \; K \; \boldsymbol{R}_r(\phi_{l,m} + \frac{\pi}{2}, \vartheta_{l,m}), \tag{B.52}$$

$$\boldsymbol{J}_{\boldsymbol{p}_c}^{(\vartheta)} \approx \sum_{m=1}^{M} \sum_{l \in \mathcal{L}} \frac{8\pi^2}{d_{l,m}^2} D_\lambda^2(\vartheta_{l,m}) \mathrm{SINR}_m \; K \; \boldsymbol{R}_r(\phi_{l,m}, \vartheta_{l,m} + \frac{\pi}{2}), \tag{B.53}$$

with the previously mentioned RDM and an SINR per anchor as SINR_m.

Bibliography

[1] D. Neunteufel, S. Grebien, and H. Arthaber, "Indoor positioning of low-cost narrowband iot nodes: Evaluation of a tdoa approach in a retail environment," *Sensors*, 2022, doi: 10.3390/s22072663.

[2] S. Sadowski and P. Spachos, "Rssi-based indoor localization with the internet of things," *IEEE Access*, 2018, doi: 10.1109/ACCESS.2018.2843325.

[3] A. Yassin, Y. Nasser, M. Awad, A. Al-Dubai, R. Liu, C. Yuen, R. Raulefs, and E. Aboutanios, "Recent advances in indoor localization: A survey on theoretical approaches and applications," *IEEE Communications Surveys and Tutorials*, 2017, doi: 10.1109/COMST.2016.2632427.

[4] D. Neunteufel, A. Fuchs, and H. Arthaber, "ToF-based indoor positioning for low-power IoT nodes," in *2020 54th Asilomar Conference on Signals, Systems, and Computers*, Nov 2020, doi: 10.1109/IEEECONF51394.2020.9443431.

[5] J. A. del Peral-Rosado, R. Raulefs, J. A. López-Salcedo, and G. Seco-Granados, "Survey of cellular mobile radio localization methods: From 1G to 5G," *IEEE Communications Surveys Tutorials*, Secondquarter 2018, doi: 10.1109/COMST.2017.2785181.

[6] P. Zand, J. Romme, J. Govers, F. Pasveer, and G. Dolmans, "A high-accuracy phase-based ranging solution with bluetooth low energy (ble)," in *2019 IEEE Wireless Communications and Networking Conference (WCNC)*, 2019, doi: 10.1109/WCNC.2019.8885791.

[7] A. Comuniello, A. Angelis, A. Moschitta, and P. Carbone, "Using bluetooth low energy technology to perform ToF-based positioning," *Electronics*, 12 2021, doi: 10.3390/electronics11010111.

[8] M. Kotaru, K. Joshi, D. Bharadia, and S. Katti, "Spotfi: Decimeter level localization using wifi," in *Proceedings of the 2015 ACM Conference on Special Interest Group on Data Communication*, 2015, doi: 10.1145/2785956.2787487.

[9] L. Wielandner, E. Leitinger, and K. Witrisal, "Rss-based cooperative localization and orientation estimation exploiting antenna directivity," *IEEE Access*, 2021, doi: 10.1109/ACCESS.2021.3070441.

[10] I. Oppermann, M. Hämäläinen, and J. Iinatti, *UWB: Theory and Applications*. NJ,USA: John Wiley and Sons: Hoboken, 2005.

[11] D. Dardari, A. Conti, U. Ferner, A. Giorgetti, and M. Z. Win, "Ranging with ultrawide bandwidth signals in multipath environments," *Proceedings of the IEEE*, Feb 2009, doi: 10.1109/JPROC.2008.2008846.

[12] K. Witrisal, E. Leitinger, S. Hinteregger, and P. Meissner, "Bandwidth scaling and diversity gain for ranging and positioning in dense multipath channels," *IEEE Wireless Communications Letters*, vol. 5, no. 4, pp. 396–399, 2016.

[13] H. Wymeersch, S. Marano, W. Gifford, and M. Win, "A machine learning approach to ranging error mitigation for uwb localization," *Communications, IEEE Transactions on*, 2012, doi: 10.1109/TCOMM.2012.042712.110035.

[14] J. Kulmer, S. Hinteregger, B. Großwindhager, M. Rath, M. S. Bakr, E. Leitinger, and K. Witrisal, "Using DecaWave UWB transceivers for high-accuracy multipath-assisted indoor positioning," in *2017 IEEE International Conference on Communications Workshops (ICC Workshops)*, May 2017, doi: 10.1109/ICCW.2017.7962828.

[15] S. Hinteregger, J. Kulmer, M. Goller, F. Galler, H. Arthaber, and K. Witrisal, "UHF-RFID backscatter channel analysis for accurate wideband ranging," in *2017 IEEE International Conference on RFID (RFID)*, May 2017, doi: 10.1109/RFID.2017.7945596.

[16] T. Wilding, S. Grebien, U. Mühlmann, and K. Witrisal, "Accuracy bounds for array-based positioning in dense multipath channels," *Sensors*, Dec 2018, doi: 10.3390/s18124249.

[17] I. Guvenc and C.-C. Chong, "A survey on toa based wireless localization and nlos mitigation techniques," *IEEE Communications Surveys and Tutorials*, 2009, doi: 10.1109/SURV.2009.090308.

[18] Y. Qi, H. Kobayashi, and H. Suda, "On time-of-arrival positioning in a multipath environment," *IEEE Transactions on Vehicular Technology*, 2006, doi: 10.1109/TVT.2006.878566.

[19] D. B. Jourdan, D. Dardari, and M. Z. Win, "Position error bound for uwb localization in dense cluttered environments," *IEEE Transactions on Aerospace and Electronic Systems*, 2008, doi: 10.1109/TAES.2008.4560210.

[20] B. Sadler and R. Kozick, "A survey of time delay estimation performance bounds," in *Fourth IEEE Workshop on Sensor Array and Multichannel Processing, 2006.*, 2006, doi: 10.1109/SAM.2006.1706138.

[21] S. Tomic, M. Beko, R. Dinis, and L. Bernardo, "On target localization using combined rss and aoa measurements," *Sensors*, 2018, doi: 10.3390/s18041266.

[22] G. Kia, L. Ruotsalainen, and J. Talvitie, "Toward accurate indoor positioning: An rss-based fusion of uwb and machine-learning-enhanced wifi," *Sensors*, 2022, doi: 10.3390/s22093204.

[23] M. A. Landolsi and R. Shubair, "Toai/aoa/rss maximum likelihood data fusion for efficient localization in wireless networks," in *2018 15th International Multi-Conference on Systems, Signals and Devices (SSD)*, 2018, doi: 10.1109/SSD.2018.8570432.

[24] G. Kia, j. talvitie, and L. Ruotsalainen, "Rss-based fusion of uwb and wifi-based ranging for indoor positioning," in *CEUR Workshop Proceedings , vol. 3097*, 11 2021.

[25] H. T. Gidey, X. Guo, K. Zhong, L. Li, and Y. Zhang, "Data fusion methods for indoor positioning systems based on channel state information fingerprinting," *Sensors*, 2022, doi: 10.3390/s22228720.

[26] A. S. Yaro, F. Maly, and P. Prazak, "A survey of the performance-limiting factors of a 2-dimensional rss fingerprinting-based indoor wireless localization system," *Sensors*, 2023, doi: 10.3390/s23052545.

[27] J. Bi, M. Zhao, G. Yao, H. Cao, Y. Feng, H. Jiang, and D. Chai, "Psosvrpos: Wifi indoor positioning using svr optimized by pso," *Expert Systems with Applications*, 2023, doi: https://doi.org/10.1016/j.eswa.2023.119778.

[28] S. R. Jondhale, V. Mohan, B. B. Sharma, J. Lloret, and S. V. Athawale, "Support vector regression for mobile target localization in indoor environments," *Sensors*, 2022, doi: 10.3390/s22010358.

[29] J. Karedal, S. Wyne, P. Almers, F. Tufvesson, and A. F. Molisch, "A measurement-based statistical model for industrial ultra-wideband channels," *IEEE Transactions on Wireless Communications*, vol. 6, no. 8, pp. 3028–3037, 2007.

[30] S. M. Kay, *Fundamentals of Statistical Signal Processing: Estimation Theory.* USA: Prentice-Hall, Inc., 1993.

[31] Z. Abu-Shaban, X. Zhou, T. Abhayapala, G. Seco-Granados, and H. Wymeersch, "Error bounds for uplink and downlink 3d localization in 5g millimeter wave systems," *IEEE Transactions on Wireless Communications*, 2018, doi: 10.1109/TWC.2018.2832134.

[32] E. Platen, "Poor, h. v., an introduction to signal detection and estimation. new york etc., springer-verlag 1988. x, 549 pp., 47 figs., dm 118,-. isbn 3–540-96667-6 (springer texts in electrical engineering)," *ZAMM - Journal of Applied Mathematics and Mechanics / Zeitschrift für Angewandte Mathematik und Mechanik*, 1989, doi: https://doi.org/10.1002/zamm.19890691219.

[33] Y. Shen and M. Z. Win, "Fundamental limits of wideband localization— part i: A general framework," *IEEE Transactions on Information Theory*, 2010, doi: 10.1109/TIT.2010.2060110.

[34] M. Arulampalam, S. Maskell, N. Gordon, and T. Clapp, "A tutorial on particle filters for online nonlinear/non-gaussian bayesian tracking," *IEEE Transactions on Signal Processing*, 2002, doi: 10.1109/78.978374.

[35] G. Steinböck, T. Pedersen, B. H. Fleury, W. Wang, and R. Raulefs, "Distance dependent model for the delay power spectrum of in-room radio channels," *IEEE Transactions on Antennas and Propagation*, 2013, doi: 10.1109/TAP.2013.2260513.

[36] A. Fuchs and K. Witrisal, "Time-of-arrival estimation for positioning in bandwidth-limited dense multipath channels," in *2022 IEEE 23rd International Workshop on Signal Processing Advances in Wireless Communication (SPAWC)*, 2022, doi: 10.1109/SPAWC51304.2022.9833995.

[37] F. Lampel, "RSS-Based Localization of Smart Labels," Master's thesis, Graz University of Technology, Austria, 2018.

[38] D. Neunteufel, S. Grebien, S. Hechenberger, K. Witrisal, and H. Arthaber, "Coherent chirp generation by narrowband transceiver chips for tof indoor localization," in *GLOBECOM 2020 - 2020 IEEE Global Communications Conference*, 2020, doi: 10.1109/GLOBECOM42002.2020.9348025.

[39] D. Neunteufel, S. Grebien, and H. Arthaber, "Bayesian CRLB for blind indoor localization with imperfect receiver synchronization," in *2021 55th Asilomar Conference on Signals, Systems, and Computers*, Oct 2021, doi: 10.1109/IEEECONF53345.2021.9723254.

[40] R. A. Scholtz, "How do you define Bandwidth?" *International Telemetering Conference Proceedings*, 1972. [Online]. Available: http://hdl.handle.net/10150/605545

C

Wideband Cooperative Localization through Generalized Cross-Correlation

Andreas Fuchs, Lukas Wielandner, Klaus Witrisal

IEEE Access 2024 doi:10.1109/ACCESS.2024.3518073

Abstract—This work proposes a novel algorithm for robust cooperative localization using wideband time-difference-of-arrival (TDoA) measurements and information coupling between nodes. The algorithm leverages a generalized cross-correlation framework to exploit the similarity of wideband measurements within the geometric vicinity of nodes. Alternatively, the algorithm uses a computationally efficient method based on perceptual hashing, a signal compression algorithm adapted from image-processing, which gives a distance-dependent metric between nodes. The algorithm is embedded within a message-passing framework, enabling the estimation of the joint-posterior probability density function of all the nodes. The paper evaluates the localization performance, using both simulated and real measurements in various challenging scenarios, and compares it with a cooperative localization method that uses additional received signal strength measurements in-between nodes. The results demonstrate that the proposed algorithm can achieve similar or superior localization accuracy, with the same computational complexity and without the need for additional measurements. The proposed algorithm shows significant improvement over non-cooperative measurements. It achieves an improvement of root-mean-square error from 2.4m to 1.3m for a large-scale scenario with approximately 1000 nodes, using a signal bandwidth of 80MHz for the TDoA measurements and six fixed, dual-antenna, anchor nodes.

The financial support by the Austrian Federal Ministry of Labour and Economy, the National Foundation for Research, Technology and Development and the Christian Doppler Research association is gratefully acknowledged.

C.1 Introduction

The advent of contemporary electronic devices has led to a demand for location-specific services and applications, with radio-based indoor localization playing a crucial role. These applications span a wide range of sectors, including retail, healthcare, tourism, and logistics, among others [1–9].

A necessary condition for this is a sufficiently good accuracy of localization results. Current systems focus on the estimation of nodes incorporating for example received signal strength (RSS) measurements from multiple devices to each other, wideband measurements to infrastructure like access points or base stations or measurements with higher bandwidths like ultra-wideband (UWB) [7, 10–16].

C.1.1 State of the Art

Different measurement methods each have their own strengths and weaknesses, largely due to the limitations imposed by the technology used [17,18]. For instance, measurements of RSS values are relatively straightforward to obtain. However, the amount of information that a single measurement can provide is limited, offering only minimal positional information. As a result, there is a need for a large number of independent measurements to enhance the position information to an acceptable level, which can be realized within a cooperative localization framework. Additionally, a significant number of fixed "anchor nodes" are required for position reference [19–24].

On the other hand, time-difference-of-arrival (TDoA) based localization that uses wideband measurements in the industrial, scientific, and medical (ISM) bands (e.g. 80 MHz at 2.4 GHz), can provide much more information with a single measurement, due to higher bandwidth and usage of angular information. However, this requires additional wideband anchor infrastructure, known as access points (APs), similar to [5] [13, Ch. 6]. In this scenario, the devices and APs are equipped with more complex radio chips to transmit and receive higher bandwidth signals. Performance with these signals is limited due to a high outlier probability, caused by multipath propagation. Chips that offer even higher bandwidths are becoming increasingly expensive and power-consuming, making them uneconomical for many applications.

Other methods use machine learning for localization, for example methods based on channel state information [25, 26], or support vector regression [27, 28]. Machine learning algorithms need training data to work, which is a major disadvantage for these algorithms.

Cooperative localization algorithms [19–24, 29–31] exploit inter-node measurements (also called cooperative measurements) to improve the positioning performance of all cooperating nodes. But additional measurements also mean additional energy consumption, and rely on the hardware being capable to perform such measurements.

Information coupling on the other hand, does not rely on additional measurements. It can be seen as a method to extract inter-node information by assuming that nodes in the vicinity of each other share some information within their measurements to base stations.

While information coupling for wideband signals has been used in literature

before [32–35], those studies focused solely on a very small number of nodes and positioning bounds thereof, demonstrating the need for information coupling algorithms that are able to deal with realistic scenarios and are computationally viable. Additionally, it should be pointed out that cooperative localization through information coupling, either using generalized cross-correlation (GCC) or perceptual hashing has not been applied in literature before.

C.1.2 Contribution

In this paper, we propose a novel algorithm that leverages information coupling within wideband TDoA measurements from multiple transmitting nodes. Additional inter-node information is utilized by a cooperative localization algorithm implemented with the sum-product-algorithm (SPA). It is extracted by using a GCC based likelihood function [36], exploiting similarity of amplitudes and channel statistics within a geometric vicinity of nodes.

Furthermore, we propose an efficient implementation for very large scenarios using perceptual hashing [37, 38] as a method to compress wideband signals, and introduce a distance metric describing correlation between the compressed signals. This algorithm allows for more accurate positioning performance, or, if estimation performance is already sufficient, it can be used to reduce hardware requirements, allowing for example less bandwidth or imperfect radio receivers.

The key contributions are:

- A novel approach to incorporate inter-node information in the form of information coupling between nodes, using a GCC for cooperative localization.
- A computationally efficient approximation, making use of perceptual hashing as a metric for the information coupling between nodes.
- A detailed complexity analysis comparing various methods.
- A validation of the efficacy of the proposed algorithm through both simulated and real-world measurements.

C.1.3 Concept

Figure C.1 provides an illustration of the proposed method, demonstrating the interaction between two nodes and two anchors. Wideband radio signals are asynchronously transmitted by the agent nodes and recorded by the anchors, one node at a time. These signals are directly incorporated into a direct positioning (TDoA and angle of arrival (AoA)-based) localization algorithm. In addition to that, the method utilizes inter-node information, as illustrated by the cross-correlation between signals ($\mathbf{z}_{l,i}$). This correlation measure can be substituted with other measures such as GCC, perceptual hashing or RSS measurements. Perceptual hashing, in particular, is a measure derived from a compressed representation of signals, adapted from image processing, where it is utilized to find similar images. Here this property is used to find similar/correlated signals. This is computationally much more efficient than GCC and permits much faster computation times. We define a posterior probability density function (PDF) integrating this cooperative information, which is approximated using a message-passing (MP) algorithm. It is

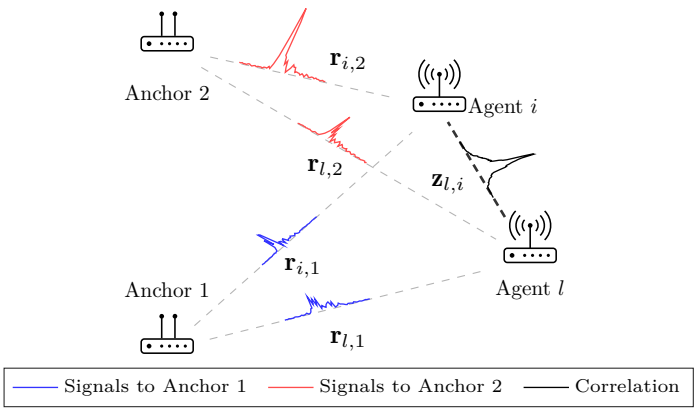

Figure C.1: Concept of wideband cooperation between two agent nodes and two anchors.

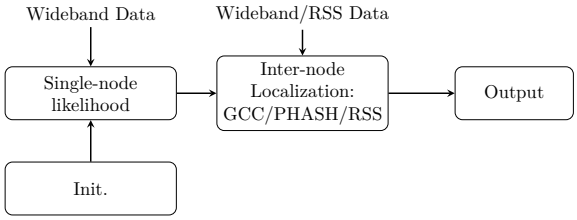

Figure C.2: Conceptual flow diagram for the proposed algorithm.

important to note that, while Figure C.1 depicts a scenario with a limited number of nodes for simplicity, this algorithm is designed to accommodate a large number of nodes, all of which can be compared with each other to evaluate the information coupling.

Figure C.2 shows a conceptual diagram of the proposed algorithm. After initialization, a single-node likelihood is calculated, using wideband data from agents to multi-antenna anchors. The resulting distribution is then fed into the cooperative localization algorithm, using either likelihood functions for GCC, perceptual hashing, or RSS. When the cooperative localization algorithm is converged, the position estimates for all nodes are saved.

Notation

Column vectors are denoted by lowercase and matrices by uppercase bold letters. The PDF of a random variable is denoted as $f(\mathbf{x})$. For any vector $\mathbf{x}$, we denote the transpose as $\mathbf{x}^T$, the Hermitian transpose as $\mathbf{x}^H$, the complex conjugate as $\mathbf{x}^*$, the vector of absolute values as $|\mathbf{x}|$, the argument as $\angle x$, the Euclidean norm as $\|\mathbf{x}\|$ and the expectation operator as $\mathbb{E}[\mathbf{x}]$. Calligraphic notation $\mathcal{L}$ denotes a set; other usages of calligraphic fonts are described at their first occurrence. The discrete Fourier transform of a vector is denoted as $F(\mathbf{x})$. $[\mathbf{X}]_{N\times N}$ is the upper left $N \times N$ subblock of a matrix. $[\mathbf{X}]_{n,m}$ denotes the n,m-th element of a matrix, and $[\mathbf{x}]_n$

denotes the n-th element of a vector. Big-O notation for complexity analysis is denoted as $O(x)$. A table of nomenclature can be found at the end of the paper in Table C.5.

C.2 Signal Models

This section defines the signal models for wideband and RSS measurements, as used in this work.

C.2.1 Wideband Signal Model

The wideband signal model is similar to [39–41]. The system configuration comprises L transmitting nodes at coordinates $\mathbf{p}_l = [p_{l,\mathrm{x}}, p_{l,\mathrm{y}}, p_{l,\mathrm{z}}]^T \in \mathbb{R}^3$ for $l \in \{1, \ldots, L\}$, and receiving antennas at positions $\mathbf{q}_{m,k} \in \mathbb{R}^3$ for $m \in \{1, \ldots, M\}$ and $k \in \{1, \ldots, K\}$. The indices k and m denote the antennas within each anchor and the anchors, respectively.

The radio channel between the transmitting node l and the receiving antenna k of anchor m is given by

$$h_{l,m,k}(t; \mathbf{p}_l) = \alpha_{l,m,k}\delta\left(t - \tau(\mathbf{p}_l, \mathbf{q}_{m,k})\right) + \nu_{l,m,k}(t), \tag{C.1}$$

with propagation delay $\tau(\mathbf{p}_l, \mathbf{q}_{m,k}) = \frac{1}{c}\left\|\mathbf{p}_l - \mathbf{q}_{m,k}\right\|$, the speed of light c, and the complex amplitude $\alpha_{l,m}$ of the received line-of-sight (LoS) signal from node l to anchor m, assuming one complex amplitude per anchor, consisting of multiple antennas. Position-dependent phase shifts between antennas are described later. The dense multipath component (DMC) $\nu_{l,m,k}(t)$ is described by a zero-mean complex Gaussian random process. Assuming uncorrelated scattering, this is modeled by the auto-correlation function

$$\begin{aligned}\mathbb{E}\left[\nu_{l,m,k}(t)\nu^*_{l',m',k'}\left(t'\right)\right] = S_\nu\left(t - \tau(\mathbf{p}_l, \mathbf{q}_m), \tilde{\boldsymbol{\eta}}_{l,m}\right)\delta\left(t - t'\right) \\ \delta\left[l - l'\right]\delta\left[m - m'\right]\delta\left[k - k'\right],\end{aligned} \tag{C.2}$$

where $\tau(\mathbf{p}_l, \mathbf{q}_m) = \frac{1}{c}\left(\left\|\mathbf{p}_l - \mathbf{q}_m\right\|\right)$ is a mean delay per anchor m, with $\mathbf{q}_m$ being the mean antenna position per anchor m. We introduce the delay power spectrum (DPS) $S_\nu(t; \tilde{\boldsymbol{\eta}})$ similar to [18, 42] as

$$S_\nu(t; \tilde{\boldsymbol{\eta}}) = \Omega_1 \frac{\gamma_f + \gamma_r}{{\gamma_f}^2} \mathrm{e}^{-t/\gamma_f}(1 - \mathrm{e}^{-t/\gamma_r})u(t), \tag{C.3}$$

where $\tilde{\boldsymbol{\eta}} = [\Omega_1, \gamma_f, \gamma_r]^T$ corresponds to the normalized power of the DMC Ω_1, the fall time γ_f, and the rise time γ_r. The step function $u(t)$ is defined as $1 \forall t \geq t$, and 0 otherwise.

Assuming each node l transmits a baseband signal $s(t)$ at frequency f_c, the received signal at anchor m and antenna k is

$$\begin{aligned}r_{l,m,k}(t) =& \tilde{\alpha}_{l,m,k} s(t - \tau(\mathbf{p}_l, \mathbf{q}_{m,k}) - \epsilon_l) \\ &+ \int s(t - \lambda)\nu_{l,m,k}(\lambda + \epsilon_l)d\lambda + w_{l,m,k}(t),\end{aligned} \tag{C.4}$$

with a complex amplitude $\tilde{\alpha}_{l,m,k} = \alpha_{l,m} \mathrm{e}^{-j2\pi f_c(\tau(\mathbf{p}_l,\mathbf{q}_{m,k})+\epsilon_l)}$ that accounts for the phase shift at antenna k with respect to the joint amplitude $\alpha_{l,m}$ at array antenna m, ϵ_l is the transmit time of node l, and $w_{l,m,k}(t)$ is additive white Gaussian noise (AWGN) with double-sided power spectral density (PSD) $N_0/2$. The sampled and stacked received signals are described as

$$\mathbf{r}_{l,m} = \mathbf{s}(\mathbf{p}_l, \mathbf{q}_m, \epsilon_l)\alpha_{l,m} + \mathbf{w}^{l,m} \in \mathbb{C}^{N_s K \times 1}, \tag{C.5}$$

where $\mathbf{r}_{l,m} = \left[\mathbf{r}_{l,m,1}^T, \ldots, \mathbf{r}_{l,m,K}^T\right]^T$ stacks the received signals of K antennas at anchor m. The noise vector $\mathbf{w}^{l,m}$ describes the DMC and AWGN. The baseband signal vector in (C.5) accounts for the phase shifts at the array antennas,

$$\begin{aligned}\mathbf{s}(\mathbf{p}_l, \mathbf{q}_m, \epsilon_l) = [&\mathrm{e}^{-j2\pi f_c(\tau(\mathbf{p}_l,\mathbf{q}_{m,1})+\epsilon_l)}\tilde{\mathbf{s}}(\tau(\mathbf{p}_l, \mathbf{q}_m) + \epsilon_l)^T, \ldots, \\ &\mathrm{e}^{-j2\pi f_c(\tau(\mathbf{p}_l,\mathbf{q}_{m,K})+\epsilon_l)}\tilde{\mathbf{s}}(\tau(\mathbf{p}_l, \mathbf{q}_m) + \epsilon_l)^T]^T\end{aligned} \tag{C.6}$$

where

$$\begin{aligned}\tilde{\mathbf{s}}(t) \in \mathbb{C}^{N_s \times 1} = [&s(-t), s(-t + T_s), \ldots, \\ &s(-t + (N_s - 1)T_s)]^T\end{aligned} \tag{C.7}$$

is a sampled version of $s(t)$ with T_s being the sampling time interval. This represents a wideband phased-array signal model with identical envelopes and phase shifts, which allow us to exploit AoA information.

The covariance matrix $\mathbf{C}^{l,m}$ characterizes the noise vector $\mathbf{w}^{l,m}$, representing AWGN and DMC. We define $\mathbf{C}^{l,m}$ as a block diagonal matrix composed of the matrices $[\mathbf{C}^{l,m}]_k$ for each antenna k of anchor m. This k-th matrix is defined as $[\mathbf{C}^{l,m}]_k = [\mathbf{C}_\nu^{l,m}]_k + [\mathbf{C}_w^{l,m}]_k \in \mathbb{C}^{N_s \times N_s}$, with $[\mathbf{C}_w^{l,m}]_k = \sigma_{l,m}^2 \mathbf{I}$, where $\mathbf{I}$ is the identity matrix of according dimensions, and noise variance $\sigma_{l,m}^2 = N_0/T_s$. The covariance for the DMC is

$$\left[\mathbf{C}_\nu^{l,m}\right]_k = \int S_\nu\left(\lambda - \tau(\mathbf{p}_l, \mathbf{q}_m) - \epsilon_l; \tilde{\boldsymbol{\eta}}_{l,m}\right) \tilde{\mathbf{s}}(\lambda)\tilde{\mathbf{s}}(\lambda)^{\mathrm{H}} d\lambda. \tag{C.8}$$

C.2.2 RSS Signal Model

The distance between two nodes l and i is denoted as $d_{l,i} = \|\mathbf{p}_l - \mathbf{p}_i\|$. Assuming the measurements adhere to a log-distance dependent model [11] [43, Sec. 9.2], the path loss $L(\mathbf{p}_l, \mathbf{p}_i, P, \rho)$ between nodes l and i is expressed as

$$L(\mathbf{p}_l, \mathbf{p}_i, P, \rho) = P - \rho\ 10 \log\left(||\mathbf{p}_l - \mathbf{p}_i||/d_0\right), \tag{C.9}$$

where P is the reference path-loss at a distance d_0, and ρ is the path-loss exponent [20]. The received RSS value $z_{l,i}^{\mathrm{RSS}}$ between nodes l and i is then given by

$$z_{l,i}^{\mathrm{RSS}} = L(\mathbf{p}_l, \mathbf{p}_i, P, \rho) + w_{l,i}, \tag{C.10}$$

with $w_{l,i}$ being the noise term, assumed to follow a Gaussian distribution $\mathcal{N} \sim (0, \sigma^2)$.

C.3 System model

In this section, we describe the posterior PDF, the single-node likelihood and the inter-node likelihoods.

C.3.1 Posterior PDF

We factorize the joint posterior PDF of all nodes l as follows:

$$f(\boldsymbol{\theta} \mid \mathbf{r}, \mathbf{z}) \propto f(\mathbf{q}) \prod_{l \in \mathcal{L}} f(\mathbf{p}_l) f(\mathbf{r}_l \mid \mathbf{p}_l, \mathbf{q}) \times \prod_{i \in \mathcal{C}_l} f(\mathbf{z}_{l,i} \mid \mathbf{p}_l, \mathbf{p}_i). \tag{C.11}$$

The stacked measurement vector is denoted by $\mathbf{r} = [\mathbf{r}_1^T, \ldots, \mathbf{r}_L^T]^T$, with $\mathbf{r}_l = \left[\mathbf{r}_{l,1}^T, \ldots, \mathbf{r}_{l,M}^T\right]^T$, $\mathbf{z}$ stacks $\mathbf{z}_{l,i} \forall l, i$ and represents cooperative measurement data, $\boldsymbol{\theta} = [\mathbf{p}_1^T, \ldots, \mathbf{p}_L^T]^T$ is a stacked vector of all position parameters of according length, and $\mathbf{q} = [\mathbf{q}_1^T, \ldots \mathbf{q}_M^T]^T$ represents a stacked vector of all anchor positions. We define the full set of nodes by $\mathcal{L} = \{1, \ldots, L\}$ and subsets $\mathcal{C}_l \subseteq \mathcal{L}$, which define the nodes for which cooperative measurements are incorporated with regard to node l. The term cooperative measurements refers to the interchangeable measurements $\mathbf{z}_{l,i}$, and is also used for measures like GCC and perceptual hashing, which are not measured directly, but rather computed from the measurements $\mathbf{r}_l$ and $\mathbf{r}_i$ as described below. The geometric prior $f(\mathbf{p}_l)$ restricts the evaluation of nodes to plausible positions within a room, $f(\mathbf{q})$ defines the anchor positions. The third term in the equation corresponds to the single-node likelihood described in Section C.3.2. The fourth term represents a cooperative likelihood. It is interchangeable, and we will present three different variants in Section C.3.3. It should be noted that we assume the single-node likelihood to be independent of the cooperative likelihoods. This is not entirely true, as we use the same sets of measurements for the single-node likelihood, and GCC and perceptual hashing respectively. For practical reasons, these dependencies are neglected, but could be taken into account in future work.

C.3.2 Single-node likelihood

Assuming the signal model in Section C.2.1, the likelihood function for a single node is given as

$$f(\mathbf{r}_l \mid \mathbf{p}_l, \mathbf{q}, \epsilon_l, \boldsymbol{\eta}_l, \boldsymbol{\alpha}_l) = \prod_{m=1}^{M} f(\mathbf{r}_{l,m} \mid \mathbf{p}_l, \mathbf{q}_m, \epsilon_l, \boldsymbol{\eta}_{l,m}, \alpha_{l,m}), \tag{C.12}$$

which assumes independence of the DMC and AWGN between anchors, where the single-node, multi-antenna likelihood function is given as

$$f(\mathbf{r}_{l,m} \mid \mathbf{p}_l, \mathbf{q}_m, \epsilon_l, \boldsymbol{\eta}_{l,m}, \alpha_{l,m}) = \frac{\mathrm{e}^{-(\mathbf{r}_{l,m} - \mathbf{s}(\mathbf{p}_l, \mathbf{q}_m, \epsilon_l)\alpha_{l,m})^{\mathrm{H}} (\mathbf{C}^{l,m})^{-1} (\mathbf{r}_{l,m} - \mathbf{s}(\mathbf{p}_l, \mathbf{q}_m, \epsilon_l)\alpha_{l,m})}}{\pi^{N_s K} \det(\mathbf{C}^{l,m})}, \tag{C.13}$$

with parameter vector $\boldsymbol{\eta}_{l,m} = \left[\sigma^2_{l,m},\ \tilde{\boldsymbol{\eta}}^T_{l,m}\right]^T$. Assuming the transmit time ϵ_l is independent, the likelihood factorizes into

$$f(\mathbf{r}_l, \epsilon_l \mid \mathbf{p}_l, \mathbf{q}, \boldsymbol{\eta}_l, \boldsymbol{\alpha}_l) = f(\epsilon_l) f(\mathbf{r}_l \mid \mathbf{p}_l, \mathbf{q}, \epsilon_l, \boldsymbol{\eta}_l, \boldsymbol{\alpha}_l), \tag{C.14}$$

where $f(\epsilon_l)$ is the prior for the parameter ϵ_l. Given ϵ_l as a nuisance parameter, we define the marginal as

$$f(\mathbf{r}_l \mid \mathbf{p}_l, \mathbf{q}, \boldsymbol{\eta}_l, \boldsymbol{\alpha}_l) = \int f(\mathbf{r}_l, \epsilon_l \mid \mathbf{p}_l, \mathbf{q}, \boldsymbol{\eta}_l, \boldsymbol{\alpha}_l)\ d\epsilon_l, \tag{C.15}$$

representing the single-node likelihood, removing the nuisance parameter ϵ_l and thus exploiting TDoA information inbetween anchors. [1] Here, $\boldsymbol{\alpha}_l = [\alpha_{l,1}, \ldots, \alpha_{l,M}]^T$, and $\boldsymbol{\eta}_l = \left[{\boldsymbol{\eta}_{l,1}}^T, \ldots, {\boldsymbol{\eta}_{l,M}}^T\right]^T$ are LoS amplitudes, and noise parameters respectively.

For computational efficiency we neglect the influence of the DMC within the estimation (but not for simulations and channel modeling), assuming that the covariance matrix $\mathbf{C}^{l,m}$ is diagonal. This corresponds to an estimation of the strongest component only, resulting in a simplified likelihood

$$f(\mathbf{r}_l \mid \mathbf{p}_l, \mathbf{q}, \boldsymbol{\sigma}^2_l, \boldsymbol{\alpha}_l) = \int f(\mathbf{r}_l, \epsilon_l \mid \mathbf{p}_l, \mathbf{q}, \boldsymbol{\sigma}^2_l, \boldsymbol{\alpha}_l)\ d\epsilon_l, \tag{C.16}$$

with the stacked noise variances $\boldsymbol{\sigma}^2_l = [{\sigma^2_{l,1}}^T, \ldots, {\sigma^2_{l,M}}^T]^T$. This can be simplified further, by incorporating the least-squares solutions for $\boldsymbol{\sigma}^2_l$ and $\boldsymbol{\alpha}_l$ as described in [44], resulting in

$$f(\mathbf{r}_l \mid \mathbf{p}_l, \mathbf{q}) = \int f(\mathbf{r}_l, \epsilon_l \mid \mathbf{p}_l, \mathbf{q})\ d\epsilon_l. \tag{C.17}$$

C.3.3 Likelihoods for inter-node coupling

Here we define the likelihoods for the inter-node coupling, meaning likelihoods between arbitrary nodes l and i within the full set of nodes $\mathcal{L}$. Note that the words "cooperative" or "cooperating" are used for inter-node information coupling from here on, as their usage within algorithms is very similar to cooperative measurements.

GCC-PHAT

The first inter-node likelihood is defined by a GCC between two signals $\mathbf{r}_l$ and $\mathbf{r}_i$ with the phase transform (PHAT) assumption [36]. This inter-node likelihood does not rely on separate measurements, but on information coupling. We introduce a Fourier-transformed version of $\mathbf{r}_{l,m,k}$ as $\mathbf{R}_{l,m,k} = F(\mathbf{r}_{l,m,k})$ which is the frequency response of the signal. With this, we define a time-shifted version as

$$[\tilde{\mathbf{R}}_{l,m,k}]_n = e^{-j\omega_n \tau_l} [\mathbf{R}_{l,m,k}]_n \tag{C.18}$$

[1] For two anchors in 2D, this function describes the well-known hyperbola of possible node locations with TDoA.

where the frequencies of the baseband signal are $\omega_n = (2\pi\frac{n}{N} - \pi)B$, with B denoting the baseband bandwidth of the signal, a delay $\tau_l = \tau(\mathbf{p}_l, \mathbf{q}_m) + \epsilon_l$ and $n = [0, \ldots, N_s - 1]^T$ being a sample index. We can then define a cross power spectral density for the PHAT between nodes l and i as

$$[_{l,i,m,k}]_n = \frac{[\tilde{\mathbf{R}}_{i,m,k}]_n [\tilde{\mathbf{R}}_{l,m,k}]_n^*}{|[\tilde{\mathbf{R}}_{l,m,k}]_n [\tilde{\mathbf{R}}_{i,m,k}]_n^*|}, \tag{C.19}$$

which relates to the differences of the arguments of the frequency responses $[\tilde{\mathbf{R}}_{l,m,k}]_n$ and $[\tilde{\mathbf{R}}_{i,m,k}]_n$. The log-likelihood for GCC with the PHAT assumption can then be expressed as

$$\log f(\mathbf{z}_{l,i}^{\mathrm{GCC}} \mid \mathbf{p}_l, \mathbf{p}_i, \epsilon_l, \epsilon_i) \propto -\frac{1}{N_s} \sum_{k=1}^{K} \sum_{m=1}^{M} \sum_{n=0}^{N_s-1} [_{l,i,m,k}]_n, \tag{C.20}$$

which is based on the assumption that the noise is uncorrelated between antennas. This has been shown to be a log-likelihood function by [36,45]. Its behaviour is illustrated below. The measurement vector for the GCC is defined as $\mathbf{z}_{l,i}^{\mathrm{GCC}} = [\mathbf{r}_l^T, \mathbf{r}_i^T]^T$. Similar to (C.14), we assume that the transmit times ϵ_l and ϵ_i are independent. As seen in the single-node likelihood, we marginalize over the parameters ϵ_l and ϵ_i, and define the marginal for GCC as

$$\begin{aligned} f(\mathbf{z}_{l,i}^{\mathrm{GCC}} \mid \mathbf{p}_l, \mathbf{p}_i) = \\ \int\int f(\epsilon_l) f(\epsilon_i) f(\mathbf{z}_{l,i}^{\mathrm{GCC}} \mid \mathbf{p}_l, \mathbf{p}_i, \epsilon_l, \epsilon_i) d\epsilon_i d\epsilon_l, \end{aligned} \tag{C.21}$$

where $f(\epsilon_l)$ and $f(\epsilon_i)$ are the priors for the parameters ϵ_l and ϵ_i respectively. The PHAT assumption, while not strictly necessary, improves the estimation for practical cases. This is similar to acoustic applications, as seen in [36,46,47] and can be explained by the similarity of reverb in acoustics to DMC in radio-based channels. Both are dependent on the room geometry, but the channel statistics are similar for close-by nodes. I.e. we can assume that $\mathbf{C}_\nu^{l,m} \approx \mathbf{C}_\nu^{i,m}$. This is depicted in Figures C.3a.i and C.3a.ii. Figure C.3a.i shows the unwrapped argument of the cross power spectral density $[_{l,i,m,k}]_n$ for measurements of two nodes l and i to one anchor with one antenna for correct and incorrect estimation of ϵ_l and ϵ_i. The measurement scenario corresponds to the mid-scale measurement scenario detailed in Section C.5. Figure C.3a.i illustrates that when the frequency responses of $\tilde{\mathbf{R}}_{l,m,k,n}$ and $\tilde{\mathbf{R}}_{i,m,k,n}$ are similar (i.e. the nodes are in proximity, here they are spaced by 0.2m), and the parameters ϵ_l and ϵ_i are estimated correctly, the argument of $[_{l,i,m,k}]_n$ is near zero, and the value of the likelihood is maximized. The left-over noise results mostly from AWGN, which illustrates that $\mathbf{C}_\nu^{l,m} \approx \mathbf{C}_\nu^{i,m}$. When a parameter is estimated incorrectly, a trend in one direction remains in the unwrapped phase, which results in a lower value for the likelihood. Figure C.3a.ii shows the same plot for two nodes l and i which are spaced farther apart (in this case approximately 6m), which results in different channel statistics ($\mathbf{C}_\nu^{l,m} \neq \mathbf{C}_\nu^{i,m}$). When this is the case, the unwrapped argument of $[_{l,i,m,k}]_n$ behaves similarly to a random-walk, independent of correct estimation of transmission times. This is due to noise in

the phase being also influenced by the dense multipath (DM), which leads to more phase noise in general. As correlation between the two signals is overall very low, both unwrapped arguments, for correct and incorrect estimation of transmission times, look similar, as in-phase noise is dominant. Figure C.3b.i and Figure C.3b.ii show the corresponding magnitude frequency responses of the evaluated nodes. Smoothing (moving average) in the frequency-domain was applied for 20 bins, as to better show the overall shape of the frequency response, and suppress noise. This illustrates the similarity of frequency responses for nodes near each other for signals from the same antennas. For higher distances, no clear correlation between frequency responses can be seen. Furthermore, Figure C.3c.i and C.3c.ii show the corresponding log-likelihoods between the same nodes, evaluated over the difference of transmission times $\epsilon_l - \epsilon_i$, incorporating measurements from 12 antennas. The black and red lines in the plot correspond to the correctly estimated and incorrectly estimated ϵ_l and ϵ_i in Figure C.3a.i and Figure C.3a.ii respectively. This illustrates a higher likelihood for nodes within a vicinity, and shows a high degree of multi-modality, due to reflections of the signals in a room. The second likelihood is less informative, but still shows some (altough much smaller) correlation at the correct difference of transmission times.

Figure C.4 shows the marginalized log-likelihood for GCC over distance in a typical scenario. This illustrates that measurements from nodes in a vicinity correlate with each other, but there are diminishing effects at larger distances. The illustrated behaviour shows that GCC is very informative for smaller distances, but increasingly uninformative for larger distances. RSS as a measurement method has diminishing performance gains for larger numbers of cooperating nodes N_c. This can be also be seen for perceptual hashing and GCC.

Perceptual Hashing likelihood

Perceptual hashing yields an efficient approximation of GCC. We define a measurement matrix for each node l as $\mathbf{X}_l = [r_{l,1}, \dots r_{l,M}]^T$. We then compute $\mathbf{X}_{\mathrm{DCT}} = \mathrm{DCT}_{\mathrm{II}}(\mathbf{X}_l)$, where $\mathrm{DCT}_{\mathrm{II}}$ denotes the type II discrete cosine transform. To focus on lower frequencies of the DCT, filtering high-frequency features consisting mostly of noise, we define a reduced version $\mathbf{X}^{\mathrm{red}}_{\mathrm{DCT}} = [\mathbf{X}_{\mathrm{DCT}}]_{N_{\mathrm{D}} \times N_{\mathrm{D}}}$, where N_{D} defines a cutoff for the used frequency bins of the DCT. We also define the average value of the reduced DCT as κ_{DCT} being the mean of all elements of $\mathbf{X}^{\mathrm{red}}_{\mathrm{DCT}}$. We apply an element-wise threshold function as follows:

$$[\mathbf{X}^{\mathrm{thr}}]_{n,m} = \begin{cases} 0 & [\mathbf{X}^{\mathrm{red}}_{\mathrm{DCT}}]_{n,m} \leq \kappa_{\mathrm{DCT}} \\ 1 & [\mathbf{X}^{\mathrm{red}}_{\mathrm{DCT}}]_{n,m} > \kappa_{\mathrm{DCT}} \end{cases}. \tag{C.22}$$

The vectorized binary representation of the matrix $\mathbf{X}^{\mathrm{thr}}$ is denoted by $z^{\mathrm{PH}}(\mathbf{r}_l)$. We then define a similarity measure between nodes l and i as

$$z^{\mathrm{PH}}_{l,i} = N_D^2 - H(z^{\mathrm{PH}}(\mathbf{r}_l), z^{\mathrm{PH}}(\mathbf{r}_i))/N_D^2, \tag{C.23}$$

where $H(z^{\mathrm{PH}}(\mathbf{r}_l), z^{\mathrm{PH}}(\mathbf{r}_i))$ is the Hamming distance between two hashes. This measure is bounded by $z^{\mathrm{PH}}_{l,i} \in [0, 1]$, with larger values indicating greater similarity between signals. It equates to a normalized Hamming distance between two perceptual hashes and behaves according to a distance-dependent model in a Euclidean

sense. The normalization is not strictly necessary, but allows the similarity measure to behave like a statistical distance (i.e. Hellinger distance, Jensen-Shannon divergence). Figure C.5 illustrates the distance-dependent difference, $z_{l,i}^{\mathrm{PH}}$, between perceptual hashes of two nodes l and i. Assuming this follows a saturated log-distance-dependent linear model, we express the likelihood for perceptual hashing as

$$f(z_{l,i}^{\mathrm{PH}} \mid \mathbf{p}_l, \mathbf{p}_i) = \frac{1}{\sqrt{2\pi\sigma^2}} \exp \frac{-(z_{l,i}^{\mathrm{PH}} - \tilde{z}_{l,i}^{\mathrm{PH}})^2}{2\sigma^2}, \tag{C.24}$$

with

$$\tilde{z}_{l,i}^{\mathrm{PH}} = P - \rho 10 \log\left((d_{l,i}/d_0) + \chi\right), \tag{C.25}$$

where P and ρ are used similarly to (C.9), and χ is a parameter describing a saturation effect for small values. This is due to a characteristic of perceptual hashing: similar measurement matrices can lead to similarity measures being 1. For further dissimilarity, the behavior is similar to a log-normal pathloss model, as the differences in the measurement matrices are also log-distance-dependent on the mean signal energy.

A saturation effect at a value of 1 signifies identical hashes, showing a limitation of perceptual hashing in distinguishing highly similar signals. The figure includes two fitted functions: a saturated log-distance fit (refer to (C.25)) and a non-saturated variant with $\chi = 0$. The saturated log-distance fit demonstrated superior results across all evaluated scenarios, thus it was exclusively used for further evaluations. To verify this, we used the odds ratio [48,49] between two models M_1 and M_2 for our measurements as

$$O_{M_1,M_2} = \frac{f(M_1 \mid z_{l,i}^{\mathrm{PH}})}{f(M_2 \mid z_{l,i}^{\mathrm{PH}})} = \frac{f(M_1)}{f(M_2)} \frac{f(z_{l,i}^{\mathrm{PH}} \mid M_1)}{f(z_{l,i}^{\mathrm{PH}} \mid M_2)} \tag{C.26}$$

which favours model M_1 over M_2 if $O_{M_1,M_2} > 1$. By using marginalization, we can rewrite the likelihood given model M as

$$f(z_{l,i}^{\mathrm{PH}} \mid M) = \int f(z_{l,i}^{\mathrm{PH}} \mid \mu_M, M) f(\mu_M) d\mu_M, \tag{C.27}$$

where $f(\mu_M)$ is the prior PDF for the model parameters of model M. Assuming a flat prior in the region of interest, we can approximate this integral using the Bayesian information criterion, as described in [50]. This leads to

$$\ln f(z_{l,i}^{\mathrm{PH}} \mid M) \approx \ln f(z_{l,i}^{\mathrm{PH}} \mid \hat{\mu}_M, M) - \frac{N_{\mu_M}}{2} \ln N_z, \tag{C.28}$$

where N_z is the number of measurements, and N_{μ_M} is the number of free model parameters. To estimate the parameters $\hat{\mu}_M$, we used a least squares fit on the likelihood $f(z_{l,i}^{\mathrm{PH}} \mid M)$, with M being either a saturated log-linear (M_1) or non-saturated log-linear (M_2) model. We verified this for all scenarios, which typically showed an odds ratio O_{M_1,M_2} of at least 1.7, favoring the saturated fit.

RSS-dependent likelihood

The inter-node likelihood for RSS depends on separate RSS measurements and is used as a comparison for the other two methods. This is a cooperative likelihood,

as nodes have to directly cooperate with each other. The cooperative likelihood for the RSS case can be expressed as:

$$f(z_{l,i}^{\mathrm{RSS}} \mid \mathbf{p}_l, \mathbf{p}_i) = \frac{1}{\sqrt{2\pi\sigma^2}} \exp \frac{-(z_{l,i}^{\mathrm{RSS}} - \tilde{z}_{l,i}^{\mathrm{RSS}})^2}{2\sigma^2}, \tag{C.29}$$

where $\tilde{z}_{l,i}^{\mathrm{RSS}}$ is defined as:

$$\tilde{z}_{l,i}^{\mathrm{RSS}} = L(\mathbf{p}_l, \mathbf{p}_i, P, \rho). \tag{C.30}$$

In this context, $\tilde{z}_{l,i}^{\mathrm{RSS}}$ represents the log-distance-dependent model discussed in Section C.2.2.

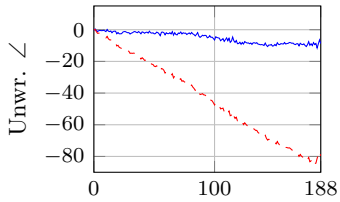

(a.i) Two nodes in vicinity (0.2m)

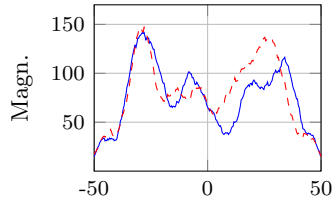

(b.i) Two nodes in vicinity (0.2m)

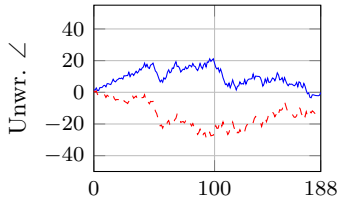

(a.ii) Two nodes far apart (6m)

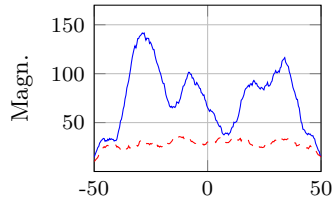

(b.ii) Two nodes far apart (6m)

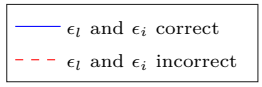

(a) Unwrapped arguments of $[_{l,i,m,k}]_n$ between two signals from one antenna over sample index n, and a comparison between correct and incorrect estimate of transmission time, at ground-truth position, real measurements. See mid-scale scenario.

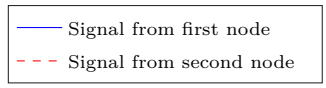

(b) Smoothed (moving average, 20 samples) magnitude frequency response (magnitude depending on gain of the measurement system) of two signals from one antenna over frequency bin n, at ground-truth position, real measurements. See mid-scale scenario.

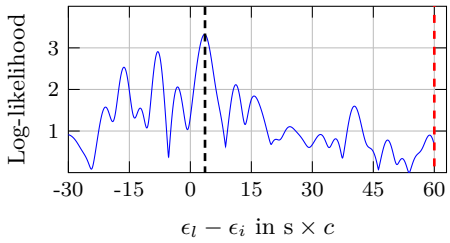

(c.i) Two nodes in vicinity (0.2m)

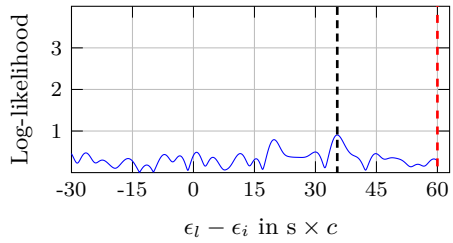

(c.ii) Two nodes far apart (6m)

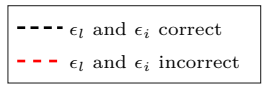

(c) Log-likelihoods between two nodes over $\epsilon_l - \epsilon_i$, real measurements, 12 antennas. Same scaling, for illustration purposes. See mid-scale scenario. X-axis scaled by c (speed of light).

Figure C.3: Different comparisons for GCC. Upper and lower plots use the same pairs of nodes.

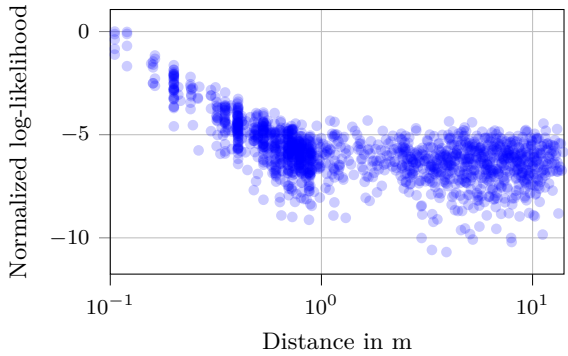

Figure C.4: Calculated GCC log-likelihood depending on real node positions ($\log f(\mathbf{z}_{l,i}^{\mathrm{GCC}} \mid \mathbf{p}_l, \mathbf{p}_i)$) and normalized to a maximum of zero. Not all links (around every 300-th) are plotted for better visibility and due to high computational complexity. See large-scale scenario.

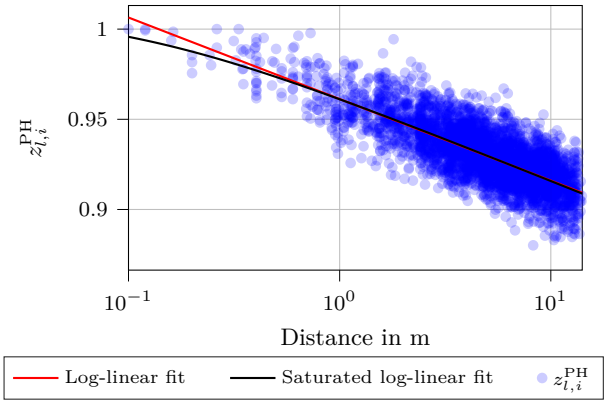

Figure C.5: Calculated difference of perceptual hashes between nodes depending on real distance, large-scale measurement scenario. Additionally plotted are a log-linear and a saturated log-linear fit. Only every 300-th hash is shown for easier visualization.

C.4 Inter-node localization

Inter-node localization algorithms (used in literature mostly as cooperative localization algorithms) yield unbiased and reliable localization results, especially when a sufficient number of inter-node links are available. This will be further discussed in the following subsections, where we describe an MP algorithm and analyze its complexity.

C.4.1 Message Passing Algorithm

For estimation of the posterior PDF, we incorporated an MP algorithm, based on the SPA, similar to [19–24, 29–31]. In general this is a method to reliably approximate the posterior PDF described in (C.11), which for example is similar to [19, Eq. 7]. For details, we refer to the previous work mentioned.

C.4.2 Complexity analysis

The computational complexity of the MP algorithm is primarily determined by the complexity of the cooperative likelihoods $f(\mathbf{z}_{l,i} \mid \mathbf{p}_l, \mathbf{p}_i)$ and the number of cooperating partners. We denote the number of cooperating partners as N_c for a single node l and the number of time-steps for marginalization as N_t. It should be noted that for full cooperation, $N_c = L$, otherwise $N_c < L$, with L being the number of nodes.

The computational complexity of the cooperative RSS-likelihood is $O(LN_c)$, indicating that the complexity scales linearly with the number of cooperating partners N_c for a fixed number of nodes L. The computational complexities of the perceptual hashing and GCC-likelihoods are $O(LN_cKMN_s)$ and $O(LN_cKMN_s^2N_t)$ respectively, suggesting that these two likelihoods also depend on the number of antennas KM, the number of samples per wideband measurement N_s, and the number of marginalization time-steps N_t (for GCC).

By pre-computing the hashes for each measurement, we can reduce the complexity for perceptual hashing to $O(LN_cKMN_s) \approx O(LN_c)$, making it comparable to RSS. In practice, this means that we compute all hashes and similarities between hashes before evaluating the MP algorithm. We can simplify this, because the datasets $z_{l,i}^{\mathrm{PH}}$ do not depend on any parameters, but solely on the measured wideband data. This is not possible for GCC, as the datasets $z_{l,i}^{\mathrm{GCC}}$ depend directly on positions of nodes and transmit times, in a multi-dimensional fashion.

Figure C.6 illustrates the mean evaluation time for one iteration of the MP algorithm using three different methods on a typical workstation in our lab. We vary the number of cooperating partners N_c until all nodes cooperate with each other, with the number of nodes fixed at $L = 96$. For each of the 100 realizations with $N_c < L$, the cooperating partners are randomly selected. The graph reveals that the computation times for RSS and perceptual hashing are very similar per iteration. Although the hashes are precomputed, their computation time is negligible compared to the MP algorithm. Despite being well-optimized, the computation time for GCC is significantly larger, highlighting the advantage of perceptual hashing over GCC for large scenarios due to its ability to perform calculations within practical computation times.

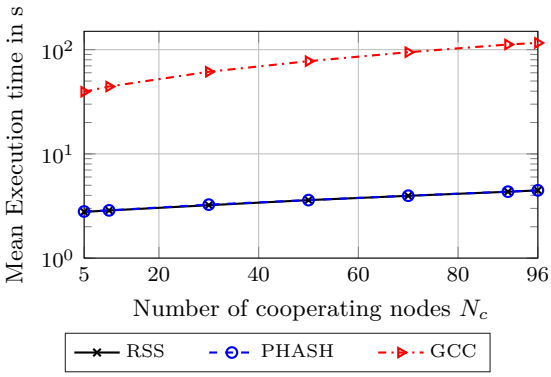

Figure C.6: Mean evaluation time for different numbers of cooperating nodes N_c, simulation with $L = 96$ nodes.

C.5 Experimental Evaluation

We perform four experiments of increasing complexity to evaluate and validate the proposed algorithm. Initially, we assess a small-scale simulation scenario with $L = 10$ nodes, demonstrating the functionality of all three variants of cooperative likelihoods within the MP algorithm. Subsequently, we execute a mid-scale simulation with $L = 96$ nodes, where we evaluate the performance dependent on the number of cooperating nodes. This evaluation is then repeated with real measurements. Finally, we carry out an evaluation on a large-scale measurement campaign with $L = 1078$ nodes in an industrial hall.

C.5.1 Common Parameters

For position estimation, we assume a uniform prior distribution within the volume: $4\,\mathrm{m} < x < 21.13\,\mathrm{m}$, $7\,\mathrm{m} < y < 15.4\,\mathrm{m}$, and $0\,\mathrm{m} < z < 2\,\mathrm{m}$. Additionally, we consider bounds for the unknown transmission time $\epsilon_{\mathrm{lb}} = \frac{-30\,\mathrm{m}}{c}$ and $\epsilon_{\mathrm{ub}} = \frac{30\,\mathrm{m}}{c}$. We discretize the time steps into 31 equally spaced intervals within ϵ_{lb} and ϵ_{ub} for marginalization over ϵ. This is done for easier evaluation within the algorithms, but could also be evaluated using particles. We additionally assume prior knowledge of all anchor positions $\mathbf{q}$. Estimation is done according to the particle-based MP algorithm described in Section C.4. For RSS measurement simulation, we use the following parameters: $\sigma = 3.56\,\mathrm{dB}$, $P = -45\,\mathrm{dB}$ and $\rho = 1.0$. Perceptual hashing is used with $N_D = 12$. The reference distance is $d_0 = 0.1\mathrm{m}$ for both RSS and perceptual hashing. The simulation and measurement environment details are provided prior to the evaluations.

C.5.2 Simulation environment

For evaluation purposes, we developed a simulation for wideband signals within a room, similar to [39]. For the wideband channel simulation, we scale the signal

amplitude according to the Friis equation [51]

$$\alpha_{l,m} = \alpha_{\text{ref}} \left(\frac{\lambda_c}{4\pi d_{l,m}} \right), \tag{C.31}$$

with $\lambda_c = \frac{c}{f_c} = \frac{c}{2.44\,\text{GHz}}$, c being the speed of light, α_{ref} being a reference amplitude at 1 m and $d_{l,m}$ being the distance between node l and anchor m. The bandwidth β of all signals is 75.3 MHz, matching the measurement bandwidth. The parameter Ω_1 of the DMC at 1 m is drawn from an i.i.d. Gaussian random process, and scaled according to the Friis equation resulting in

$$[\Omega_1]_{l,m\,\text{dB}} \sim \mathcal{N}\left(\mu, \sigma^2 \times \left(\frac{\lambda_c}{4\pi d_{l,m}} \right)^2 \right), \tag{C.32}$$

with the fall and rise time parameters of the DMC fixed at $\gamma_r = 5\,\text{ns}$ and $\gamma_f = 20\,\text{ns}$, typical for an indoor scenario [42, 52]. A comprehensive analysis of the Cramér-Rao lower bound (CRLB) of measurements and a simulation of similar wideband scenarios without cooperation can be found in [5, 39, 53].

C.5.3 Small-scale simulation

The simulation utilizes $M = 6$ anchors, matching physical positions of the real measurement scenario. The anchors consist of $K = 2$ antennas each, spaced 6cm apart in y-direction, with center of gravity at the anchor positions indicated in Figure C.7.

We choose the mean normalized energy in the DMC as μ of Ω_1 as $-20\,\text{dB}$, the variance of the realisations σ^2 of Ω_1 therein as 2.16 dB, and the signal-to-noise ratio (SNR) $\frac{\alpha_{l,m}^2}{\sigma_{l,m}^2}$ at 1 m as 25 dB.

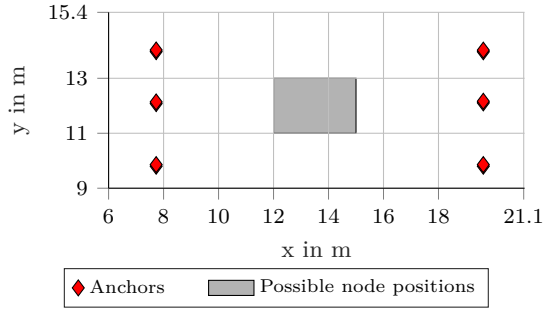

Figure C.7: Small-scale: Overview of small-scale simulation scenario with anchors (red) and area with possible node positions (grey area).

We simulate $L = 10$ nodes within the grey area shown in Figure C.7. The height of all simulated nodes is fixed at 1 m. We compare a non-cooperative case with three cooperative likelihoods for the MP algorithm. Model parameters for RSS and perceptual hashing are assumed to be known from a large number of node realizations. We use 500 particles. The number of particles was chosen empirically to give good and reproducible results, larger numbers did not lead to better results.

Variant:	No Coop	RSS	GCC	PHASH
RMSE:	3.48 m	1.71 m	2.52 m	3.03 m

Table C.1: Small-scale: Comparison of root-mean-square error (RMSE) for small-scale scenario.

Table C.1 shows results for the small-scale scenario. The results show that the wideband single-node likelihood, which operates without any cooperation, has the poorest performance. On the other hand, RSS yields the best performance, likely because these measurements contain the most information. Given the short distances between nodes in the simulation, RSS improves results quickly, even with just a small number of cooperating nodes. GCC doesn't perform as well, which is in line with expectations, as the additional gain from information coupling is smaller per measurement, due to relatively strong DMC. Finally, perceptual hashing lags behind RSS and GCC in these simulations. This is anticipated because perceptual hashing condenses the information from wideband measurements into a single hash value, and like GCC, it is also influenced by DMC, unlike the RSS measurements.

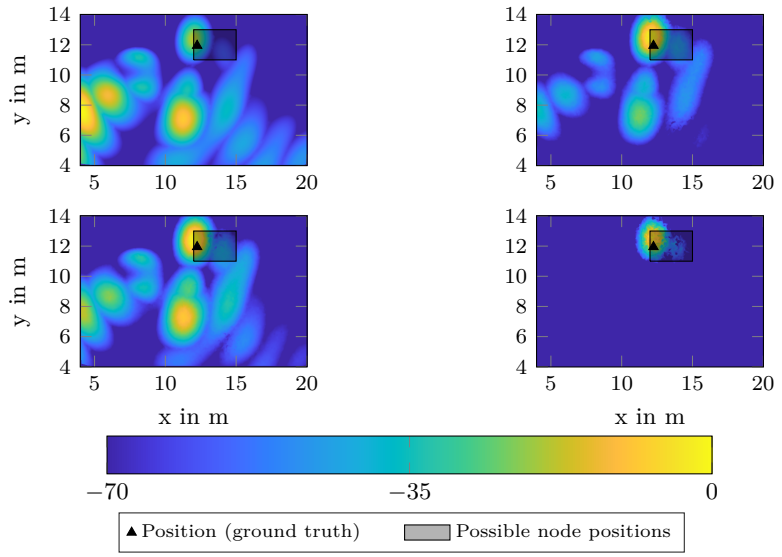

Figure C.8: Small-scale: Comparison of log-posteriors of one realisation and node for the small-scale scenario. Cut-off for the visualization is at a value of -70, and normalized to a maximum of 0. Upper left: No Cooperation. Upper right: Perceptual hashing. Lower left: RSS. Lower right: GCC.

Figure C.8 presents the log-posterior PDFs for a single node for these methods Without cooperation, the likelihood exhibits a multimodal distribution due to multipath propagation. The information coupling and cooperative likelihood suppress incorrect modes, with GCC showing the strongest effect, and perceptual hashing and RSS being comparable. Plots are normalized to a maximum of 0. This figure, calculated with 12000 particles and interpolated between them, serves as a conceptual example. It should be noted that in this single example GCC looks superior.

This is due to the right mode dominating results with GCC in this example, which is not always the case.

C.5.4 Mid-scale simulation and measurement

In this subsection, we assess the performance of a single node l in a mid-scale scenario against the number of cooperating nodes N_c .

Intersections:	0	1	2	3
μ of Ω_1	-15 dB	-12 dB	-2 dB	-8 dB
σ^2 of Ω_1	2.16 dB	5.30 dB	7.15 dB	6.40 dB
$\frac{\alpha_{l,m}^2}{\sigma_{l,m}^2}$ at 1 m	25 dB	21.42 dB	19.46 dB	19.56 dB

Table C.2: Simulation: Change of parameters depending on number of intersections between anchor and node.

For mid and large scale simulations, parameters are scaled according to (geometric) intersections/obstacles between anchors and nodes. This change of parameters for the simulation is described in Table C.2, where μ of Ω_1 describes the mean of the signal energy in the DMC, σ^2 of Ω_1 describes the corresponding variance, and $\frac{\alpha_{l,m}^2}{\sigma_{l,m}^2}$ describes the SNR for the amplitude $\alpha_{l,m}$ depending on number of intersections. Note here that $\alpha_{l,m}$ is implicitly described by $\frac{\alpha_{l,m}^2}{\sigma_{l,m}^2}$.

Figure C.9 depicts a top-view and a corresponding isometric view of the synthetic (and measurement) scenario. Green/blue nodes are used for mid and large-scale evaluations, black nodes are used only for large-scale evaluations. Anchors are depicted in red.

We determine the model parameters (P, ρ, χ) for the log-distance saturated model based on the full set of nodes and the exact node and anchor positions. However, a well-fitted model can be computed from only a minor percentage of nodes already [19,31]. This evaluation allows us to compare the performance for a small number of cooperating nodes within a scenario with a total of $L = 96$ nodes. For $N_c < L$, cooperating nodes are randomly selected once per evaluation. This implies that the cooperating nodes remain constant for one evaluation with five iteration steps of the MP algorithm, but vary for new realizations of the channel. Five iteration steps were sufficient for this evaluation, as the algorithm always converged within this number of iterations. For this evaluation we use 500 particles. The number of particles is chosen empirically to give good and reproducible results. Larger numbers do not lead to better results.

Figure C.10a presents the RMSE performance of the three methods against the number of cooperating nodes N_c. Additionally the 95% error intervals are depicted. The GCC method exhibits the best performance in most evaluated cases, which can be attributed to its higher information content compared to the single measurements of RSS and the compressed measurements of perceptual hashing.

Although the performance of RSS is comparable to GCC, an offset persists for larger values of N_c due to the higher uncertainty of RSS. As expected, the performance of perceptual hashing is overall inferior due to the lower information content within the compressed hashes. For full cooperation ($N_c = L$), the performance does

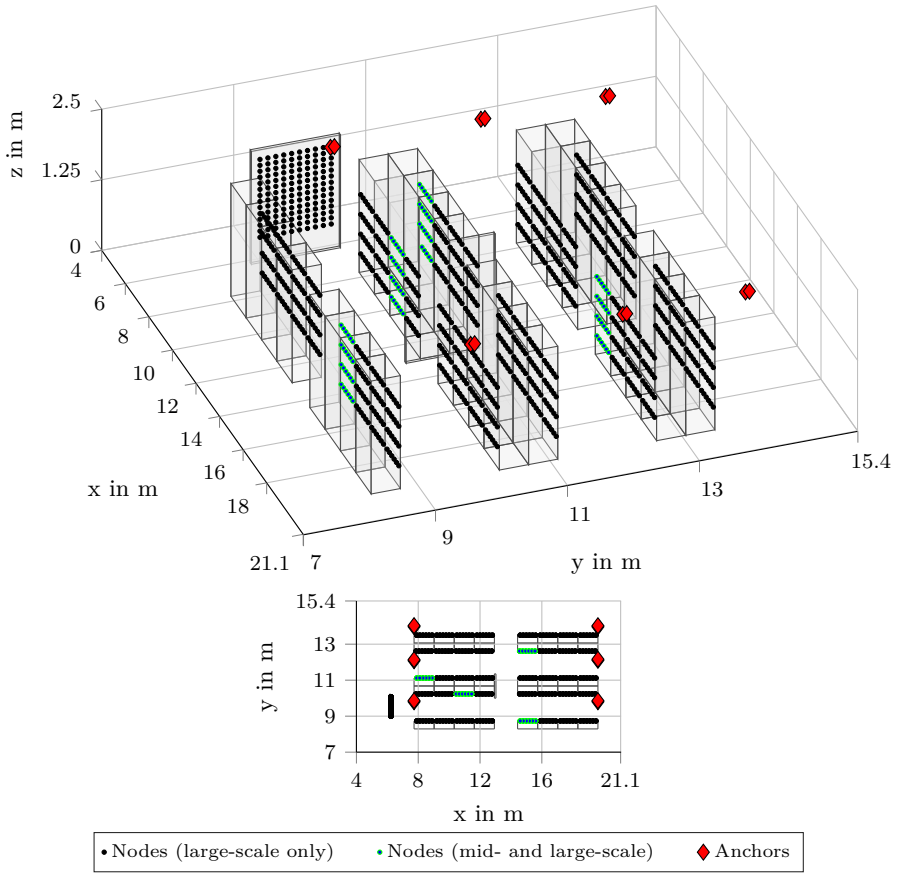

Figure C.9: Large and mid-scale: Overview of scenario with large-scale nodes (black and green/blue), mid and large-scale nodes (green/blue only) and anchors (red).

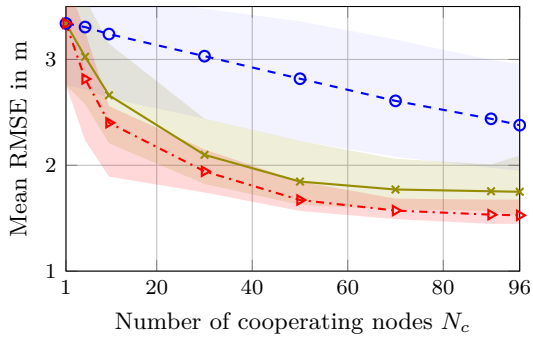

(a) Mid-scale simulation: Evaluation of mean RMSE (over realisations) for different numbers of cooperating nodes N_c for simulated mid-scale scenario with $L = 96$, 100 realizations of channel simulation and cooperation selection, with corresponding 95% error intervals.

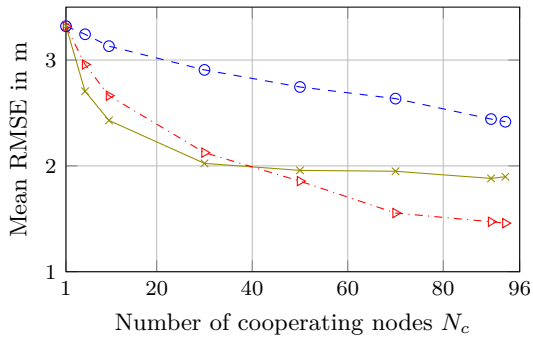

(b) Mid-scale measurement: Evaluation of mean RMSE (over realisations) for different numbers of cooperating nodes N_c for measured mid-scale scenario with $L = 93$, 100 realizations of cooperation selection

Figure C.10: Mid-scale simulation and measurement: Evaluations over different numbers of cooperating nodes N_c.

not attain either the performance of RSS or GCC, but an improvement is still visible, suggesting further improvements for more nodes and better performance for larger scenarios when using perceptual hashing.

As previously described, the computational complexity of perceptual hashing is significantly lower than that of GCC. This suggests that perceptual hashing can achieve a significant performance gain within approximately the same computation time as RSS, but without the need for additional measurements. This demonstrates the ability to directly extract information from the wideband measurements, exploiting information coupling between nodes.

In addition to the simulated measurements, we conducted real measurements in an industrial hall with a similar geometry and floorplan as depicted in Figure C.9. The measurement settings were consistent with those of the simulation. The nodes facilitated wideband measurements to anchors using a proprietary protocol and chirp transmission in the ISM-band at 2.4 GHz, as described in detail in [5].

We also retrieved cooperative RSS measurements between nodes.

The node positions are equal to those in the simulation environment, but not all nodes could be measured, resulting in the inclusion of only 93 nodes in this evaluation. As in the previous sub-section, model parameters were fitted for known node positions.

Moreover, not all nodes could obtain RSS measurements from every other node. Therefore, for RSS measurements, N_c represents the maximum number of allowed cooperating nodes. This limitation does not significantly limit the overall results, as less than 10% of RSS measurements were unavailable.

As with previous evaluations, cooperating nodes were selected randomly. However, in this case, only one set of measurements was evaluated. For this evaluation we again used 500 particles.

Figure C.10b presents the results for the three different methods. Overall, the real measurements yield very similar results to the simulation, with almost all results being in the error intervals seen in Figure C.10a. For the RSS measurements, we observe a marginally improved gain for a small numbers of cooperating nodes N_c. This can be attributed to the fact that real RSS measurements are attenuated when the LoS is blocked. This leads to rightly-confident measurements when LoS conditions exist between nodes, resulting in enhanced performance even when only a few LoS measurements are available. This effect is not as pronounced for GCC and perceptual hashing. Overall, GCC delivers the best performance for full cooperation, but shows only minor improvements at $N_c > 70$. Perceptual hashing yields the weakest performance of all three methods overall, but shows steady improvement with the number of cooperating nodes N_c, indicating better performance for larger scenarios, which will be validated in the subsequent subsection. All outliers for GCC from the error interval seen in Figure C.10a can be reasonably attributed to small offsets between simulation parameters and real measurements.

C.5.5 Large-scale measurements

To further compare RSS and perceptual hashing, we assess a large-scale scenario with $L = 1078$ nodes, using all nodes depicted in Figure C.9. Again these evaluations were conducted with different cooperation variants: Synthetic RSS measurements, real RSS measurements, and perceptual hashing based on real wideband measurements. Synthetic RSS measurements were generated according to the model in Section C.2.2 with a variance $\sigma^2 = 3.5$dB and other parameters corresponding to the fitted models. It should be noted that synthetic RSS measurements do not incorporate any model for shadowing or multipath propagation. The log-distance saturated model for perceptual hashing and log-distance model for RSS were fitted according to known positions. For synthetic RSS and perceptual hashing the nodes cooperated fully, i.e. $N_c = L$. For real RSS measurements not all links were available, particularly from distant nodes, effectively resulting in the availability of around 75% of all measurements. Evaluations for GCC were not conducted for this scenario, due to excessive computational complexity (i.e., calculation time) and additional memory constraints. This evaluation utilized 1200 particles, chosen empirically again.

The results in Table C.3 indicate that synthetic RSS measurements yield the best overall RMSE. This can be attributed to the availability of full cooperation,

Variant:	No Coop	RSS (synth.)	RSS	PHASH
RMSE:	2.41 m	0.96 m	1.21 m	1.33 m

Table C.3: Large-scale: Comparison of RMSE between methods for large-scale scenario.

and the synthetic RSS model not being affected by multipath propagation. The performance of measured RSS and perceptual hashing is comparable, with perceptual hashing performing marginally worse. This suggests that for a large-scale scenario, we can omit additional cooperative measurements like RSS with very similar results, by using information coupling from wideband measurements, achieving far superior results over a non-cooperative evaluation.

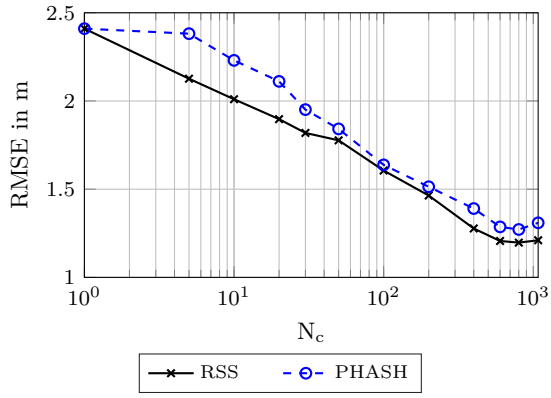

Figure C.11: Large-scale measurement: Evaluation of RMSE for different numbers of cooperating nodes N_c for measured large-scale scenario with $L = 1078$. Cooperation partners chosen by largest value of either RSS or perceptual hashing.

Figure C.11 shows an evaluation of the RMSE as a function of the number of cooperating nodes N_c for the large-scale measurements. With consideration of execution time, we chose the N_c cooperation partners by sorting the values of RSS and perceptual hashing descending by value, meaning that for any node l we chose the nodes i for which we measured the strongest links. Both methods show that for a larger number of cooperations, the RMSE improves. We reason that the information content of perceptual hashing is smaller per cooperation than for RSS, but more available links (i.e. full cooperation) leads to a comparable performance. For a large number of cooperation (i.e. larger than $N_c = 400$) we can observe diminishing performance gains for both methods. For both methods, it seems that performance is worse for full cooperation over slightly less cooperation. This is most probably only an artifact of the particle-based estimation method, which leads to slight discrepancies even between realisations with the same measurements.

Figure C.12 shows a cumulative frequency plot of the estimation error for perceptual hashing with full cooperation ($N_c = 1078$), with partial cooperation ($N_c = 100$, see Figure C.11) and no cooperation as a comparison. It can be seen that not only the overall estimation error is lower for more cooperation partners with perceptual hashing, but also the number of outliers is significantly reduced.

Scenario:	No Coop	RSS (synth.)	RSS	GCC	PHASH	RSS only
Small-scale:	3.48m	1.71m	–	**2.52**m	**3.03**m	–
Mid-scale synthetic	3.34m	1.75m	–	**1.53**m	**2.38**m	–
Mid-scale measured	3.32m	–	1.90m	**1.46**m	**2.42**m	–
Large-scale:	2.41m	0.96m	1.21m	–	**1.33**m	1.12m

Table C.4: (Mean) RMSE result overview for all different scenarios. Most relevant results are highlighted in boldface.

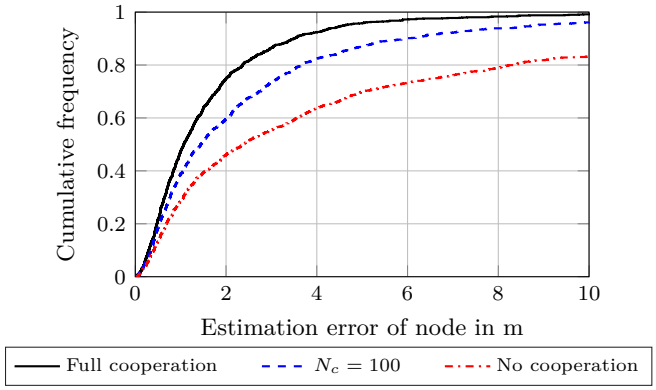

Figure C.12: Large-scale measurement: Cumulative frequency of full cooperation against 100 cooperation partners for perceptual hashing and no cooperation.

C.5.6 Evaluation results overview

This section shows an overview of the evaluations in this paper, and gives an additional comparison to an existing algorithm using RSS measurements without wideband measurements.

The results are shown in Table C.4. The additional algorithm for the large-scale scenario can be seen in the column RSS only. This shows the RMSE for an alternative cooperative localization algorithm, which needs additional fixed anchor positions of nodes, see [31, Table 4.1]. This alternative algorithm shows a better overall localization performance, at the disadvantage that about 10% of node positions have to be known beforehand. This is not the case for our proposed algorithm, while still retaining a very comparable performance. Other comparable methods are not applicable, as machine-learning based methods need training datasets, and methods based on virtual anchors [41, 54] do not work well for bandwidths where discrete multipath components cannot be discerned reliably.

C.6 Conclusion

This paper introduces an algorithm that leverages information coupling from measurements across a multitude of nodes. Information coupling exploits mutual information from different measurements, for example similar statistical properties. The proposed algorithm is based on wideband TDoA measurements, where the information coupling between nodes is exploited as cooperative information. Two methods for this are explained in detail, one based on the generalized cross-correlation be-

tween wideband measurements of all available nodes, and a simplification based on perceptual hashing. The latter yields slightly diminished positioning results, but much faster computation times. Both approaches perform comparable to a scenario where additional RSS measurements are used as cooperative information. The solution is presented within an MP framework, enabling the estimation of the joint-posterior PDF across a large number of nodes.

Previous algorithms that incorporate information coupling between nodes have been limited to a small number of nodes (10 or less). The algorithm developed in this paper offers an efficient solution for a larger number of nodes, rendering such problems manageable.

The algorithm has the potential to enhance the localization performance, particularly in scenarios involving a large number of low-power and low-end hardware nodes where single measurements to infrastructure may not provide sufficient quality.

Overall, this paper proposes a new possibility to improve the localization performance of multiple wideband measurements significantly. In a large-scale scenario with 1078 nodes the performance improves from an RMSE of 2.41m for wideband measurements only, to 1.33m using our proposed algorithm with perceptual hashing. This shows a clear advantage in localization performance, with the only downside being additional computation time.

While this paper presents significant advancements, there remains room for future developments. Subsequent work will explore the fusion of multiple measurement methods with the aim of further enhancing performance. Additional research could also aim at incorporating neural-enhanced cooperative-localization approaches, as seen for example in [55]. This ongoing research underlines the potential and versatility of the proposed algorithm.

Acknowledgment

We thank Daniel Neunteufel, Christoph Hufnagl and Holger Arthaber from the Institute of Electrodynamics, Microwave and Circuit Engineering at the Technical University of Vienna for contributing to this work with the design of a reliable measurement system for wideband signals, enabling the measurements used. Supported by TU Graz Open Access Publishing Fund.

Symbol	Domain	Usage
L	$\mathbb{N}$	Number of nodes
l	$\{1,\ldots,l\}$	Index of node
M	$\mathbb{N}$	Number of anchors
m	$\{1,\ldots,M\}$	Index of anchor
K	$\mathbb{N}$	Number of antennas per anchor
k	$\{1,\ldots,K\}$	Antenna index per anchor
N_s	$\mathbb{N}$	Number of samples per wideband measurement
$\mathbf{p}_l$	$\mathbb{R}^3$	Node position in 3 dimensions
$p_{l,\mathrm{x}}$	$\mathbb{R}$	Node position in x dimension
$p_{l,\mathrm{y}}$	$\mathbb{R}$	Node position in y dimension
$p_{l,\mathrm{z}}$	$\mathbb{R}$	Node position in z dimension
$\mathbf{q}_{m,k}$	$\mathbb{R}^3$	Antenna position in 3 dimensions
$\mathbf{q}_m$	$\mathbb{R}^3$	Mean anchor position in 3 dimensions
t	$\mathbb{R}$	Continuous time
c		Speed of light
$h_{l,m,k}(t;\mathbf{p}_l)$	$\mathbb{C}$	Receiving channel of l,m,k
$\alpha_{l,m,k}$	$\mathbb{C}$	Complex amplitude of l,m,k
$\tau(\mathbf{x},\mathbf{y})$	$\mathbb{R}$	Propagation delay between position $\mathbf{x}$ and $\mathbf{y}$
$\nu_{l,m,k}(t)$	$\mathbb{C}$	DMC
$\frac{N_0}{2}$	$\mathbb{R}^+$	Double sided PSD
$S_\nu(t;\tilde{\boldsymbol{\eta}})$	$\mathbb{C}$	PDP
$\tilde{\boldsymbol{\eta}}$	$[\Omega_1,\gamma_f,\gamma_r]^T$	Parameters for the PDP
Ω_1	$\mathbb{R}_0^+$	Normalized energy in the DM
γ_f	$\mathbb{R}^+$	Fall time of the PDP
γ_r	$\mathbb{R}^+$	Rise time of the PDP
$s(t)$	$\mathbb{C}$	Baseband signal
f_c	$\mathbb{R}$	Center frequency
$r_{l,m,k}(t)$	$\mathbb{C}$	Received signal at time t from node l and antenna m,k
$w_{l,m,k}(t)$	$\mathbb{C}$	AWGN
$\tilde{\alpha}_{l,m,k}$	$\mathbb{C}$	Complex amplitude of l,m,k, accounting for phase shift between antennas at anchor
$\mathbf{r}_{l,m}$	$\mathbb{C}^{N_sK\times 1}$	Stacked received signals of K antennas at anchor m
$\mathbf{r}_{l,m,k}$	$\mathbb{C}^{N_s\times 1}$	Received signals at anchor m and antenna K
$\alpha_{l,m}$	$\mathbb{C}$	Joint complex amplitude of node l at anchor m
$\mathbf{w}^{l,m}$	$\mathbb{C}^{N_sK\times 1}$	Noise vector describing DMC and AWGN
ϵ_l	$\mathbb{R}$	Unknown transmit time of node l
$\mathbf{s}(\mathbf{p}_l,\mathbf{q}_m,\epsilon_l)$	$\mathbb{C}^{N_sK\times 1}$	Baseband signal vector accounting for phase shifts at the array antennas
$\tilde{\mathbf{s}}(t)$	$\mathbb{C}^{N_s\times 1}$	Baseband signal vector for one antenna

T_s	$\mathbb{R}^+$	Sampling interval
$\mathbf{C}^{l,m}$	$\mathbb{C}^{N_s K \times N_s K}$	Covariance matrix characterizing $\mathbf{w}^{l,m}$
$[\mathbf{C}^{l,m}]_k$	$\mathbb{C}^{N_s \times N_s}$	Block of covariance matrix for antenna k of anchor m
$[\mathbf{C}_\nu{}^{l,m}]_k$	$\mathbb{C}^{N_s \times N_s}$	DMC block of covariance matrix for antenna k of anchor m
$[\mathbf{C}_\mathbf{w}{}^{l,m}]_k$	$\mathbb{C}^{N_s \times N_s}$	AWGN block of covariance matrix for antenna k of anchor m
$\sigma^2_{l,m}$	$\mathbb{R}_0^+$	Noise Variance at anchor m
$d_{l,i}$	$\mathbb{R}_0^+$	Distance between two nodes l and i
$L(\mathbf{p}_l, \mathbf{p}_i, P, \rho)$	$\mathbb{R}_0^-$	Path loss between nodes l and i
d_0	$\mathbb{R}^+$	Reference distance for path-loss model
P	$\mathbb{R}$	Reference path loss at distance d_0
ρ	$\mathbb{R}$	path-loss exponent
$z^{\text{RSS}}_{l,i}$	$\mathbb{R}$	Received RSS value between nodes l and i
$w_{l,i}$	$\mathbb{R}$	Noise term for RSS
σ^2	$\mathbb{R}$	Noise variance for RSS
$\mathbf{r}$	$[\mathbf{r}_1^T, \ldots, \mathbf{r}_L^T]^T$	Stacked wideband measurement vector for all nodes l
$\mathbf{r}_l$	$\left[\mathbf{r}_{l,1}^T, \ldots, \mathbf{r}_{l,M}^T\right]^T$	Stacked wideband measurement vector for all anchors of a single node l
$\mathbf{z}$	$\mathbf{z}_{l,i} \forall l, i$	Stacked cooperative measurement vector
$\boldsymbol{\theta}$	$[\mathbf{p}_1^T, \ldots, \mathbf{p}_L^T]^T$	Stacked position vector for all nodes l
$\mathbf{q}$	$[\mathbf{q}_1^T, \ldots \mathbf{q}_M^T]^T$	Stacked position vector for all anchors m
$\mathcal{L}$	$\{1, \ldots, L\}$	Set of all nodes l
$\mathcal{C}_l$	$\mathcal{C}_l \subseteq \mathcal{L}$	Subset of all nodes for which cooperative measurements are used
$\boldsymbol{\eta}_{l,m}$	$\left[\sigma^2_{l,m},\ \tilde{\boldsymbol{\eta}}^T_{l,m}\right]^T$	Stacked noise parameter vector for one node l and anchor m
$\boldsymbol{\alpha}_l$	$[\alpha_{l,1}, \ldots, \alpha_{l,M}]^T$	Stacked amplitudes for all antennas and anchors of node l
$\boldsymbol{\eta}_l$	$\left[\boldsymbol{\eta}_{l,1}{}^T, \ldots, \boldsymbol{\eta}_{l,M}{}^T\right]^T$	Stacked noise parameter vector for all anchors of node l
$\mathbf{R}_{l,m,k}$	$F(\mathbf{r}_{l,m,k})$	Fourier transformed receive vector
ω_n	$\mathbb{R}^+$	Frequencies of the baseband signal
B	$\mathbb{R}^+$	Baseband bandwidth of signal
$_{l,i,m,k}$	$\mathbb{C}^{N_s \times 1}$	Cross power spectral density between nodes l and i at one antenna k and anchor m
$\mathbf{z}^{\text{GCC}}_{l,i}$	$[\mathbf{r}_l^T, \mathbf{r}_i^T]^T$	Measurement vector for GCC for nodes l and i
$\mathbf{X}_l$	$[r_{l,1}, \ldots r_{l,M}]^T$	Measurement matrix for perceptual hashing
$\mathbf{X}_{\text{DCT}}$	$\text{DCT}_{\text{II}}(\mathbf{X}_l)$	Type two discrete cosine transformed measurement matrix for perceptual hashing

$\mathbf{X}_{\mathrm{DCT}}^{\mathrm{red}}$	$[\mathbf{X}_{\mathrm{DCT}}]_{N_{\mathrm{D}} \times N_{\mathrm{D}}}$	Reduced submatrix of $\mathbf{X}_{\mathrm{DCT}}$
N_{D}	$\mathbb{N}$	Number of elements for the cutoff of the reduced submatrix $\mathbf{X}_{\mathrm{DCT}}^{\mathrm{red}}$
κ_{DCT}	$\mathbb{R}_0^+$	Threshold for perceptual hashing
$[\mathbf{X}^{\mathrm{thr}}]_{n,m}$	$\mathbb{N}$	Threshold matrix for perceptual hashing
$z_{l,i}^{\mathrm{PH}}$	$z_{l,i}^{\mathrm{PH}} \in [0,1]$	Measurement scalar for perceptual hashing between nodes l and i
O_{M_1,M_2}	$\mathbb{R}_0^+$	Odds ratio between models M_1 and M_2
μ_M	$\mathbb{R}^{N_{\mu_M}}$	Model parameters for model M
$\hat{\mu}_M$	$\mathbb{R}^{N_{\mu_M}}$	Estimated model parameters for model M
N_{μ_M}	$\mathbb{N}^+$	Number of model parameters for model M
N_z	$\mathbb{N}^+$	Number of measurements
$z_{l,i}^{\mathrm{RSS}}$	$\mathbb{R}$	Log-distance dependent model for RSS
N_c	$\mathbb{N}^+$	Number of cooperating partners
N_t	$\mathbb{N}^+$	Number of time-steps for marginalization
ϵ_{lb}	$\mathbb{R}$	Lower bound for the estimation of the unknown transmit time ϵ_l
ϵ_{ub}	$\mathbb{R}$	Upper bound for the estimation of the unknown transmit time ϵ_l
α_{ref}	$\mathbb{R}$	Reference amplitude for wideband simulation
λ_c	$\frac{1}{f_c}$	Wavelength of the wideband signal
$d_{l,m}$	$\mathbb{R}_0^+$	Distance between node l and anchor m

Table C.5: Table of nomenclature

Bibliography

[1] K. Witrisal, P. Meissner, E. Leitinger, Y. Shen, C. Gustafson, F. Tufvesson, K. Haneda, D. Dardari, A. F. Molisch, A. Conti, and M. Z. Win, "High-Accuracy Localization for Assisted Living: 5G systems will turn multipath channels from foe to friend," *IEEE Signal Processing Magazine*, 2016, doi: 10.1109/MSP.2015.2504328.

[2] A. Yassin, Y. Nasser, M. Awad, A. Al-Dubai, R. Liu, C. Yuen, R. Raulefs, and E. Aboutanios, "Recent Advances in Indoor Localization: A Survey on Theoretical Approaches and Applications," *IEEE Communications Surveys and Tutorials*, 2017, doi: 10.1109/COMST.2016.2632427.

[3] D. Neunteufel, A. Fuchs, and H. Arthaber, "ToF-based Indoor Positioning for Low-power IoT Nodes," in *2020 54th Asilomar Conference on Signals, Systems, and Computers*, Nov 2020, doi: 10.1109/IEEECONF51394.2020.9443431.

[4] J. A. del Peral-Rosado, R. Raulefs, J. A. López-Salcedo, and G. Seco-Granados, "Survey of Cellular Mobile Radio Localization Methods: From 1G to 5G," *IEEE Communications Surveys Tutorials*, Secondquarter 2018, doi: 10.1109/COMST.2017.2785181.

[5] D. Neunteufel, S. Grebien, and H. Arthaber, "Indoor Positioning of Low-Cost Narrowband IoT Nodes: Evaluation of a TDoA Approach in a Retail Environment," *Sensors*, 2022, doi: 10.3390/s22072663.

[6] P. Zand, J. Romme, J. Govers, F. Pasveer, and G. Dolmans, "A high-accuracy phase-based ranging solution with Bluetooth Low Energy (BLE)," in *2019 IEEE Wireless Communications and Networking Conference (WCNC)*, 2019, doi: 10.1109/WCNC.2019.8885791.

[7] A. Comuniello, A. Angelis, A. Moschitta, and P. Carbone, "Using Bluetooth Low Energy Technology to Perform ToF-Based Positioning," *Electronics*, 12 2021, doi: 10.3390/electronics11010111.

[8] S. Sadowski and P. Spachos, "RSSI-Based Indoor Localization With the Internet of Things," *IEEE Access*, 2018, doi: 10.1109/ACCESS.2018.2843325.

[9] M. Kotaru, K. Joshi, D. Bharadia, and S. Katti, "SpotFi: Decimeter Level Localization Using WiFi," in *Proceedings of the 2015 ACM Conference on Special Interest Group on Data Communication*, 2015, doi: 10.1145/2785956.2787487.

[10] S. Kumar, "Performance Analysis of RSS-Based Localization in Wireless Sensor Networks," *Wireless Personal Communications*, Sep 2019, doi: 10.1007/s11277-019-06428-5.

[11] T. Gigl, G. J. Janssen, V. Dizdarevic, K. Witrisal, and Z. Irahhauten, "Analysis of a UWB Indoor Positioning System Based on Received Signal Strength," in *2007 4th Workshop on Positioning, Navigation and Communication*, 2007, doi: 10.1109/WPNC.2007.353618.

[12] J. Tiemann, F. Schweikowski, and C. Wietfeld, "Design of an UWB indoor-positioning system for UAV navigation in GNSS-denied environments," in *2015 International Conference on Indoor Positioning and Indoor Navigation (IPIN)*, Oct 2015, doi: 10.1109/IPIN.2015.7346960.

[13] I. Oppermann, M. Hämäläinen, and J. Iinatti, *UWB: Theory and Applications*. NJ,USA: John Wiley and Sons: Hoboken, 2005.

[14] J. Kulmer, S. Hinteregger, B. Großwindhager, M. Rath, M. S. Bakr, E. Leitinger, and K. Witrisal, "Using DecaWave UWB transceivers for high-accuracy multipath-assisted indoor positioning," in *2017 IEEE International Conference on Communications Workshops (ICC Workshops)*, May 2017, doi: 10.1109/ICCW.2017.7962828.

[15] D. Dardari, A. Conti, U. Ferner, A. Giorgetti, and M. Z. Win, "Ranging with Ultrawide Bandwidth Signals in Multipath Environments," *Proceedings of the IEEE*, Feb 2009, doi: 10.1109/JPROC.2008.2008846.

[16] G. Kia, L. Ruotsalainen, and J. Talvitie, "Toward Accurate Indoor Positioning: An RSS-Based Fusion of UWB and Machine-Learning-Enhanced WiFi," *Sensors*, 2022, doi: 10.3390/s22093204.

[17] M. Bal, M. Liu, W. Shen, and H. Ghenniwa, "Localization in cooperative Wireless Sensor Networks: A review," in *2009 13th International Conference on Computer Supported Cooperative Work in Design*, 2009, doi: 10.1109/CSCWD.2009.4968098.

[18] K. Witrisal, E. Leitinger, S. Hinteregger, and P. Meissner, "Bandwidth Scaling and Diversity Gain for Ranging and Positioning in Dense Multipath Channels," *IEEE Wireless Communications Letters*, vol. 5, no. 4, pp. 396–399, 2016.

[19] L. Wielandner, E. Leitinger, and K. Witrisal, "RSS-Based Cooperative Localization and Orientation Estimation Exploiting Antenna Directivity," *IEEE Access*, 2021, doi: 10.1109/ACCESS.2021.3070441.

[20] N. Patwari, J. Ash, S. Kyperountas, A. Hero, R. Moses, and N. Correal, "Locating the nodes: cooperative localization in wireless sensor networks," *IEEE Signal Processing Magazine*, 2005, doi: 10.1109/MSP.2005.1458287.

[21] M. Win, F. Meyer, Z. Liu, W. Dai, S. Bartoletti, and A. Conti, "Efficient Multisensor Localization for the Internet of Things: Exploring a New Class of Scalable Localization Algorithms," *IEEE Signal Processing Magazine*, 09 2018, doi: 10.1109/MSP.2018.2845907.

[22] P. Corke, T. Wark, R. Jurdak, W. Hu, P. Valencia, and D. Moore, "Environmental Wireless Sensor Networks," *Proceedings of the IEEE*, 12 2010, doi: 10.1109/JPROC.2010.2068530.

[23] B. Cakmak, D. Urup, F. Meyer, T. Pedersen, B. Fleury, and F. Hlawatsch, "Cooperative Localization for Mobile Networks: A Distributed Belief Propagation - Mean Field Message Passing Algorithm," *IEEE Signal Processing Letters*, 12 2015, doi: 10.1109/LSP.2016.2550534.

[24] H. Wymeersch, J. Lien, and M. Win, "Cooperative Localization in Wireless Networks," *Proceedings of the IEEE*, 03 2009, doi: 10.1109/JPROC.2008.2008853.

[25] H. T. Gidey, X. Guo, K. Zhong, L. Li, and Y. Zhang, "Data Fusion Methods for Indoor Positioning Systems Based on Channel State Information Fingerprinting," *Sensors*, 2022, doi: 10.3390/s22228720.

[26] A. S. Yaro, F. Maly, and P. Prazak, "A Survey of the Performance-Limiting Factors of a 2-Dimensional RSS Fingerprinting-Based Indoor Wireless Localization System," *Sensors*, 2023, doi: 10.3390/s23052545.

[27] J. Bi, M. Zhao, G. Yao, H. Cao, Y. Feng, H. Jiang, and D. Chai, "PSOSVRPos: WiFi indoor positioning using SVR optimized by PSO," *Expert Systems with Applications*, 2023, doi: https://doi.org/10.1016/j.eswa.2023.119778.

[28] S. R. Jondhale, V. Mohan, B. B. Sharma, J. Lloret, and S. V. Athawale, "Support Vector Regression for Mobile Target Localization in Indoor Environments," *Sensors*, 2022, doi: 10.3390/s22010358.

[29] L. Wielandner, E. Leitinger, F. Meyer, and K. Witrisal, "Message Passing-Based 9-D Cooperative Localization and Navigation With Embedded Particle Flow," *IEEE Transactions on Signal and Information Processing over Networks*, 2023, doi: 10.1109/TSIPN.2023.3239697.

[30] L. Wielandner, E. Leitinger, F. Meyer, B. Teague, and K. Witrisal, "Message Passing-Based Cooperative Localization with Embedded Particle Flow," in *ICASSP 2022 - 2022 IEEE International Conference on Acoustics, Speech and Signal Processing (ICASSP)*, 2022, doi: 10.1109/ICASSP43922.2022.9747585.

[31] L. Wielandner, "Bayesian methods for cooperative localization and navigation," dissertation, Graz University of Technology, Austria, 2022.

[32] S. Mazuelas, Y. Shen, and M. Z. Win, "Information Coupling in Cooperative Localization," *IEEE Communications Letters*, 2011, doi: 10.1109/LCOMM.2011.060111.110402.

[33] X. Shen, Y. Liu, and Y. Shen, "On the Spatial Information Coupling in Relative Localization Networks," in *ICC 2021 - IEEE International Conference on Communications*, 2021, doi: 10.1109/ICC42927.2021.9500501.

[34] S. Mazuelas, Y. Shen, and M. Z. Win, "Spatiotemporal Information Coupling in Network Navigation," *IEEE Transactions on Information Theory*, 2018, doi: 10.1109/TIT.2018.2859330.

[35] Y. Li, W. Yu, and X. Guan, "Hybrid TOA-AOA Cooperative Localization for Multiple AUVs in the Absence of Anchors," *IEEE Transactions on Industrial Informatics*, 2024, doi: 10.1109/TII.2023.3266362.

[36] C. Knapp and G. Carter, "The generalized correlation method for estimation of time delay," *IEEE Transactions on Acoustics, Speech, and Signal Processing*, 1976, doi: 10.1109/TASSP.1976.1162830.

[37] Buchner, J., "Imagehash Python Library," 2022, accessed Mar. 4, 2024. [Online]. Available: https://pypi.org/project/ImageHash/

[38] S. Kozat, R. Venkatesan, and M. Mihcak, "Robust perceptual image hashing via matrix invariants," in *2004 International Conference on Image Processing, 2004. ICIP '04.*, 2004, doi: 10.1109/ICIP.2004.1421855.

[39] A. Fuchs, L. Wielandner, D. Neunteufel, H. Arthaber, and K. Witrisal, "Wideband TDoA Positioning Exploiting RSS-Based Clustering," *Sensors*, 2023, doi: 10.3390/s23125772.

[40] S. Grebien, E. Leitinger, K. Witrisal, and B. H. Fleury, "Super-Resolution Estimation of UWB Channels including the Dense Component — An SBL-Inspired Approach," *IEEE Transactions on Wireless Communications*, 2024, doi: 10.1109/TWC.2024.3371352.

[41] E. Leitinger, M. Fröhle, P. Meissner, and K. Witrisal, "Multipath-assisted maximum-likelihood indoor positioning using UWB signals," in *2014 IEEE International Conference on Communications Workshops (ICC)*, 2014, doi: 10.1109/ICCW.2014.6881191.

[42] J. Karedal, S. Wyne, P. Almers, F. Tufvesson, and A. F. Molisch, "A Measurement-Based Statistical Model for Industrial Ultra-Wideband Channels," *IEEE Transactions on Wireless Communications*, vol. 6, no. 8, pp. 3028–3037, 2007.

[43] T. Rappaport, *Wireless communications: Principles and practice*. Prentice Hall, 1996.

[44] S. Grebien, F. Galler, D. Neunteufel, U. Mühlmann, S. J. Maier, H. Arthaber, and K. Witrisal, "Experimental Evaluation of a UHF-MIMO RFID System for Positioning in Multipath Channels," in *2019 IEEE International Conference on RFID Technology and Applications (RFID-TA)*, Sep. 2019, doi: 10.1109/RFID-TA.2019.8892179.

[45] V. H. MacDonald and P. M. Schultheiss, "Optimum Passive Bearing Estimation in a Spatially Incoherent Noise Environment," *The Journal of the Acoustical Society of America*, 07 1969, doi: 10.1121/1.1911659.

[46] B. Lee, A. Said, T. Kalker, and R. W. Schafer, "Maximum Likelihood Time Delay Estimation with Phase Domain Analysis in the Generalized Cross Correlation Framework," in *2008 Hands-Free Speech Communication and Microphone Arrays*, 2008, doi: 10.1109/HSCMA.2008.4538695.

[47] C. Zhang, Z. Zhang, and D. Florencio, "Maximum Likelihood Sound Source Localization for Multiple Directional Microphones," in *2007 IEEE International Conference on Acoustics, Speech and Signal Processing - ICASSP '07*, 2007, doi: 10.1109/ICASSP.2007.366632.

[48] S. T. Buckland, K. P. Burnham, and N. H. Augustin, "Model Selection: An Integral Part of Inference," *Biometrics*, vol. 53, no. 2, pp. 603–618, 1997. [Online]. Available: http://www.jstor.org/stable/2533961

[49] W. von der Linden, V. Dose, and U. von Toussaint, *Bayesian Probability Theory: Applications in the Physical Sciences: Applications in the Physical Sciences*. United Kingdom: Cambridge University Press, Jun. 2014, doi: 10.1017/CBO9781139565608.

[50] A. A. Neath and J. E. Cavanaugh, "The Bayesian information criterion: background, derivation, and applications," *WIREs Computational Statistics*, 2012, doi: https://doi.org/10.1002/wics.199.

[51] G. Steinböck, T. Pedersen, B. H. Fleury, W. Wang, and R. Raulefs, "Distance Dependent Model for the Delay Power Spectrum of In-room Radio Channels," *IEEE Transactions on Antennas and Propagation*, 2013, doi: 10.1109/TAP.2013.2260513.

[52] A. Fuchs and K. Witrisal, "Time-of-Arrival Estimation for Positioning in Bandwidth-Limited Dense Multipath Channels," in *2022 IEEE 23rd International Workshop on Signal Processing Advances in Wireless Communication (SPAWC)*, 2022, doi: 10.1109/SPAWC51304.2022.9833995.

[53] T. Wilding, S. Grebien, U. Mühlmann, and K. Witrisal, "Accuracy Bounds for Array-based Positioning in Dense Multipath Channels," *Sensors*, Dec 2018, doi: 10.3390/s18124249.

[54] E. Leitinger, "Cognitive Indoor Positioning and Tracking using Multipath Channel Information," dissertation, Graz University of Technology, Austria, 2015.

[55] M. Liang and F. Meyer, "Neural Enhanced Belief Propagation for Multiobject Tracking," *IEEE Transactions on Signal Processing*, 2024, doi: 10.1109/TSP.2023.3314275.

D

Performance Bounds for Coherent Chirp Synthesis in Multiband Signals

Andreas Fuchs, Andreas Feiersinger, Klaus Witrisal

Submitted and accepted at EuCAP 2025

Abstract—Radio-based position estimation is severely affected by multipath radio propagation. A sufficiently large signal bandwidth allows for a separation of the line-of-sight signal component from the multipath components and ensures, therefore, accurate positioning. This paper investigates the possibility of combining multiple, consecutively transmitted subband signals into a combined signal with a scaled-up effective bandwidth. The Cramér-Rao lower bound (CRLB) is derived for this time-of-arrival-estimation problem in order to analyze its scaling behavior. It is found that an overlap of the subband signals in the frequency domain can be exploited to increase the effective signal bandwidth. However, this method is only effective in presence of multipath propagation, it does not yield any gain in additive white Gaussian noise (AWGN) channels without multipath. Theoretical results are validated by means of computer simulations for chirp-based radio signals.

The financial support by the Austrian Federal Ministry of Labour and Economy, the National Foundation for Research, Technology and Development and the Christian Doppler Research association is gratefully acknowledged.

D.1 Introduction

D.1.1 State of the Art

In indoor positioning, larger bandwidths generally allow for better delay estimation due to the neccessity to resolve the line-of-sight signal component from multipath [1]. However, generation of coherent signals across large bandwidths is posing a multitude of problems. Practical transceiver chips are often not capable of generating signals with bandwidths larger than a few MHz [2, 3]. With the desire to use, for example, the entire industrial, scientific, and medical (ISM) band, some works attempt to transmit multiple frequency-shifted signals, and synthesize a phase-coherent combined signal by recovering their phase offsets. This enables some coherence between signals and improves indoor positioning performance.

D.1.2 Contribution

This work investigates a method to improve delay estimation for indoor positioning scenarios by exploiting the information from the dense multipath component (DMC) in areas of overlapping frequency bands between multiband signals. The Cramér-Rao lower bound (CRLB) is derived for this estimator to study the effective bandwidth of this technique. The CRLB is compared to a simulation of the algorithm, varying the amount of energy in the DMC with respect to the line-of-sight.

D.1.3 Concept

The concept of the investigated method is demonstrated using simple chirps signals. Figure D.1 shows a frequency overlap between multiple so-called subchirps,

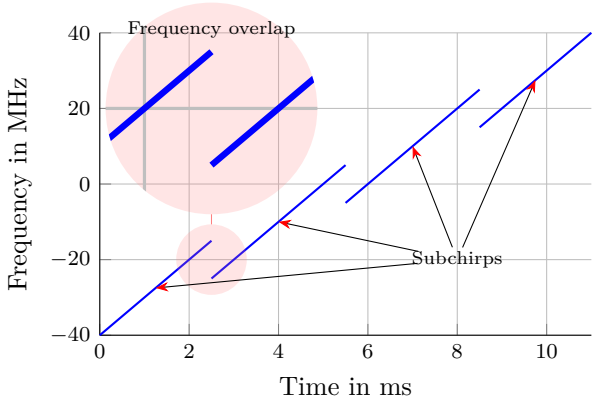

Figure D.1: Concept for overlapping multiband subchirps

spanning an overall bandwidth of 80MHz. These subchirps have a different starting phase, due to the transmitter generating them incoherently [2, 3], but the overall timing between subchirps is known. To use all information efficiently, this work shows a way to improve delay estimation performance by exploiting the characteristic of the dense multipath (DM) being the same for sufficiently short time-periods within overlapping frequency bands. This works by a two step estimation, where the phase differences in the overlapping bands are estimated first by a generalized cross-correlation (GCC), and afterwards a coherent signal model is used to estimate a joint delay for all subchirps with a maximum likelihood (ML) approach.

Notation

Column vectors are denoted by lowercase and matrices by uppercase bold letters. The probability density function (PDF) of a random variable is denoted as $f(\boldsymbol{x})$. For any vector $\boldsymbol{x}$, we denote the transpose as $\boldsymbol{x}^T$, the Hermitian transpose as $\boldsymbol{x}^H$, the complex conjugate as $\boldsymbol{x}^*$, the vector of absolute values as $|\boldsymbol{x}|$, the argument as $\angle x$, the Euclidean norm as $\|\boldsymbol{x}\|$ and the expectation operator as $\mathbb{E}[\boldsymbol{x}]$. Furthermore, we introduce a trace operator as $\mathrm{tr}\{\boldsymbol{X}\}$ for a matrix $\boldsymbol{X}$. $[\boldsymbol{X}]_{n,m}$ denotes the n,m-th element of a matrix, and $[\boldsymbol{x}]_n$ denotes the n-th element of a vector. Zero matrices

are written as $\mathbf{0}_a \times b$, where $a \times b$ describes the dimension. Diagonal matrices are notated as $\text{diag}([\boldsymbol{x}]_{n=l}^{L})$, with indices of the diagonal elements ranging from l to L.

D.2 Signal Model

D.2.1 Chirp-Train Signal

In this section, we explain the model for the chirp-train signal. The overall number of samples are denoted by M, the number of additonal samples for the DM by L and the number of samples without DM by N. The instantaneous frequency of the i-th subchirp with the starting frequency f_i and the chirp rate c is expressed as

$$f_i(t) = ct + f_i, \tag{D.1}$$

with index $i = [1, \ldots, P]$ and P representing the number of subchirps. The instantaneous phase of the i-th subchirp is derived by integrating the instantaneous frequency with an initial phase ϕ_i:

$$\phi_i(t) = \phi_i + 2\pi \left(\frac{ct^2}{2} + f_i t \right). \tag{D.2}$$

The i-th chirp signal is expressed as

$$s_i(t) = \exp(j\phi_i(t)), \tag{D.3}$$

with a sampled version of $s_i(t)$ being

$$s_i[n] = \exp\left(j\phi_i + j2\pi \left(\frac{c\,(nT_s)^2}{2} + f_i n T_s \right) \right), \tag{D.4}$$

where the sample index is $n = [0, \ldots, N_c]$, with N_c being the length of each subchirp, and T_s being the sampling period. Substituting with a sampling frequency normalized chirp rate $m = cT_s$ leads to

$$s_i[n] = x_i[n] p_i, \tag{D.5}$$

where

$$x_i[n] = \exp(j2\pi T_s \left(\frac{mn^2}{2} + f_i n \right)), \tag{D.6}$$

is the i-th subchirp signal without initial phase shift and $p_i = \exp(j\phi_i)$ is the i-th initial phase shift term. For the representation of the chirp train a vector notation is used. First of all, the chirp signal $x_i[n]$ is expressed as

$$\boldsymbol{x}_i = \left[\mathbf{0}_{1\times(i-1)N_c}, x_i[1], \ldots, x_i[N_c], \mathbf{0}_{1\times(L+N_c(P-(i-1)))} \right]^T, \tag{D.7}$$

such that $\boldsymbol{x} = \sum_{i=1}^{P} \boldsymbol{x}_i$. Additionally, L zeros are appended to provide space for a time-shifting operation. The vector form which contains all phase-shifted subchirps is given by $\boldsymbol{s} = \boldsymbol{X}\boldsymbol{p}$, where $\boldsymbol{X} = [\boldsymbol{x}_1, \boldsymbol{x}_1, \ldots, \boldsymbol{x}_P]$ is a stacked representation of the individual vectors from Equation (D.7), and $\boldsymbol{p} = [p_1, \ldots, p_P]^T$ is a vector which contains all phase terms. Furthermore, the matrix representation of the chirp train

vector $\boldsymbol{s}$ where the i-th column contains the phase shifted subchirp $\boldsymbol{x}_i p_i$ is defined as $\boldsymbol{S} = \boldsymbol{X}\,\mathrm{diag}(\boldsymbol{p})$ where the diagonal matrix $\mathrm{diag}(\boldsymbol{p})$ has the diagonal entries $[\mathrm{diag}(\boldsymbol{p})]_{ii} = p_i$.

The sampled time derivative signal of the i-th subchirp can be expressed as

$$\dot{x_i}[n] = j2\pi(mn + f_i)x_i[n], \tag{D.8}$$

which can be expressed in a matrix notation as $\dot{\boldsymbol{s}} = \dot{\boldsymbol{X}}\boldsymbol{p}$, using the time derivative matrix $\dot{X} = [\dot{\boldsymbol{x}}_1, \ldots, \dot{\boldsymbol{x}}_P]$, with the entries of the time derivative vector as

$$\dot{\boldsymbol{x}}_i = \left[\boldsymbol{0}_{1\times(i-1)N_c}, \dot{x}_i[1], \ldots, \dot{x}_i[N_c], \boldsymbol{0}_{1\times(L+N_c(P-(i-1)))}\right]^T, \tag{D.9}$$

to allow the time derivative vector $\dot{\boldsymbol{x}}$ to be expressed as $\dot{\boldsymbol{x}} = \sum_{i=1}^{P} \dot{\boldsymbol{x}}_i$. The matrix representation of the derivative chirp train vector $\dot{\boldsymbol{s}}$ is $\dot{\boldsymbol{S}} = \dot{\boldsymbol{X}}\,\mathrm{diag}(\boldsymbol{p})$. The received signal is then described as

$$r(t) = \alpha s(t-\tau) + (s * \nu)(t) + w(t)\ , \tag{D.10}$$

where α is the complex amplitude of the signal. The stochastic process $\nu(t)$ is described using the power delay profile $S_\nu(t-\tau)$ and the uncorrelated scattering assumption [4, 5] where

$$\mathbb{E}[\nu(t_2)\nu^*(t_1)] = S_\nu(t_1-\tau)\delta(t_2-t_1), \tag{D.11}$$

which means that the process is uncorrelated when $t_1 \neq t_2$ and therefore $\nu(t) \sim \mathcal{CN}(0, S_\nu(t-\tau))$. Under the assumption that the sampling frequency f_s is sufficiently large, Equation (D.10) can be discretized as

$$r[n] = \alpha s(nT_s - \tau) + T_s(s * v)[n] + w[n], \tag{D.12}$$

which can be rewritten into a vector notation as

$$\boldsymbol{r}_{\mathrm{pre}} = \alpha \boldsymbol{W}^H \boldsymbol{P}(\tau)\boldsymbol{W}\boldsymbol{s} + T_s\bar{\boldsymbol{S}}\boldsymbol{\nu} + \boldsymbol{w} \tag{D.13a}$$

$$= \alpha \boldsymbol{W}^H \boldsymbol{P}(\tau)\boldsymbol{W}\boldsymbol{s} + \boldsymbol{n} \in \mathbb{C}^M, \tag{D.13b}$$

where $\boldsymbol{\nu}$ is a realization of the DM process, $\boldsymbol{n}$ is the sum of the two processes,

$$\bar{\boldsymbol{S}} = [\bar{\boldsymbol{s}}_1, \ldots, \bar{\boldsymbol{s}}_M]^T \in \mathbb{C}^{M\times L}, \tag{D.14}$$

is the convolution matrix with entries

$$\bar{\boldsymbol{s}}_k = [s[k], s[k-1], \ldots, s[k-L]]\,. \tag{D.15}$$

where $s[k] = 0$ for $k < 0$.

In the case that the phase vector p is unknown, the line-of-sight (LoS) channel coefficient α simplifies to $|\alpha|$, leading to

$$\boldsymbol{r} = |\alpha|\boldsymbol{W}^H \boldsymbol{P}(\tau)\boldsymbol{W}\boldsymbol{s} + \boldsymbol{n}. \tag{D.16}$$

The noise vector $\boldsymbol{n}$ is distributed according to $\boldsymbol{n} \sim \mathcal{CN}(0, \boldsymbol{C}_n)$. Assuming that additive white Gaussian noise (AWGN) and the DM are uncorrelated the covariance matrix $\boldsymbol{C}_n$ can be expressed as

$$\boldsymbol{C}_n = T_s^2\bar{\boldsymbol{S}}\boldsymbol{C}_\nu\bar{\boldsymbol{S}}^H + \frac{N_0}{T_s}\boldsymbol{I}_M, \tag{D.17}$$

with the identity matrix $\boldsymbol{I}_M$ of according size. The covariance matrix of the DM process which contains the power delay profile (PDP) $S_\nu(t)$ is defined as

$$\boldsymbol{C}_\nu = \operatorname{diag}\Big(\Big[S_\nu(kT_s - \tau)\Big]_{k=1}^{L}\Big). \tag{D.18}$$

A double-exponential PDP is assumed, defined as

$$S_\nu(t-\tau) = \begin{cases} \Omega_1 \left(1 - \exp(-\frac{t-\tau}{\gamma_r})\right) \exp(-\frac{t-\tau}{\gamma_f}) & \text{if } t \geq \tau \\ 0 & \text{otherwise,} \end{cases} \tag{D.19}$$

where Ω_1 is the normalized energy in the DM, describing the energy ratio between the PDP and the LoS. The parameters γ_r and γ_f specify the rise and fall time respectively. The average energy of the DM components can be obtained as

$$\mathbb{E}\Big[\sum_{n=0}^{M-1} |T_s(s * \nu)[n]|^2\Big] = T_s^2 \sum_{n=0}^{M-1} (p_s * S_\nu)[n], \tag{D.20a}$$

where $p_s[n] = |s[n]|^2$ is the signal power at the sample index n. Assuming that N is much larger than L such that $M \approx N$ and $p_s[n] = 1$, Equation (D.20a) can be approximated as

$$\mathbb{E}\Big[\sum_{n=0}^{M-1} |T_s(s * \nu)[n]|^2\Big] \approx T_s^2 N \sum_{k=0}^{\infty} S_\nu[k]. \tag{D.21}$$

Using the above assumptions for the chirp train signal and the approximation from Equation (D.21), we can define an average energy ratio between the LoS and DM as [6]

$$K_{\text{LOS}} = \frac{|\alpha|^2}{T_s \Omega_1}, \tag{D.22a}$$

with the energy normalization factor of the PDP

$$\Omega_1 = \sum_{k=0}^{\infty} S_\nu[k] T_s. \tag{D.23}$$

D.2.2 Maximum likelihood estimator

A ML estimator for the delay of the signal neglecting information from overlaps can be found as [5, 7]

$$\begin{aligned} f_1(\boldsymbol{r} \mid \tau, \boldsymbol{p}, |\alpha|) \propto \exp((\boldsymbol{r} - |\alpha| \boldsymbol{W}^H \boldsymbol{P}(\tau) \boldsymbol{W} \boldsymbol{X} \boldsymbol{p})^H \boldsymbol{C}_n^{-1} \times \\ (\boldsymbol{r} - |\alpha| \boldsymbol{W}^H \boldsymbol{P}(\tau) \boldsymbol{W} \boldsymbol{X} \boldsymbol{p})). \end{aligned} \tag{D.24}$$

For a first estimation of the transmit delay τ, we omit the estimation of DM parameters for computational efficiency. Exploiting this, we can estimate all parameters jointly by maximizing

$$\hat{\tau}, \hat{\boldsymbol{p}}, |\hat{\alpha}| = \underset{\tau, \boldsymbol{p}, |\alpha|}{\arg\max}(-\|\boldsymbol{r} - |\alpha| \boldsymbol{W}^H \boldsymbol{P}(\tau) \boldsymbol{W} \boldsymbol{X} \boldsymbol{p}\|), \tag{D.25}$$

which gives us an estimated parameter set $\hat{\tau}, \hat{\boldsymbol{p}}, |\hat{\alpha}|$ for delay, phases and amplitude respectively. This is possible due to $\boldsymbol{C}_n$ simplifying to a diagonal matrix when we assume only AWGN.

D.2.3 Maximum likelihood estimator with overlap exploitation

Assuming that DM does not change within the transmission time-frame of all subchirps, we can exploit the additional energy within the DM for an estimation of phase differences between subchirps. Using the GCC [8,9], we can find a maximum likelihood estimator for the overlap between two subsequent subchirps as

$$\begin{aligned} f(\boldsymbol{r} \mid \phi_i, \phi_{i+1}) =& |(\boldsymbol{r}[t_{l,i}, \ldots, t_{u,i}] \exp(-j\phi_i)) \times \\ & (\boldsymbol{r}[t_{l,i+1}, \ldots, t_{u,i+1}] \exp(-j\phi_{i+1}))^H|, \end{aligned} \tag{D.26}$$

where $t_{l,i}$ and $t_{u,i}$ and $t_{l,i+1}$ and $t_{u,i+1}$ describe the lower and upper frequency overlap samples between two subsequent subchirps i and $i+1$. Assuming $\phi_i = 0$, one can iteratively estimate all differences between starting phases ϕ_i and ϕ_{i+1}. This assumes that there is no parametric dependency between phases $\boldsymbol{p}$ with delay τ and amplitude $|\alpha|$. Assuming there is no prior information for the first phase ϕ_1, we can notate a joint maximum-likelihood estimator incorporating (D.26) as

$$f(\boldsymbol{r} \mid \tau, \boldsymbol{p}, |\alpha|) \propto f_1(\boldsymbol{r} \mid \tau, \boldsymbol{p}, |\alpha|) \prod_{i=1}^{P-1} f(\boldsymbol{r} \mid \phi_i, \phi_{i+1}), \tag{D.27}$$

which describes a joint distribution with the previous estimator in (D.25), which similarly can now be maximized again to find the delay.

D.3 Cramér-Rao lower bound

D.3.1 Without overlap exploitation

The parameter vector for the CRLB is $\boldsymbol{\theta} = [\tau, |\alpha|, \phi_1^T, \ldots, \phi_N^T]^T$. As the noise vector $\boldsymbol{n}$ has unknown phases due to AWGN, we assume that the covariance matrix $\boldsymbol{C}_n$ is independent of the phases $\boldsymbol{\phi}$. The Fisher information matrix (FIM) element for the time delay τ is:

$$[\boldsymbol{\mathcal{I}}(\boldsymbol{\theta})]_{1,1} = 2\mathrm{Re}\left(\frac{\partial \boldsymbol{\mu}(\boldsymbol{\theta})}{\partial \tau}\right)^H \boldsymbol{C}_n^{-1} \frac{\partial \boldsymbol{\mu}(\boldsymbol{\theta})}{\partial \tau} + \mathrm{tr}[\bullet] \tag{D.28a}$$

$$= 2\mathrm{Re}|\alpha|^2 \boldsymbol{s}^H \boldsymbol{C}_{n,-\tau}^{-1} \boldsymbol{s} + \mathrm{tr}[\bullet] \tag{D.28b}$$

$$= 2|\alpha|^2 \dot{\boldsymbol{s}}^H \boldsymbol{C}_{n,-\tau}^{-1} \dot{\boldsymbol{s}} + \mathrm{tr}[\bullet] \tag{D.28c}$$

$$= \frac{2|\alpha|^2}{\sigma_w^2} \|\dot{\boldsymbol{s}}\|_{\mathcal{H}}^2 + \mathrm{tr}[\bullet]. \tag{D.28d}$$

with

$$\mathrm{tr}[\bullet] = \mathrm{tr}\left[\boldsymbol{C}_n^{-1} \frac{\partial \boldsymbol{C}_n}{\partial \tau} \boldsymbol{C}_n^{-1} \frac{\partial \boldsymbol{C}_n}{\partial \tau}\right], \tag{D.29}$$

and

$$\boldsymbol{D} = \frac{2\pi j f_s}{M} \mathrm{diag}\left(\left[-\frac{M}{2}, \ldots, \frac{M}{2} - 1\right]\right), \tag{D.30}$$

being the frequency domain time derivative matrix for the sampling frequency f_s, and $\boldsymbol{C}_{n,-\tau}$ being a cyclically shifted version of $\boldsymbol{C}_n$ by $-\tau$. We define the time derivative vector of $\boldsymbol{s}$ as

$$\dot{\boldsymbol{s}} = \boldsymbol{W}^H \boldsymbol{D} \boldsymbol{W} \boldsymbol{s}. \tag{D.31}$$

It is assumed that the additional time delay information tr[•], which is mainly caused by the increased received signal length due to the convolution of the chirp-train signal with DM, is negligible for high signal-to-noise ratio (SNR) values and Equation (D.28c) is rewritten by a projection into the Hilbert space to Equation (D.28d), similarly to [10].

For the magnitude $|\alpha|$ of the LoS the FIM element evaluates to

$$[\boldsymbol{\mathcal{I}}(\boldsymbol{\theta})]_{2,2} = 2\mathrm{Re}\left(\frac{\partial \boldsymbol{\mu}(\boldsymbol{\theta})}{\partial |\alpha|}\right)^H \boldsymbol{C}_n^{-1} \frac{\partial \boldsymbol{\mu}(\boldsymbol{\theta})}{\partial |\alpha|} \tag{D.32a}$$

$$= 2\boldsymbol{s}^H \boldsymbol{C}_{n,-\tau}^{-1} \boldsymbol{s} \tag{D.32b}$$

$$= \frac{2}{\sigma_w^2} \|\boldsymbol{s}\|_{\mathcal{H}}^2. \tag{D.32c}$$

The signal energy in the Hilbert space $\mathcal{H}$ is responsible for the information of the magnitude. For the phases $\boldsymbol{\phi} = [\phi_1^T, \ldots, \phi_N^T]^T$ of the chirptrain signal model the corresponding FIM entry is calculated as

$$[\boldsymbol{\mathcal{I}}(\boldsymbol{\theta})]_{i,i} = 2\mathrm{Re}\left(\frac{\partial \boldsymbol{\mu}(\boldsymbol{\theta})}{\partial \boldsymbol{\phi}}\right)^H \boldsymbol{C}_n^{-1} \frac{\partial \boldsymbol{\mu}(\boldsymbol{\theta})}{\partial \boldsymbol{\phi}} \tag{D.33a}$$

$$= 2|\alpha|^2 \mathrm{Re}\ \mathrm{diag}(\boldsymbol{p})^H \boldsymbol{X}^H \boldsymbol{C}_{n,-\tau}^{-1} \boldsymbol{X}\ \mathrm{diag}(\boldsymbol{p}) \tag{D.33b}$$

$$= 2|\alpha|^2 \mathrm{Re} \boldsymbol{S}^H \boldsymbol{C}_{n,-\tau}^{-1} \boldsymbol{S} \tag{D.33c}$$

$$= \frac{2|\alpha|^2}{\sigma_w^2} \mathrm{Re}\langle \boldsymbol{S}, \boldsymbol{S} \rangle_{\mathcal{H}}, \tag{D.33d}$$

where the index $i = 3, \ldots, P+2$ corresponds to the n_ϕ-th phase of the chirptrain model. The information of the n_ϕ-th phase is provided by the signal energy of the n_ϕ-th subchirp in the Hilbert space $\mathcal{H}$. For the time delay $\boldsymbol{\tau}$ and the magnitude $|\alpha|$ of the LoS channel coefficient the corresponding FIM element evaluates to

$$[\boldsymbol{\mathcal{I}}(\boldsymbol{\theta})]_{1,2} = 2\mathrm{Re}\left(\frac{\partial \boldsymbol{\mu}(\boldsymbol{\theta})}{\partial \tau}\right)^H \boldsymbol{C}_n^{-1} \frac{\partial \boldsymbol{\mu}(\boldsymbol{\theta})}{\partial |\alpha|} \tag{D.34a}$$

$$= -2|\alpha| \mathrm{Re} \dot{\boldsymbol{s}}^H \boldsymbol{C}_{n,-\tau}^{-1} \boldsymbol{s} \tag{D.34b}$$

$$= -\frac{2|\alpha|}{\sigma_w^2} \mathrm{Re}\langle \boldsymbol{s}, \dot{\boldsymbol{s}} \rangle_{\mathcal{H}}. \tag{D.34c}$$

For the time delay $\boldsymbol{\tau}$ and the phases $\boldsymbol{\phi}$ of the train signal model the FIM entry calculates to

$$[\boldsymbol{\mathcal{I}}(\boldsymbol{\theta})]_{1,i} = 2\mathrm{Re}\left(\frac{\partial \boldsymbol{\mu}(\boldsymbol{\theta})}{\partial \tau}\right)^H \boldsymbol{C}_n^{-1} \frac{\partial \boldsymbol{\mu}(\boldsymbol{\theta})}{\partial \boldsymbol{\phi}} \tag{D.35a}$$

$$= 2|\alpha|^2 \mathrm{Im} \dot{\boldsymbol{s}}^H \boldsymbol{C}_{n,-\tau}^{-1} \boldsymbol{S} \tag{D.35b}$$

$$= \frac{2|\alpha|^2}{\sigma_w^2} \mathrm{Im}\langle \boldsymbol{S}, \dot{\boldsymbol{s}} \rangle_{\mathcal{H}}. \tag{D.35c}$$

For the magnitude $|\alpha|$ of the LoS channel coefficient and the phases $\boldsymbol{\phi}$ of the train signal model the FIM element is expressed as

$$[\boldsymbol{\mathcal{I}}(\boldsymbol{\theta})]_{2,i} = 2\mathrm{Re}\left(\frac{\partial \boldsymbol{\mu}(\boldsymbol{\theta})}{\partial |\alpha|}\right)^H \frac{\partial \boldsymbol{\mu}(\boldsymbol{\theta})}{\partial \boldsymbol{\phi}} \tag{D.36a}$$

$$= -2|\alpha|\mathrm{Im}\boldsymbol{s}^H \boldsymbol{C}_{n,-\tau}^{-1} \boldsymbol{S} \tag{D.36b}$$

$$= -\frac{2|\alpha|}{\sigma_w^2}\mathrm{Im}\langle \boldsymbol{S}, \boldsymbol{s}\rangle_{\mathcal{H}}. \tag{D.36c}$$

The time-delay error bound is calculated using the Schur complement as

$$[\boldsymbol{\mathcal{I}}^{-1}(\boldsymbol{\theta})]_{1,1} = \left(2\frac{|\alpha|^2}{\sigma_w^2}\left(F - \boldsymbol{G}\boldsymbol{H}^{-1}\boldsymbol{G}^T\right)\right)^{-1} \tag{D.37}$$

with

$$F = |\alpha|^2 \|\dot{\boldsymbol{s}}\|_{\mathcal{H}}^2 + \frac{\sigma_w^2}{2|\alpha|^2}\,\mathrm{tr}[\bullet] \in \mathbb{R}, \tag{D.38}$$

$$\boldsymbol{G} = [-\mathrm{Re}\langle \boldsymbol{s}, \dot{\boldsymbol{s}}\rangle_{\mathcal{H}}, |\alpha|\mathrm{Im}\langle \boldsymbol{S}, \dot{\boldsymbol{s}}\rangle_{\mathcal{H}}] \in \mathbb{R}^{1\times P}, \tag{D.39}$$

and

$$\boldsymbol{H} = \begin{bmatrix} \|\boldsymbol{s}\|_{\mathcal{H}}^2 & -|\alpha|\mathrm{Im}\langle \boldsymbol{S}, \boldsymbol{s}\rangle_{\mathcal{H}} \\ -|\alpha|\mathrm{Im}\langle \boldsymbol{S}, \boldsymbol{s}\rangle_{\mathcal{H}}{}^T & |\alpha|^2\mathrm{Re}\langle \boldsymbol{S}, \boldsymbol{S}\rangle_{\mathcal{H}} \end{bmatrix} \in \mathbb{R}^{P\times P}. \tag{D.40}$$

Therefore, Equation (D.37) can be rewritten as

$$[\boldsymbol{\mathcal{I}}^{-1}(\boldsymbol{\theta})]_{1,1} = \left(2\frac{|\alpha|^2}{\sigma_w^2}\left(\|\dot{\boldsymbol{s}}\|_{\mathcal{H}}^2 - \boldsymbol{G}\boldsymbol{H}^{-1}\boldsymbol{G}^T\right) + \mathrm{tr}[\bullet]\right)^{-1}. \tag{D.41}$$

It can be seen that the time-delay error bound from Equation (D.41) has a term which accounts for the unknown phases $\boldsymbol{\phi}$ of the chirp-train signal. It should be noted that the time-delay error bound in general depends on those phase shifts.

D.3.2 With overlap exploitation

As described in Section D.2.3, we can exploit the assumption that the realisation of the dense multipath does not change within a single-shot measurement. Therefore we can exploit overlapping parts of chirps in the frequency domain. Using the estimator in (D.27), we can define a prior information term for $\boldsymbol{\phi}$ as

$$[\boldsymbol{\mathcal{B}}(\boldsymbol{\theta})]_{i,i} = \widetilde{\mathrm{SNR}}\; 2\tilde{N} \tag{D.42}$$

for all $i \geq 4$, meaning additional information is available for all ϕ_{n_ϕ} with $n_\phi \geq 2$ and the number of overlapping samples in the frequency domain for two chirps $\tilde{N}$. This is similar to [11, p. 33, Ex 3.4], which describes the estimation of a phase term in AWGN. The additional SNR is defined as

$$\widetilde{\mathrm{SNR}} = \frac{\sigma_\nu}{\sigma_w}, \tag{D.43}$$

which is the ratio between the variance of the dense multipath and the variance of the AWGN. Note that this neglects the energy in the signal $\boldsymbol{s}$, as no additional information can be gained from the signal energy when it is already used in the estimator described in (D.25). Combining the prior information term $[\boldsymbol{\mathcal{B}}(\boldsymbol{\theta})]_{i,i}$ with the phase information from the signal energy as described in (D.33), we derive a modified phase information term

$$[\widetilde{\boldsymbol{\mathcal{I}}}(\boldsymbol{\theta})]_{i,i} = [\boldsymbol{\mathcal{B}}(\boldsymbol{\theta})]_{i,i} + [\boldsymbol{\mathcal{I}}(\boldsymbol{\theta})]_{i,i} \tag{D.44}$$

for all $i \geq 4$. All further derivations are similar to subsection D.3.1.

D.4 Evaluation

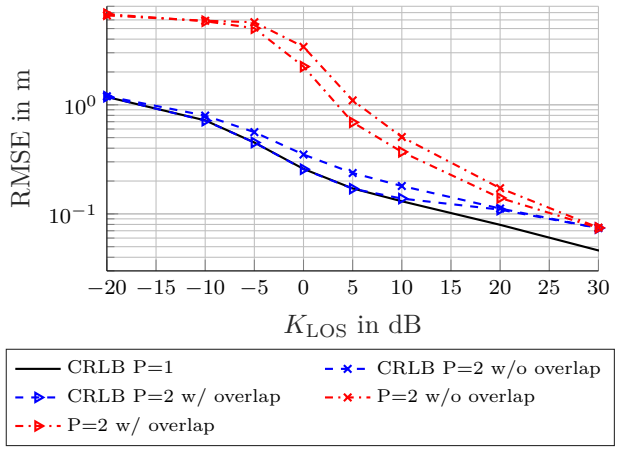

Figure D.2: CRLB and root-mean-square error (RMSE) for 2 subchirps. Comparison with CRLB of one subchirp. 200 realizations for evaluation, SNR = 40dB, $\gamma_r = 5$ns, $\gamma_f = 20$ns

We simulated 200 realizations of the DMC under varying transmission times, maintaining a constant overall SNR across different values of K_{LOS}. The SNR was defined as SNR $= \frac{|\alpha|^2/T_s+\sigma_\nu}{\sigma_w}$, representing the ratio of signal energy and DM to noise. A particle-based estimator with 5000 particles was used to jointly estimate delay and phases. The full bandwidth for single chirps was chosen as 80MHz, and $N = 300$ samples were used. For evaluations with 2 and 4 subchirps, the subchirps were split equally over the frequency band, with an overlap factor of 20%, maintaining total signal energy. As one can see in Figure D.2, for large values of K_{LOS}, all evaluations converge to the the same value. This shows that with negligible energy in the DM, the estimation of phases in overlapping frequency bands does not benefit the delay estimation. This leads to the estimator without prior information for phases to be efficient. For very small values of K_{LOS}, the estimators diverge from the CRLB, being limited only by the estimation prior for the delay. In this region there is negligible energy in the LoS, and thus additional information for the phases between chirps leads to no additional coherency for chirps in the LoS. In the region between, the CRLB without overlap exploitation

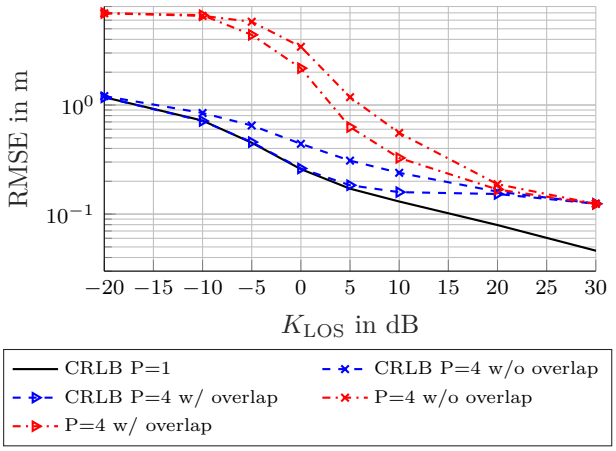

Figure D.3: CRLB and RMSE for 4 subchirps. Comparison with CRLB of one subchirp. 200 realizations for evaluation, SNR = 40dB, $\gamma_r = 5$ns, $\gamma_f = 20$ns

has a significant offset from the CRLB for a continuous chirp ($P = 1$). This is due to the two subchirps not being perfectly coherent, as the phase estimation diminishes the available information. When exploiting the overlap, one can see that for smaller values of K_{LOS}, the CRLB almost attains the CRLB for a continuous chirp. The evaluations could not attain the CRLB in this threshold range. But a significant improvement can be seen between the curves exploiting the overlap and those without overlap exploitation. These performance gains are comparable to the gains seen in the CRLB. Figure D.3 shows very similar behaviour, but all evaluations are shown for $P = 4$ subchirps. For extremes of K_{LOS}, the behaviour is again similar with or without overlap exploitation. For the threshold region, behaviour is again very similar, but the performance gains from overlap exploitation are slightly larger. This can be explained by the more significant loss from phase estimation, which can be compensated to a higher degree with additional energy from the DM due to more overlapping parts of the signal in the frequency domain. It should be noted that the performance for multiple phase-offset chirps decreases even for LoS conditions directly with the number of chirps due to additional nuisance parameters. Additional information could be available when a transceiver chip is able to switch between bands with coherent phases. In the case where phases are known perfectly, the accuracy is equivalent to a single coherent chirp.

D.5 Conclusion

This work shows a method to improve the ranging accuracy in signals with overlapping frequency bands in scenarios with DM, and their respective performance bounds. An estimator and these bounds were derived for any number of signals with overlapping bands. A comparison was done with the performance neglecting the joint frequency bands between signals, and with one single coherent signal. These evaluations show a significant margin for improvement, which could be applied to a variety of different scenarios. These scenarios are not constrained to

indoor localization, but this additional information gain could potentially be used generally for many different wireless communication networks.

Bibliography

[1] A. Quazi, "An overview on the time delay estimate in active and passive systems for target localization," *IEEE Transactions on Acoustics, Speech, and Signal Processing*, June 1981, doi: 10.1109/TASSP.1981.1163618.

[2] D. Neunteufel, A. Fuchs, and H. Arthaber, "ToF-based Indoor Positioning for Low-power IoT Nodes," in *2020 54th Asilomar Conference on Signals, Systems, and Computers*, Nov 2020, doi: 10.1109/IEEECONF51394.2020.9443431.

[3] D. Neunteufel, S. Grebien, S. Hechenberger, K. Witrisal, and H. Arthaber, "Coherent Chirp Generation by Narrowband Transceiver Chips for ToF Indoor Localization," in *GLOBECOM 2020 - 2020 IEEE Global Communications Conference*, 2020, doi: 10.1109/GLOBECOM42002.2020.9348025.

[4] Witrisal, Klaus and Meissner, Paul and Leitinger, Erik and Shen, Yuan and Gustafson, Carl and Tufvesson, Fredrik and Haneda, Katsuyuki and Dardari, Davide and Molisch, Andreas F. and Conti, Andrea and Win, Moe Z., "High-Accuracy Localization for Assisted Living: 5G systems will turn multipath channels from foe to friend," *IEEE Signal Processing Magazine*, 2016, doi: 10.1109/MSP.2015.2504328.

[5] A. Fuchs and K. Witrisal, "Time-of-Arrival Estimation for Positioning in Bandwidth-Limited Dense Multipath Channels," in *2022 IEEE 23rd International Workshop on Signal Processing Advances in Wireless Communication (SPAWC)*, 2022, doi: 10.1109/SPAWC51304.2022.9833995.

[6] D. Neunteufel, S. Grebien, and H. Arthaber, "Indoor Positioning of Low-Cost Narrowband IoT Nodes: Evaluation of a TDoA Approach in a Retail Environment," *Sensors*, 2022, doi: 10.3390/s22072663.

[7] S. Grebien, F. Galler, D. Neunteufel, U. Mühlmann, S. J. Maier, H. Arthaber, and K. Witrisal, "Experimental Evaluation of a UHF-MIMO RFID System for Positioning in Multipath Channels," in *2019 IEEE International Conference on RFID Technology and Applications (RFID-TA)*, Sep. 2019, doi: 10.1109/RFID-TA.2019.8892179.

[8] C. Knapp and G. Carter, "The generalized correlation method for estimation of time delay," *IEEE Transactions on Acoustics, Speech, and Signal Processing*, 1976, doi: 10.1109/TASSP.1976.1162830.

[9] V. H. MacDonald and P. M. Schultheiss, "Optimum Passive Bearing Estimation in a Spatially Incoherent Noise Environment," *The Journal of the Acoustical Society of America*, 07 1969, doi: 10.1121/1.1911659.

[10] K. Witrisal, E. Leitinger, S. Hinteregger, and P. Meissner, "Bandwidth Scaling and Diversity Gain for Ranging and Positioning in Dense Multipath Channels," *IEEE Wireless Communications Letters*, vol. 5, no. 4, pp. 396–399, 2016.

[11] S. M. Kay, *Fundamentals of Statistical Signal Processing: Estimation Theory*. USA: Prentice-Hall, Inc., 1993.

Graz University of Technology